

UNCLASSIFIED

AD NUMBER
AD838041
NEW LIMITATION CHANGE
TO Approved for public release, distribution unlimited
FROM Distribution authorized to DoD only. Other requests shall be referred to Naval Training Device Ctr., Code 424, Orlando, FL 32813.
AUTHORITY
Naval Training Device Ctr. ltr dtd 3 Jul 1972

THIS PAGE IS UNCLASSIFIED

Technical Report: NAVTRADEVCEM 66-C-0031-1

STUDY, SIMULATION OF OCEANOGRAPHIC AND
GEOPHYSICAL SPACE-SENSOR DISPLAYS

David T. Chang
William K. Widger, Jr.

Allied Research Associates, Inc.
Concord, Massachusetts
Contract N61559-66-C-0031

January 1968

AUG 23 1968

~~STATEMENT IS UNCLASSIFIED~~

Each transmittal of this document outside the Department of
Defense must have prior approval of _____

NAVAL TRAINING DEVICE CENTER

ORLANDO, FLORIDA

code 424

**STUDY, SIMULATION OF OCEANOGRAPHIC AND
GEOPHYSICAL SPACE-SENSOR DISPLAYS**

ABSTRACT

Detailed analyses have been performed of the factors which affect the acquisition of geophysical data by earth oriented satellites. These factors include geophysical, instrumental and display. Based on these analyses, techniques for the simulation of satellite data and for the training of personnel participating in satellite geophysics are discussed.

Devices useful for training have been conceptually designed. In particular, the design and the use of an APT (Automatic Picture Transmission) simulator trainer are analyzed in detail.

Reproduction of this publication in whole or in part is
permitted for any purpose of the United States Government

FOREWORD

This report is the result of a study of space-obtained weather data and the simulation techniques applicable thereto for presentations, in a dynamic manner, based on operational sensors. The study provides performance evaluation of satellite sensor characteristics and evaluation of the visual parameters to be considered for training systems and devices for aiding observers of the ocean state.

The study determines the feasibility of simulating visual displays of oceanographic and geophysical data as sensed by space vehicle equipment for training in the comprehension, interpretation and utilization of satellite telemetered data for fleet logistical application.

The study also provides atmospheric and oceanographic intelligence data parameters for air/ocean interface characteristics, and proposes techniques for their simulation, detection, acquisition, storage and display in experimental multi-sensor space surveillance simulators.

Robert Lee Wyener

ROBERT LEE WYENER
Project Engineer
NAVAL TRAINING DEVICE CENTER

TABLE OF CONTENTS

	Page
FOREWORD	i
LIST OF FIGURES	ix
LIST OF TABLES	xvi
SECTION I: INTRODUCTION	1
1.1 Statement of the Problem	1
1.2 Scope of the Study	3
SECTION II: ORBITAL PARAMETERS PERTINENT TO SATELLITE GEOPHYSICS	7
2.1 Orbit Velocities and Periods for a Non-Rotating Earth	7
2.1.1 Circular Orbit Velocities	7
2.1.2 Circular Orbit Periods	10
2.1.3 Elliptical Orbits	11
2.2 Orbit Orientation	13
2.2.1 Orbit Inclination	13
2.2.2 Ascending Node	14
2.3 Effect of Earth Rotation	15
2.3.1 Subpoint Tracks and Heading Lines	15
2.3.2 Satellite Velocities Over Earth's Surface	22
2.4 Effects of the Oblateness of the Earth	22
2.4.1 Precession of the Plane of the Orbit	23
2.4.2 Rotation of the Orbital Ellipse in its Own Plane	26
2.5 Computation of Orbital Elements and Ephemerides	32
2.6 Satellite Viewing Geometry	38
2.7 Errors in Geographical Locations of Data	42

TABLE OF CONTENTS (cont)

	<u>Page</u>
SECTION VI: SATELLITE SENSOR SYSTEM EFFECTS	101
6.1 Introduction	101
6.2 Spectral Selectivity	103
6.2.1 Spectral Response	103
6.2.2 Spectral Resolution	104
6.3 Spatial Resolution and Geometric Distortions of Non-Imaging Systems	106
6.3.1 Spatial Resolution	106
6.3.2 Distortions Introduced by Sensing and Recording Systems	111
6.4 Imaging Systems	116
6.4.1 The Television Camera	118
6.4.2 Distortions and Degradations in a Television Camera System	126
6.5 Contrast Considerations	129
6.6 The Effects of Noise	135
6.7 A Note on the Calibration of IR Sensors	137
6.8 The Effects of the Display Format on Satellite Acquired Data	140
6.8.1 Examples of Some Common Display Formats	142
SECTION VII: EARTH-SYNCHRONOUS SATELLITES	151
7.1 Introduction	151
7.2 Problems Associated with Sensor Resolution from Synchronous Altitudes	154
7.3 A Note on ATS-B	157
SECTION VIII: A BRIEF SURVEY OF SATELLITE OBSERVATIONS	161
8.1 Surface Temperature	161
8.2 Atmospheric Temperature	162
8.3 Humidity	163
8.4 Clouds	163
8.5 Storms, Hurricanes, Fronts and Synoptic Patterns	164
8.6 Sea State	164
8.7 Hydrological Features	165
8.8 General Surface Observations	165
8.9 Summary of Sensor/Data Systems	166

TABLE OF CONTENTS (cont)

	<u>Page</u>
SECTION IX: OBSERVATIONS AND MEASUREMENTS IN THE VISIBLE	169
9.1 Introduction	169
9.2 A Note on the Application of Visible Observations from Satellites to Surface Surveillance	170
9.3 Examples of Some of the Visible Observations Made from Satellites	173
9.3.1 Determination of Cloud Altitudes	173
9.3.2 Observations of Surface Features	174
9.3.3 Meteorological Observations	174
9.4 Applications of Optical Lasers to Geophysical Observations from Satellites	183
9.4.1 Introduction	183
9.4.2 Lasers	183
9.4.3 Obscurations and Targets	184
9.4.4 Laser Probing Systems in Use	185
9.4.5 Presentation of Data	187
SECTION X: INFRARED OBSERVATIONS AND MEASUREMENTS	189
10.1 Introduction	189
10.2 Infrared Window Observations	194
10.2.1 Geophysical Degradation Factors in Infrared Window Measurements	194
10.2.2 Geophysical Parameters Deducible from Infrared Window Measurements	200
10.3 Measurements in Atmospheric Infrared Absorption Bands	231
10.3.1 Introduction	231
10.3.2 Geophysical Factors Degrading Absorption Band IR Measurements	235
10.3.3 Parameters Deducible from IR Absorption Band Measurements	236
10.3.4 Examples of Satellite Measurements in IR Absorption Bands	244
10.4 Measurements of Total Outgoing Radiation	247
10.5 Importance of Simultaneous Multispectral Measurements in the IR	248

NAVTRADEVCECEN 66-C-0031-1
TABLE OF CONTENTS (cont)

	<u>Page</u>
SECTION XI: MICROWAVE OBSERVATIONS AND MEASUREMENTS	251
11.1 Microwave Radiometry	251
11.1.1 Introduction	251
11.1.2 Equation of Transfer	253
11.1.3 Parameters Deducible from Micro- wave Radiometric Measurements	253
11.2 Radar Observations from Satellites	255
11.2.1 Introduction	255
11.2.2 Display Techniques	256
11.2.3 Terrestrial Applications of Space- craft Radars	258
SECTION XII: DATA COLLECTION SATELLITES	261
12.1 Introduction	261
12.2 Methods for the Location of Moving Platforms	262
12.3 Training Problems	265
SECTION XIII: SATELLITE TRANSMISSION OF FACSIMILE WEATHER CHARTS (WEFAX)	267
13.1 Introduction	267
13.2 Types and Numbers of Charts Available from WEFAX	268
13.3 Training Requirements	272
SECTION XIV: THE GROUND COMPLEX REQUIRED TO SUPPORT A SATELLITE	275
14.1 Introduction	275
14.2 Tracking	275
14.3 Data Acquisition	276
14.4 Data Processing and Dissemination	277
SECTION XV: BRIEF ANALYSIS OF TRAINING REQUIREMENTS FOR NAVY PERSONNEL	283
15.1 Introduction	283
15.2 Delineation of the Areas Requiring Training	286
15.2.1 Nephys	286
15.2.2 Modifications to FNWF Input Data	287
15.2.3 APT Mode of Data Acquisition	287
15.2.4 Background Training in the Fundamentals of Satellite Geophysics	289

TABLE OF CONTENTS (cont)

	<u>Page</u>
SECTION XVI: SIMULATION AND TRAINING TECHNIQUES	291
16.1 Introduction	291
16.2 Simulation of Satellite Data	291
16.2.1 Available Space-Acquired Data	291
16.2.2 Computer Simulation of Satellite Data	292
16.3 Training Techniques and Devices Pertinent to Interpretation of Satellite Data	298
16.3.1 Introduction	298
16.3.2 Source of Interpretation Practices and Procedures	299
16.3.3 Demonstration Devices	303
16.3.4 Case Studies for Laboratory Practice	307
16.4 Devices for Simulating Satellite Orbital Geometry	319
16.4.1 Global Simulator	319
16.4.2 Polar Projection Plotting-Board	321
16.5 Techniques for the Demonstration of the Effects of Satellite Viewing Geometry	323
16.6 Techniques for the Demonstration of Radiation Processes of Significance to Satellite Geophysics	323
SECTION XVII: APT TRAINING SIMULATOR	329
17.1 Introduction	329
17.2 Summary of Operational Procedures Associated with the APT	329
17.3 Description of Ancillary Equipment	330
17.3.1 Tracking Board and its Associated Orbital Overlay and Tracking Diagram	331
17.3.2 Charts and Tables	331
17.3.3 Geographical Grids	331
17.4 Simulation of APT Procedures	336
17.5 Simulator Description	337
REFERENCES	343

LIST OF FIGURES

<u>Figure</u>		<u>Page</u>
1a	Geometry and Definitions for an Elliptical Orbit	8
1b	Orbital Definitions	8
2a	Velocity and Period of an Earth Satellite in a Circular Orbit at Various Altitudes	8
2b	Velocity and Period of an Earth Satellite in a Circular Orbit at Various Altitudes	8
2c	Speed of a Satellite in an Elliptic Orbit, for a Series of Values of Average Height	8
3a	Subpoint Tracks for Several Typical TIROS Orbits (TIROS VI, Orbits 2202-2205)	16
3b	Typical Nimbus (Quasi-polar) Orbits	16
4	Depiction of Satellite Orbit, Heading Line, and Subpoint Track	18
5	Geometry of Heading Line or Subpoint Track	18
6	Rate of Rotation of Satellite Orbital Plane	18
7	Day-to-Day Change of Illuminated Latitudinal Belt Observable from a Single TIROS in a 58° Inclination Orbit	27
8	Orbital Period, Number of Orbits per Day, and Inclination of a Sun Synchronous Orbit	27
9	Relationships Between Perigee, and Argument for an Elliptical Orbit	27
10	Rate of Rotation of Elliptical Orbit in its Own Plane	30
11	Satellite Viewing Geometry	30
12a	Height of a Satellite vs. Great-Circle Distance from Subpoint of Objects at Different Nadir Angles	30
12b	Heights and Nadir Angles Needed for TIROS	30
13	Spacecraft Axes	43
14	Yaw Error Lever Arm	43
15	Electromagnetic Spectrum	46
16	Radiometer Geometry	51
17	Solid Angle Geometry	51
18	Blackbody Curves	59

LIST OF FIGURES (cont)

<u>Figure</u>		<u>Page</u>
19	Normalized Blackbody Curve for $T = 300^{\circ}\text{K}$	55
20	IR Emissivity of a Water Surface	66
21	Spectral Emissivity of Soil Sample from Pawnee Grassland, Colorado	69
22	Spectral Emissivity of Soil Sample from Rosemond Dry Lake, California	69
23	IR Reflectivity and Emissivity of a Water Surface as a Function of Angle	73
24	Solar Irradiance at the Top of the Atmosphere	73
25	Normalized Blackbody Curves for $T = 6000^{\circ}\text{K}$ and $T = 800^{\circ}\text{K}$	75
26	Solar Irradiance at the Surface of the Earth	75
27	Spectral Reflectivities of Unvegetated Surfaces	77
28	Spectral Reflectivities of Vegetated Surfaces	78
29	Atmospheric Absorption Spectrum in the IR	85
30	Atmospheric Absorption Spectrum in the Microwave	85
31	Attenuation Coefficient for Air at Three Representative Heights	89
32	Absorption in an Infinitesimal Layer	89
33	Molecular Scattering Attenuation in the Visible	94
34a	Generalized Block Diagram of a Satellite Sensor System	192
34b	Block Diagram of the Nimbus HRIR	102
35	Spectral Response Function of the HRIR	105
36	Variation of Resolution with Nadir Angle	105
37	Derivative of Earth Scan with Respect to Recorder Scan as a Function of Object Nadir Angle, for Nimbus II	115
38	Reduced-Scale DRIR Latitude-Longitude Grid	115
39	Rectifications of Nimbus I HRIR Data	117
40	Schematic of a Television Camera System	119
41	Television Camera Viewing Geometry	119
42	APT vs. AVCS coverage	119
43	Geometry of a Television Camera Viewing at Nadir Angles Other than Zero	119

LIST OF FIGURES (cont)

<u>Figure</u>		<u>Page</u>
44	Correction for TIROS Lens Distortion	128
45	Types of Electronic Distortions	128
46	Nimbus AVCS Fiducial Matrix	130
47	Transfer Functions	130
48	Nimbus AVCS Photograph with Grey Scale Wedge	134
49	In-Flight Calibrations of Transfer Functions of Nimbus I AVCS Cameras	134
50	Calibration Curve of Nimbus HRIR	136
51a	Nimbus I HRIR Scan 276, Illustrating Oscillatory Noise Superimposed on the Data	138
51b	Suppression of Oscillatory Noise by Computing Running Means	138
52	Nimbus I HRIR Analog Trace	143
53a	Photofacsimile Display	143
53b	Digital Display	143
54a	Computer Analysis Display of Typhoon Sally	145
54b	HRIR Photofacsimile Depiction of Typhoon Sally	145
55	Pictorial Display of Nimbus II MRIR Data	146
56a	HRIR View of a Cloud Vortex, a Frontal Cloud Band and a Hurricane	147
56b	Nephanalysis Prepared from Figure 56a	147
57a	TIROS VII Television Mosaic	148
57b	Nephanalysis Prepared from Figure 57a	148
58	Local Object Zenith Angles of Points within Range of ATS-B	152
59	ATS-B Geographic Grid	153
60	Cloud Photograph from Synchronous Altitude	159
61a	Selected Terrestrial Features	175
61b	Selected Terrestrial Features	176
61c	Selected Terrestrial Features	177
61d	Selected Terrestrial Features	178
62	Satellite Depictions of Tropical Storms and Cyclones	180
63	Satellite Depictions of Cyclones at Various Stages of Development	181

LIST OF FIGURES (cont)

<u>Figure</u>		<u>Page</u>
64	Gemini 10 Photograph of the Northeast Coast of South America	182
65	Nimbus Photograph of the Northeast Coast of South America	182
66	Schematic of a Stratified Atmosphere	191
67	Clear Sky Temperature Corrections for Window Channel of TIROS VII	197
68	Clear Sky Temperature Corrections for Nimbus HRIR	197
69	Quantitative Relationships between Temperature of a Radiating Surface, Total Radiation as Measured by HRIR, and Solar Reflectivity	199
70a	Field of Effective Temperatures from TIROS II, Orbit 367 at 0547 EST, 18 December 1960	199
70b	Synoptic Chart for 18 December 1960, 0500 EST and 0600 EST	199
71	Sea Surface Temperature Pattern as Observed by TIROS VII, Orbit 779, in the Vicinity of the Kuroshio Current	202
72a	TIROS II Radiation Data, 8 to 12 Micron Window, 1810 GMT, 23 November 1963	204
72b	Cloud Cover Chart for 1800 GMT, 23 November 1960	204
73a	HRIR View of a Well Developed Shortwave Trough	206
73b	Lee Waves as Observed in the HRIR	206
74	HRIR Mosaic for 18 September 1964	207
75	HRIR Mosaic with NMC 500 mb Analysis and Russian Frontal Analysis, 0000 GMT, 19 September 1964	207
76a	Field of Effective Temperatures from TIROS II, Orbit 406, at 2150 CST, 20 December 1960, Superimposed on Cloud Cover Analysis	208
76b	Surface Air Temperatures and Reported Snow Cover, 2100 CST, 20 December 1960	208
77	Illustration of the Effects of the Latitudinal and Frontal Temperature Gradients on HRIR Data	210

LIST OF FIGURES (cont)

<u>Figure</u>		<u>Page</u>
78	Cloud Top Height Determination Using HRIR Data (Hurricane Gladys)	210
79	Height of Cloud Tops, 1800 GMT, 23 November 1960, as Estimated from TIROS II Radiation Measurements	212
80	Comparison Between Cloud Top Height Determined from Radiosonde Data and that Deduced from Satellite Radiation Data in the Presence of Subsidence Inversion	214
81a	Nimbus I HRIR Daylight View of Western Europe and the Mediterranean	216
81b	Nimbus I HRIR Daylight View of the Western United States and Eastern Pacific Ocean	216
82	HRIR Mosaic with NMC 500 mb Analysis and Russian Frontal Analysis, 16-17 September 1964	220
83	HRIR Mosaic with NMC 500 mb Analysis and Russian Frontal Analysis, 17-18 September 1964.	221
84	HRIR Observations of Cloud Vortices and Frontal Bands	221
85	HRIR Ocean and Terrain Temperatures Over the South- western U.S. on 30 August 1964	227
86	HRIR "Photograph" of an Iceberg	227
87	HRIR Observations Over South America, 14 September 1964	227
88	Geometry for Target Detection	229
89	Vertical Profile of (ϵ_j, τ'_j) for the 15μ Channel of TIROS VII	229
90a	Schematic of the Vertical Profiles of ϵ_j and τ'_j for a Well-Mixed Gas	229
90b	Schematic of the Vertical Profile of (ϵ_j, τ'_j) for a Well- Mixed Gas	229
91	Weighting Functions for the 15μ Channel of TIROS VII	234
92	Weighting Functions at Six Spectral Intervals in the 15μ Band	234
93	Solutions to the Temperature Inversion Problem for Four Selected Radiosonde Observations	239
94a	Weighting Functions of TIROS Radiometer	241

NAVTRADEVCEEN 66-C-0031-1
LIST OF FIGURES (cont)

<u>Figure</u>		<u>Page</u>
94b	Moller Diagram for the Evaluation of Relative Humidity from Satellite Radiation Measurements	243
95	Mean Stratospheric Temperatures for 19-28 June 1963, as Determined by TIROS VII	245
96	Mean Stratospheric Temperatures for 16-25 January 1964 as Determined by TIROS VII	245
97	Mapping of Mean Tropospheric Relative Humidity Based on TIROS III Channel 1 Data, (Orbit 61)	246
98	Transfer of Microwave Radiation	254
99	Maximum WEFAX Coverage (on Overhead Pass) that would be Acquired by a Station at 40°N from a Sun-Synchronous Transmission	270
100	Simplified Block Diagram of the Nimbus Data Acquisition Facility	278
101	Block Diagram of NOMSS Data Processing System	279
101a	Simplified Satellite Data Flow Chart	285
102a	Map of Simulated IR Window Effective Temperatures Over the U.S.	297
102b	Surface Map, 0000 GMT, 6 March 1959	297
103	Comparison between Aircraft and Satellite View of Clouds	306
104a	Conventional Surface Analysis, 0000 GMT, 9 September 1964	308
104b	NMC 500 mb Analysis, 1200 GMT, 9 September 1964	308
104c	Nimbus I HRIR Data for Orbit 174, 9 September 1964	309
104d	Nephanalysis Prepared from Orbit 174 of Nimbus I HRIR	309
104e	TIROS VII Television Picture Mosaic, 8 September 1964	310
104f	Nephanalysis Prepared from Mosaic of Figure 104e	311
105	Relation of Observed Window IR Cloud Pattern to TV Picture and Conventional Data, 2215 GMT, 9 April 1962	312

LIST OF FIGURES (cont)

<u>Figure</u>		<u>Page</u>
106	Relation of Observed Window IR Cloud Pattern to TV Picture and Conventional Data, 2140 GMT, 10 April 1962	313
107	Relation of Observed Window IR Cloud Pattern to TV Picture and Conventional Data, 2100 GMT, 11 April 1962	314
108	Relation of Observed Window IR Cloud Pattern to TV Picture and Conventional Data, 1955 GMT, 11 April 1962	315
109	Relation of Observed Window IR Cloud Pattern to TV Picture and Conventional Data, 1915 GMT, 11 April 1962	316
110	Schematic of Global Orbital Simulator	320
111	APT Tracking Board	322
112	Sample APT Daily Message	332
113	Sample APT Grids	335
114	Sketch of APT Training Simulator	338
115	Block Diagram of APT Simulator	339
116	Students Control Panel	340

LIST OF TABLES

<u>Table</u>		<u>Page</u>
1	Some Frequently Used Orbital Parameters as Functions of Altitude	12
2	Argument of a Satellite as a Function of Latitude and Orbit Inclination	34
3	Subpoint to Object Distance	40
4	Air Mass Corresponding to Different Zenith Angles	41
5	Definitions of Radiation Terms	54
6	T-Power Dependence	60
7	Mean IR Emissivities for the 8-12 μ Region	70
8	Albedos of Some Typical Surfaces	81
9	Average Albedos for Various Cloud Surfaces as Determined from Satellite TV Pictures	98
10	Linear Resolution at Subsatellite Point of a Synchronous Satellite	154
11	Resolution from Synchronous Altitude	155
12	Summary of Sensor/Data Systems	167
13	Contrast Degradation of the Atmosphere	172
14	Average Number and Types of Weather Charts Received Daily by a Station at 40°N Latitude	273
15	Summary of Geophysical Observations from Space	293
16	Camera Characteristics	325
17	Nimbus Camera Fields of View	325
18	Approximate Best Practically Available Resolution of Satellite Cameras	326
19	Key to APT Daily Message	333

SECTION I

INTRODUCTION

1.1 Statement of the Problem

The development of the earth-orbiting satellite has provided the Navy with new methods for making many of the geophysical observations required to support both naval operations and research programs. Suitable satellites can provide daily global observations which might otherwise not be available due to inadequate coverage by a network of conventional observation stations, reconnaissance aircraft and ships. In times of hostilities, satellites can provide data coverage over enemy controlled areas of strategic or tactical significance.

Furthermore, the satellite provides a vantage point uniquely suitable for many types of geophysical observations, and so has made possible types of observations which cannot otherwise be obtained. For example, features of such a scale that they are too large to be identified from a single point, but too small to be detected by a conventional observing grid, have been identified in analyses of satellite pictures of both surface geographical features and cloud cover. Measurements of the albedo and the thermal emission of the earth and its atmosphere can now be available on a daily basis and at a scale of a few tens of miles, whereas previously even monthly means for significant fractions of the earth were difficult to estimate.

In the field of oceanography, a capability for sea surface temperature measurements has been shown. In some circumstances, an estimate of the sea state can be derived from the size and intensity of a sunglint. Sea ice can be identified, mapped, and its day-to-day changes followed. Advanced sensors, such as passive microwave radiometers and side-looking radar, have been proposed or are under development as possible means of improved measurements of sea surface temperature, roughness, and other parameters.

The capabilities of satellites to provide geographical and geological data have been demonstrated by analyses of TIROS, Mercury, Nimbus, and Gemini data. These studies, and extrapolations from analyses of aerial photography, indicate the satellite data can be of significant value in both research and operational mappings of the littoral regions, including changes due to storms and the continually eroding forces of less severe waves and currents.

NAVTRADEVGEN 66-C-0031-1

The most extensive geophysical applications of the satellite data have been, to date, in the field of meteorology. The television pictures have been applied with great success to both operations and research. Although the infrared data have been used mainly in research, techniques for the operational use of the IR data have been developed and await only an infrared instrumented operational satellite for their implementation. The satellite data are already being used by the Navy to determine the extent and amount of cloud cover and the locations and severity of both tropical and extratropical storms, and to improve synoptic analyses over the data sparse ocean areas. When conventional analyses for the Atlantic and Pacific Ocean areas have been subjectively modified on the basis of available satellite observations, they have consistently led to improvements in Fleet Numerical Weather Facility forecasts.

The value of satellite data to the Navy will, however, be limited by the degree to which naval personnel have been adequately trained in the many areas of satellite geophysics. For instance, a satellite in orbit may be hundreds, or even thousands, of miles from the earth and all but a very small fraction of its atmosphere. In order to determine geophysical parameters directly from such a satellite, remote electromagnetic sensing techniques have to be employed. These measurements are very often not uniquely related to any single physical parameter of the geophysical target or feature being observed. Consequently, such measurements have to be interpreted in terms of the often complex physical processes in the atmosphere and on the earth which give rise to the measured radiation, and the characteristics of the sensor which made the measurements.

Furthermore, the geometry of the satellite orbit introduces constraints on the areas of data coverage possible as well as on the spatial resolutions of the measurements obtained. These orbital factors are not only significant to the programming of satellite observations but are also significant in the interpretation and use of satellite data. Even in its role as a storage and relay of contact measurements made from oceanographic buoys, meteorological balloons, and automatic weather stations, the satellite significantly influences the quantities of the data, or the frequencies of observations that are feasible.

It must also be understood, however, that the satellite data, like any other single set of geophysical observations, have both characteristic strong points and fundamental weaknesses. They should be used within the philosophy, that satellites provide only another, although a particularly powerful, means of observing the earth and its atmosphere. Accordingly, the satellite data should be integrated with available

conventional or other geophysical data in whatever proportion is most suitable to the job at hand. The most appropriate blend may range from no use of the satellite data, through various ranges of partial use, to sole use in those cases where no other data are available or suitable. As mentioned above, specific situations where the satellite data can be indispensable include:

1. In otherwise data sparse areas, such as much of the oceans, the tropics, and the southern hemisphere, where the amounts, frequency, and reliability of other observations are usually grossly inadequate.

2. When the parameter of interest is one particularly well observed by satellites, such as albedo, various specific components of terrestrial long wave radiation, cloud top altitudes, and spatially contiguous aspects of cloud cover.

In view of the many unique aspects of satellite acquired geophysical data and their potential applications, the U.S. Naval Training Device Center requested the Geophysics Division of Allied Research Associates, Inc., to perform a study of satellite geophysics for the purposes of designing training simulators and training techniques. In particular, the following items were to be analyzed:

1. The factors, geophysical, instrumental, and satellite orbital geometry, which affect the acquisition of geophysical data by earth oriented satellites.

2. The basic techniques by which geophysical parameters of significance to Naval operations may be obtained by satellite sensors operating in the different wavelength regions of the electromagnetic spectrum and the degradation factors inherent in these techniques.

3. Techniques whereby satellite data can be simulated for training purposes.

4. Techniques and devices useful for the training of personnel participating in the many areas of satellite geophysics.

This report represents the results of this study. The topics covered in this report are delineated in greater detail in the following section.

1.2 Scope of the Study

This study covered a large number of topics in satellite geophysics. Because of this, an annotated Table of Contents is provided below in which the chapters in the report are discussed in terms of their significances to the training problem.

Chapter II covers the many aspects of satellite orbital geometry. A basic understanding of these matters is required not only of those personnel who have the responsibilities of satellite programming and management, but is also required of those who are participants in the ground acquisition, data interpretation and utilization phases of satellite geophysics. It is shown in this section that the orbital geometry places constraints on the areas of data coverage, sensor resolution and aspects of satellite data acquisition which might render the acquired data difficult to interpret.

An understanding of the basic properties of electromagnetic radiation is essential to the interpretation of many types of satellite acquired data. A satellite in orbit is hundreds, and even thousands of miles from the surface of the earth. In order for a sensor located on the satellite to make observations or measurements of physical properties of the surfaces of the earth and of the lower atmosphere, it must do so through the measurements of electromagnetic radiation propagating from these sources. As a consequence, many types of satellite acquired data are based on the measurements of electromagnetic radiation which penetrate through the atmosphere to the satellite. The interpretation of these measured radiation data are based on relationships between the measured radiation and (a) the sources of radiation on the surfaces of the earth and in the atmosphere, and (b) the geophysical factors which affect the propagation of the radiation through the atmosphere to the satellite.

These topics are discussed in detail in Sections III, IV, and V. In Section III, the definitions and concepts of electromagnetic radiation most often used in remote sensing techniques are presented. In particular, the concepts of emissivity and blackbody radiation are analyzed in terms of their applicability to remote sensing. Sections IV and V deal specifically with the radiation characteristics of the earth and its atmosphere. The discussions contained in these two sections form the basis of the later analysis of sensor/parameter combinations.

In Section VI, the effects of the satellite sensor on the measured data are discussed. The notion of a satellite sensor system as being a combination of many elements located both on the spacecraft and on the ground is introduced and analyzed. The analysis covers such topics as spatial and spectral resolutions, distortions, contrast degradations, and noise. A topic of particular significance in the training of interpretive personnel is the effect of the display format on the measured data.

NAVTRADEVCEEN 66-C-0031-1

This topic is also analysed in detail in this section. Examples of different data display formats, both machine produced and manually prepared, are included to illustrate the points made in the discussion.

With the advent of the ATS-B (now known as ATS-1) satellite, geophysical observations from synchronous altitude became available for the first time. Problems associated with such observations are discussed in Section VII.

Sections VIII, IX, X and XI present analyses of sensor/parameter combinations. The types of geophysical parameters observable by satellite sensors in the various spectral regions are first summarized in Section VIII. Sections IX, X and XI analyze in detail the observation techniques, the parameters observed and the geophysical degradation factors in the visible, infrared and microwave regions of the spectrum. Both passive and active techniques are discussed. Numerous examples, taken from available space acquired imagery, are included as illustrations. In these sections, examples of radiation transfer equations are developed.

In Sections XII and XIII, the uses of an orbiting satellite as a data storage and relay system are discussed. Section XII discusses the data collection satellite and analyzes the training problems associated with such a satellite, while in Section XIII the use of a satellite for the transmission of meteorological charts and other graphic materials (WEFAX) is discussed.

Section XIV presents a short summary of the ground complex necessary to support a geophysical satellite.

Based on the discussions presented in all these previous sections, the training requirements for Navy personnel participating in the many areas of satellite geophysics are briefly analyzed in Section XV.

Section XVI presents analyses of techniques for

1. Simulation of satellite data
2. Techniques and devices useful for the training of personnel.

Because of the significance of the APT (Automatic Picture Transmission) mode of satellite data acquisition in the current and foreseeable future scheme of satellite geophysics in providing "real time" satellite data to local units, the design and use of an APT training simulator is separately discussed in Section XVII. It is recommended that such a simulator be made available for training purposes as soon as possible.

SECTION II

ORBITAL PARAMETERS PERTINENT TO
SATELLITE GEOPHYSICS

All satellite orbits used for geophysical observations are ellipses, with the center of the earth at one focus of the ellipse (Fig. 1a). Accordingly, the instantaneous intersection of the orbit plane and the surface of the earth will always be a great circle (Fig. 1b).

In general, orbits of satellites used for geophysical observations will be as circular as possible, since this leads to simplicity in the programming of the observations and to homogeneity in observational coverage and resolution. Deviations from circular orbits may be anticipated, however, due either to errors during the launch, or to requirements imposed by other assigned missions.

2.1 Orbit Velocities and Periods for a Non-Rotating Earth

2.1.1 Circular Orbit Velocities

The relationships between orbit altitude, velocity, and the period of an orbital revolution can most easily be understood by first considering a circular orbit.

Let:

- R = mean radius of earth (3435 nautical miles, or 6370 km)[†]
- h = height of satellite above earth's surface
- r = distance from center of earth to satellite = R + h
- m = mass of satellite
- v = velocity of satellite in orbit
- g_h = acceleration of gravity at orbit altitude

[†] Later empirical studies, using actual TIROS data, suggest that 6381 km would be a better value when K (see later) has the value used in this study, and that NASA's Goddard Space Flight Center uses a value of about 6378 km.

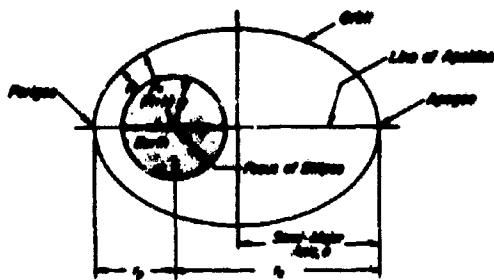


Figure 1a. Geometry and Definitions for an Elliptical Orbit

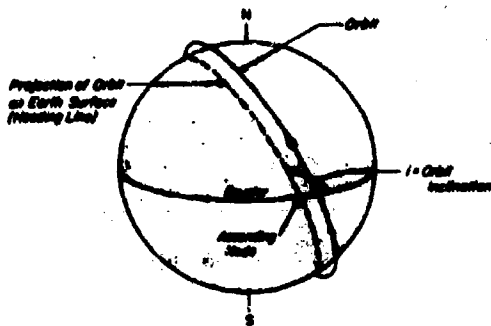


Figure 1b. Orbital Definitions

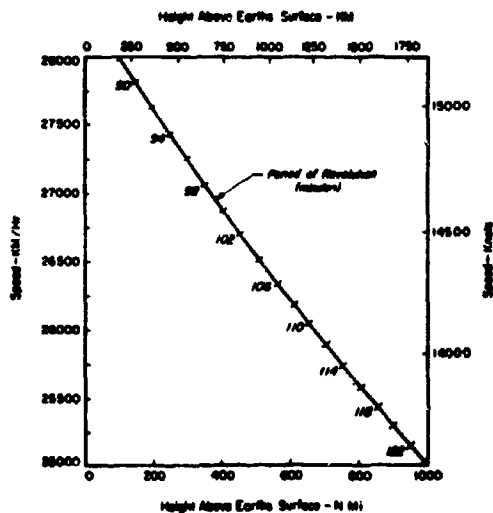


Figure 2a. Velocity and Period of an Earth Satellite in a Circular Orbit at Various Altitudes

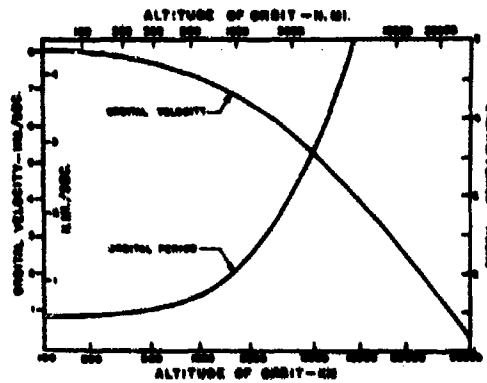


Figure 2b. Velocity and Period of an Earth Satellite in a Circular Orbit at Various Altitudes

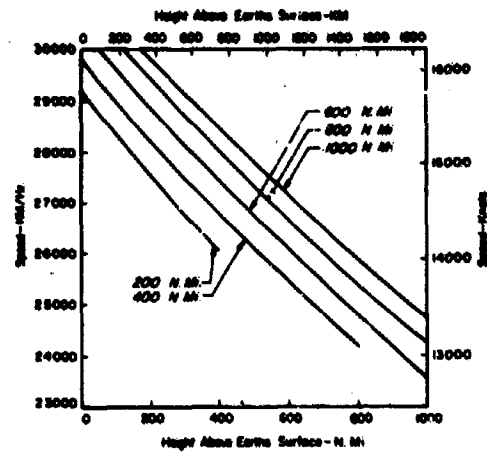


Figure 2c. Speed of a Satellite in an Elliptic Orbit, for a Series of Values of Average Height

For a circular orbit, the centripetal acceleration of the satellite, mv^2/r , is equal to the force of gravity, mg_h , or

$$\frac{mv^2}{r} = mg_h \quad (1)$$

$$v = \sqrt{rg_h} \quad (2)$$

But, from the laws of gravitation,

$$g_h = \frac{GM}{r^2} \quad (3)$$

where

G = universal gravitational constant

M = mass of earth,

$$v = \sqrt{\frac{GM}{r}} = \sqrt{\frac{GM}{R+h}} \quad (4)$$

For the earth, both G and M are constants. Let $GM = K$. Since orbit altitude is usually expressed in either kilometers or nautical miles, K , when expressed in appropriate units, is found to be:

$$K = 3.99 \times 10^5 \text{ kilometers}^3/\text{seconds}^2$$

$$K = 8.15 \times 10^{11} \text{ nautical miles}^3/\text{hour}^2$$

Accordingly

$$v = \frac{631}{\sqrt{r}} \text{ km/sec, or} \quad (5)$$

$$v = \frac{631}{\sqrt{6370+h}} \text{ km/sec} \quad (6)$$

$$v = \frac{2.27 \times 10^6}{\sqrt{r}} = \frac{2.27 \times 10^6}{\sqrt{6370+h}} \text{ km/hr} \quad (7)$$

when r or h are expressed in kilometers.

$$v = \frac{9.04 \times 10^5}{\sqrt{r}} = \frac{9.04 \times 10^5}{\sqrt{3435 + h}} \text{ knots.} \quad (8)$$

when r or h are expressed in nautical miles.

When designing some types of experiments, the more crucial velocity may be that over the earth's surface. Neglecting, for the present, the effects of earth rotation,[†] and letting v'_g be the velocity over the surface of a non-rotating earth

$$v'_g = \left(\frac{R}{R+h} \right) v = \left(\frac{R}{R+h} \right) \sqrt{\frac{K}{R+h}} \quad (9)$$

$$v'_g = \frac{1.446 \times 10^{10}}{(6370 + h)^{3/2}} \text{ km/hr} \quad (10)$$

when h is expressed in kilometers.

$$v'_g = \frac{3.10 \times 10^9}{(3435 + h)^{3/2}} \text{ knots} \quad (11)$$

when h is expressed in nautical miles.

2.1.2 Circular Orbit Periods

The orbital period for a circular orbit can be determined by noting that

$$P = \frac{2\pi(R+h)}{v} = 2\pi \frac{(R+h)^{3/2}}{\sqrt{K}} \quad (12)$$

$$P = 2.77 \times 10^{-6} (6370 + h)^{3/2} \text{ hours} \quad (13)$$

$$= 1.661 \times 10^{-4} (6370 + h)^{3/2} \text{ minutes} \quad (14)$$

when h is expressed in kilometers.

$$P = 0.696 \times 10^{-5} (3435 + h)^{3/2} \text{ hours} \quad (15)$$

$$= 4.17 \times 10^{-4} (3435 + h)^{3/2} \text{ minutes} \quad (16)$$

when h is expressed in nautical miles.

[†] The effects of earth rotation are introduced in Section 2.3.2.

The orbital velocities and periods for various orbit altitudes are shown in Figure 2 and tabulated in Table 1. The significance of the other values in Table 1 will be explained later. †

A unique orbit period of considerable interest for some types of geophysical observations is that of twenty-four hours, in which case a satellite in an equatorial orbit would remain stationary relative to the earth.

A satellite in such an orbit is often referred to as earth synchronous, or merely as synchronous. As Equation (15) or Table 1 show, this condition would exist at an altitude of about 35,815 km, or 19,326 nautical miles.

2.1.3 Elliptical Orbits

All satellite orbits can be expected to be at least slightly elliptical since the precision required for an exactly circular orbit is unattainable in practice. (In several TIROS orbits, however, the departure from circularity was so small that it could be neglected for many purposes.)

When in an elliptical orbit (see Fig. 1a), the satellite increases its velocity as it falls from apogee (the orbital point farthest from the earth's center) to perigee (the orbital point nearest to the earth's center). Conversely, the velocity decreases again from perigee to apogee. The velocity at perigee must be greater than that for a circular orbit at the same altitude, otherwise the satellite would not have the extra kinetic energy required to climb back to apogee. Similarly, the velocity at apogee must be less than that for a circular orbit at the apogee altitude.

Since the derivation of velocities in an elliptical orbit is rather complex, only the result will be stated here. In addition to the previous notations, let (see Fig. 1a):

- r_p = satellite distance from center of earth at perigee
- = $R + h_p$, where h_p is the orbit altitude at perigee
- r_a = satellite distance from center of earth at apogee
- = $R + h_a$, where h_a is the orbit altitude at apogee

† Since many aspects of Table 1 depend on the specific choice of R (radius of earth, see Section 2.4), the values should be considered as primarily for preliminary estimates and not as necessarily suitable, in all cases, for final engineering designs.

Table 1 Some Frequently Used Orbital Parameters as Functions of Altitude,
for R = 6370 Km or 3435 Nautical Miles

Orbit Altitude (Km)	Orbit Altitude N. Miles	R + h Km	R + h N. Miles	$\left(\frac{R+h}{R}\right)^2 \left(\frac{R}{R+h}\right)$	Orbital Velocity km/hr	Orbital Velocity knots	Ground Velocity (Non-Rotating Earth) km/hr	Orbital Period hours	Weekend Displace. Deg. Long.	Sun- Synchronous Inclination Degrees	Approx. Max. Latitude (Degrees)	Horizon Radius Angle α_H	Horizon Distance (KCA)
150	81	6520	3516	1.034	28111	15245	27464	1.458	21.87	94.15	83.85	77.49	12.31
185	100	6555	3535	1.039	28089	15203	27285	1.473	22.02	94.27	83.73	76.34	13.46
200	108	6570	3543	1.041	28064	15180	27150	1.478	22.14	94.33	83.67	75.81	14.19
250	135	6620	3570	1.059	27901	15138	26846	1.492	22.30	94.39	83.51	74.30	16.42
300	162	6670	3597	1.064	27839	15099	26675	1.498	22.53	94.59	83.41	73.20	18.00
350	182	6720	3627	1.067	27795	15074	26524	1.503	22.64	94.74	83.33	72.35	19.25
400	200	6770	3655	1.069	27760	15051	26425	1.507	22.89	94.85	83.25	71.71	20.35
450	216	6820	3683	1.071	27734	15030	26346	1.511	23.05	94.92	83.18	71.19	21.35
500	233	6870	3711	1.073	27713	15011	26280	1.514	23.15	94.96	83.12	70.71	22.22
550	249	6920	3739	1.075	27696	14994	26226	1.517	23.26	95.00	83.06	70.29	23.02
600	265	6970	3767	1.077	27682	14979	26180	1.519	23.36	95.03	83.00	69.91	23.72
650	281	7020	3795	1.079	27671	14965	26141	1.521	23.46	95.06	82.94	69.56	24.38
700	297	7070	3823	1.081	27662	14952	26107	1.523	23.56	95.08	82.88	69.25	25.00
750	313	7120	3851	1.083	27654	14940	26077	1.525	23.66	95.10	82.82	68.96	25.58
800	329	7170	3879	1.085	27648	14929	26050	1.527	23.76	95.12	82.76	68.69	26.12
850	345	7220	3907	1.087	27643	14919	26026	1.529	23.86	95.14	82.70	68.43	26.63
900	361	7270	3935	1.089	27639	14910	26004	1.531	23.96	95.16	82.64	68.18	27.11
950	377	7320	3963	1.091	27636	14901	25984	1.533	24.06	95.18	82.58	67.94	27.56
1000	393	7370	3991	1.093	27633	14893	25965	1.535	24.16	95.20	82.52	67.71	28.00
1050	409	7420	4019	1.095	27631	14885	25947	1.537	24.26	95.22	82.46	67.48	28.42
1100	425	7470	4047	1.097	27629	14877	25930	1.539	24.36	95.24	82.40	67.26	28.82
1150	441	7520	4075	1.099	27627	14870	25913	1.541	24.46	95.26	82.34	67.04	29.20
1200	457	7570	4103	1.101	27625	14862	25897	1.543	24.56	95.28	82.28	66.83	29.58
1250	473	7620	4131	1.103	27623	14855	25881	1.545	24.66	95.30	82.22	66.62	30.00
1300	489	7670	4159	1.105	27621	14847	25866	1.547	24.76	95.32	82.16	66.42	30.38
1350	505	7720	4187	1.107	27619	14840	25851	1.549	24.86	95.34	82.10	66.22	30.76
1400	521	7770	4215	1.109	27617	14832	25836	1.551	24.96	95.36	82.04	66.02	31.12
1450	537	7820	4243	1.111	27615	14825	25821	1.553	25.06	95.38	81.98	65.82	31.48
1500	553	7870	4271	1.113	27613	14817	25806	1.555	25.16	95.40	81.92	65.62	31.82
1550	569	7920	4299	1.115	27611	14810	25791	1.557	25.26	95.42	81.86	65.42	32.16
1600	585	7970	4327	1.117	27609	14802	25776	1.559	25.36	95.44	81.80	65.22	32.50
1650	601	8020	4355	1.119	27607	14795	25761	1.561	25.46	95.46	81.74	65.02	32.82
1700	617	8070	4383	1.121	27605	14787	25746	1.563	25.56	95.48	81.68	64.82	33.16
1750	633	8120	4411	1.123	27603	14780	25731	1.565	25.66	95.50	81.62	64.62	33.50
1800	649	8170	4439	1.125	27601	14772	25716	1.567	25.76	95.52	81.56	64.42	33.82
1850	665	8220	4467	1.127	27599	14765	25701	1.569	25.86	95.54	81.50	64.22	34.16
1900	681	8270	4495	1.129	27597	14757	25686	1.571	25.96	95.56	81.44	64.02	34.50
1950	697	8320	4523	1.131	27595	14750	25671	1.573	26.06	95.58	81.38	63.82	34.82
2000	713	8370	4551	1.133	27593	14742	25656	1.575	26.16	95.60	81.32	63.62	35.16
2050	729	8420	4579	1.135	27591	14735	25641	1.577	26.26	95.62	81.26	63.42	35.50
2100	745	8470	4607	1.137	27589	14727	25626	1.579	26.36	95.64	81.20	63.22	35.82
2150	761	8520	4635	1.139	27587	14720	25611	1.581	26.46	95.66	81.14	63.02	36.16
2200	777	8570	4663	1.141	27585	14712	25596	1.583	26.56	95.68	81.08	62.82	36.50
2250	793	8620	4691	1.143	27583	14705	25581	1.585	26.66	95.70	81.02	62.62	36.82
2300	809	8670	4719	1.145	27581	14697	25566	1.587	26.76	95.72	80.96	62.42	37.16
2350	825	8720	4747	1.147	27579	14690	25551	1.589	26.86	95.74	80.90	62.22	37.50
2400	841	8770	4775	1.149	27577	14682	25536	1.591	26.96	95.76	80.84	62.02	37.82
2450	857	8820	4803	1.151	27575	14675	25521	1.593	27.06	95.78	80.78	61.82	38.16
2500	873	8870	4831	1.153	27573	14667	25506	1.595	27.16	95.80	80.72	61.62	38.50
2550	889	8920	4859	1.155	27571	14660	25491	1.597	27.26	95.82	80.66	61.42	38.82
2600	905	8970	4887	1.157	27569	14652	25476	1.599	27.36	95.84	80.60	61.22	39.16
2650	921	9020	4915	1.159	27567	14645	25461	1.601	27.46	95.86	80.54	61.02	39.50
2700	937	9070	4943	1.161	27565	14637	25446	1.603	27.56	95.88	80.48	60.82	39.82
2750	953	9120	4971	1.163	27563	14630	25431	1.605	27.66	95.90	80.42	60.62	40.16
2800	969	9170	5000	1.165	27561	14622	25416	1.607	27.76	95.92	80.36	60.42	40.50
2850	985	9220	5028	1.167	27559	14615	25401	1.609	27.86	95.94	80.30	60.22	40.82
2900	1001	9270	5056	1.169	27557	14607	25386	1.611	27.96	95.96	80.24	60.02	41.16
2950	1017	9320	5084	1.171	27555	14600	25371	1.613	28.06	95.98	80.18	59.82	41.50
3000	1033	9370	5112	1.173	27553	14592	25356	1.615	28.16	96.00	80.12	59.62	41.82
3050	1049	9420	5140	1.175	27551	14585	25341	1.617	28.26	96.02	80.06	59.42	42.16
3100	1065	9470	5168	1.177	27549	14577	25326	1.619	28.36	96.04	80.00	59.22	42.50
3150	1081	9520	5196	1.179	27547	14570	25311	1.621	28.46	96.06	79.94	59.02	42.82
3200	1097	9570	5224	1.181	27545	14562	25296	1.623	28.56	96.08	79.88	58.82	43.16
3250	1113	9620	5252	1.183	27543	14555	25281	1.625	28.66	96.10	79.82	58.62	43.50
3300	1129	9670	5280	1.185	27541	14547	25266	1.627	28.76	96.12	79.76	58.42	43.82
3350	1145	9720	5308	1.187	27539	14540	25251	1.629	28.86	96.14	79.70	58.22	44.16
3400	1161	9770	5336	1.189	27537	14532	25236	1.631	28.96	96.16	79.64	58.02	44.50
3450	1177	9820	5364	1.191	27535	14525	25221	1.633	29.06	96.18	79.58	57.82	44.82
3500	1193	9870	5392	1.193	27533	14517	25206	1.635	29.16	96.20	79.52	57.62	45.16
3550	1209	9920	5420	1.195	27531	14510	25191	1.637	29.26	96.22	79.46	57.42	45.50
3600	1225	9970	5448	1.197	27529	14502	25176	1.639	29.36	96.24	79.40	57.22	45.82
3650	1241	10020	5476	1.199	27527	14495	25161	1.641	29.46	96.26	79.34	57.02	46.16
3700	1257	10070	5504	1.201	27525	14487	25146	1.643	29.56	96.28	79.28	56.82	46.50
3750	1273	10120	5532	1.203	27523	14480	25131	1.645	29.66	96.30	79.22	56.62	46.82
3800	1289	10170	5560	1.205	27521	14472	25116	1.647	29.76	96.32	79.16	56.42	47.16
3850	1305	10220	5588	1.207	27519	14465	25101	1.649	29.86	96.34	79.10	56.22	47.50
3900	1321	10270	5616	1.209	27517	14457	25086	1.651	29.96	96.36	79.04	56.02	47.82
3950	1337	10320	5644	1.211	27515	14450	25071	1.653	30.06	96.38	78.98	55.82	48.16
4000	1353	10370	5672	1.213	27513	14442	25056	1.655	30.16	96.40	78.92	55.62	48.50
4050	1369	10420	5700	1.215	27511	14435	25041	1.657	30.26	96.42	78.86	55.42	48.82
4100	1385	10470	5728	1.217	27509	14427	25026	1.659	30.36	96.44	78.80	55.22	49.16
4150	1401	10520	5756	1.219	27507	14420	25011	1.661	30.46	96.46	78.74	55.02	49.50
4200	1417	10570	5784	1.221	27505	14412	25006	1.663	30.56	96.48	78.68	54.82	49.82
4250	1433	10620	5812	1.223	27503	14405	24991	1.665	30.66	96.50	78.62	54.62	50.16
4300	1449	10670	5840	1.225	27501	14397	24976	1.667	30.76	96.52	78.56	54.42	50.50
4350	1465	10720	5868	1.227	27499	14390							

$$a = \frac{r_a + r_p}{2} = \text{semi-major axis of the orbital ellipse, or}$$

average distance from earth center to orbit

v_p and v_a : orbital velocity at perigee and apogee, respectively.

It can be shown that:

$$v = \sqrt{K \left(\frac{2}{r} - \frac{1}{a} \right)} \quad (17)$$

$$v_p = \sqrt{K \left(\frac{2}{r_p} - \frac{1}{a} \right)} = \sqrt{\frac{K(2a - r_p)}{a r_p}} \quad (18)$$

$$v_a = \sqrt{K \left[\frac{2}{(2a - r_p)} - \frac{1}{a} \right]} = \sqrt{\frac{K r_p}{a(2a - r_p)}} \quad (19)$$

$$\frac{v_a}{v_p} = \frac{2a - r_p}{r_p} \quad (20)$$

$$P = 2\pi \sqrt{\frac{a^3}{K}} \quad (21)$$

$$P = 2\pi \sqrt{\frac{[R + 1/2 (h_p + h_a)]^3}{K}} \quad (22)$$

Figure 2c illustrates the velocities of satellites in elliptical orbits. Since Equation (22) has the same form as Equation (12), Figure 2a or 2b, or Table 1, can be used to determine the periods of elliptical orbits provided the orbit altitude is taken as the length of the semi-major axis, a , minus the radius of the earth, R , or as $1/2 (h_p + h_a)$.

2.2 Orbit Orientation

2.2.1 Orbit Inclination

So far only the shape of an orbit has been considered. Its orientation in space will now be considered. The orientation of the orbit plane is specified in

terms of the inclination (see Fig. 1b) and of the ascending node (northbound equator crossing).

The orbit inclination, i , is the angle between the earth's equatorial plane and the plane of the orbit (Fig. 1b). The inclination is measured counterclockwise, from the equatorial plane to the orbit plane. Orbits with inclinations less than 90° are known as prograde, since a component of the orbit velocity is in the same direction as the rotation of the earth. Orbits with inclinations greater than 90° are known as retrograde. Inclinations of retrograde orbits are frequently specified as the supplement of the inclination ($180^\circ - i$), followed by the word "retrograde;" i. e., an orbit with an inclination of 101° would be given as 79° , retrograde.

The orbit inclination, or its supplement for retrograde orbits, determines the maximum latitude over which the orbit passes. The orbit will cross or reach all latitudes $\leq i$, or $\leq 180^\circ - i$, whichever is less. Thus, the inclination places one limitation on the extent of earth coverage a satellite can provide.

2.2.2 Ascending Node

The other aspect of orbit orientation is given by specifying the ascending node, the point of northbound equator crossing of the satellite. Since the earth is rotating, the primary coordinate system for specifying ascending node is right ascension (the astronomical equivalent of longitude). Right ascension is the angular distance of a point on the celestial sphere measured eastward from the vernal equinox. The measurement is made along the celestial equator from the vernal equinox, eastward to the hour circle (meridian of longitude) corresponding to ascending node.

When relating the orbit to the earth, the ascending node of any single orbital revolution is specified as the longitude and time at which a satellite crosses the equator northbound. The relationships between ascending node as given in terms of right ascension and in terms of longitude can be determined from the equation of time, or from appropriate nautical almanacs.¹ The Air Almanac, which is published in three volumes a year, gives the right ascension of Greenwich at 10 minute intervals, thus making it easy to interpolate the needed values.

By convention, the number of the orbital pass (one complete rotation of the satellite) increases by one at each ascending node. Orbit One starts with the first ascending node, with the partial orbit from launch to the first ascending node known as Orbit Zero.

Although less frequently used as a reference, it is convenient to define here the descending node. As would be expected, it is the point (or time) of southbound equator crossing of the orbit or satellite.

2.3 Effect of Earth Rotation

Because of the rotation of the earth, the subpoint track (the projection of the satellite positions on the earth's surface) does not retrace from one orbit to the next (with the exception of the special case of equatorial orbits, $i = 0^\circ$ or 180°). Rather, the ascending node and the subpoint of every point on the orbit are displaced westward by an amount in longitude equal to the angular rotation of the earth during an orbital period.

Since the earth rotates 360° in 24 hours, or 1440 minutes, this longitudinal displacement from one orbit to the next, $\Delta\lambda$, is given by

$$\Delta\lambda = \frac{360 P}{1440} = 0.25 P, \quad (23)$$

where P is the orbital period in minutes. Values of $\Delta\lambda$ for various orbit altitudes are given in Table 1. Subpoint tracks of typical TIROS ($h \approx 380$ n. mi., $i = 58^\circ$) and nimbus ($h \approx 600$ n. mi., $i \approx 80^\circ$, retrograde) orbits are illustrated in Figures 3a and 3b, respectively. As Figure 3a shows, the subpoint track when plotted on a Mercator or similar map projection is wave-shaped, with a wavelength of $(360 - \Delta\lambda)^\circ$ longitude for prograde orbits, $(360 + \Delta\lambda)^\circ$ for retrograde orbits, and an amplitude of i ($180^\circ - i$ for a retrograde orbit).

2.3.1 Subpoint Tracks and Heading Lines

Because of the earth's rotation, the subpoint track (projection of the consecutive positions of the satellite on the earth's surface), and the instantaneous intersection of the orbital plane and the earth's surface, are not the same. To take account of this difference, the term Heading Line has been adopted. The heading line is the instantaneous projection on the earth's surface of the orbital plane. Looking along the orbit in the direction of satellite motion, the heading line is directed slightly (about $0 - 5^\circ$, at the orbit altitudes of likely interest) to the east of

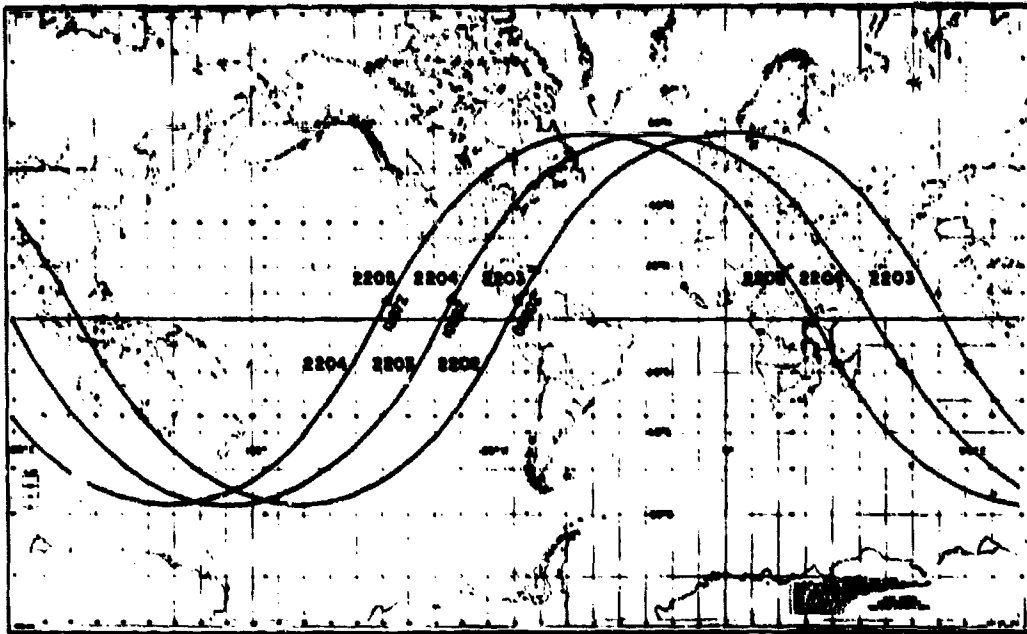


Figure 3a Subpoint Tracks for Several Typical TIROS Orbits (TIROS VI Orbits 2202-2205) Times at Which Satellite Crossed the Equator Northbound on These Orbits are Shown.

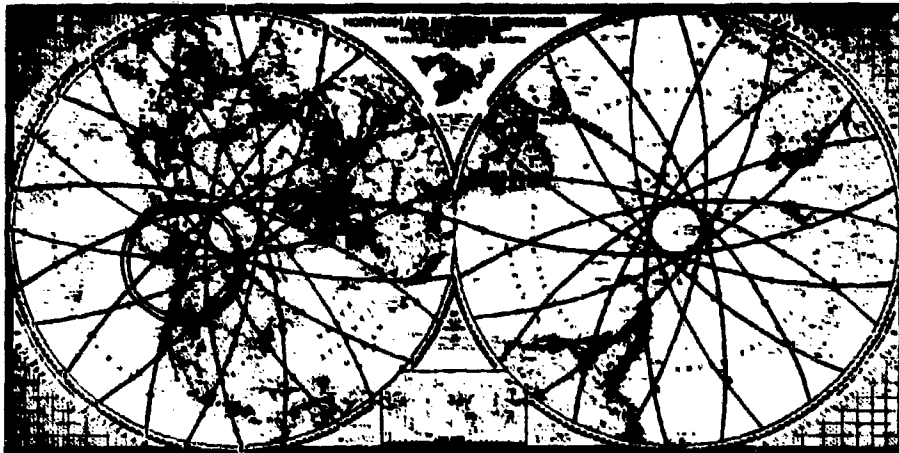


Figure 3b Typical Nimbus (Quasi-polar) Orbits. The Double Circle Indicates the Approximate Limits of Range of the Fairbanks, Alaska, Command and Data Acquisition Station.

the subpoint track (except at the northernmost and southernmost limits of the orbit, where the heading line is tangent to the subpoint track). Figure 4 provides a qualitative picture of these relationships.

These differences between the subpoint track and the heading line may be significant if experiment design or simulation is to be precise. For a satellite with three axis stabilization (such as Nimbus), a sensor rotating about an axis parallel to the satellite roll axis (the satellite velocity vector for perfect stabilization) will produce a scan perpendicular to the heading line, rather than to the subpoint track. The Nimbus HRIR and MRIR radiometers have such a scanning pattern. Neglect of this matter can lead to errors of up to 1.5° of great circle arc in the geographical location of observed points.

The analytical expressions for heading lines and subpoint tracks can be developed² using Figure 5.

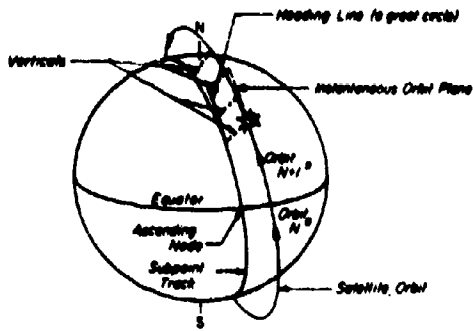
Let:

- λ = longitude west of ascending node
- ϕ = latitude
- l = angular distance along the orbit (or heading line) measured from ascending node. (Note this is also the argument of the satellite, which will be specifically defined later)
- I = supplement of inclination, or $180^\circ - i$
- P = nodal period (orbital period between successive ascending nodes) in minutes

In Figure 5, first assume the earth as non-rotating, in which case l is measured (in units of great circle arc) along the heading line and so along a great circle. The right spherical triangle in the diagram (that with sides ϕ , λ , and l) leads to the relationships:

$$\left. \begin{aligned} \sin \phi &= \sin I \sin l \\ \tan \lambda &= \cos I \tan l \end{aligned} \right\} \quad (24)$$

Note also that, while the relationships here are expressed in terms of l (argument, or angular distance along the orbit), they could equally well be expressed in time (assuming now a circular orbit).



(Orbit number increases by one at Ascending Node)

Figure 4. Schematic Depiction of Satellite Orbit, Heading Line, and Subpoint Track

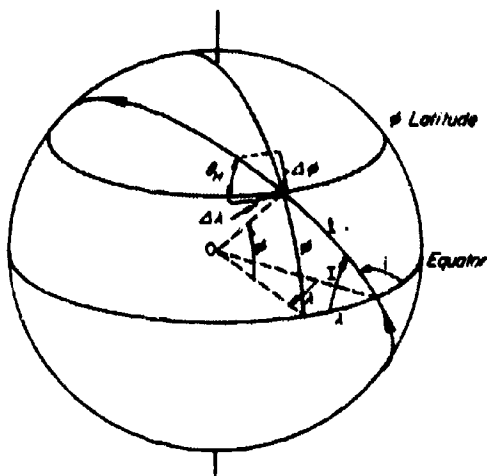


Figure 5. Geometry of Heading Line or Subpoint Track

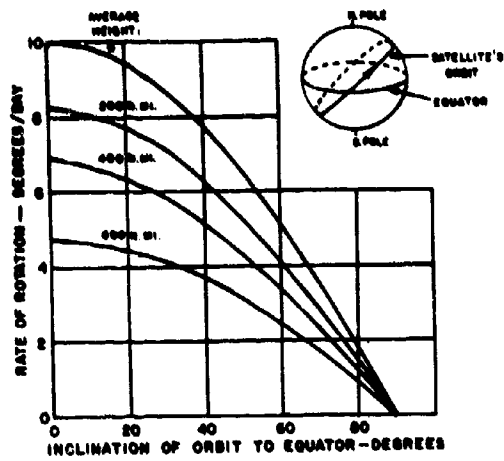


Figure 6. The Rate of Rotation of the Orbital Plane of a Satellite about the Earth's Axis, Caused by the Equatorial Bulge. Numbers on the Curves Indicate the Average Height of the Satellite Above the Earth's Surface.

Since l goes from $0-360^\circ$ during one period, P :

$$\frac{l}{360} = \frac{t}{P}, \text{ or} \quad (25)$$

$$dl = \frac{360}{P} dt \quad (26)$$

The next step is to derive the slope of the heading line. Differentiating Equation (24) gives:

$$\left(\frac{d\phi}{dl}\right)_H = \frac{\sin I \cos l}{\cos \phi} \quad (27)$$

$$\left(\frac{dl}{d\lambda}\right)_H = \frac{\sec^2 \lambda}{\cos I \sec^2 l} \quad (28)$$

The product of Equations (27) and (28) gives:

$$\left(\frac{d\phi}{d\lambda}\right)_H = \frac{\sin I \cos l \sec^2 \lambda}{\cos I \sec^2 l \cos \phi} \quad (29)$$

where in each case the subscript, H , indicates the heading line. Equation (29) is an expression for the slope or orientation of the heading line.

Using Equation (24) to eliminate l and λ , after suitable rearrangement and simplification, the following expression is obtained:

$$\left(\frac{d\phi}{d\lambda}\right)_H = \frac{\cos \phi}{\cos I} \sqrt{\sin^2 I - \sin^2 \phi} \quad (30)$$

in which latitude, ϕ , is the only independent variable, since I ($180^\circ - i$) is a constant for any orbit.

Since the scale of λ varies with ϕ , it is more convenient to measure the orientation of the heading line in terms of its angle, θ_H , relative to the equator or to any convenient parallel of latitude. To make this transformation, note that:

$$\left(\frac{d\phi}{d\lambda}\right)_H = \tan \theta_H \cos \phi, \text{ or} \quad (31a)$$

$$\tan \theta_H = \frac{\sqrt{\sin^2 I - \sin^2 \phi}}{\cos I} \quad (31b)$$

Combination of Equations (30) and (31a) leads to:

$$\cos \theta_H = \frac{\cos I}{\cos \phi} \quad (32)$$

(This last expression could also have been obtained directly from Figure 5.)

Analysis of Equation (30) shows that, at the equator ($\phi = 0$), $\left(\frac{d\phi}{d\lambda}\right)_H$ is a maximum. Equation (32) gives this value as $\theta_H = I$, as would be anticipated. When $\phi = I$, its maximum value, both $\left(\frac{d\phi}{d\lambda}\right)_H$ and $\theta_H = 0$, as also would be expected.

To develop analogous expressions for the subpoint track, recall Equations (24), which can be rewritten as:

$$\phi = \arcsin(\sin I \sin l) \quad (33a)$$

$$\lambda = \arctan(\cos I \tan l) \quad (33b)$$

As discussed earlier, the only difference between the heading line and the subpoint track is that due to the eastward rotation of the earth within the orbit, as expressed in Equation (23). (The precession of the orbit is neglected here. This effect, discussed in Section 2.4.1, is normally only a small fraction of the effect of the earth's rotation.) Using Equation (23), it can be shown that:

$$\frac{\Delta\lambda}{360} = \frac{P}{1440} = \frac{d\lambda}{dl} = A \quad (34)$$

To find the expression for the subpoint track, it is only necessary to add the additional movement in longitude, due to the earth's rotation, to Equation (33b):

$$\left. \begin{aligned} \phi &= \arcsin(\sin I \sin l) \\ \lambda &= \arctan(\cos I \tan l) + Al \end{aligned} \right\} \quad (35)$$

Transforming Equation (35) to the format of Equation (24) gives:

$$\left. \begin{aligned} \sin \phi &= \sin I \sin l \\ \tan(\lambda - Al) &= \cos I \tan l \end{aligned} \right\} \quad (36)$$

Differentiating, multiplying, rearranging, and simplifying Equations (36) lead to:

$$\left(\frac{d\phi}{d\lambda}\right)_S = \left(\frac{d\phi}{d\lambda}\right)_H \left\{ \frac{\cos I}{\cos I + A \cos^2 \phi} \right\}, \text{ or} \quad (37)$$

$$\left(\frac{d\phi}{d\lambda}\right)_S = \frac{\cos \phi \sqrt{\sin^2 I - \sin^2 \phi}}{\cos I + A \cos^2 \phi}, \text{ and} \quad (38)$$

$$\tan \theta_S = \frac{\sqrt{\sin^2 I - \sin^2 \phi}}{\cos I + A \cos^2 \phi} \quad (39)$$

$$\cos \theta_S = \frac{\cos I + A \cos^2 \phi}{\cos \phi \sqrt{1 + 2 A \cos I + A^2 \cos^2 \phi}} \quad (40)$$

where the subscript, S, identifies the subpoint track.

Analysis of the expressions for $\left(\frac{d\phi}{d\lambda}\right)_S$ or θ_S shows both values to be a maximum at the equator ($\phi = 0$), and zero when $\phi = I$, its maximum value. It can also be shown that the difference between $\left(\frac{d\phi}{d\lambda}\right)_H$ and $\left(\frac{d\phi}{d\lambda}\right)_S$, or between θ_H and θ_S , is a maximum at the equator. It has already been shown that all of these parameters are zero when $\phi = I$.

As an illustration of these relationships, assume:

$$\phi = 0^\circ$$

$$I = 90^\circ \text{ (i = } 90^\circ \text{)}$$

$$P = 100 \text{ minutes}$$

$$A = \frac{100}{1440} = 0.0695; \frac{1}{A} = 14.4; \text{ from Equation (34)}$$

$$\text{From Equation (31b), } \tan \theta_H = \infty, \theta_H = 90^\circ$$

$$\text{From Equation (39), } \tan \theta_S = \frac{1}{A} = 14.4; \theta_S \approx 86^\circ; \theta_H - \theta_S \approx 4^\circ$$

$$\text{From Equation (32), } \cos \theta_H = 0; \theta_H = 90^\circ$$

$$\text{From Equation (40), } \cos \theta_S = \frac{A}{\sqrt{1 + A^2}} = 0.069; \theta_S \approx 86^\circ; \theta_H - \theta_S \approx 4^\circ$$

2.3.2 Satellite Velocities Over Earth's Surface

In Equation (9) (Section 2.1), it was shown that the satellite velocity over the surface of a non-rotating earth, v_g' , was related to the orbit velocity, v , by the expression:

$$v_g' = \left(\frac{R}{R+h} \right) v \quad (41)$$

Expressions for the orbit velocity are given in Equations (4), (5), (6), (7), (8), (17), (18), and (19).

v_g' is the surface velocity of the satellite along the heading line. It can be resolved into its latitudinal (ϕ) and longitudinal (λ) components by use of θ_H , as given in Equations (31) and (32).

To determine the actual satellite velocity over the earth's surface, v_g , (that along the subpoint track), note that:

$$(v_g)_\phi = (v_g')_\phi \quad (42)$$

$$(v_g)_\lambda = (v_g')_\lambda \pm v_E \cos \phi, \quad (43)$$

where v_E is the linear velocity of the earth's surface at the equator due to the earth's rotation. v_E equals 1670 kilometers per hour, or 905 knots. The plus sign is used for retrograde orbits, the minus for prograde orbits.

2.4 Effects of the Oblateness of the Earth

So far, the earth has been treated as a perfect sphere. Actually, due at least in part to its rotation, it is an oblate spheroid with the polar radius some 21.4 kilometers or 11.6 nautical miles less than the equatorial radius.³ This has several influences which it would be necessary to take into account if very precise design or simulation were to be desired. These include:

a. Gravity is greatest at the poles (9.832 meters per second per second) and least at the equator (9.780 meters per second per second).

b. There is a slight difference between geocentric latitude (latitude taken as the angle between the equatorial plane and a radius to the point of concern) and geodetic latitude (latitude taken as the angle between the equatorial plane and a local

vertical, where the vertical is that defined by a plumb bob). Because of the oblate shape of the earth, the pull of gravity and the direction of the local vertical (except at the poles and along the equator) are not directed exactly towards the geometric center of the earth, but rather toward a direction slightly equatorward of the geometric center. The geodetic latitude, which is that usually given, is very slightly greater than the geocentric latitude.¹

c. The actual satellite height is usually slightly different than $r - R$.

Since for the most part these influences are relatively minor, they will not be discussed in detail here. Detailed discussions have been provided by Fujita.¹

There are, however, two effects of the oblateness of the earth that cannot be ignored. One is the precession of the plane of the orbit, and the second is the rotation of the orbit within its own plane.

2.4.1 Precession of the Plane of the Orbit

Due to the oblate shape of the earth, an orbit does not remain fixed in space, but rather the plane of the orbit rotates slowly around the axis of the earth when considered from the viewpoint of absolute space (the fixed stars). This rotation is of great significance for many types of satellite geophysical observations, since it determines the periods and areas of solar illumination.

The plane of the orbit precesses in Right Ascension (astronomical longitude; see Section 2.2.2) at the rate of a few degrees per day. The precise rate depends on orbit inclination and altitude. This motion of the orbit is known as the regression of the nodes, since it produces a movement, in right ascension, of the ascending and descending nodes.

The cause of this orbital motion has been described in some detail by Bandeen.⁴ The most pertinent points are summarized below:

"For purposes of illustration the satellite orbit can be considered a huge wheel. The gravitational attraction between the equatorial bulge and the rim of the orbit wheel exerts forces directed outside the orbital plane (slightly towards the equator) which create a torque about the (plane of the orbit), tending to turn the orbital plane into the earth's equatorial plane."

The total resultant reactions are, however, like those of a gyroscope so that the orbit plane does not actually rotate towards the equatorial plane, but rather about the earth's axis. (This is analogous to the rotation in the horizontal of a gyroscope axis when suspended by one end, rather than the unsuspended end falling towards the

NAVTRADEVGEN 66-C-0031-1

earth.) As King-Hele⁵ points out, this is also analogous to the wobble (or precession) of a spinning top when the axis is tilted away from the vertical.

Returning to Bandeen's discussion, this results "in a conical motion or precession of the (orbit plane) about a fixed axis - in this case the earth's axis. Hence, the inclination angle of the orbital plane remains constant (within the scope of this discussion) but the line of nodes (plane of the orbit) regresses (i. e., it moves around the equator in a direction opposite to the motion of the satellite in orbit). For a satellite revolving in orbit in the direction of the earth's rotation (i. e., from west to east or prograde), the nodal regression is from east to west; and for a satellite revolving in orbit against the direction of rotation of the earth (a retrograde orbit), the nodal regression is from west to east."

King-Hele⁵ provides the rate of precession of the orbit plane as:

$$9.97 \frac{R}{a}^{3.5} \cos i \text{ degrees per day,} \quad (44)$$

where

R = radius of the earth

a = mean distance of satellite in orbit from center of earth

i = orbit inclination

This equation is graphed in Figure 6.

Approximate values of this orbit precession in absolute space for TIROS and Nimbus orbits are:

<u>Satellite</u>	<u>Orbit Altitude</u>	<u>Orbit Inclination</u>	<u>Approx. Precession (in absolute space)</u>
TIROS	400 miles	48°	5° per day (westward)
TIROS	400 miles	58°	4° per day (westward)
Nimbus	600 nautical miles	80° (retrograde)	1° per day (eastward)

So far, this orbital precession has been considered relative only to absolute space or the fixed stars. When considering illumination for satellite observation, it is necessary to consider precession relative to the sun. Assume first an orbit with no absolute precession (a purely polar orbit); then, relative to the sun, it would precess from east-to-west at about one degree a day due to the movement of the earth in its orbit around the sun (the exact rate would be $\frac{360}{365}$ or 0.9856 degrees

NAVTRADEVGEN 66-C-0031-1

per day). If the satellite started with such an orbit so that it crossed the equator at noon and midnight, three months later the orbit would appear to have rotated 90° relative to the sun and it would have become a "dawn-dusk" orbit.

Accordingly, for considering illumination, the absolute and the "solar" precessions must be algebraically added to get the total precession relative to the sun. In doing so, the following approximate values result:

<u>Satellite</u>	<u>Orbit Altitude</u>	<u>Orbit Inclination</u>	<u>Approx. Precession (relative to sun)</u>
TIROS	400 miles	48°	6° per day (westward)
TIROS	400 miles	58°	5° per day (westward)
Nimbus	600 nautical miles	80° (retrograde)	0° per day

When determining the subpoint track or satellite velocity, as discussed in Sections 2.3.1 and 2.3.2, the precession of the orbit plane can be taken into account by a modification to the A of Equation (34). A has the dimensions of degrees of latitude per degree of argument, l . 360° of argument occur in one period, P . The rate of regression of the nodes is usually given in degrees of right ascension per day.

Let:

$$A = A_E + k A_S \pm k A_N \quad (45)$$

where

$$A_E = \text{the } A \text{ of Equation (34)} = \frac{P}{1440}$$

$$A_N = \text{the rate per day of the regression of the nodes in degrees of right ascension}$$

$$A_S = \text{the rate in degrees per day of the rotation of the earth around the sun} = 0.9856 \text{ degrees per day}$$

$$k = P/(360)(1440) = 1.93 \times 10^{-6} P$$

$$\left. \begin{aligned} A &= \frac{P}{1440} + 1.93 \times 10^{-6} P (A_S \pm A_N) \\ A &= \frac{P}{1440} + 1.93 \times 10^{-6} P (0.9856 \pm A_N) \end{aligned} \right\} \quad (46)$$

The plus sign applies to a prograde orbit, and the minus sign to a retrograde orbit.

NAVTRADEVGEN 66-C-0031-1

For most orbits, the principal effect of the regression of the nodes is to vary, from day to day, the latitudes over which the satellite passes during the illuminated portion of its orbit.^{6,7} This is illustrated by Figure 7, which is drawn for a TIROS in a 58° orbit at an altitude of about 400 nautical miles. It can be seen that the band of illuminated latitudes varies cyclically over about a 76 day period.

A unique set of orbits which is particularly desirable for many types of geophysical observations is that where, from Equation (44):

$$9.97 \left(\frac{R}{a} \right)^{3.5} \cos i = -0.9856 \quad (47)$$

In that case, the angle between the orbit plane and the sun remains a constant, and the ascending node occurs at the same local time on each orbit. Such an orbit is often referred to a sun-synchronous.

In a sun-synchronous orbit, the solar illumination on the dayside of the orbit will be an essentially fixed function of latitude, except for the slow seasonal changes resulting from the precession of the earth's axis relative to the sun. The degree of illumination will, of course, depend on the local time of ascending or descending node.

The relationships between orbit altitude and inclination for a sun-synchronous orbit are provided in Figure 8 and Table 1.

Nimbus satellites are placed in sun-synchronous orbits with an ascending node at noon. ESSA satellites are also sun-synchronous, with a nominal 0900 (local time) descending node for the APT version, and a 1500 (local time) ascending node for the AVCS version.

2.4.2 Rotation of the Orbital Ellipse in its Own Plane

The second major effect of the oblate shape of the earth is a rotation, in its own plane and without change of shape, of the orbital ellipse. While this rotation is of negligible significance for essentially circular orbits, in the case of elliptical orbits it produces a variation with time of the orbit altitude, and of the satellite ground velocity, at any given point or latitude.⁸ This orbital perturbation is known as the rotation of the line of the apsides, the apsides being perigee and apogee.

Once a satellite has been injected into orbit, the shape of the orbit, relative only to the center of the earth, is essentially constant at the altitudes normal to meteorological or geophysical satellites (i. e., about a few hundred miles).

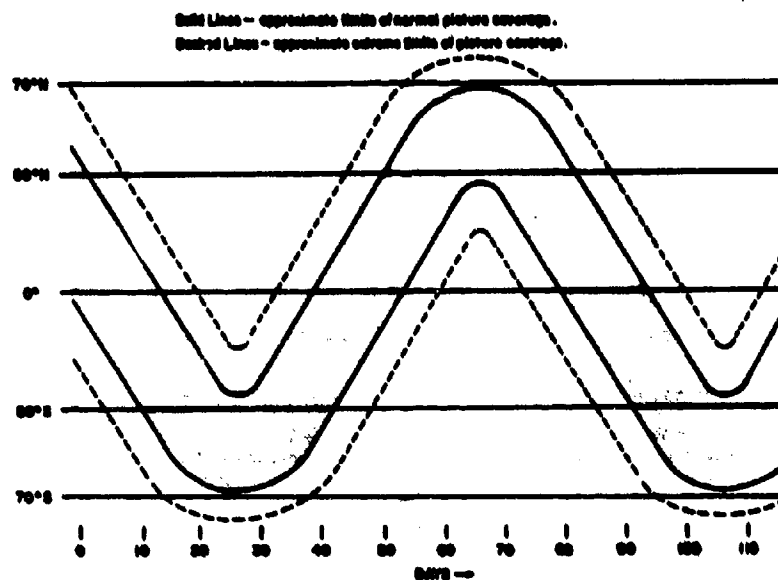


Figure 7. Day-to-Day Change of Illuminated Latitudinal Belt Observable from a Single TIROS in an Orbit with a 98° Inclination

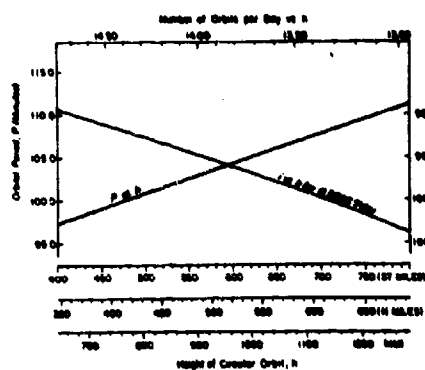


Figure 8. Orbital Period P , Number of Orbits Per Day, and Inclination Angle i of a Sun-Synchronous Orbit ($\Omega = 0.9884$ degrees/day) Versus Height h of a Circular Orbit

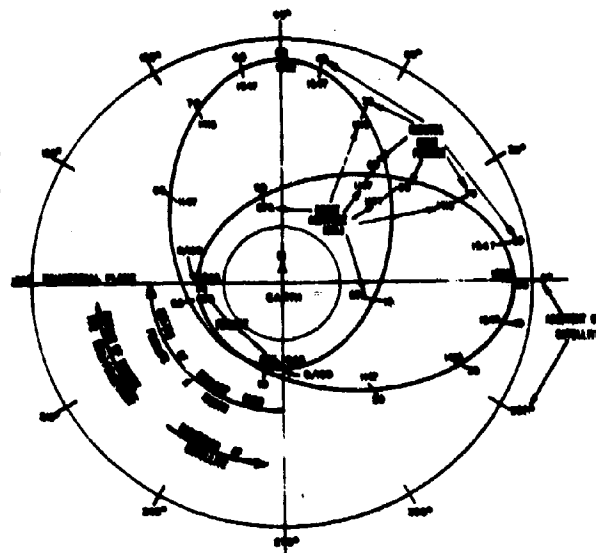


Figure 9. Relationships Between Perigee, Time from Perigee, and Argument, for an Elliptical Orbit

Figure 9 illustrates an elliptical orbit about the earth. (Some aspects have been deliberately exaggerated for clarity of illustration.) Consider first only one of the two orbit orientations shown, that where perigee is near the south pole.

First, however, to insure Figure 9 is understood:

1. The large outer circle depicts the argument of the satellite. The argument of a satellite is the angular distance, measured in degrees of great circle arc in the orbital plane (the plane of Figure 9) and in the direction of satellite motion, from ascending node to the position of the satellite. The satellite is moving counterclockwise in Figure 9. Argument is zero at the right of Figure 9 (the northbound crossing of the equatorial plane) and increases counterclockwise.

2. An arbitrary orbit with a 100 minute period is used. The times in minutes from perigee that it requires the satellite to reach various points on its orbit are indicated just outside each of the two orbits.

3. Orbit altitudes in kilometers (arbitrarily chosen to illustrate pertinent points) are indicated at various points just inside each orbit.

Returning now to the orbit with perigee near the south pole, note that the times, to cover equal portions of the orbit as expressed in argument, vary widely. Near perigee, where the satellite is moving most rapidly, it covers a large distance in argument in a short period of time (i. e., about 80° of argument in 10 minutes in Figure 9). Near apogee, the satellite moves more slowly and covers only about 10° in argument in a similar 10 minute interval.

It should be obvious from Figure 9 that equal distances in argument represent also essentially equal distances over the earth's surface. Accordingly, the distance the satellite moves across the earth during a given time interval also varies from one part of the orbit to another (see Section 2.1.3).

Although the shape of an orbit will remain essentially constant for long periods of time, its orientation in space will not normally do so. In addition to the precession of the plane of the orbit, already considered in Section 2.4.1, there is a second change in orientation, a slow and constant rotation of an elliptical orbit in its own plane. (This is illustrated in Figure 9 by the rotation from an initial perigee near the south pole to a perigee near the equatorial plane on the left side of the diagram.) The direction and rate of this rotation are functions of (1) the orbital inclination, (2) the average altitude over the entire orbit, and (3) the direction of satellite motion.

NAVTRADEVGEN 66-C-0031-1

The rate of rotation, in degrees per day, is given by:

$$4.98 \left(\frac{R}{a} \right)^{3.5} (5 \cos^2 i - 1) \quad (48)$$

where

- R = the radius of the earth
- a = the mean radius of the orbit or the semi-major axis
- i = the orbit inclination

and the rate derived is graphed in Figure 10.

For altitudes near those planned for Nimbus, the rate of rotation is about 2-3° per day (in argument). The direction of rotation depends solely on inclination. For orbital inclinations greater than 63.4°, the direction of orbital rotation is opposite to the direction of motion of the spacecraft (i.e., towards smaller values of argument). For inclinations less than 63.4°, the rotation of the orbit and the motion of the satellite are in the same direction.

In Figure 9, the two orbits shown are intended to illustrate the rotation of a Nimbus orbit that might occur over an interval of about a month.

For the immediately following discussion, it will be convenient to temporarily consider the earth as non-rotating, since it is necessary to consider points on the earth itself only in terms of their latitude. For any given value of orbit inclination, each value of argument always has a corresponding value of latitude (see Eq. (24)). (Factors related to the rotation of the earth are taken into consideration by (a) the change in longitude, from one orbit to another, of ascending node (see Section 2.3); (b) the plotting of data, in actual practice, along a subpoint track; and (c) the difference between the subpoint track and the heading line - see Section 2.3.1.)

From Figure 9, it is obvious that any point that can be identified along the orbit ellipse rotates (in argument and about the earth) at the same (essentially constant) rate as the entire ellipse. For example, in Figure 9, while the ellipse and its perigee rotate 90°, the point 70 minutes from perigee rotates from about 115° (in argument) to about 25°, or also 90°. Furthermore, since there is no significant change in the shape of the orbit, each point retains its orbit altitude as it rotates (1416 km in the case of the above discussed 70 minute point), neglecting the rather small effects of the non-spherical shape of the earth (which introduces an error, at most, of about 6 nautical miles, or 10 km). Accordingly, if the rate of rotation of any one point of the orbit and the shape of the orbit are known, the future position and altitude of any point on the orbit at any given time, can be predicted.

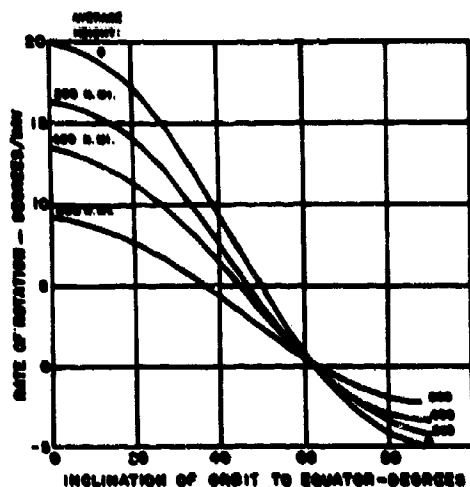


Figure 10 Rate of Rotation of Elliptical Satellite Orbit in its Own Plane, Caused by the Earth's Equatorial Bulge. Rotation in the Same Direction as the Satellite is Going Around is Taken Positive.

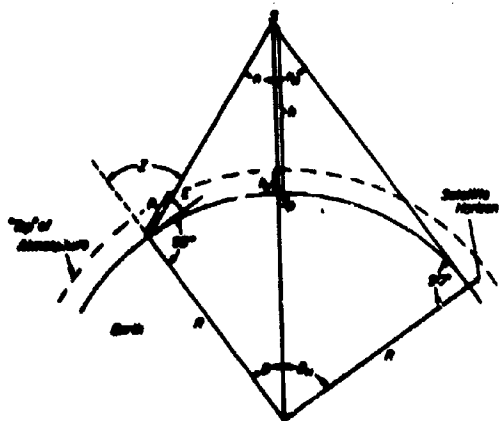


Figure 11 Satellite Viewing Geometry

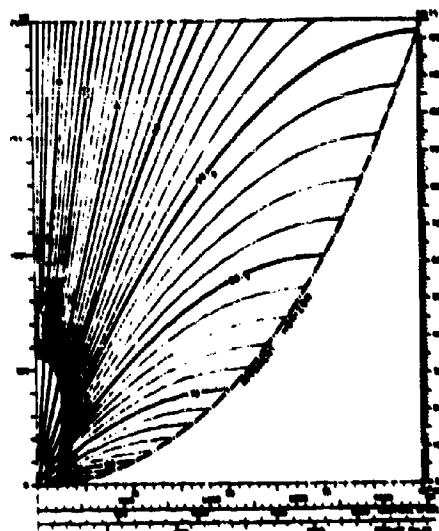


Figure 12a Height of a Satellite vs Great-Circle Distance from Subpoint of Objects with Different Nadir Angles. The Great-Circle Distance for a Given Satellite Height and a Nadir Angle is Obtained by Drawing a Horizontal Straight Line Through the Satellite Height. The Abscissa of the Points of Intersection of the Line and the Curves of each Nadir Angle represent the Great-Circle Distance from the Subpoint

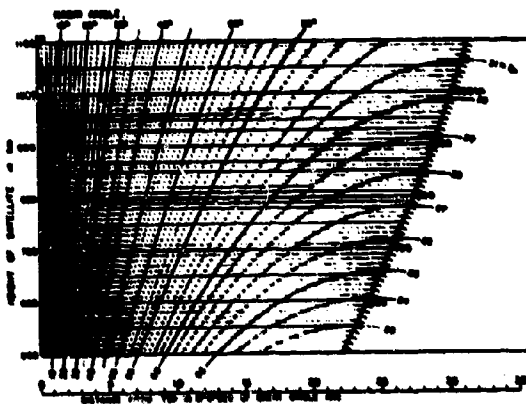


Figure 12b An Enlarged Section of the Previous Diagram. This Diagram Covers the Heights and Nadir Angles Needed for TIROS

By a convention long established in astronomy, perigee is chosen as the unique point on the orbit whose motion is determined, and as the point to which all other points are referenced (in terms of time from perigee as the satellite moves around its orbit). When an orbit ephemeris is calculated, the time (Universal) and the argument (angular distance from ascending node) of perigee are determined for a specified orbital revolution (or numbered orbit). By the fixed relationships between argument and latitude, for a known inclination, the latitude of perigee on that orbit can then easily be determined, thus relating the position of perigee to the earth's surface. The computations also provide the rate of motion of perigee (in argument), thus allowing the prediction of the position of perigee (in either argument or latitude) at any future time. (Note: a given change in argument does not lead to an equal change in latitude, and this is especially true at high latitudes.)

By accepted practice, the longitude of perigee is usually not given directly, but is established by implication when the longitude of ascending node is computed. (Of course, the longitude of perigee and that of ascending node will rarely be the same.)

Figure 9 also can be used to illustrate the troubles that would arise if this rotation of a non-circular orbit is not taken into account. On the initial orbit (that with its perigee near the south pole), the times (relative to perigee) from 60 to 89 minutes (about 29 minutes along the orbit) cover some 80° in argument (from 100° to 180°), which, for a near-polar Nimbus orbit, is also equal to nearly 80° in latitude. Yet, only 30 days later (the second orbit), the times from 90 to 100 minutes (only 10 minutes along the orbit) cover nearly the same distance and the same band of latitudes along the earth. Obviously, this makes a great difference when relating time, relative to an equator crossing, to distance from the equator. Furthermore, on the initial orbit, the orbit altitude at an argument of 100° (about a latitude of 80°) is over 1500 km, while 30 days later it is less than 900 km; this difference in altitude leads to a significant difference in the scale of satellite pictures and the proper location of points other than near the picture center.

Because of this rotation of perigee, the anomalistic period (the orbital period measured from one perigee to the next) and the nodal period (that measured from one ascending node to the next) will usually be slightly different (the order of 0.3 minutes or less).

2.5 Computation of Orbital Elements and Ephemerides

Programs for computing orbital elements and ephemerides (tabulations of the spatial positions of satellites as a function of time) are readily available.^{9, 10}

These programs can be used to compute either a set of orbital elements or an ephemeris from a set of satellite tracking station observations, or to compute an ephemeris from a set of orbital elements.

Ephemerides most frequently tabulate the spatial position of a satellite (latitude, longitude, and altitude) at equal intervals of time relative to either ascending node or perigee.

A typical set of orbital elements is given below:

THE FOLLOWING ARE THE ORBITAL ELEMENTS FOR SATELLITE
1963 24-A ONE
TIROS VII COMPUTED FROM MINITRACK OBSERVATIONS AT THE
NASA COMPUTING CENTER AND ISSUED ON 15 MAY 1964 BY THE
GODDARD SPACE FLIGHT CENTER
EPOCH 64 Y 05 M 06 D AT 10 HOURS 02.00 MIN. UT

SEMI-MAJOR AXIS	007013.39	KILOMETERS
ECCENTRICITY	0.00192	
INCLINATION	058.235	DEGREES
MEAN ANOMALY	051.491	DEGREES
ARGUMENT OF PERIGEE	088.569	DEGREES
/MOTION PLUS	01.3771	DEG. PER DAY
R.A. OF ASCEND. NODE	185.624	DEGREES
/MOTION MINUS	03.7621	DEG. PER DAY
ANOMALISTIC PERIOD	0097.41757	MINUTES
/MOTION MINUS	0.00002	MIN. PER DAY
HEIGHT OF PERIGEE	000621.54	KILOMETERS
HEIGHT OF APOGEE	000649.46	KILOMETERS
VELOCITY AT PERIGEE	027193	KM. PER HR
VELOCITY AT APOGEE	027089	KM. PER HR
GEOC. LAT OF PERIGEE	58.206	DEGREES

The following abbreviated glossary¹¹ defines the terms used in a set of orbital elements and others frequently used in connection with satellite orbits:

ANOMALY: The geocentric angle of a point along a satellite orbit as measured from perigee.

ANOMALISTIC PERIOD: The time elapsing between successive passages of a satellite through its perigee.

APOGEE: The point in its orbit at which a satellite is farthest from the center of the earth.

ARGUMENT (Of a Point in a Satellite's Orbit): The geocentric angle of the point measured, from ascending node, in the orbital plane and in the direction of motion.

As can be noted from Equation (24), argument is a function only of satellite inclination and latitude. Table 2 is a tabulation of argument for several quasi-polar orbit inclinations.

ARIES: A designation for the Vernal Equinox, since Aries is the first sign of the Zodiac. (Actually the vernal equinox no longer occurs at the time the sun is in Aries.)

ASCENDING NODE: The point in its orbit, usually given in degrees of longitude or as a time, at which a satellite crosses the equator from the southern to the northern hemisphere.

DECLINATION: The angular distance [north (+) or south (-)] from the celestial equator of a point on the celestial sphere. It is measured along the hour circle passing through the point.

ECCENTRICITY: The ellipticity of an orbit - the ratio between the distance from the center of the ellipse to one of the foci, and the length of the semi-major axis. It is equal to $\frac{a - r_p}{a}$, or $\frac{r_a - r_p}{r_a + r_p}$.

EPHEMERIS: A table of calculated coordinates of a satellite (plural: EPHEMERIDES).

EPOCH: The instant of time to which the data in a set of orbital elements are referenced.

INCLINATION (of Satellite Orbit): The angle between the orbital plane of a satellite and the equatorial plane.

MEAN ANOMALY: The geocentric angle which would be swept out by a satellite radius vector, since the last passage through perigee, if the satellite moved at a uniform speed. It is directly proportional to the time since passage through perigee.

NODAL PERIOD: The time elapsing between successive passages of the satellite through its ascending node.

PERIGEE: The point in its orbit at which a satellite is closest to the center of the earth.

RIGHT ASCENSION: The angular distance of a point on the celestial sphere measured eastward from the vernal equinox. The measurement is made along the celestial equator from the vernal equinox, to the hour circle passing through the point.

TABLE 2

ARGUMENT OF SATELLITE AS A FUNCTION
OF LATITUDE AND ORBIT INCLINATION

Approximate Sun-Synchronous Orbit Altitude (n. mi.)	250	400	500	600	725
Inclination	i = 97.0 (83.0)	i = 98.0 (82.0)	i = 99.0 (81.0)	i = 100.0 (80.0)	i = 101.0 (79.0)
Argument of Satellite	Latitude	Latitude	Latitude	Latitude	Latitude
0.00	0.00	0.00	0.00	0.00	0.00
2.00	1.98	1.98	1.97	1.96	1.96
4.00	3.97	3.96	3.95	3.93	3.92
6.00	5.95	5.94	5.92	5.90	5.88
8.00	7.93	7.92	7.90	7.87	7.85
10.00	9.92	9.90	9.87	9.84	9.81
12.00	11.90	11.88	11.85	11.81	11.77
14.00	13.89	13.86	13.82	13.78	13.73
16.00	15.87	15.84	15.79	15.75	15.69
18.00	17.86	17.81	17.77	17.71	17.65
20.00	19.84	19.79	19.74	19.68	19.61
22.00	21.82	21.77	21.71	21.64	21.57
24.00	23.80	23.75	23.68	23.61	23.53
26.00	25.79	25.72	25.65	25.57	25.48
28.00	27.77	27.70	27.62	27.53	27.44
30.00	29.75	29.67	29.59	29.49	29.39
32.00	31.73	31.65	31.56	31.45	31.34
34.00	33.71	33.62	33.52	33.41	33.29
36.00	35.69	35.59	35.48	35.37	35.23
38.00	37.66	37.56	37.45	37.32	37.18
40.00	39.64	39.53	39.41	39.27	39.12
42.00	41.61	41.49	41.36	41.22	41.05
44.00	43.58	43.46	43.32	43.16	42.99
46.00	45.55	45.42	45.27	45.10	44.92
48.00	47.52	47.38	47.22	47.04	46.84
50.00	49.49	49.33	49.16	48.97	48.76
52.00	51.45	51.29	51.10	50.89	50.67
54.00	53.41	53.23	53.04	52.81	52.57
56.00	55.37	55.18	54.96	54.73	54.46
58.00	57.32	57.11	56.88	56.63	56.34
60.00	59.26	59.04	58.79	58.52	58.22
62.00	61.20	60.96	60.70	60.40	60.08
64.00	63.13	62.87	62.58	62.26	61.91
66.00	65.05	64.77	64.46	64.11	63.73
68.00	66.96	66.65	66.31	65.93	65.52
70.00	68.85	68.52	68.14	67.73	67.28
72.00	70.72	70.35	69.94	69.48	69.00
74.00	72.57	72.15	71.70	71.20	70.66
76.00	74.37	73.91	73.40	72.85	72.26
78.00	76.13	75.61	75.03	74.42	73.77
80.00	77.81	77.21	76.57	75.89	75.17
82.00	79.38	78.70	77.98	77.21	76.42
84.00	80.79	80.01	79.19	78.35	77.48
86.00	81.94	81.06	80.15	79.23	78.30
88.00	82.72	81.75	80.78	79.80	78.82
90.00	83.00	82.00	81.00	80.00	79.00

TABLE 2 (cont)

ARGUMENT OF SATELLITE AS A FUNCTION
OF LATITUDE AND ORBIT INCLINATION

Approximate Sun-Synchronous Orbit Altitude (n. mi.)	250	400	500	600	725
Inclination	i = 97.0 (83.0)	i = 98.0 (82.0)	i = 99.0 (81.0)	i = 100.0 (80.0)	i = 101.0 (79.0)
Argument of Satellite	Latitude	Latitude	Latitude	Latitude	Latitude
92.00	82.72	81.75	80.78	79.80	78.82
94.00	81.94	81.06	80.15	79.29	78.30
96.00	81.19	80.31	79.49	78.59	77.48
98.00	79.38	78.70	77.98	77.21	76.42
100.00	77.81	77.21	76.57	75.89	75.17
102.00	76.13	75.61	75.03	74.42	73.77
104.00	74.37	73.91	73.40	72.89	72.26
106.00	72.57	72.15	71.70	71.20	70.66
108.00	70.72	70.35	69.94	69.48	69.00
110.00	68.85	68.52	68.14	67.73	67.28
112.00	66.96	66.65	66.31	65.91	65.52
114.00	65.05	64.77	64.46	64.11	63.79
116.00	63.13	62.87	62.58	62.26	61.91
118.00	61.20	60.96	60.70	60.40	60.08
120.00	59.26	59.04	58.79	58.52	58.22
122.00	57.32	57.11	56.88	56.63	56.35
124.00	55.37	55.18	54.96	54.73	54.46
126.00	53.41	53.23	53.04	52.81	52.57
128.00	51.45	51.29	51.10	50.89	50.67
130.00	49.49	49.33	49.16	48.97	48.76
132.00	47.52	47.38	47.22	47.04	46.84
134.00	45.55	45.42	45.27	45.10	44.92
136.00	43.58	43.46	43.32	43.16	42.99
138.00	41.61	41.49	41.36	41.22	41.05
140.00	39.64	39.53	39.41	39.27	39.12
142.00	37.66	37.56	37.45	37.32	37.18
144.00	35.69	35.59	35.48	35.37	35.23
146.00	33.71	33.62	33.52	33.41	33.29
148.00	31.73	31.65	31.56	31.45	31.34
150.00	29.75	29.67	29.59	29.49	29.38
152.00	27.77	27.70	27.62	27.53	27.44
154.00	25.79	25.72	25.65	25.57	25.48
156.00	23.80	23.75	23.68	23.61	23.53
158.00	21.82	21.77	21.71	21.64	21.57
160.00	19.84	19.79	19.74	19.68	19.61
162.00	17.86	17.81	17.77	17.71	17.65
164.00	15.87	15.84	15.79	15.75	15.69
166.00	13.89	13.86	13.82	13.78	13.73
168.00	11.90	11.88	11.85	11.81	11.77
170.00	9.92	9.90	9.87	9.84	9.81
172.00	7.93	7.92	7.90	7.87	7.85
174.00	5.95	5.94	5.92	5.90	5.88
176.00	3.97	3.96	3.95	3.93	3.92
178.00	1.98	1.98	1.97	1.96	1.96
180.00	.00	.00	.00	.00	.00

TABLE 2 (cont)

ARGUMENT OF SATELLITE AS A FUNCTION
OF LATITUDE AND ORBIT INCLINATION

Approximate Sun-Synchronous Orbit Altitude (n. mi.)	250	400	500	600	725
Inclination	i = 97.0 (83.0)	i = 98.0 (82.0)	i = 99.0 (81.0)	i = 100.0 (80.0)	i = 101.0 (79.0)
Argument of Satellite	Latitude	Latitude	Latitude	Latitude	Latitude
182.00	-1.98	-1.98	-1.97	-1.96	-1.96
184.00	-3.97	-3.96	-3.95	-3.95	-3.92
186.00	-5.95	-5.94	-5.92	-5.90	-5.88
188.00	-7.93	-7.92	-7.90	-7.87	-7.85
190.00	-9.92	-9.90	-9.87	-9.84	-9.81
192.00	-11.90	-11.88	-11.85	-11.81	-11.77
194.00	-13.89	-13.86	-13.82	-13.78	-13.73
196.00	-15.87	-15.84	-15.79	-15.75	-15.69
198.00	-17.86	-17.81	-17.77	-17.71	-17.65
200.00	-19.84	-19.79	-19.74	-19.68	-19.61
202.00	-21.82	-21.77	-21.71	-21.64	-21.57
204.00	-23.80	-23.75	-23.68	-23.61	-23.53
206.00	-25.79	-25.72	-25.65	-25.57	-25.48
208.00	-27.77	-27.70	-27.62	-27.53	-27.44
210.00	-29.75	-29.67	-29.59	-29.49	-29.39
212.00	-31.73	-31.65	-31.56	-31.45	-31.34
214.00	-33.71	-33.62	-33.52	-33.41	-33.29
216.00	-35.69	-35.59	-35.48	-35.37	-35.23
218.00	-37.66	-37.56	-37.45	-37.32	-37.18
220.00	-39.64	-39.53	-39.41	-39.27	-39.12
222.00	-41.61	-41.49	-41.36	-41.22	-41.05
224.00	-43.58	-43.46	-43.32	-43.16	-42.99
226.00	-45.55	-45.42	-45.27	-45.10	-44.92
228.00	-47.52	-47.38	-47.22	-47.04	-46.84
230.00	-49.49	-49.33	-49.16	-48.97	-48.76
232.00	-51.45	-51.29	-51.10	-50.89	-50.67
234.00	-53.41	-53.23	-53.04	-52.81	-52.57
236.00	-55.37	-55.18	-54.96	-54.73	-54.46
238.00	-57.32	-57.11	-56.88	-56.64	-56.35
240.00	-59.26	-59.04	-58.79	-58.52	-58.22
242.00	-61.20	-60.96	-60.70	-60.40	-60.08
244.00	-63.13	-62.87	-62.58	-62.26	-61.91
246.00	-65.05	-64.77	-64.46	-64.11	-63.73
248.00	-66.96	-66.65	-66.31	-65.93	-65.52
250.00	-68.85	-68.52	-68.14	-67.71	-67.28
252.00	-70.72	-70.35	-69.94	-69.48	-69.00
254.00	-72.57	-72.15	-71.70	-71.20	-70.66
256.00	-74.37	-73.91	-73.40	-72.85	-72.26
258.00	-76.13	-75.61	-75.03	-74.42	-73.77
260.00	-77.81	-77.21	-76.57	-75.89	-75.17
262.00	-79.38	-78.70	-77.98	-77.21	-76.42
264.00	-80.79	-80.01	-79.19	-78.35	-77.48
266.00	-81.94	-81.06	-80.15	-79.23	-78.30
268.00	-82.72	-81.75	-80.78	-79.80	-78.82
270.00	-83.00	-82.00	-81.00	-80.00	-79.00

TABLE 2 (cont)

ARGUMENT OF SATELLITE AS A FUNCTION
OF LATITUDE AND ORBIT INCLINATION

Approximate Sun-Synchronous Orbit Altitude (n. mi.)	250	400	500	600	725
Inclination	i = 97.0 (83.0)	i = 98.0 (82.0)	i = 99.0 (81.0)	i = 100.0 (80.0)	i = 101.0 (79.0)
Argument of Satellite	Latitude	Latitude	Latitude	Latitude	Latitude
272.00	-82.72	-81.75	-80.78	-79.80	-78.82
274.00	-81.94	-81.06	-80.15	-79.21	-78.30
276.00	-80.79	-80.01	-79.19	-78.35	-77.48
278.00	-79.38	-78.70	-77.98	-77.21	-76.42
280.00	-77.81	-77.21	-76.57	-75.89	-75.17
282.00	-76.13	-75.61	-75.03	-74.42	-73.77
284.00	-74.37	-73.91	-73.40	-72.85	-72.26
286.00	-72.57	-72.15	-71.70	-71.20	-70.66
288.00	-70.72	-70.35	-69.94	-69.48	-69.00
290.00	-68.85	-68.52	-68.14	-67.73	-67.28
292.00	-66.96	-66.65	-66.31	-65.93	-65.52
294.00	-65.05	-64.77	-64.46	-64.11	-63.73
296.00	-63.13	-62.87	-62.58	-62.26	-61.91
298.00	-61.20	-60.96	-60.70	-60.40	-60.08
300.00	-59.26	-59.04	-58.79	-58.52	-58.22
302.00	-57.32	-57.11	-56.88	-56.63	-56.35
304.00	-55.37	-55.18	-54.96	-54.73	-54.46
306.00	-53.41	-53.23	-53.04	-52.81	-52.57
308.00	-51.45	-51.29	-51.10	-50.89	-50.67
310.00	-49.49	-49.34	-49.16	-48.97	-48.76
312.00	-47.52	-47.38	-47.22	-47.04	-46.84
314.00	-45.55	-45.42	-45.27	-45.10	-44.92
316.00	-43.58	-43.46	-43.32	-43.16	-42.99
318.00	-41.61	-41.49	-41.36	-41.22	-41.05
320.00	-39.64	-39.53	-39.41	-39.27	-39.12
322.00	-37.66	-37.56	-37.45	-37.32	-37.18
324.00	-35.69	-35.59	-35.48	-35.37	-35.23
326.00	-33.71	-33.62	-33.52	-33.41	-33.29
328.00	-31.73	-31.65	-31.56	-31.45	-31.34
330.00	-29.75	-29.67	-29.59	-29.49	-29.39
332.00	-27.77	-27.70	-27.62	-27.53	-27.44
334.00	-25.79	-25.72	-25.65	-25.57	-25.48
336.00	-23.81	-23.75	-23.68	-23.61	-23.53
338.00	-21.82	-21.77	-21.71	-21.64	-21.57
340.00	-19.84	-19.79	-19.74	-19.68	-19.61
342.00	-17.86	-17.81	-17.77	-17.71	-17.65
344.00	-15.87	-15.84	-15.79	-15.75	-15.69
346.00	-13.89	-13.86	-13.82	-13.78	-13.73
348.00	-11.90	-11.88	-11.85	-11.81	-11.77
350.00	-9.92	-9.90	-9.87	-9.84	-9.81
352.00	-7.93	-7.92	-7.90	-7.87	-7.85
354.00	-5.95	-5.94	-5.92	-5.90	-5.88
356.00	-3.97	-3.96	-3.95	-3.93	-3.92
358.00	-1.98	-1.98	-1.97	-1.96	-1.96
360.00	-0.00	-0.00	-0.00	-0.00	-0.00

NAVTRADEVCE 66-C-0031-1

SEMI-MAJOR AXIS: The distance from the center of an ellipse to the point of either perigee or apogee.

SUBPOINT: The subsatellite point - the intersection with the earth's surface of the local vertical passing through the satellite.

TRUE ANOMALY: The geocentric angle of a satellite, measured in its orbital plane and in the direction of motion, from its perigee.

VERNAL EQUINOX: The point of intersection of the celestial equator with the ecliptic, at the point where the sun crosses the equator when moving from the southern to the northern hemisphere. It is the point on the celestial sphere of the sun at the time of the spring equinox in the northern hemisphere.

2.6 Satellite Viewing Geometry

From the orbital elements and or ephemerides, the position of a satellite in space (latitude, longitude, and altitude) can be determined at any desired time. Factors influencing the view of a sensor, from a satellite position which is assumed to be known, will now be examined.

In Figure 11, a satellite or a satellite sensor, S, is at a known height, h, over a known subpoint, S_P. Let the line of sight be defined from the satellite in terms of n, the nadir angle or the angle between the line of sight and the vertical. A point on the earth is defined in terms of its geocentric distance, in degrees of great circle arc, from S_P. A degree of great circle arc is, for practical purposes, equal to 60 nautical miles or 111 kilometers.

Considering the right side of Figure 11, it is seen that the extreme limit of coverage, the line of sight from the satellite to the horizon, is given by:

$$\sin n_H = \cos B_H = \frac{R}{R + H} \quad (49)$$

Values of n_H and B_H for various satellite altitudes are given in Table 1.

Using the left hand side of Figure 11, and the law of sines, it is found that for any arbitrary nadir angle $n (\leq n_H)$,

$$\frac{R}{\sin n} = \frac{R + h}{\sin (180^\circ - n - B)} \quad (50)$$

$$B = 180^\circ - n - \arcsin \left[\left(\frac{R + h}{R} \right) \sin n \right] \quad (51)$$

subject to the constraint that

$$\arcsin \left[\left(\frac{R+h}{R} \right) \sin n \right] \approx 90^\circ \quad (52)$$

Equation (51) can also be written as:

$$B = \arcsin \left[\left(\frac{R+h}{R} \right) \sin n \right] - n \quad (53)$$

if

$$\arcsin \left[\left(\frac{R+h}{R} \right) \sin n \right] \leq 90^\circ \quad (54)$$

These relationships are graphed in Figure 12 and tabulated in Table 3.

If B is known, the solution for n is:

$$n = \arccot \left[\left(\frac{R+h}{R} \right) \csc B - \cot B \right] \quad (55)$$

For some purposes, the zenith angle, Z, at the point observed is of significant interest. Simple trigonometry shows that:

$$Z = n + B \quad (56)$$

$$Z = \arcsin \left[\left(\frac{R+h}{R} \right) \sin n \right] \quad (57)$$

$$Z = \arccot \left[\left(\frac{R+h}{R} \right) \csc B - \cot B \right] + B \quad (58)$$

Another angle of concern, especially² when determining satellite tracking data (as for the APT procedures)¹² is E, the elevation angle from a point on the ground to the satellite. Since

$$E = 90^\circ - Z \quad (59)$$

E can be expressed in terms of n or B as:

$$E = \arccos \left[\left(\frac{R+h}{R} \right) \sin n \right] \quad (60)$$

$$E = \arctan \left[\cot B - \left(\frac{R}{R+h} \right) \csc B \right] \quad (61)$$

TABLE 3
SUB-POINT TO OBJECT DISTANCE (DEGREES OF GREAT CIRCLE ARC)

HAZAR ANGLE	HEIGHT (Statute Miles)									
	400	425	450	475	500	525	550	575	600	
	HEIGHT RANGE (Kilometers)									
	718 to 764	765 to 810	811 to 856	857 to 903	904 to 949	950 to 995	996 to 1042	1043 to 1088	1089 to 1134	
0	0.0	0.0	0.0	0.0	0.0	0.0	0.0	0.0	0.0	0.0
2	0.2	0.2	0.2	0.2	0.2	0.3	0.3	0.3	0.3	0.3
4	0.4	0.4	0.5	0.5	0.5	0.6	0.6	0.6	0.6	0.6
6	0.7	0.7	0.7	0.8	0.8	0.9	0.9	0.9	0.9	0.9
8	0.9	0.9	1.0	1.1	1.1	1.2	1.2	1.2	1.2	1.2
10	1.1	1.2	1.3	1.3	1.4	1.5	1.5	1.6	1.6	1.6
12	1.4	1.5	1.5	1.6	1.7	1.8	1.9	1.9	2.0	2.1
14	1.6	1.7	1.8	1.9	2.0	2.1	2.2	2.3	2.3	2.5
16	1.9	2.0	2.1	2.2	2.4	2.5	2.6	2.7	2.8	2.8
18	2.1	2.3	2.4	2.5	2.7	2.8	3.0	3.1	3.2	3.2
20	2.4	2.5	2.7	2.9	3.0	3.2	3.3	3.5	3.6	3.6
22	2.7	2.8	3.0	3.2	3.4	3.5	3.7	3.9	4.0	4.0
24	3.0	3.1	3.3	3.5	3.7	3.9	4.1	4.3	4.5	4.5
26	3.2	3.5	3.7	3.9	4.1	4.3	4.5	4.7	4.9	4.9
28	3.6	3.8	4.0	4.2	4.5	4.7	4.9	5.2	5.4	5.4
30	3.9	4.1	4.4	4.6	4.9	5.1	5.4	5.6	5.9	5.9
32	4.2	4.5	4.8	5.0	5.3	5.6	5.9	6.2	6.4	6.4
34	4.6	4.9	5.2	5.5	5.8	6.1	6.4	6.7	7.0	7.0
36	5.0	5.3	5.6	5.9	6.3	6.6	6.9	7.3	7.6	7.6
38	5.4	5.7	6.1	6.4	6.8	7.2	7.5	7.9	8.3	8.3
40	5.8	6.2	6.6	7.0	7.4	7.8	8.2	8.6	9.0	9.0
42	6.3	6.7	7.1	7.5	8.0	8.4	8.9	9.3	9.7	9.7
44	6.8	7.3	7.7	8.2	8.7	9.1	9.6	10.1	10.6	10.6
46	7.4	7.9	8.4	8.9	9.4	10.0	10.5	11.0	11.6	11.6
48	8.0	8.6	9.1	9.7	10.3	10.9	11.5	12.1	12.7	12.7
50	8.7	9.3	10.0	10.6	11.3	11.9	12.6	13.3	14.1	14.1
52	9.5	10.2	11.0	11.7	12.4	13.2	14.0	14.8	15.7	15.7
54	10.5	11.3	12.1	13.0	13.9	14.8	15.7	16.7	17.6	17.6
56	11.7	12.6	13.6	14.6	15.7	16.8	18.0	19.3	20.7	20.7
58	13.1	14.3	15.5	16.8	18.2	19.7	21.5	23.7	26.8	26.8
60	15.1	16.6	18.3	20.2	22.6	25.4	28.6	33.7	40.8	40.8
64	18.2	20.7	24.7	29.2	34.6	41.4	49.8	60.7	75.8	75.8

NAVTRADEVGEN 66-C-0031-1

When considering atmospheric absorption of radiation measured by a satellite, it is frequently convenient to consider the ratio of the slant path length through the atmosphere, p , to the vertical path length, h_a . h_a is often referred to as one optical air mass.

For zenith angles, Z , less than about 65° , it can be shown that:

$$p \approx h_a \sec Z \quad (62)$$

For greater zenith angles, it would be necessary to resort to relatively complex analytical expressions and so the values given in Table 4 are usually employed.¹³

Table 4
Air Mass, p/h_a , Corresponding to Different Zenith Angles, Z

Zenith Angle	Zenith Angle								
	0°	1°	2°	3°	4°	5°	6°	7°	8°
Air Mass (p/h_a)									
0	1.00								
10	1.02					1.04			
20	1.06	1.07	1.08	1.09	1.09	1.10	1.11	1.12	1.13
30	1.15	1.17	1.18	1.19	1.20	1.22	1.23	1.25	1.27
40	1.30	1.32	1.34	1.37	1.39	1.41	1.44	1.46	1.49
50	1.55	1.59	1.62	1.66	1.70	1.74	1.78	1.83	1.88
60	2.00	2.06	2.12	2.19	2.27	2.36	2.45	2.55	2.65
70	2.90	3.05	3.21	3.39	3.59	3.82	4.07	4.37	4.72
80	5.60	6.18	6.88	7.77	8.90	10.39	12.44	15.36	19.79

The zenith angle can, of course, be determined from Equations (57) or (58).

While analytical expressions between p/h_a and either n or B (as a function of h) could be derived, they are too complex for general use.

2.7 Errors in Geographical Locations of Data

Errors in the location of satellite data arise from a number of sources, including errors in (1) subpoint position, (2) satellite altitude, and (3) satellite or sensor orientation.

Errors in subpoint position will be directly reflected in data locations. Errors in the subpoints of operationally available ephemerides are estimated to be about five miles. A frequent source of error is that as to the precise instant the data are observed, since satellite velocities over the earth are of the order of four n. mi. per second (see Table 1).

The effects of altitude errors can be obtained by differentiating Equation (53):

$$\frac{dB}{dh} = \frac{\sin n}{R \sqrt{1 - \left(\frac{R+h}{R}\right)^2 \sin^2 n}} = \frac{\sin n}{\sqrt{R^2 - (R+h)^2 \sin^2 n}} \quad (63)$$

The error is zero for $n = 0$, and increases with increasing n . It is to be noted that there are limits to the practically attainable accuracy due to the variations and uncertainties as to cloud top heights and the height of terrain (both of which may vary from sea level to the order of 10 km), and to the variations of the earth's radius with latitude. Fujita¹ cites errors of a few tenths of a degree of great circle arc for satellite height errors of about 10 km.

Errors of satellite or sensor orientation are usually defined in terms of roll, pitch, and yaw, as a carry-over from aeronautics. The axes are shown in Figure 13. Pitch is a nose-up or -down motion of an aircraft and, therefore, a tilting forward or backward (from the vertical) of the spacecraft. The pitch axis is a horizontal line running left-to-right (perpendicular to the orbit plane) through the spacecraft. Roll in an aircraft is a rotation around the long axis, or a wing-up or -down attitude. For spacecraft, it is a tilt to left or right. The roll axis is a horizontal line from front to back. Yaw is a rotation to the left or right about the vertical (or yaw) axis.

Errors due to pitch or roll can be determined from:

$$\Delta B_n = \left[\frac{\cos n}{\sqrt{\left(\frac{R}{R+h}\right)^2 - \sin^2 n}} - 1 \right] \Delta n \quad (64)$$

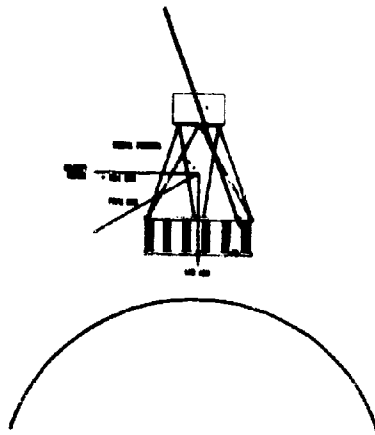


Figure 13. Spacecraft Axes

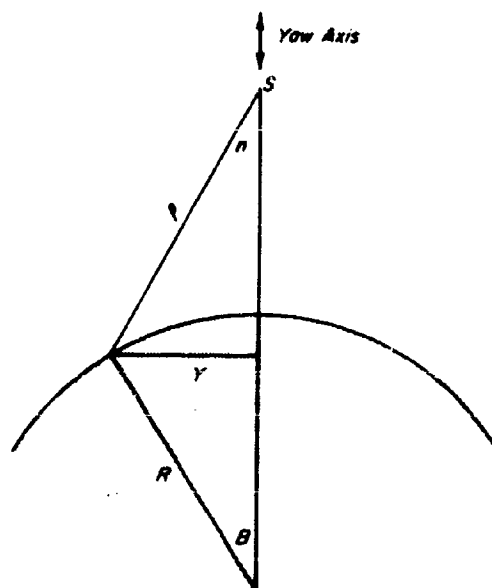


Figure 14. Yaw Error Lever Arm

where now

Δn = error in satellite or sensor nadir angle
 ΔB_n = error, measured radially from subpoint,
 in degrees of great circle arc

The increase of ΔB_n with increasing n has already been illustrated.

To determine the effects of yaw errors, note in Figure 14 that yaw errors are magnified by a lever arm of length Y , where

$$Y = R \sin B \quad (65)$$

If n is known, rather than B , B can of course be determined from Equation (53).

The linear error of position, Δx , due to yaw error, is then

$$\left. \begin{aligned} \Delta x &= Y \sin \Delta y = R \sin B \sin \Delta y, \text{ or} \\ \Delta x &= R \sin B \Delta y, \text{ if } \Delta y \text{ is small,} \end{aligned} \right\} \quad (66)$$

where Δy is the angular error in yaw, and the error, Δx , is in a direction perpendicular to the line from the point in question to the subpoint. In many cases, a yaw error can be adequately compensated for merely by a relative rotation, around the subpoint, of either the data, or a geographical grid or map.

When errors in pitch, roll, and yaw are small, the necessary corrections can be considered as independent for many purposes. As they become larger, the errors interact and the correction procedures become complex.

In most present satellites, the direct determination of pitch, roll, and yaw is not as accurate as would be desired. Accordingly, maximum accuracy in the location of the data usually results from the identification and matching of landmarks, or from the use of horizons if they are present and can be identified in the data. In the absence of landmarks, azimuth may be especially difficult to determine or confirm, and there is often little alternative to the assumption that the satellite or sensor is properly oriented relative to the heading line. If horizons are present, and identifiable in the data, they often provide a good basis for determining errors in pitch and/or roll. ³⁷

SECTION III

ELECTROMAGNETIC RADIATION: DEFINITIONS AND CONCEPTS

In Section I, it was stated that remote observations of the geophysical system from satellites can only be achieved by measurements of the radiant energy propagating from the earth and atmosphere. It is therefore necessary to establish in this section the nomenclature, definitions, and concepts of electromagnetic radiation of significance to satellite remote sensing techniques.

3.1 Electromagnetic Spectrum

Electromagnetic radiation is a propagating wave phenomenon. As such it has a characteristic propagation speed, and a wavelength. In a vacuum, the propagation speed, c , is independent of wavelength and is a fundamental physical constant with a value of $\sim 3 \times 10^{10}$ cm - sec⁻¹. Otherwise, the speed of propagation depends somewhat on the wavelength, and especially on the medium through which it propagates, i. e. on the index of refraction.

The wavelengths of electromagnetic radiation are measured in units of length. In the cm-gm-sec system of units, the basic unit of length is the centimeter (cm). The wavelength of radiation spans many orders of magnitude. For example, wavelengths of visible radiation (light) are characteristically of the order of 10^{-5} cm, while wavelengths used in standard radio broadcasts are in excess of 10^4 cm. The interval between 10^{-5} cm and 10^4 cm is but a fraction of the total span of wavelengths encountered in nature. This span of possible wavelengths is called the electromagnetic spectrum.

For convenience, the electromagnetic spectrum is divided into subspectrums and given names such as ultraviolet (U. V.), visible, infrared (IR) and others. While the divisions are made on the basis of wavelengths, the specific wavelengths which separate one subspectrum from another are not well defined. For this reason, a spectral breakdown of the different portions of the electromagnetic spectrum, such as that shown in Figure 15, can only serve as a general guide.

The basic unit of wavelength, the centimeter, is inconvenient to use when the wavelengths are many times shorter or longer than 1 cm. Accordingly, other units, which differ from the centimeter by factors of ten, are often used. In the shorter

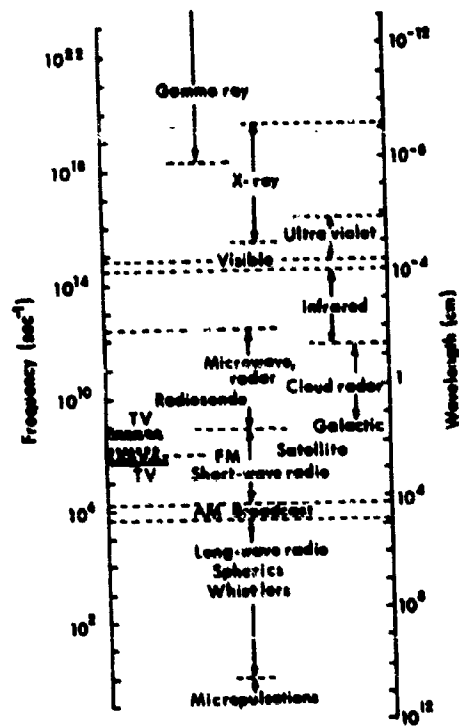


Figure 15. Electromagnetic Spectrum

NAVTRADEVGEN 66-C-0031-1

wavelength regions of the visible and IR. for example, wavelengths are often specified in units of the Angstrom and/or the micron. These are defined as follows:

$$1 \text{ Angstrom } (\text{\AA}) = 10^{-8} \text{ cm}$$

$$1 \text{ Micron } (\mu) = 10^{-4} \text{ cm.}$$

At longer wavelengths, other more conventional units of lengths are used. These are:

$$1 \text{ Millimeter (mm)} = 10^{-1} \text{ cm}$$

$$1 \text{ Meter (m)} = 10^2 \text{ cm}$$

Since radiation is a propagating wave phenomenon, its wave-like characteristic can also be specified in terms of its frequency of oscillations. The frequency, ν , in cycles per sec, is related to the wavelength, λ , in centimeters, by the following simple relationship:

$$\nu = \frac{c}{\lambda} \quad (67)$$

where

$$c = \text{speed of propagation in cm} \cdot \text{sec}^{-1}.$$

In vacuum, c = constant. Consequently, a one-to-one correspondence exists between the wavelength and the frequency for radiation propagating through a vacuum. Although c is not strictly a constant in a medium such as air, for most practical purposes it may be approximated by the constant speed in a vacuum. On the left hand margin of Figure 15, the frequencies corresponding to the wavelengths of the right hand margin are shown computed on the basis of $c = 3 \times 10^{10} \text{ cm} \cdot \text{sec}^{-1}$.

As in the case of the centimeter, the basic unit of frequency, cycles per sec (abbreviated to sec^{-1}),[†] is often not convenient to use. Units which are factors of ten larger than this are used in the higher frequency (i.e., shorter wavelengths) regions. These units are:

$$1 \text{ kilocycle per second (kc/sec)} = 1 \text{ KHz} = 10^3 \text{ cycles sec}^{-1}$$

$$1 \text{ megacycle per sec (mc/sec)} = 1 \text{ MHz} = 10^6 \text{ cycles sec}^{-1}$$

$$1 \text{ gigacycle per sec (gc/sec)} = 1 \text{ GHz} = 10^9 \text{ cycles sec}^{-1}$$

[†] The convention now is to use the Hertz (Hz) which is defined simply as 1 Hz = 1 cycle per sec.

Another parameter used to specify the wave-like character of radiation is the wave number $\tilde{\nu}$ which is defined simply as

$$\tilde{\nu} = \frac{1}{\lambda} \quad \text{cm}^{-1} \quad (68)$$

where

λ is given in cm

No units other than the cm^{-1} (inverse centimeter) is used to specify wave numbers.

The wavelength, frequency, or wave number, property of electromagnetic radiation, as discussed above, is called its spectral characteristic. The radiation emitted or reflected by the geophysical system is highly dependent on the spectral characteristics of the radiation. As a consequence, meaningful interpretations of satellite acquired radiation measurements can only be made if the spectral characteristic of the energy measured by the sensors is known. For instance, surface temperatures can be observed from satellites only when measurements are made in a number of spectral regions in the IR (or microwave) known as atmospheric windows. An example of such a window is that between 3.4 μ and 4.2 μ .

In remote sensing techniques, monochromatic radiation, i.e. radiation at a single wavelength, frequency or wavenumber, is not measured. What is measured is the energy within a spectral interval $\Delta\lambda$, $\Delta\nu$ or $\Delta\tilde{\nu}$, centered about some mean value λ_0 , ν_0 or $\tilde{\nu}_0$. In the conversion of spectral intervals from wavelength intervals to frequency or wave number intervals, the following approximations may be used

$$\Delta\nu \sim \frac{c}{\lambda_0^2} \Delta\lambda \quad (69a)$$

$$\Delta\tilde{\nu} \sim \frac{1}{\lambda_0^2} \Delta\lambda \quad (69b)$$

Equations (69a) and (69b) show that for a given wavelength interval $\Delta\lambda$, its corresponding intervals in frequency or wave number units are dependent on the mean wavelength of the interval in question. For example, a wavelength interval $\Delta\lambda = 10^{-4}$ cm (i.e., 1 micron) has a corresponding wave number interval $\Delta\tilde{\nu} = 10^4 \text{ cm}^{-1}$ when $\lambda_0 = 10^{-4}$ cm. However if λ_0 is 10^{-3} cm (i.e., 10 μ), $\Delta\tilde{\nu} = 10^2 \text{ cm}^{-1}$. Care must therefore be exercised when converting spectral intervals.

3.2 Energy Units

3.2.1 Basic Units

The basic unit of energy in the cm-gm-sec system of units is the erg. However, the erg is often too small a unit to use conveniently. In radiation studies, the joule is more appropriate, and is defined as

$$1 \text{ joule} = 10^7 \text{ ergs.}$$

In meteorology, another unit of energy is often used, especially in the specification of the solar energy received by the atmosphere (the solar constant). This unit is the gm-calorie. The relation between the gm-calorie and the joule is

$$1 \text{ gm - calorie} = 4.183 \text{ joules.}$$

The above relations permit the easy conversion of energy values from one system of units to another.

Radiation is generally emitted by a surface or received at a surface over a period of time. During the time interval, the energy content may be varying. As a result, it is often necessary to specify the energy emitted or received in a unit time interval. This quantity is known as the radiant power. If the total energy emitted by an object in time Δt secs is E joules, then the power in watts is given by

$$P \text{ (watts)} = \left[\frac{E \text{ joules}}{\Delta t \text{ secs}} \right] \quad (70)$$

i.e., one watt of radiant power is equal to one joule of energy emitted (or received) in one second.

3.2.2 Geometric Considerations

Apart from the basic units of energy and power discussed previously, there are units which are related to the geometry of the emitting surface and of the detectors used to measure the energy. Some of these units, of particular significance to remote sensing are discussed below.

3.2.2.1 Point Sources

Consider the radiation emitted by a point source. The energy emitted propagates in all directions. A sensor, viewing the source, measures only a small fraction of the emitted power. This fraction is defined by the cone with the area of the sensor surface as the base and the point source as the apex. The geometry is shown in Figure 16a. A cone, such as that illustrated in the figure, can be specified in terms of the solid angle ω which it subtends (in a manner similar to the specification of a sector of a circle by the plane angle it subtends). In the figure shown, the solid angle is given by

$$\omega = \frac{A_r}{h^2} \text{ steradians} \quad (71)$$

where

A_r = area of the receiving surface

h = distance of the receiver surface from the point source.

Steradian is the unit used to specify the magnitude of solid angles (just as the radian is used to specify plane angles). There are 4π steradians in a sphere (just as there are 2π radians in a circle).

Of interest, in a measurement situation such as that shown in Figure 16a, is the power emitted into the cone of solid angle ω . The unit which specifies this is the radiant intensity, j , and is defined as

$j \equiv$ power emitted by a source into a cone of unit solid angle.

The units of radiant intensity are

$$\text{watts} - \text{sr}^{-1}$$

where steradian is abbreviated to sr. The total power received by the sensor is then given by

$$P(\text{sensor}) = j \times \omega_s \text{ (watts)}$$

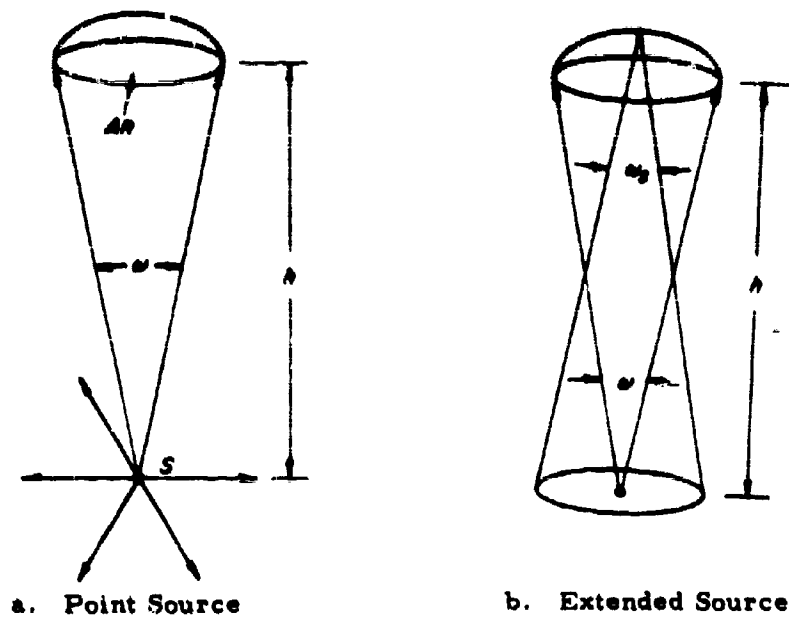
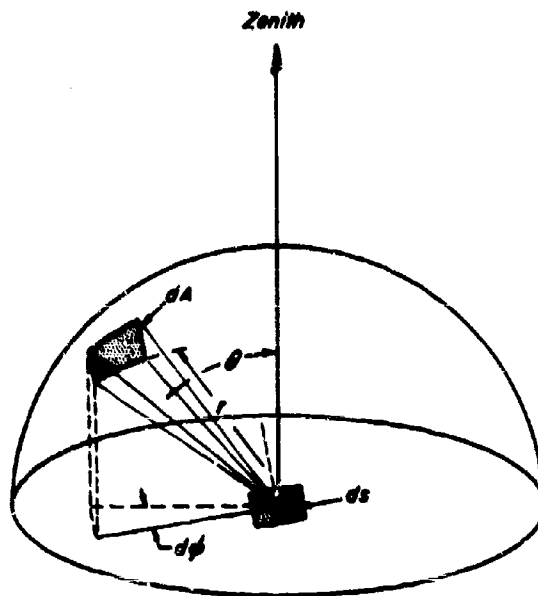


Figure 16. Radiometer Geometry



$d\omega$ = Solid angle subtended by the beam with cross sectional area dA at distance r from emitting surface.

$$= \frac{dA}{r^2}$$

$$= \sin \theta \, d\theta \, d\phi$$

Where θ = Zenith Angle

ϕ = Azimuthal Angle

Figure 17. Solid Angle Geometry

3.2.2.2 Extended Sources

With extended sources, there are two geometric considerations. Besides the solid angle consideration discussed above, there is also the area of the surface viewed by the sensor. The situation is illustrated in Figure 16b.

Every point on the extended source can be treated as a point source. The sensor, however, views only a limited portion of the surface, that defined by the intersection of the sensor beam and the surface. In the situation shown, the area viewed by the sensor is given by (from the definition of solid angle given previously)

$$A_s = \omega_s h^2 \quad (72)$$

where

- A_s = area of the source viewed
- ω_s = solid angle of the sensor beam
- h = distance of the sensor from the source.

As a consequence of the limited area viewed by the sensor, the radiation parameter of interest is the power emitted by a unit area of the source and this is defined as the radiant emittance of the source, denoted by the symbol W . W has the units watts - cm^{-2} .

The radiant emittance of the source specifies the power emitted by a unit surface area of the source, into all directions in the upper hemisphere shown in the Figure 16b. As in the case of point sources, for each point on the unit area viewed by the sensor, only that portion of the emitted energy which is contained in the cone, with the sensor area as base and the point as apex, is received by the sensor. Combining these two geometric effects, another radiation parameter results. This is the radiance, denoted by N , which is the power emitted by a unit area of the source into a cone of unit solid angle. N has the dimensions of watts - $\text{cm}^{-2} \cdot \text{sr}^{-1}$.

In the case shown in Figure 16b, the power received by the sensor is then given by

$$P(\text{sensor}) = N \times A_s \times \omega_s$$

where the terms have been defined previously.

3.2.3 Reflected Energy

In satellite remote sensing techniques, measurements of energy reflected by surfaces are often made. While the energy reflected by a surface is dependent on the properties of the surface itself, it is also dependent on the energy which the surface receives. The radiation parameter which is used to specify this quantity is known as the irradiance and is denoted by the symbol H . H is defined as the power which a unit area of the reflecting surface receives from the source.

When treated as a source of energy, the radiant power reflected by a surface can be specified in terms of the parameters discussed previously for emissive surfaces. For instance, the power reflected by a surface in the direction of a satellite sensor can be specified in terms of its equivalent radiance, i.e., it can be treated as if it had originated from a source located at the surface. A fuller discussion of these relationships can be found in Section IV.

3.2.4 Spectral Energy Units

It was stated previously that radiation exhibits spectral (wavelength) dependence. Sensors generally measure radiant energy only within a finite spectral interval. In the specification of the energy content of radiation, it is therefore, often necessary to specify the energy or power within a unit spectral interval. Each of the terms discussed previously has its corresponding spectral dependent term. For example, the spectral radiance, denoted by N_λ , is defined as the radiance emitted by a source in a unit spectral interval.

3.2.5 Summary of Radiation Terms

Table 5 summarizes the symbols, definitions and the dimensions of the terms discussed above.

3.2.6 Isotropic Surfaces and Lambert's Law

An assumption often made in satellite measurements is that the emitting and reflecting surfaces radiate isotropically (i.e., equally in all directions). According to Lambert's Cosine Law, the radiance radiated by an isotropic surface in any zenith angle direction, θ , is proportional to the cosine of θ , i.e.

Table 5. Definitions of Radiation Terms

Term	Symbol	Units	Definition
Radiant power	P	Watts	The radiant energy emitted by a surface per unit time.
Spectral radiant power	P_λ	Watts/micron	The amount of radiant energy emitted by a surface per unit time within a specified small spectral interval.
Radiant intensity	J	Watts/ster.	The radiant energy emitted by a source into a unit solid angle per unit time.
Spectral radiant intensity	J_λ	Watts/ster./micron	The radiant energy power emitted by a source into a solid angle per unit spectral interval.
Radiant emittance	W	Watts/m ²	The radiation power emitted by unit area of the source (into entire hemisphere).
Spectral radiant emittance	W_λ	Watts/m ² /micron	The radiant power emitted by a unit area or the source per specified unit spectral interval.
Radiance	N	Watts/m ² /ster.	The radiation power emitted by unit area of the source into a unit solid angle normal to the surface.
Spectral radiance	N_λ	Watts/m ² /ster./micron	The radiation power emitted by unit area of the source per unit solid angle per specified unit spectral interval.
Irradiance	H	Watts/m ²	The radiation power incident on unit area of a surface.

$$N(\theta) \propto \cos \theta$$

$$= N \cos \theta$$

where N , the constant of proportionality, is known as the isotropic radiance.

The power emitted or reflected into the total hemisphere, by a unit area of the surface, i.e. the radiant emittance W , is then given by

$$W = \int_0^{2\pi} N \cos \theta \, d\omega \quad (73)$$

where

$d\omega$ is the increment of solid angle.

The limits 0 to 2π denote integration over all the solid angles contained in a hemisphere.

From Figure 17, it is seen that

$$d\omega = \frac{dA}{R^2}$$

and

$$dA = dl_1 \times dl_2$$

$$dl_1 = R \sin \theta \, d\varphi$$

$$dl_2 = R \, d\theta$$

where

φ is the azimuth angle

Therefore,

$$d\omega = \sin \theta \, d\theta \, d\varphi \quad (74)$$

Changing the limits of integration to:

$$\varphi \text{ from } 0 \text{ to } 2\pi$$

$$\theta \text{ from } 0 \text{ to } \frac{\pi}{2} .$$

Equation (73) becomes

$$W = \int_0^{2\pi} \int_0^{\frac{\pi}{2}} N \cos \theta \sin \theta \, d\theta \, d\phi$$

$$= \pi N. \quad (75)$$

Equation (75) shows that a unique relation exists between the radiant emittance from an isotropic surface and its isotropic radiance. This relation does not hold for other surfaces, since, $N(\theta)$ is then not simply equal to $N \cos \theta$.

3.3 Absorptivity, Transmissivity, Reflectivity and the Concept of a Blackbody Radiator

The radiation incident on an object is either absorbed, transmitted or reflected by the object. The fraction absorbed is called the absorptivity; the fraction transmitted is the transmissivity; and the fraction reflected, the reflectivity. The parameters, absorptivity, transmissivity and reflectivity are properties of the composition and surface characteristics of the object. They are also spectrally dependent. For example, ordinary window glass transmits quite effectively, visible light (i.e. high transmissivity in the visible), but it is not very effective in transmitting infrared radiation (low transmissivity in the IR).

The spectral dependent terms are known respectively as monochromatic absorptivity (a_λ), monochromatic transmissivity (τ_λ) and monochromatic reflectivity (r_λ). Since these parameters specify the fractions of incident radiation at wavelength λ , which is absorbed, transmitted or reflected, the following holds

$$0 \leq a_\lambda \leq 1, \quad 0 \leq \tau_\lambda \leq 1, \quad 0 \leq r_\lambda \leq 1 \quad (76)$$

and

$$a_\lambda + \tau_\lambda + r_\lambda = 1 \quad (77)$$

As a consequence of Equation (77), an object which has a high monochromatic absorptivity at wavelength λ must have proportionately lower transmissivities and reflectivities at the same wavelength of particular significance as an object which has, in theory, a monochromatic absorptivity, a_λ , equal to 1 at all wavelengths,

i.e. it absorbs all the radiation which is incident on it, irrespective of the wavelength. Such an object is known as a blackbody.

A blackbody is only a theoretical concept. No real object has the property of total energy absorption at all wavelengths. While it is possible to fabricate objects which have monochromatic absorptivities which approach unity over a finite spectral interval, it is impossible to construct an object which has $a_\lambda = 1$ for all wavelengths. In spite of the theoretical aspects of a blackbody, it is extremely useful as a standard against which the radiation characteristics of real objects can be compared and specified. This is especially true in the case of satellite IR sensing. It is therefore extremely important that the radiation properties of a blackbody radiator be understood. In the following paragraphs, a summary of these properties is included to provide the basis of the later analysis of the radiation properties of the earth and atmosphere.

While a blackbody is defined by its unique absorption characteristic, the properties of its emission (a consequence of its absorption characteristics) are of greater significance in the analysis of satellite sensing techniques. These emission characteristics are summarized in Planck's law, which states that the energy emitted by a unit surface area of a blackbody, at a given wavelength, is only dependent on the temperature (in $^{\circ}\text{K}$) of the blackbody emitter. If the spectral energy unit is the spectral radiant emittance, W_λ , Planck's Law is analytically given by

$$W_{b\lambda} = \frac{c_1}{\lambda^5} \left(e^{\frac{c_2}{\lambda T}} - 1 \right)^{-1} \quad (78)$$

where

$W_{b\lambda}$ = spectral radiant emittance of a blackbody (denoted by the subscript b) at wavelength λ (watts-cm $^{-2}$ - μ $^{-1}$)

T = absolute temperature of the blackbody emitter in $^{\circ}\text{K}$

e = base of the natural logarithm = 2.718.

c_1 and c_2 are constants:

c_1 = 3.74×10^{-12} watts - cm 2

c_2 = 1.439 cm - $^{\circ}\text{K}$.

From Planck's Law it can be seen that the only parameter of the blackbody itself which determines the spectral radiant emittance is its temperature. Figure 18, computed from Planck's Law shows this temperature dependence graphically. Each curve describes the spectral radiant emittance of a blackbody at the temperature indicated. In Figure 18a, are drawn the Planck curves for temperatures corresponding to the surfaces of the earth and of the atmosphere, while in Figure 18b, are drawn the curves for temperatures approximating those of the sun. It should be noted that the units of spectral radiant emittance in Figure 18b (kilowatts-cm⁻²-micron⁻¹) is greater than that used in Figure 18a (watts-cm⁻²-micron⁻¹) by a factor of 10³. The following features of the curve should be noted:

1. $W_{b\lambda}$, at any given λ , is dependent on, and completely specified by, the temperature of the blackbody, with $W_{b\lambda}$ increasing with increasing temperature, regardless of λ .

2. While the curves shown have similar general appearances; i.e., each has a single maximum value of $W_{b\lambda}$, with a gradual slope to the long wavelength side and a much steeper slope to the short wavelength side, the wavelength of maximum spectral radiant emittance decreases with increasing temperature. This wavelength is denoted by λ_{\max} and the emitting blackbody temperature. This relation is expressed, by Wien's Displacement Law, as

$$\lambda_{\max} = \frac{K}{T} \quad (79)$$

where

$$\begin{aligned} K &= \text{constant} \\ &= 0.2897 \text{ cm } ^\circ\text{K}, \text{ if } \lambda_{\max} \text{ is in cm} \\ &= 2.897 \mu \text{ } ^\circ\text{K}, \text{ if } \lambda_{\max} \text{ is in microns.} \end{aligned}$$

Wien's Displacement Law is a direct consequence of Planck's Law and can be mathematically derived from Equation (78) by differentiation.

3. The total area under each of the curves is proportional to the total radiant emittance of the blackbody at the given temperature. From Figure 18, it is seen that this area increases with increasing temperature. In fact, the dependence is again unique and is analytically given, by the Stefan-Boltzman Law, as:

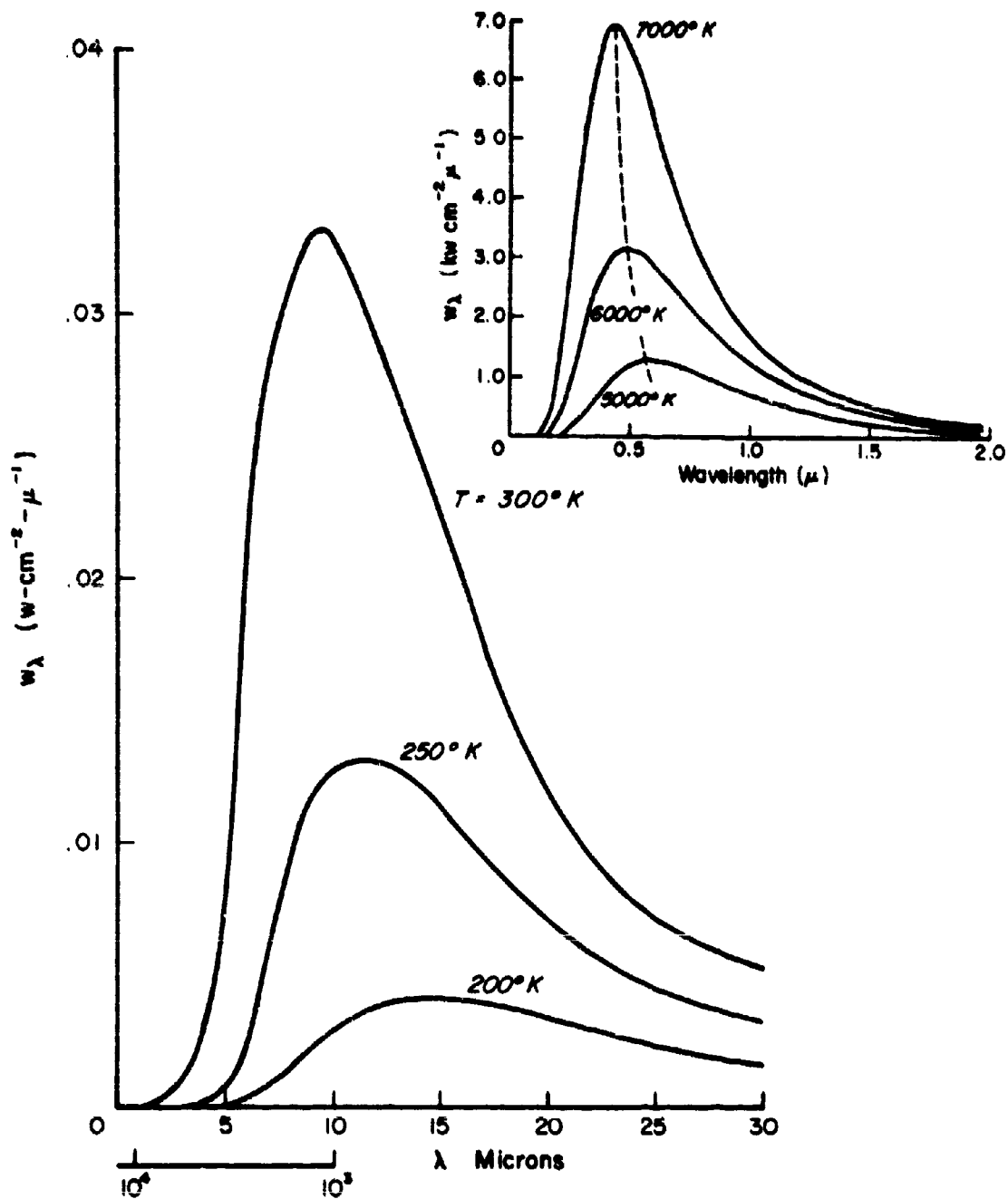


Figure 18. Blackbody Curves

$$W_b = \int_{\lambda=0}^{\lambda=\infty} W_{b\lambda} d\lambda = \sigma T^4 \quad (80)$$

where

W_b = blackbody radiant emittance
 σ = Stefan-Boltzmann's Constant
 $= 5.673 \times 10^{-12} \text{ watt-cm}^{-2} \cdot \text{°K}^{-4}$

Again, the Stefan-Boltzmann Law is another direct consequence of Planck's Law, and can be derived by the integration of Planck's Law as indicated in Equation (80).

It should be pointed out that, while the Stefan-Boltzmann Law indicates that W_b has a fourth power dependence on temperature, its application in remote sensing techniques is rather limited. In practice, a radiation sensor measures energy within a finite spectral interval which does not fulfill the $\lambda = 0$ to $\lambda = \infty$ requirements of Stefan-Boltzmann's Law. As a consequence, the increase in measured energy may not be proportional to the 4th power of the temperature. The following table, taken from Kellogg et al.²⁷, shows the temperature dependence of the spectral radiant emittance, in different portions of the spectrum, for a blackbody at $T \sim 300^\circ\text{K}$.

Table 6
T-Power Dependence†

λ	T-Power
4 μ	10
6.3 μ	6
8 - 12 μ	4
15 μ	4
20 μ	2
0.8cm	1
>0.8cm	1

† T-power = Power of T corresponding to $W_{b\lambda}$, e.g. $W_{b\lambda} \sim T^{10}$, when $\lambda \approx 4\mu$

The significance of Planck's Law and its consequences to remote sensing techniques may be seen by considering the fact that temperature is a prime geophysical parameter. The temperature of a blackbody, could be uniquely determined by any one of the following:

(a) λ_{max}

(b) $W_{b\lambda}$ at any wavelength λ

(c) $W_{b\Delta\lambda} = \int_{\lambda_1}^{\lambda_2} W_{b\lambda} d\lambda$, between any two wavelengths λ_1 and λ_2

(d) $W_b = \int_0^{\infty} W_{b\lambda} d\lambda$

Although in theory every one of the above parameters can be determined by remote sensing techniques, in practice, the determination of temperature is made by remotely measuring (c).

Another feature of a blackbody radiator is that it radiates according to Lambert's Cosine Law. Therefore, using Equation (9), the following hold:

$$W_b = \pi N_b$$

and

$$W_{b\lambda} = \pi N_{b\lambda}$$

where

N_b and $N_{b\lambda}$ are the blackbody radiance and the blackbody spectral radiance respectively. That is, for a blackbody radiator, the radiant emittance and the radiance differ only by the constant factor π .

3.4 The Concept of Emissivity

The equations and laws discussed in the previous section are strictly applicable only to perfect blackbodies, which were defined as objects having monochromatic absorptivities, a_λ , equal to 1 at all wavelengths.

Real objects do not absorb all incident radiation, nor are they equally effective or ineffective as absorbers of radiation of different wavelengths. That is to say, the absorptivity of a given object may be highly spectrally dependent, and in general, must be specified in terms of the monochromatic absorptivity a_λ . Unlike a blackbody then, real objects have the following properties

$$a = a_\lambda \text{ (i.e. absorptivity is dependent on wavelength)}$$

$$a_\lambda < 1 \text{ (i.e. monochromatic absorptivity is less than 1).}$$

According to theoretical considerations, an object which is effective as an absorber of radiation at a particular wavelength λ (i.e. a_λ is large), is equally effective as an emitter of radiation of the same wavelength λ . Since a blackbody has a monochromatic absorptivity equal to one (which is the maximum value possible) at all wavelengths, it is the most efficient emitter of radiation at all wavelengths. In fact, the spectral radiant emittance of a blackbody, $W_{b\lambda}$, is the theoretical limit which can be attained for any object at the same temperature. As a consequence, the spectral radiant-emittance of real objects at any wavelength λ can be given by

$$W_\lambda(T) = \epsilon_\lambda W_{b\lambda}(T) \quad (81)$$

where

$$W_\lambda(T) = \text{spectral radiant emittance of the object at temperature } T.$$

$$W_{b\lambda}(T) = \text{spectral radiant emittance of a blackbody at the same wavelength and at the same temperature } T.$$

ϵ_λ is a decimal fraction having values between 0 and 1. When $\epsilon_\lambda = 1$, then the spectral radiant emittance of object is equal to that of a blackbody at the same wavelength. In general, $\epsilon_\lambda < 1$, (e.g. in specially constructed laboratory "black-bodies" used for calibration purposes, values of ϵ_λ on the order of 0.98 - 0.99 are the best that have been achieved in the infrared).

The term, ϵ_λ , in Equation (81) is known as the monochromatic emissivity of the object and, as with the monochromatic absorptivity a_λ , is dependent on the composition (and to a more limited extent, the texture) of the object. In fact, ϵ_λ and a_λ are very simply related by Kirchoff's Law which states that

$$\epsilon_\lambda = a_\lambda$$

The significance of the concept of monochromatic emissivity to remote geophysical sensing may be seen by considering the dependences of the radiant emittance of real objects. From Equations (61) and (78), W_λ is given by

$$W_\lambda = \epsilon_\lambda \frac{c_1}{\lambda^5} \left(e^{\frac{c_2}{\lambda T}} - 1 \right)^{-1} \quad (82)$$

While W_λ is still dependent on temperature, T , as in the case of an ideal black-body radiator, it is also dependent on the monochromatic emissivity. If the temperature of the object is to be remotely determined by radiometric means, the monochromatic emissivity of the object, in the spectral interval, in which the emitted energy is measured, must be known. In other words, a unique relation between only the radiant emittance and the emitting temperature does not exist for real surfaces.

SECTION IV

THE EARTH AS A SOURCE OF RADIATION

4.1 Introduction

The surfaces of the earth contain many elements and parameters which are of interest to satellite remote sensing. But, in order for these to be observed or measured from satellite altitudes, radiation characteristic to these elements and parameters must propagate from the surface to the satellite. In other words, the surfaces of the earth must be sources of radiation energy useful to remote sensing techniques.

The surfaces of the earth are sources of electromagnetic radiation in two respects. They are sources (1) of emitted radiation and (2) of reflected radiation. In the following sections, some of the significant features of the earth as a source of radiation are discussed.

4.2 The Earth As An Emissive Source

The surfaces of the earth are thermal emitters of electromagnetic radiation. The spectral radiant emittance of a blackbody radiator corresponding to the range of temperatures characteristic of the surfaces of the earth can be approximately represented by the curve for $T = 300^{\circ}\text{K}$ shown in Figure 18. This curve shows that very little energy is emitted at wavelengths, λ , less than 3μ . Most of the energy is concentrated in the infrared region of the spectrum. In fact, application of Wein's Displacement Law shows that λ_{max} is at approximately 11μ . Some energy is emitted all the way out to the microwave region of the spectrum. However, as the wavelength increases, the energy emitted becomes less and less. Figure 19 illustrates this point much more dramatically. The parameter plotted in the curve is the ratio R_{λ} defined as

$$R_{\lambda} = \frac{W_{b\lambda}(T = 300^{\circ}\text{K})}{W_{b\lambda_{\text{max}}}(T = 300^{\circ}\text{K})} \quad (83)$$

The curve essentially compares the energy emitted at any wavelength λ with that emitted at λ_{max} .

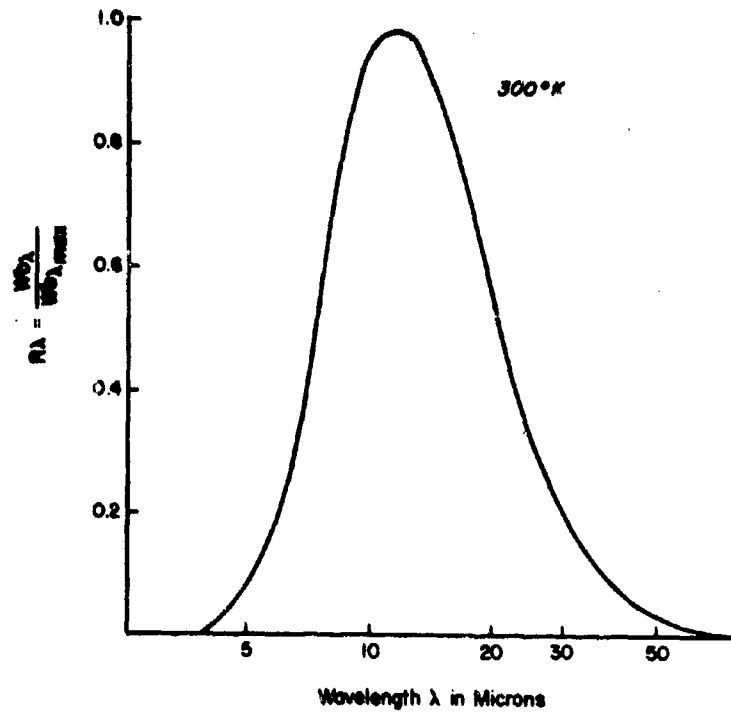


Figure 19. Normalized Blackbody Curve for $T = 300^\circ K$

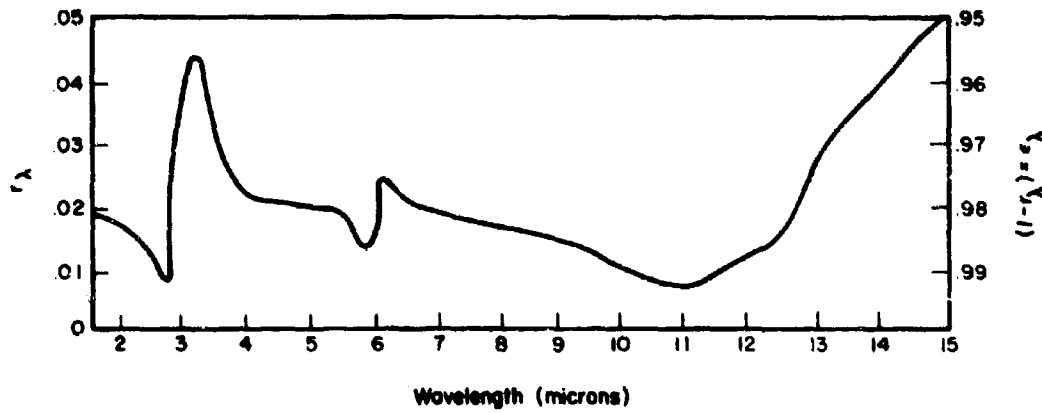


Figure 20. IR Emissivity of a Water Surface

Figure 19 shows that, for remote measurements of the radiation emitted by the surfaces of the earth, advantage should be taken of the IR portion of the spectrum due to the relatively large amounts of energy available. This indeed has been the case. Satellite measurements of surface emitted energy, like those of the TIROS and Nimbus satellites have, so far, been restricted to the IR portion of the spectrum. The advanced state-of-the-art in detector development in the microwave region, however, makes it also possible to obtain microwave emissive measurements from satellite altitudes, in spite of the fact that significantly less energy is emitted in the microwave region.

From these considerations, it may be concluded that, in terms of satellite remote emissive measurements, the surfaces of the earth are significant sources in the infrared and microwave regions of the spectrum.

4.2.1 Surface Emissivities

In the two spectral regions in which surface emitted energies are of interest for satellite remote sensing techniques, the emissivities of natural surfaces in the infrared have been more extensively investigated than in the microwave region. This is due, in part to the fact that IR sensing techniques from spacecraft are already in existence, while similar microwave techniques are still in the developmental stages.

In the following paragraphs, some of the more important features of surface emissivities in these two spectral regions are summarized.

4.2.1.1 Surface Emissivities in the IR

A number of laboratory measurements of IR emissivities of different types of surface materials have been made (e.g. Hovis,¹⁴ Kern,¹⁵ and Lyon¹⁶). Most of these data have been obtained by measuring the spectral reflectivities of the surface materials in question. For a large number of surfaces, the absorption of incident IR radiation is total within a very thin surface layer. As a consequence, Equation (77) of Section 3.3 can be simply expressed as

$$r_{\lambda} + a_{\lambda} = 1 \quad \text{where } \tau_{\lambda} = 0$$

or

$$r_{\lambda} + \epsilon_{\lambda} = 1$$

and

$$r_{\lambda} = 1 - \epsilon_{\lambda}$$

Spectral emissivity can then be determined from spectral reflectivity measurements. An example of such deduced spectral emissivity data from spectral reflectivity measurements is shown in Figure 20. The surface material investigated was water. The left hand ordinate values (increasing upwards) are the measured reflectivities. The right hand ordinate values (increasing downwards) are the deduced spectral emissivities.

The generally high IR emissivity of a water surface shown in Figure 20 is also characteristic of a number of soil samples investigated by Hovis.¹⁴ Figures 21 and 22, taken from his measurements, show the spectral emissivities of soil samples from Pawnee Grassland, Colorado, and Rosamond Dry Lake, California. These figures show that, while the emissivity curves exhibit peaks and dips, the overall surface emissivities in the IR are relatively high.

High values of IR emissivities for vegetation have also been measured. For example, Gates and Trantrapon¹⁵ have reported IR emissivities of plant leaves to be of the order of 0.96.

Of particular interest to satellite remote sensing of the surfaces of the earth are the surface emissivities averaged over the spectral regions known as atmospheric windows. Within these window regions, atmospheric degradation effects on surface emitted radiant energy are minimum (see Section V). The window located between 8μ to 12μ is of particular significance. This spectral region corresponds to the approximate peak of the spectral radiant emittance of a blackbody at temperatures corresponding to those of the surfaces of the earth. The averaged emissivities of a number of surface materials, both natural and man made, in this window have been systematically studied by Kern.¹⁵ The results of his measurements are summarized in Table 7.

The relatively high IR emissivities of most natural surfaces have made it possible to approximate their radiant emittance in the IR by that of a blackbody at the same temperature. Within the sensitivities and accuracies of current satellite IR sensors, the errors in the interpretation of data resulting from this approximation are generally insignificant. Even so, a number of types of surfaces have been identified in current IR window measurements by their characteristically lower surface emissivities. As the state-of-the-art in satellite IR sensor development improves, variations in surface emissivities would obviously be a factor to be considered in the interpretation of the satellite acquired data.

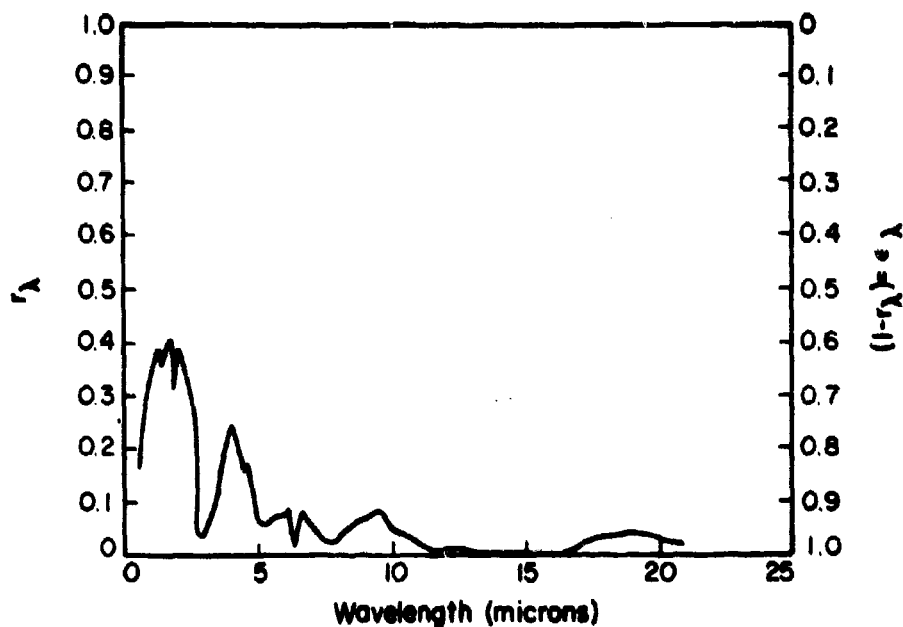


Figure 21. Spectral Emissivity of Soil Sample from Pawnee Grassland, Colorado

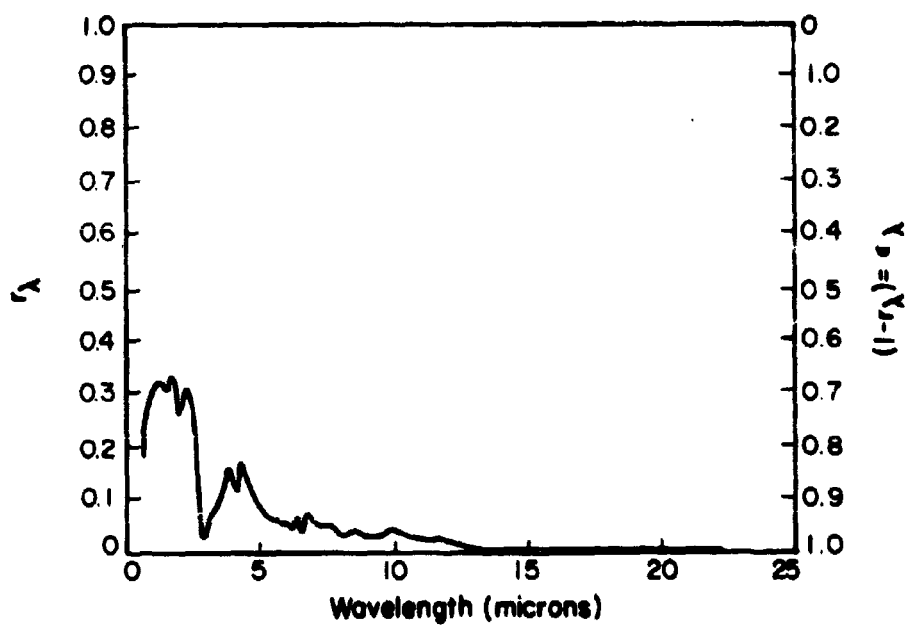


Figure 22. Spectral Emissivity of Soil Sample from Rosamond Dry Lake, California

Table 7
Mean IR Emissivities for the 8-12 μ Region
 (Taken from Kern)¹⁵

Material	ϵ
Quartz (agate)	0.712
Granite	.815
Feldspar	.870
Obsidian	.862
Basalt	.904
Dunite	.856
Granite, rough side	.898
Obsidian, rough side. broken glass appearance	.837
Basalt, rough side, shiny	.934
Dunite, rough side	.892
Silicon sandstone, polished side	.909
Silicon sandstone, rough side	.935
Dolomite, polished side	.929
Dolomite, rough side	.958
Dolomite gravel, 0.5 cm size rocks	.959
Plate silicon glass	.865
Parson's Black on Al sheet (no grooves)	.988
Plywood sheet	.962
Human skin	.980
Sand, quartz large grain	.914
Sand, quartz large grain wet with water (nearly saturated)	.936
Sand, Monterey, quartz small grain	.928
Concrete walkway, dry	.966
Asphalt paving	.956
Water, pure	.993
Water, plus thin film petroleum oil	.972
Water, plus thin film corn oil	.966
Water, covered by a thin sheet of polyethylene	.961

4.2.1.2 Surface Emissivities in the Microwave

IR emissivities are often in excess of 0.9, as shown by the results summarized in the previous section. Microwave emissivities for the same surface materials are characteristically lower.

In a series of experimental measurements using an aircraft mounted microwave radiometer, Hyatt¹⁸ obtained averaged microwave emissivities of 0.85 for land and 0.53 for ocean waters. Other systematic measurements of emissivities in the microwave regions (e.g. Barath¹⁹) confirm these relatively low values.

These low microwave emissivities make it impossible to apply the blackbody assumption in the interpretation of satellite acquired data. Another difficulty is encountered in the interpretation of microwave data. This difficulty arises from the fact that since ϵ_λ is low, r_λ can be significant. In other words, the microwave radiant energy propagating from a surface can be made up of both emitted and reflected energies, which cannot in practice be separated. Since each of these components are individually related to different properties of the surface being investigated, the interpretation of the measured data becomes difficult. Although a similar situation can exist in the infrared, the reflected component is less significant due to the high emissivity values.

Another source of difficulty in the interpretation of microwave measurements lies in the fact that most surface materials are transparent to microwave radiation. That is, the radiation can penetrate through a layer of the material many centimeters thick. As a result, the emitted signal does not come only from the surface, but also from a thick layer. A notable exception to this is water. Penetration effects are negligible and the radiation can be considered to originate from the surface.

In spite of these problems, and in spite of the fact that the dependence of signals on temperature shrinks to a simple proportionality to surface temperature (see Table 6), microwave observations of the earth's surfaces have one significant characteristic which similar observations in the IR lack. Radiation at wavelengths $\lambda > 0.1$ cm are not affected by non-precipitating clouds. As a consequence, surface features and surface parameters can be detected by microwave techniques even in the presence of cloud cover.

4.2.1.3 Angular Dependence of Surface Emissivities

A natural surface does not radiate according to Lambert's Cosine Law. That is, its spectral emissivity at any wavelength may depend on the direction of measurement. This angular dependence is generally not critical except at large zenith angles. Figure 23 shows the angular dependence of the surface emissivity of a water surface. For zenith angles $< 60^\circ$, the variations of emissivity is not significant.

4.3 The Earth As a Reflective Source

The surfaces of the earth reflect incident radiant energy. The spectral energy distribution reflected by a given surface depends on both the spectral distribution of the energy which it receives and the spectral reflectivity of the surface.

Of all the sources of illumination which the earth receives, the most significant is the sun. Because of the important role it plays in remote sensing techniques, the spectral energy properties of the sun are first summarized in the following paragraphs.

4.3.1 Solar Irradiance

Although the energy emitted by the sun is not the result of simple thermal processes, its spectral energy emission approximates that of a blackbody radiating at 6000°K . The spectral radiant emittance of a blackbody at 6000°K is shown in Figure 18 of Section III.

In considering solar energy in relation to remote sensing of the geophysical system, the energy parameter of interest is not so much the spectral radiant emittance of the sun, but the energy which is intercepted by the earth. The sun's energy is radiated uniformly in all directions. Nearly all of this energy is lost to space. The earth having a cross sectional area of $\sim 12 \times 10^7 \text{ km}^2$ and located at 93 million miles away from the sun, intercepts but a small fraction of the total emitted energy. As a consequence, while the 6000°K curve in Figure 18 can be used to approximate the relative spectral distribution of the solar energy incident on the top of the earth's atmosphere, it does not indicate the absolute values of these spectral energies, i.e., the spectral irradiance of solar radiation, H_λ . Figure 24, taken from Gast,²¹ shows two curves. The dashed curve represents the spectral irradiance at the top of the atmosphere if the sun were replaced by an equivalent blackbody radiating at $\sim 6000^\circ\text{K}$. The continuous curve with its irregular peaks, is the actual solar spectral irradiance as measured "outside" the atmosphere.

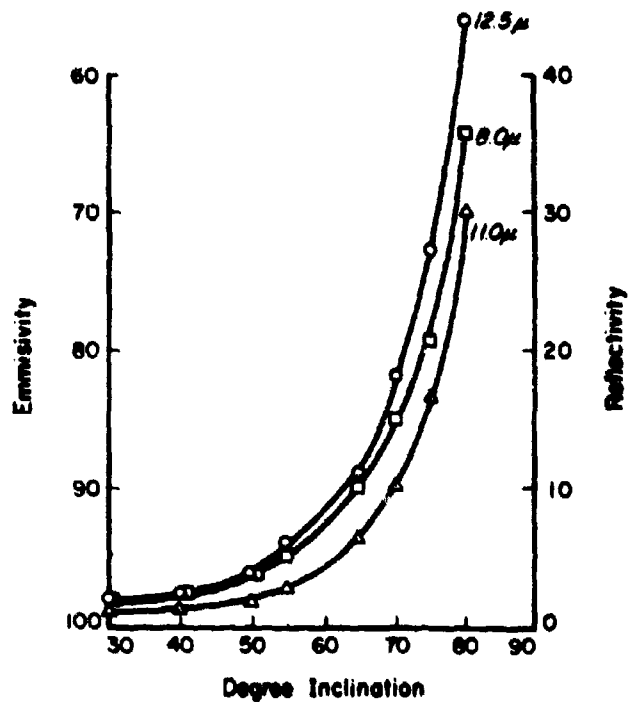


Figure 23. IR Reflectivity and Emissivity of a Water Surface as a Function of Angle

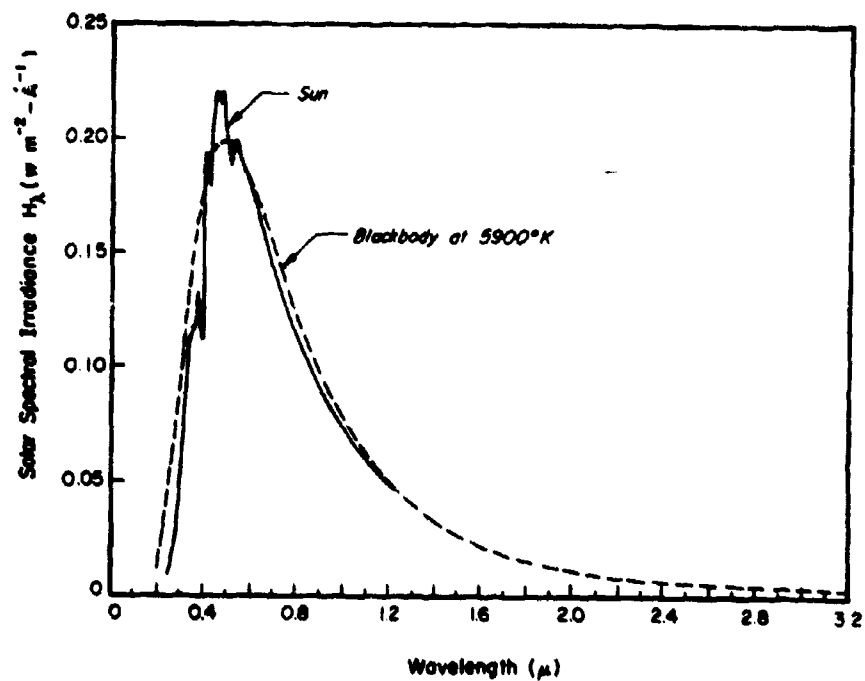


Figure 24. Solar Irradiance of the Top of the Atmosphere

Comparison of Figure 24 and Figure 18 shows that the power received by a unit area of the earth's surface, normal to the sun's rays, within a one micron wavelength interval is many orders of magnitude less than that emitted by a unit area of the sun's surface in the same spectral interval, although these two parameters have the same units - i.e., watts - cm^{-2} - micron^{-1} . In the one parameter, spectral radiant emittance, the cm area refers to the emitting surface, while in the other, the spectral irradiance, the area refers to the receiver, which in this case, is the top of the atmosphere.

It should be noted that the area under the solar spectral irradiance curve shown in Figure 24, is the solar constant (SC), since the solar constant is defined as the solar energy received by a unit surface area, normal to the sun's rays, located outside the atmosphere at a distance equal to the mean distance of the earth from the sun. According to this definition, the solar constant may be computed from the following:

$$SC = \int_{\lambda=0}^{\lambda=\infty} H_{\lambda}(\text{sun}) d\lambda \quad (84)$$

which is the area under the curve shown in Figure 24.

The spectral energy distribution of solar energy is concentrated in the visible portion of the spectrum. This can be seen in Figure 24. The radiation emitted by the earth was shown to be concentrated in the IR. As a consequence, the spectral characteristics of these two primary sources of radiation are distinctly different. Figure 25 shows this rather dramatically. In the figure, the normalized spectral curve for the sun, i.e.,

$$R_{\lambda} = \frac{H_{\lambda}(\text{sun})}{H_{\lambda \text{ max}}(\text{sun})} \quad (85)$$

is shown together with the curve for the normalized emission corresponding to the surface of the earth (Fig. 19). It is apparent that the two curves are separated into two spectral ranges above and below λ about 4μ . This distinction makes it possible to treat the two types of radiation separately in a number of cases involving remote sensing techniques. For instance, daylight measurements of surface emitted radiation in the 8μ to 12μ "window" have been made with no appreciable effects due to reflected solar energy. However, measurements made in the 3.8μ "window" (HRIR)

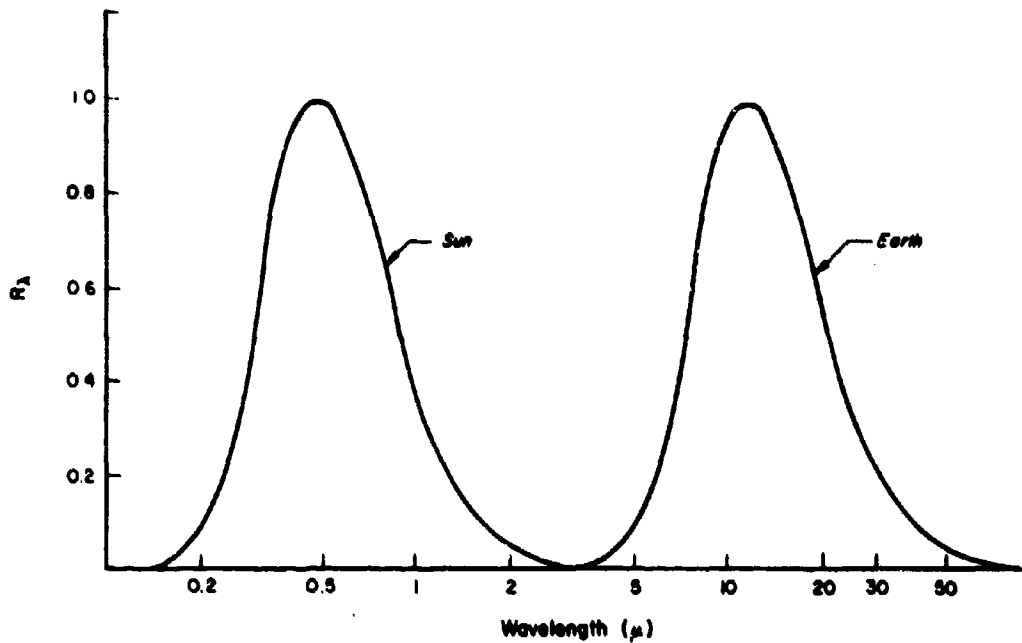


Figure 25. Normalized Blackbody Curves for $T = 6000^{\circ}\text{K}$ and $T = 800^{\circ}\text{K}$

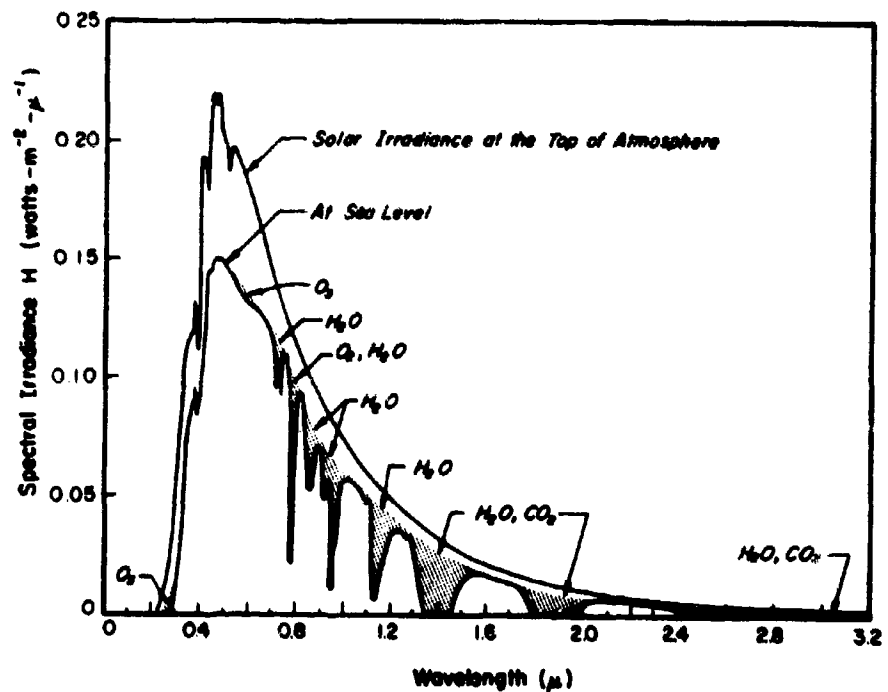


Figure 26. Solar Irradiance at the Surface of the Earth

during daylight hours have shown considerable contamination by reflected solar energy. This is due to the fact that (1) solar irradiance in the near IR is still significant and (2) the surface reflectivities in the 3.8μ region are high enough so that a significant fraction of the solar irradiance is reflected.

While the curve in Figure 24 shows the mean spectral radiance as received by a surface normal to the sun's rays and located at the top of the atmosphere, it does not accurately describe the energy received by the surfaces of the earth. Two main effects reduce the illumination received by these surfaces. The first is the attenuation of the solar energy by the atmosphere, and the second is the result of non-normal incidence.

Figure 26 shows the spectral solar irradiance at sea level. The curve for solar irradiance at the top of the atmosphere is also included for comparison purposes. The solar energy, in its passage through the atmosphere, becomes depleted as a result of scattering and absorption. These atmospheric processes are discussed in detail in Section V. It is sufficient, at this point, to note that the irregular dips in the curve are due to absorption by the atmospheric gases O_2 , CO_2 , H_2O , and O_3 .

The actual solar irradiance received by a surface area is dependent on the solar zenith angle. When the sun is not directly overhead, i.e., solar zenith angle $\theta \neq 0^\circ$, then the irradiance received by the earth's surface is given by

$$H(\theta) = H(\theta = 0) \cos \theta \quad (86)$$

This cosine θ dependence is due to the fact that at low sun (large zenith angle), a given bundle of solar rays is spread out over a larger area. This area increases by $[\cos \theta]^{-1}$. As a consequence, the decrease in irradiance, i.e. the power received per unit area is proportional to $\cos \theta$.

4.3.2 Spectral Reflectivities of Surfaces

Only a limited number of spectral reflectivity measurements have been made in the visible. The measurements of Krinov²² are representative. These measurements are summarized in the two graphs shown in Figures 27 and 28. The first of these graphs show the spectral reflectivities of unvegetated surfaces.

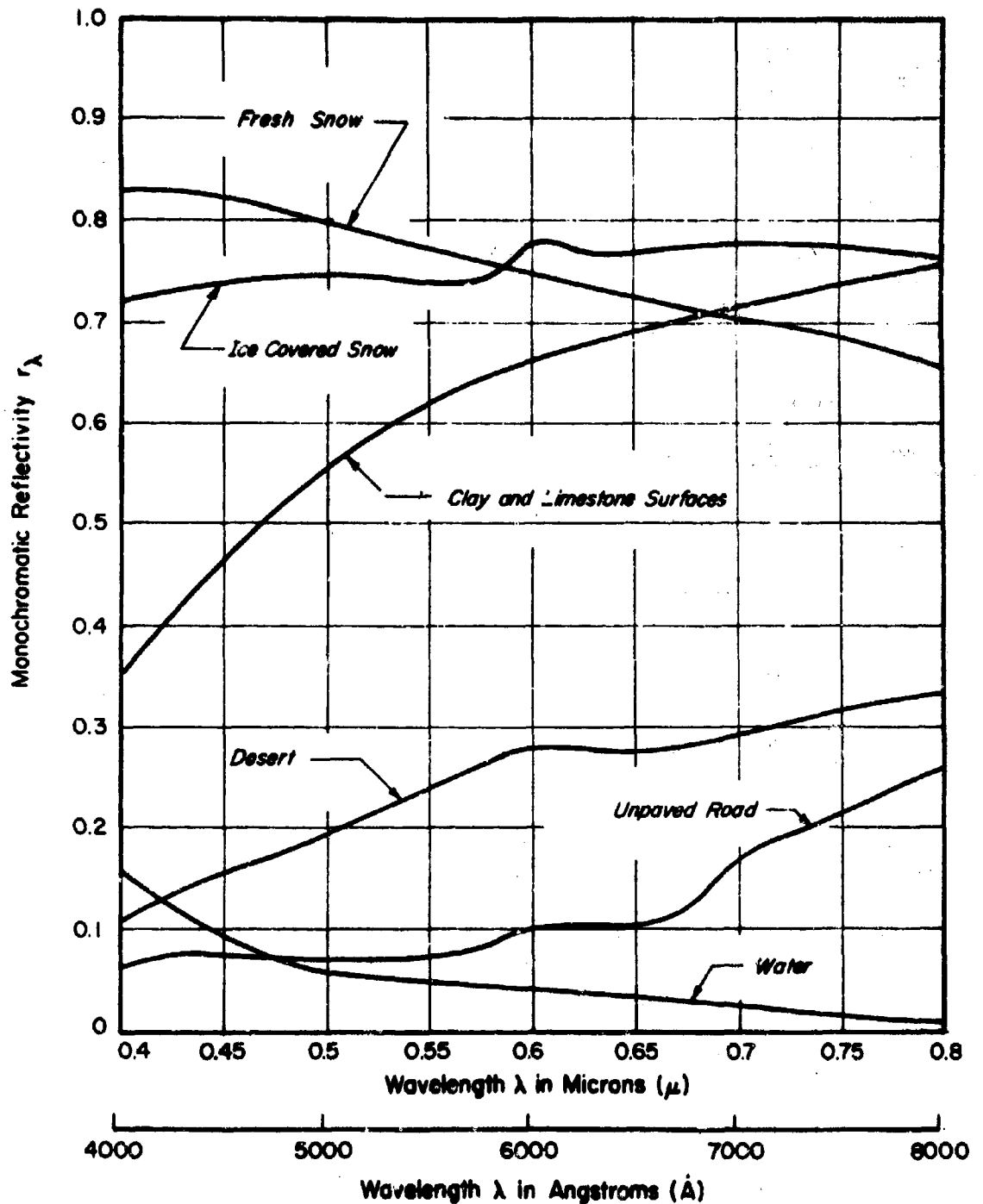


Figure 27. Spectral Reflectivities of Unvegetated Surfaces.

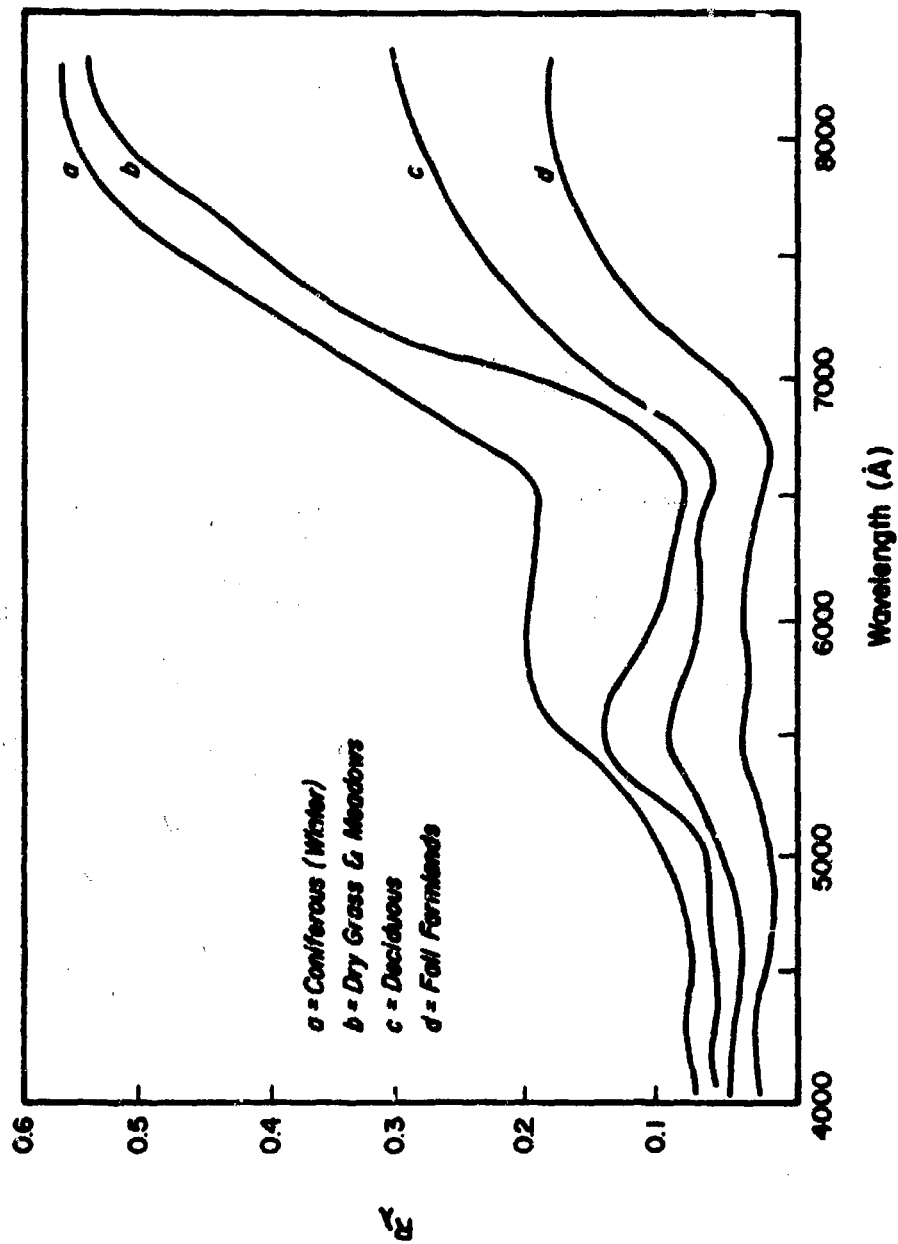


Figure 26. Spectral Reflectivities of Vegetated Surfaces.

With the exception of snow covered surfaces, the reflectivities of typical surfaces in the visible are rather low. This is especially true for the case of a water surface. Throughout the visible portions of the spectrum, the reflectivity of a water surface is characteristically less than 0.1. These low reflectivity values have been borne out in the analysis of satellite acquired television pictures made using reflected solar radiation. Coast lines can often be identified by the contrast (brightness difference) between the darker ocean surfaces and the brighter land surfaces.

It should be noted that the reflectivities shown in Figures 27 and 28, while being representative of the given surfaces, are not always applicable. This is due to the fact that these surfaces are not diffuse reflectors or Lambert surfaces. Consequently, the spectral reflectivity is in general dependent on the angle of incidence of the illuminating radiation and on the direction of the measured radiation. In general, the directional dependence of reflectivity is not a serious factor to contend with in satellite remote observations and the assumption is often made that the surfaces reflect essentially as Lambert surfaces. With this assumption, the spectral radiance reflected by a surface is related to the irradiance by

$$N_{\lambda} = \frac{r_{\lambda} H_{\lambda} \cos \theta}{\pi} \quad (87)$$

where

θ is the solar zenith angle

Equation (87) is based on the equation for a Lambert surface, where the irradiance $H_{\lambda} \cos \theta$ replaces the radiant emittance term.

4.3.3 Albedo

Albedo is a term frequently used in meteorology. According to the Glossary of Meteorology,²³ albedo is the ratio of the amount of electromagnetic radiation reflected by a body to the amount incident upon it. As it is often used, there is an implicit assumption that the incident energy in question is the solar irradiance and the reflected energy is that which is reflected by the object into the whole upper hemisphere. Loosely speaking, the albedo of a surface can then be defined as the mean reflectivity of the surface averaged over the wavelength interval in which solar irradiance is significant. In a number of determinations of surface albedos

from satellite measurements (e.g. Conover²⁴), the spectral interval is further restricted to only the visible portion of the solar spectrum. Since most of the solar energy is concentrated in the visible, this restriction does not introduce serious degradation effects.

A number of satellite sensors, such as the television cameras, and the "visible" channels of the radiometers of Nimbus and TIROS, have made solar reflective measurements and observations over broad spectral intervals spanning the visible. The contrast variations in the measurements made by these sensors can be described in terms of the albedo variations of the surfaces viewed rather than by the spectral reflectivities of these surfaces. Some measurements of albedos of typical surfaces of the earth have been made from aircraft. These have been summarized in a table by Penndorf,²⁵ and are reproduced in Table 8.

4.3.4 Reflectivities in Other Spectral Regions

The surfaces of the earth are significant sources of reflected radiation if the reflectivities of these surfaces are relatively high. In the infrared, especially in the 8 to 12 μ region, it was shown that surface emissivities of most natural surfaces are in excess of 0.9. The IR reflectivities of these surfaces are correspondingly low. Therefore, the surfaces of the earth are not significant sources of reflected IR radiation.

On the other hand, it was shown that the surface emissivities in the microwave region are significantly lower, and the reflectivities correspondingly higher. While the reflected microwave energies are not normally of interest in passive techniques, they can be sufficiently high enough to cause problems in interpretation.

In active microwave techniques such as those employing microwave radars, these high microwave reflectivities makes it possible to obtain meaningful observations and measurements of the surfaces of the earth.

Table 8
Albedos of Some Typical Surface

	Smithsonian Tables	Sewing Handbook	Krinov	Schlumpf, Aachenbrenner
<u>Water Surfaces</u>				
Bay	3-4			
Bay and river	6-10			
Inland water	8-10		5	
Ocean	3-7			
Ocean, deep	3-5			
<u>Bare Areas and Soils</u>				
Snow, fresh fallen	70-86		77	
Snow, covered with ice			75	
Limestone, clay			63	
Calcareous rocks		30		
Granite		12		
Mountain tops, bare			24	
Sand, dry		31	24	
Sand, wet		18		
Clay soil, dry		15		
Clay soil, wet		7.5	9	
Ground, bare, rich soil, dry	10-20	7.2	9	
Ground bare, rich soil, wet		5.5		
Ground, black earth, sand loam			3	
Field, plowed, dry	20-25			
<u>Vegetative Formations</u>				
Coniferous forest, winter			3	
Coniferous forest, summer	3-10		8	
Deciduous forest, summer			10	
Deciduous forest, fall			15	
Dark hedges		1		
Coniferous forest, summer, from airplane			3	2
Meadow, dry; grass	3-6		8	
Grass, lush	15-25		10	
Meadow, low grass, from airplane			8	7
Field crops, ripe	7		15	
<u>Roads and Buildings</u>				
Earth roads			3	
Black top roads		8	9	
Concrete road, smooth, dry		35		
Concrete road, smooth, wet		15		
Concrete road, rough, dry		35		
Concrete road, rough, wet		25		
Buildings			9	
Limestone tiles		25		

SECTION V

ATMOSPHERIC EFFECTS

5.1 Introduction

The atmosphere is an inhomogeneous medium made up of gases, dispersed solid and liquid particulate materials, and clouds. Electromagnetic radiation propagating through this medium can become attenuated through the processes of absorption and scattering. Furthermore, the gases and particulates are at temperatures above 0°K. As a consequence, they are thermal emitters of radiant energy. Other interactions in the atmosphere can also give rise to electromagnetic radiation. For example, the electromagnetic radiation generated as spheres in a thunderstorm is not the result of thermal processes. Another atmospheric source of non-thermal radiation is airglow.

As far as surface observations from satellites are concerned, the atmosphere can be treated as a significant source of degradation. The atmosphere degrades surface observations in two main ways. It attenuates (i.e. depletes) the radiation propagating from the surfaces of the earth, and since the atmosphere is a source of radiation itself, it provides an undesirable "background" against which the surface observations must be made. (The term "background" here should be taken in a signal versus noise sense, since the atmospheric originating radiation actually is created between the surface and the satellite.)

However, physical parameters relating to the atmosphere itself are of great significance in geophysics. Many of these parameters can be deduced from radiation characteristics of the atmosphere which can be measured or observed from satellites. Thus, the radiation processes within the atmosphere can also be regarded as providing significant sources of information in satellite geophysics.

As a result of atmospheric radiation processes, the radiation which arrives at the top of the atmosphere (and therefore at the satellite) is a rather complex combination of radiation which originates

- (a) at the surface (reflected or emitted)
- (b) in the atmosphere (emitted by gases, clouds etc., reflected by clouds, or scattered by particles).

These processes are all spectrally dependent. In some spectral regions, the atmosphere, even in the presence of clouds, is almost perfectly transparent to surface sources. In others, the atmosphere is totally opaque. Still in others, it is partially transparent. The types of remote measurements possible from satellites are therefore dependent on the spectral region(s) used in the measurements, and the interpretation of satellite acquired data requires a full understanding of the radiation processes in the atmosphere.

5.2 The Effects of Atmospheric Gases

The radiation processes in a purely gaseous atmosphere, of importance to remote sensing techniques, are (1) absorption, (2) emission and (3) scattering. The significance of these processes are discussed below.

5.2.1 Gas Absorption: Atmospheric Absorption Spectrum

Of the different gases in the atmosphere, the principal absorbers of radiation in the UV, visible, IR and microwave regions are:

- (1) Ozone (O_3)
- (2) Water Vapor (H_2O)
- (3) Carbon dioxide (CO_2)
- (4) Oxygen (O_2)

Other gases also absorb radiation in these spectral regions. However, their overall effects are generally insignificant, either because the atmosphere contains only small traces of these gases, or because their absorption is not sufficiently intense.

The absorption of radiation by a gas is characteristically confined to discrete spectral intervals, known as absorption lines and bands. The totality of these absorption lines and bands over the whole E-M spectrum and for a given gas, is known as the absorption spectrum of the gas. While each gas has its own characteristic absorption spectrum, the absorption bands of two different gases may overlap in some spectral regions. Figures 29 a, b, c,²⁵ show the IR portions of the absorption spectra for H_2O , CO_2 , and O_3 . (In the figures, measured absorption increases downwards.) The high spectral selectivity of absorption by a gas is clearly shown. For example, in the O_3 spectrum, significant absorption is confined to the three

NAVTRADEVCEEN 66-C-0031-1

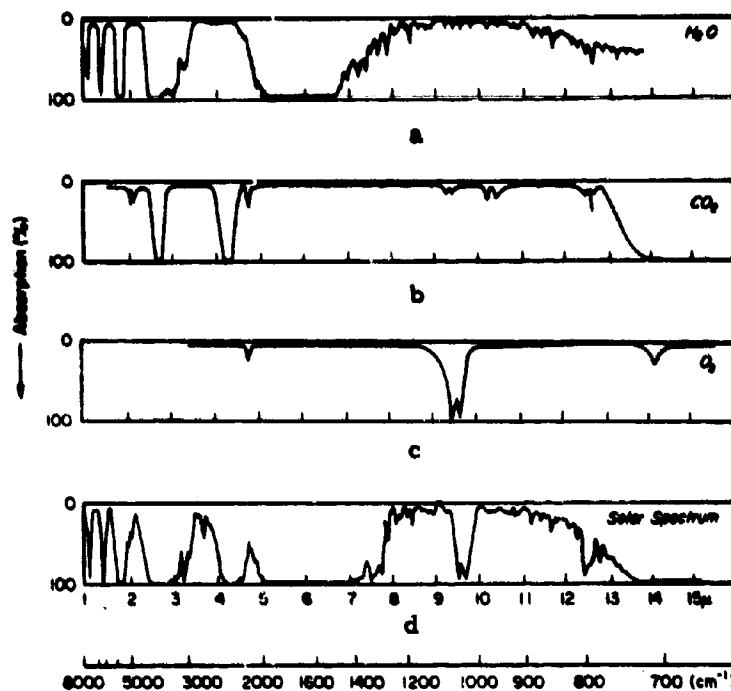


Figure 29. Atmospheric Absorption Spectrum in the IR

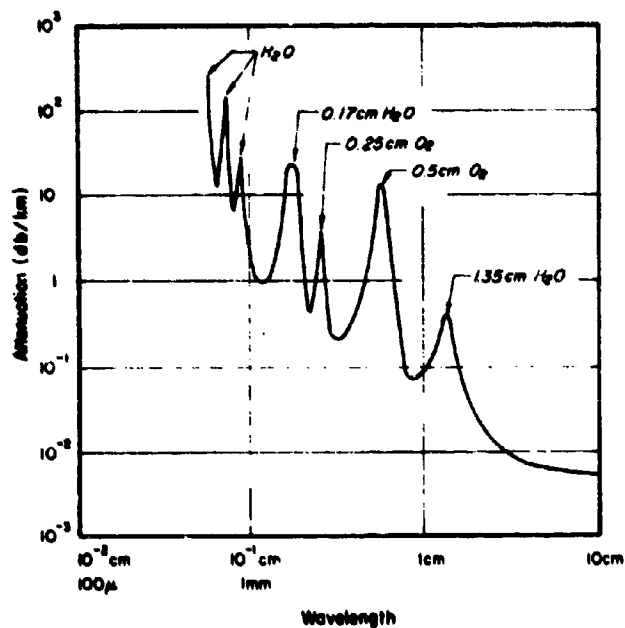


Figure 30. Atmospheric Absorption in the Microwave

rather narrow spectral intervals centered at $\lambda = 4.8\mu$, $\lambda = 9.6\mu$, and $\lambda = 14.1\mu$. Between those isolated absorption bands, O_3 is transparent to incident radiation.

The IR absorption spectrum of water vapor shows a much more complex structure, especially in the spectral region beyond $\lambda = 7\mu$. In this region, the spectrum shows that, on the whole, absorption is not very intense (compared with the absorption shown for the spectral region between $\lambda = 5\mu$ and $\lambda = 7\mu$). However, the intensity of absorption is still very dependent on the wavelength.

CO_2 has two intense absorption bands in the near IR (with band centers at $\lambda \sim 2.7\mu$ and $\lambda \sim 4.3\mu$). More significant, however, is the broad CO_2 absorption band located at $\lambda = 15\mu$. Radiometric measurements in this spectral band region are expected to provide, in the near future, data of the vertical distribution of atmospheric temperature.

When the absorption spectra of all the atmospheric gases are combined together, the result is the absorption spectrum of the atmosphere. Figure 29d shows the atmosphere absorption spectrum in the IR. This spectrum was made using the sun at the source. The ordinate values (0-100) indicate the percent absorption, by the total atmosphere, of solar irradiance. This figure shows the spectral locations of the major atmospheric absorption bands in the IR region extending from 1μ to 15μ . Comparison of Figure 29d with Figures 29a, b, c, confirms that the principal atmosphere absorbers of IR radiation are H_2O , CO_2 , and O_3 .

Figure 29 shows that, in the spectral interval shown, the total atmosphere absorbs completely (100% absorption) the radiation in a number of spectral regions. For instance, absorption is complete between 2.5μ and 3μ , and between 5μ and 7μ . In most of the other spectral regions, the total atmosphere exhibits only partial absorption. Of particular interest are the spectral regions located between 8μ and 12μ , and between 3μ and 4μ . While the atmosphere is not totally transparent to radiation in these spectral regions, the residual absorption effects are sufficiently minor for significant portions of the energy from surface sources to penetrate through the atmosphere to the satellite. These spectral regions (and others like them) are known as atmospheric window regions, or just "windows." It is only through such windows that useful surface observations can be made from satellite altitudes.

Besides these two atmospheric windows, the significant spectral regions in the IR are the 15μ CO_2 absorption band and the 6.3μ water vapor absorption band. Measurements in these two spectral regions have already been achieved, providing useful information of atmospheric temperature and atmospheric water vapor. Examples of these measurements, and their interpretation, are given in a subsequent section.

A similar band structure of the atmospheric absorption exists in other spectral regions. In Figure 26 of Section IV, the atmospheric absorption spectrum in the solar UV and in the visible was illustrated. The specific atmospheric gas (or gases) corresponding to each of the absorption bands is indicated in the figure. Again, the principle absorbing gases are O_3 , CO_2 , and H_2O , with O_2 having a narrow absorption band centered at $\sim 0.8\mu$. It should be noted that O_3 absorption totally obliterates solar UV radiation of wavelength less than 0.3μ . The atmosphere, as far as absorption attenuation is concerned, is relatively transparent to radiation in the visible portion of the spectrum (with some residual absorption due to O_3). This broad region from 0.4μ to 0.8μ is another significant atmospheric window through which surface observations can be made. Beyond the 0.8μ limit of this visual window, H_2O absorption bands begin to dominate.

In the far IR spectral region ($15\mu - 1\text{ mm}$), the absorption spectrum of the atmosphere has been less well studied and documented. It is reported²⁷ that there is a semi-transparent window at $\sim 20\mu$.

The atmospheric absorption spectrum in the microwave region is dominated by the absorption lines of H_2O (centered at 1.35 cm, 1.63 mm, and 0.94 mm) and of O_2 (at 0.5 cm, and 0.25 cm). Figure 30 shows the locations and relative intensities of these lines at sea level. In this figure, the absorption attenuation is given in terms of the convention used by radio engineers, i.e., db/km where

$$db = 10 \log_{10} \frac{H}{H_0}$$

and H/H_0 is the fraction of power attenuated by the atmosphere. Consequently, attenuation increases upwards in this figure.

Radiation of wavelengths greater than 3 cm is not appreciably attenuated by atmospheric gas absorption, (until the ionospheric cutoff is reached at about 10 Mhz i.e. $\sim 30\text{ m}$). This is indicated in Figure 30 for the region out to 10 cm.

5.2.2 Beer's Law

The preceding discussion and diagrams are useful in delineating the spectral regions in which the atmospheric gases absorb radiation, and, more importantly, the atmospheric windows. The figures, however, provide quantitative information regarding the absorption characteristics of the atmosphere only under specific conditions. For instance, in the IR absorption spectrum shown in Figure 29d, the

percent of absorption shown is only applicable to the conditions under which the measurements were made. These conditions include

1. Propagation of the radiation through the entire atmosphere
2. Specific vertical distributions of the absorbing gases in the atmosphere at the time of measurement.

Consequently, the percent absorptions shown are not applicable in all instances. For example, it will be shown in Section 5.3, thick clouds are essentially radiation blackbodies in the infrared. When and where present, they form effective lower "surfaces" seen by satellite IR sensors. Since clouds are located above the actual surfaces of the earth, the total path through the atmosphere of cloud emitted radiation is less than that of a similar target located at the surface of the earth. As a consequence, the attenuation effects of the atmosphere on cloud emitted radiation would also be less. Consider also the situations in which the satellite sensor views a surface target at nadir angles other than zero degrees (the air mass effect, see Section II). The radiation propagating from the target to the sensor must traverse a longer path through the atmosphere due to the inclination. As a result, the atmospheric effects should be proportionately increased.

More important, is the fact that the absorption measurements shown in Figure 29d were made with specific amounts of the absorbing gases along the paths of propagation of the radiation. The total amount of some atmospheric gases in a vertical column may be variable; this is especially true of O_3 and H_2O .

The absorption characteristic of the atmosphere at any wavelength is complex and dependent on the distributions of (1) pressure, (2) temperature and (3) the concentration of the absorbing gas (or gases) along the path of propagation. Pressure and temperature effects can change the spectral width as well as the intensity of a particular absorption band. Figure 31 is an example of these effects. The absorption band in question is the 0.5 cm absorption band of oxygen. The variations in absorption per unit length of propagation (given in db/km) are shown for three altitudes. At sea level ($h = 0$), where the pressure is greatest, the band is most intense and exhibits little or no structure. At higher altitudes where the pressure is less, the band breaks down into discrete lines with the attenuation coefficients significantly reduced.

In an analysis of the absorption effects of the atmosphere, it is convenient (and often necessary in practice) to consider the atmosphere as stratified into a large number of layers such that the temperature, pressure and absorber concentration

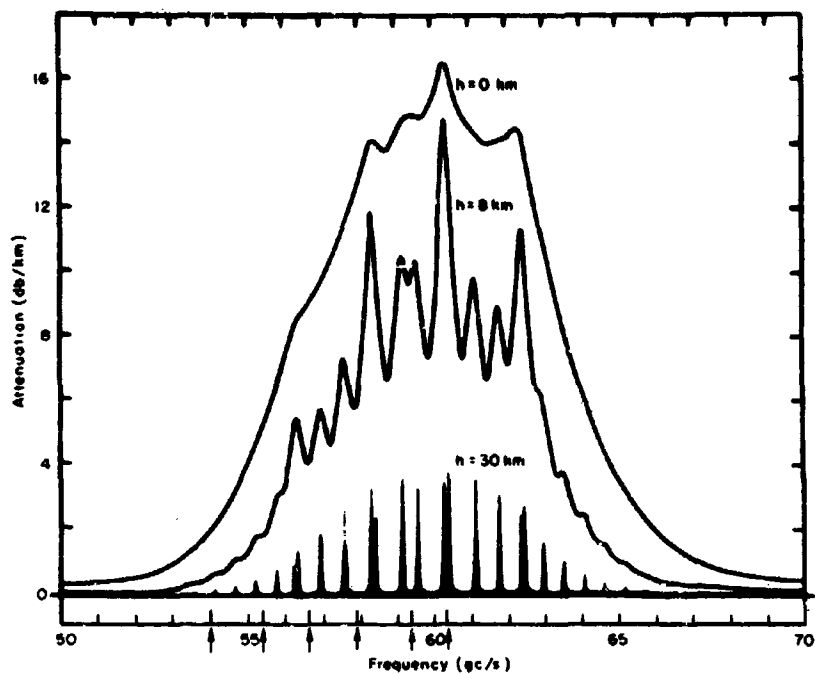


Figure 31. Attenuation Coefficient for Air at Three Representative Heights

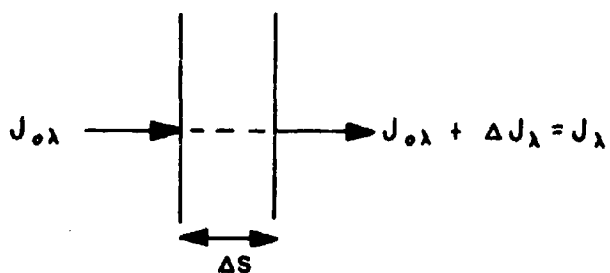


Figure 32. Absorption in an Infinitesimal Layer

within each of the layers can be considered to be constant. In addition, it is often the practice to consider only the absorption effects on radiation at a single wavelength (i.e., monochromatic radiation). The absorption effect for a given wavelength interval is then obtained by summation techniques.

With the above assumptions, it is then possible to analyze the effects of gas absorption in terms of Beer's Law, as follows.

Figure 32 shows a stratified layer of the atmosphere of thickness Δh . A beam of monochromatic radiation, at wavelength λ , is shown as incident on the bottom of the layer. Let the intensity of the incident beam be denoted by J_{λ_0} , and the intensity of the beam emerging from the top of layer be J_λ . In general, J_{λ_0} and J_λ are not equal, due to the radiation processes within the layer. Consequently, J_λ can be written as

$$J_\lambda = J_{\lambda_0} + \Delta J_\lambda \quad (88)$$

In the case of atmospheric gas absorption only, ΔJ_λ is proportional to

1. The incident intensity, J_{λ_0}
2. The density of the absorbing gas, ρ
3. The path length of the beam in the layer $\Delta z = \Delta h (\sec \theta)$
where θ = angle made by the beam and the normal to the layer.

Since absorption attenuates or (depletes) the original beam intensity, ΔJ_λ is a negative quantity and is therefore given by

$$\Delta J_\lambda = -k \rho J_{\lambda_0} \Delta z \quad (89)$$

where

k is the constant of proportionality and is known as the absorption coefficient.

For a given situation, ρ , J_{λ_0} , and Δz are fixed. But, from the discussions of the spectral dependence of atmospheric gas absorption effects, it is apparent that k , the absorption coefficient, is spectrally dependent, and should properly be denoted by k_λ .

Equation (89) assumes a constant absorbing gas density within the layer. It is obvious that, for the vertical variations in gas densities found in the atmosphere, the thinner the layer being considered, the better is the approximation. In the limit,

Equation (89) can be written as

$$dJ_{\lambda} = -k_{\lambda} \rho J_{\lambda 0} dz \quad (89a)$$

The effect on the propagating beam in its passage through a large number of such atmospheric layers can then be obtained by integrating Equation (89a). The result is:

$$J_{\lambda}(h) = J_{\lambda 0} e^{-\int_0^h k_{\lambda} \rho(\sec \theta) dh} \quad (90)$$

where

$J_{\lambda}(h)$ = the intensity of the emergent beam after its passage through an atmospheric layer of thickness h .

$J_{\lambda 0}$ = the intensity of the original incident beam

k_{λ} = absorption coefficient

ρ = density of the absorbing gas

e = base of the natural logarithm

θ = zenith angle of the propagating beam.

Equation (90) is known as Beer's Law.

It should be noted that k_{λ} is a function of the pressure, and to a more limited extent, of the temperature, of the atmospheric layer in question. These parameters are in turn functions of altitude. Consequently, k_{λ} is a function of altitude and cannot be taken out of the integral. Since the absorbing gas density is also a function of altitude, the evaluation of the absorption or attenuation integral involves (1) the evaluation of the term $k_{\lambda} \rho$ at each level in the atmosphere and (2) summing these terms over the range of h of concern (for satellite observations, usually from the top of the atmosphere to some lower level).

Extensive tables, and mathematical procedures and techniques, exist for the evaluation of the absorption coefficient, k_{λ} , for different pressures and temperatures. A good summary of these can be found in a study by Kellogg, et al.²⁷ However, it should be noted that the procedures are often very complex and not always accurate.

Examination of Equation (90) shows that the exponential term is the decimal fraction of J_{λ_0} which is transmitted by the atmospheric layer of thickness h . As a consequence, it is equivalent to the monochromatic transmissivity, τ_λ , used in the analysis of radiation processes in relation to solid and liquid surfaces (see Section III). In fact, Equation (90) can be written as

$$J_\lambda(h) = J_{\lambda_0} \tau_\lambda(h) \quad (91)$$

where

$$\tau_\lambda(h) = \exp - \int_0^h k_\lambda \rho (\sec \theta) dh$$

i.e., $\tau_\lambda(h)$ is the monochromatic transmissivity of the atmospheric layer of thickness h .

Equations (90) or (91) apply to any layer within the atmosphere, or to the total atmosphere (where the limits of the integral would be at $h = 0$ and at $h = \text{top}$ of the atmosphere), or to the total atmosphere above any level. It, therefore, provides a means of evaluating the absorption effects of the atmosphere at any wavelength.

Besides the difficulties encountered with the determination of k_λ , the application of Equation (90) requires that the vertical distribution of the absorbing gas density be known. With the well mixed gases such as carbon dioxide and oxygen, this does not present an insurmountable problem. However, the vertical distributions of the other two principle atmospheric absorbers, O_3 and H_2O , are highly variable in time and space. While radiosondes do make observations of vertical moisture distribution, and some ozonesonde measurements are made, the spacing, both temporal and spatial, of these observations are seldom sufficiently dense for the evaluation of their effects on satellite observations made in spectral regions in which they have absorption bands. A case in point is the measurements made in the 8μ to 12μ IR window by the TIROS scanning radiometer. Figure 29 shows that there is residual absorption by both O_3 and H_2O in this window. In order to deduce surface characteristics, it is necessary to determine and adjust for the effects of the absorption by these two gases. Since it is not possible to obtain the distributions of O_3 and H_2O corresponding to all the satellite data, Equation (90) cannot be applied directly in most instances. Other techniques, based on climatology and statistics, have to be applied. These are discussed in Section X.

5.2.3 Scattering Effects of Atmospheric Gases

The gases in the atmosphere are composed of molecules (and atoms). As such they are particles even though their sizes are small. When a directed beam of radiation is incident on a particle, the energy of the beam is scattered, i.e. there is a redistribution of the beam energy to directions other than the original propagation direction. Even though there is no net loss in radiation when only scattering occurs, the energy content of the directed beam becomes depleted by this scattering process. (Of course, scattering and absorption may occur concurrently.)

The effect of scattering is a function of many parameters, including the size of the particle in relation to the wavelength of the incident radiation, and the optical properties of the scattering particle itself. For the gas molecules of concern in the atmosphere, the scattering attenuation effects can be described in terms of the Rayleigh Law. This law states that the intensity scattered out of a directed beam by a volume of gas is inversely proportional to the fourth power of the wavelength of the incident radiation. A scattering equation of a form similar to that used to describe absorption attenuation effects can be derived as

$$J_{\lambda}(h) = J_{\lambda_0} \exp - \int_0^h \frac{k(h)}{\lambda^4} dh \quad (92)$$

where

$k(h)$ is independent of wavelength but a function of molecular number density.

Equation (91) shows that, as λ increases, the scattering attenuation effect decreases. In fact, molecular scattering attenuation is only significant in the visible and the UV. Figure 33, based on the data of Eltermann,²⁸ shows the transmissivity of the total atmosphere due to molecular scattering alone. In the IR and microwave regions, the losses of energy due to molecular scattering can be neglected.

5.2.4 Atmospheric Gases as Sources of Radiation

According to Kirchhoff's Law, an object which is an effective absorber of radiation is also an effective emitter of radiation at the same wavelength. Consequently, in the spectral regions in which the atmosphere has absorption bands, the atmosphere is also an effective radiator. However, the intensity of the emitted

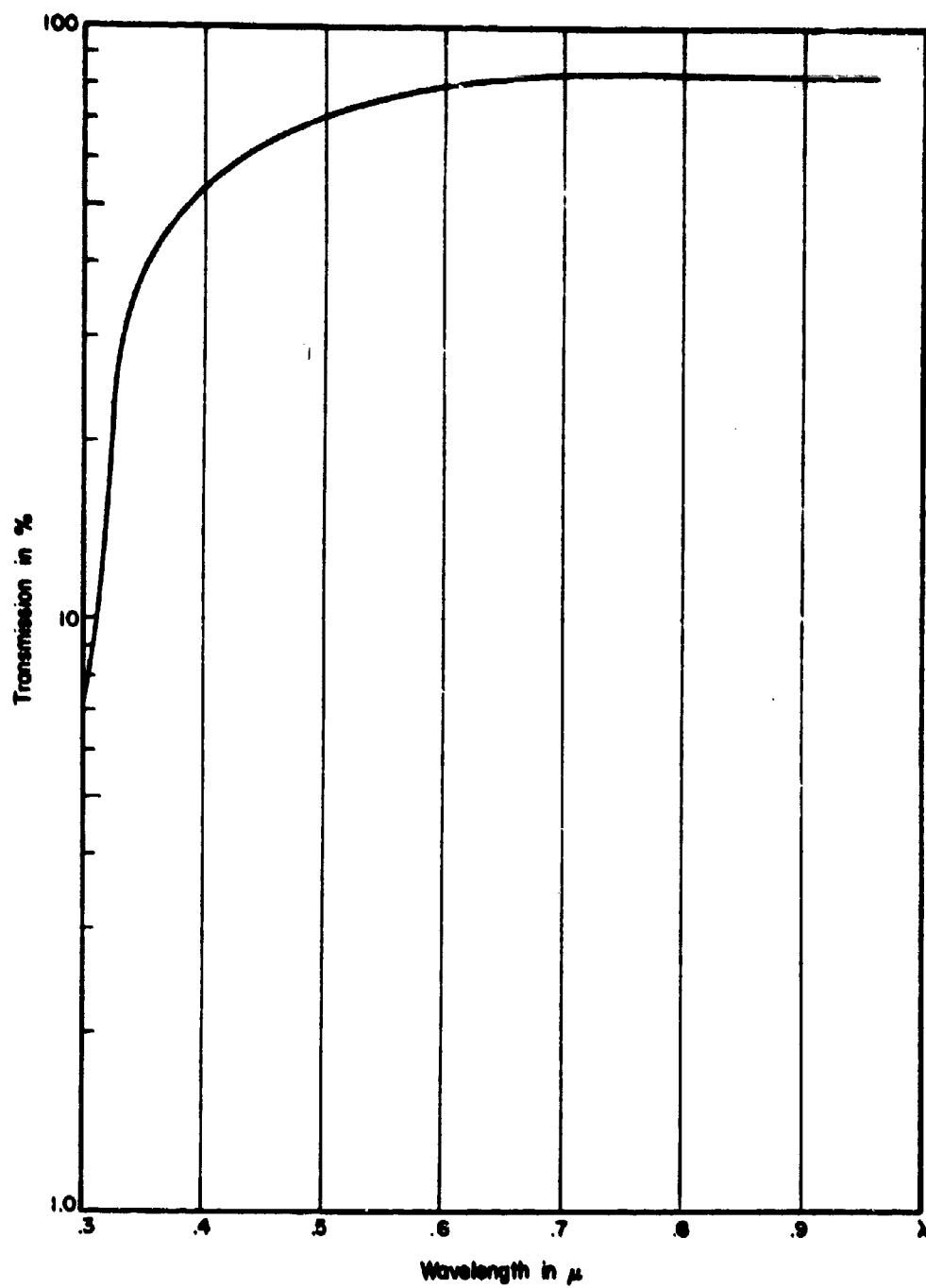


Figure 33. Molecular Scattering Attenuation in the Visible.

radiation is proportional to the temperature of the atmospheric layer in question and so need not be equal to that which it absorbs, (which is principally a function of gas concentration).

At the range of temperatures corresponding to the atmosphere, Planck's Law states that the radiation emitted is concentrated in the infrared and microwave regions of the spectrum. It was shown in the previous section that scattering by molecules can be neglected in these longer wavelength regions. As a consequence, in the absence of atmospheric aerosol and clouds, the only significant processes which occur in an atmospheric layer are absorption, emission and transmission. For a given layer in the atmosphere, similar to that described in Section 5.2.2, and shown in Figure 32, the spectral radiant emittance can be given by

$$W_{\lambda} = \epsilon_{\lambda}(\text{layer}) W_{b\lambda}(T) \quad (93)$$

where

$\epsilon_{\lambda}(\text{layer})$ = the spectral emissivity of the layer,

$W_{b\lambda}$ = blackbody spectral radiant emittance, and

T is the temperature of the layer.

Again, the assumption is made that the layer thickness, Δh , is sufficiently small for T to be treated as a constant throughout the layer.

Using Kirchoff's Law, it is seen that the layer emissivity, $\epsilon_{\lambda}(\text{layer})$, is related to the layer transmissivity $\tau_{\lambda}(\text{layer})$, by

$$\epsilon_{\lambda}(\text{layer}) = 1 - \tau_{\lambda}(\text{layer})$$

It is possible, therefore, to determine the emissivity of a layer in the atmosphere from the transmissivity of the layer at the same wavelength.

From the above discussion, it is seen that the emission characteristics of the atmosphere are intimately related to its absorption characteristics and to its temperature. An obvious fact which should be noted is then: In those regions in which the atmosphere does not absorb radiation ($\tau_{\lambda} = 1$), it does not emit radiation ($\epsilon_{\lambda} = 0$), regardless of the temperature.

The fact that the atmosphere emits radiation in certain spectral intervals, and absorbs radiation in the same intervals, coupled with the peculiar vertical distributions of gas densities and temperatures, provides a number of useful measurements of the atmospheric structure which can be made from satellites. Some of these have already been made. A discussion of these possibilities is given in Section X.

Except for airglow and aurorae, the atmosphere does not emit radiation in the visible. However, just as the surfaces of the earth reflect incident visible radiation, thus becoming effective sources, the atmospheric gas molecules scatter back some of the solar radiation (and radiation from man made sources, such as lasers) through the top of the atmosphere. This backscattering of incident radiation is again proportional to the λ^{-4} law.

In photographic techniques, the backscattering of radiation by gas molecules provides an unwanted "background" (again a "background" between the surfaces and the sensor) against which surface observations must be made. The addition of this non-image forming light reduces the contrast in the pictures obtained. Since the intensity of the scattered non-image forming light has the λ^{-4} dependence, many of the photographic sensors (e.g. satellite television cameras) are provided with optical filters which eliminate most of the "blue" part of the visible spectrum, where these effects are maximum. For example, the TIROS camera filter cut off most radiation at wavelengths shorter than $\sim 0.5\mu$.

While the mechanism of backscattering by molecules is a source of degradation to imaging techniques, the same mechanism has been proposed for use in optical (laser) radar techniques for obtaining the distribution of molecular densities. Consequently, as in the case of gas absorption and emission, molecular scattering by the atmosphere is both a source of degradation and a source of useful radiation.

5.3 Effects of Clouds

Radiation of wavelength longer than 3 cm is little affected by non-precipitating clouds. Consequently, surface emitted microwave radiation can penetrate through these clouds to a satellite sensor with little or no attenuation. This fact permits microwave measurements and observations of surface features and parameters, even in the presence of cloud cover.

Radiation in the shorter wavelength regions of the IR and visible cannot penetrate through thick clouds. In other words, visible and IR observations of the surfaces below these clouds cannot be made from satellites. However, the fact that these clouds are opaque to IR and visible radiation, also renders these clouds significant sources of emitted radiant energy (in the IR) and of reflected radiant energy (in the visible). The cloud energy, as measured or observed by a satellite sensor, can then be used in the determination of a number of parameters relating to cloud cover distributions, cloud types, cloud movement, and cloud top heights. These cloud parameters are not only significant in themselves, but are also useful in the determination of other meteorological parameters such as the locations of storms and frontal systems, and the general nature of the wind, pressure, and temperature patterns.

Since a cloud is at a temperature above zero degrees Kelvin, it emits thermal radiation. Again, at the range of temperatures characteristic of clouds, the radiation emitted is concentrated in the IR. It has been generally assumed that, for a sufficiently thick cloud (an exception is tenuous cirrus), the thermal emission in the IR corresponds to that of a blackbody at the same temperature as that near or at the top surfaces of the cloud. Clouds are therefore usually treated as blackbody radiators in the IR, with emissivities approximately equal to one.

In IR measurements of surface features, the presence of clouds can generally be detected in the measured data by their characteristically lower emitting temperatures. Clouds are located above the surface of the earth, and the temperature structure of the normal atmosphere (at least in the tropospheric region) is most frequently such that a decrease in temperature corresponds to an increase in altitude. The spectral radiant emittance or the spectral radiance from the tops of clouds is therefore usually lower than that measured in a cloud free area. However, there is not always this clear-cut distinction between cloud emitted and surface emitted IR radiation. When the difference between cloud top temperature and the surrounding surface temperatures is not sufficiently large (e.g., low clouds over a snow covered region), difficulties can be encountered in the interpretation of the data. These problems are more fully discussed in Section X.

In the visible, clouds are effective reflectors of incident radiation. The generally higher albedos of clouds over those of the surfaces of the earth (except for snow or ice) provide the necessary target signature in visible observations such

as those made by satellite television cameras. Conover²⁴ has systematically studied the albedo of various surfaces and of different types of clouds as revealed in TIROS satellite television pictures. While the albedos he determined are generally higher than those measured by conventional means (e.g., see Smithsonian Meteorological Tables), they nevertheless provide significant information on the albedo contrast between clouds and surfaces as viewed from satellites. The results of his investigation are reproduced in Table 9. It can be seen from this table that except in the cases of snow covered surfaces and desert sands, the albedos of surfaces are characteristically much lower than those of clouds.

Table 9
(Taken from Ref. 24)

Average Albedos (in percent) for Various Cloud Surfaces
As Determined from Satellite TV Pictures

Cloud type	Albedo
Cumulonimbus - large and thick	92
Cumulonimbus - small	86
Cirrostratus - thick with lower clouds and precipitation	74
Cirrostratus alone, over land	32
Cirrus alone, over land	36
Stratus - thick, approx. 0.5 km, over ocean	64
Stratus - thin, over ocean	42
Stratocumulus masses with cloud sheet over ocean	60
Stratocumulus - MCO, over land	68
Cumulus and stratocumulus - MCO, over land	69
Cumulus of fair weather - MCO, over land	29

5.4 The Effects of Haze and of Thin Cirrus-Type Clouds

The particles in haze and in thin cirrus-type clouds are generally very small and the particle concentrations are such that some IR and visible radiation from below the cloud layer or haze layer do penetrate through. Consequently, such layers cannot be treated simply as the lower surface boundaries in either visible or IR measurements.

The scattering effects of haze is to reduce photographic contrast in the visible. These effects have been extensively studied in connection with atmospheric effects on long range oblique aerial photography. For a detailed discussion of these effects, the reader is referred to References 29 and 30.

In the IR regions of the spectrum, the tenuous nature of these clouds render them partially transparent to radiation incident from below. Consequently, they cannot be treated as simple blackbody radiators. It has been postulated that these tenuous clouds are the cause of degradation in IR window measurements which cannot be attributed to residual atmospheric gas absorption. Hale³⁰ et al, have made detailed calculations on the attenuation effects of such clouds on IR measurements. Their results agree quite well with the observed degradations. Their calculations were based on assumptions made of the thickness of these tenuous clouds as well as their particle size, distributions, and number concentrations. All of these parameters are not well known.

While the theoretical tools exist for the exact treatment of these degradation effects, in practice, these effects can only be treated by gross approximations, since, as it is pointed out in Reference 27, the exact solution to this complex problem would tax even the largest of the present generation of computers.

5.5 Sferics and Airglow

Electromagnetic radiation generated by lightning discharges in thunderstorms are known as sferics. The detection and location of the sources of sferics can be useful in the location of severe weather phenomena associated with thunderstorms.

In order for a satellite to detect and locate the sources of sferics, the radiation must propagate through the ionosphere. Most of the sferic radiation emitted by a return stroke of lightning is distributed in the lower frequency ranges of the VLF (~ 10 kc band). According to the accepted theory of electromagnetic wave propagations, such low frequency waves cannot penetrate through the ionosphere to reach the satellite sensor. While receivers operating at 10 kc are useful for sferics detection on the ground, they cannot be used in a satellite.

Richards³¹ states, however, that satellite sferics detection is possible if the radiation resulting from the step leader of lightning is measured. The spectrum of the energy emitted by step leaders extend all the way to the microwave regions. These shorter wavelength (higher frequency) radiations can penetrate through the ionosphere to the satellite. Richards suggests that the optimum operating frequency of a satellite sferics detector should be 60 megacycles/sec.

Airglow is the radiation emitted by the atmospheric gases as a result of chemical processes. On the whole, airglow is neither a significant source of energy nor a source of degradations as far as current geophysical observations pertinent to Navy operations are concerned. However, when nighttime photographic techniques are developed which make use of the light from the moon as the source of illumination, airglow can be a source of unwanted background radiation between the satellite sensor and the earth.

SECTION VI

SATELLITE SENSOR SYSTEM EFFECTS

6.1 Introduction

A satellite sensing system is made up of a number of individual components, located both on the spacecraft and on the ground. The components on the spacecraft perform the functions of (1) spatially and spectrally selecting the radiant energy to be measured, (2) transducing the measured energies to electrical signals susceptible to radio telemetry techniques, and (3) recording of the data (when necessary) for transmission at a later time. On the ground, the components consist of receiving and demodulating systems, and data recording, retrieval, and processing equipment. Regardless of the specific measurements involved, the various components of a satellite system can be represented in a generalized functional block diagram, similar to that shown in Figure 34a.

Figure 34b shows specifically, the block diagram of the High Resolution Infrared Radiometer (HRIR) system of Nimbus. A schematic of the actual sensor itself is shown in the insert. In the following paragraphs, the signal flow within the HRIR system is briefly described to indicate the complex processes involved in an actual satellite sensor system.

In the HRIR system, spatial selection of the measured energy is achieved by the combination of mirrors and lenses in the sensor assembly. The optical filter, inserted between the relay mirrors, spectrally selects the radiant energy which is incident on the lead solenoid (PbSc) detector. The output of the detector is in the form of an electrical voltage signal proportional to the radiant power incident on the detector.

Because of telemetry requirements, the voltage output of the detector is frequency modulated. The modulated signal is then fed into a multichannel tape recorder, along with the timing signals generated by a clock on board the spacecraft. Tape recording of the signal is essential since the data is telemetered to the ground only when the satellite is within acquisition range of a Data Acquisition Facility (DAF). (When operated in the DRIR mode, i.e. Direct Readout Infrared, the data are transmitted without being stored on the satellite.)

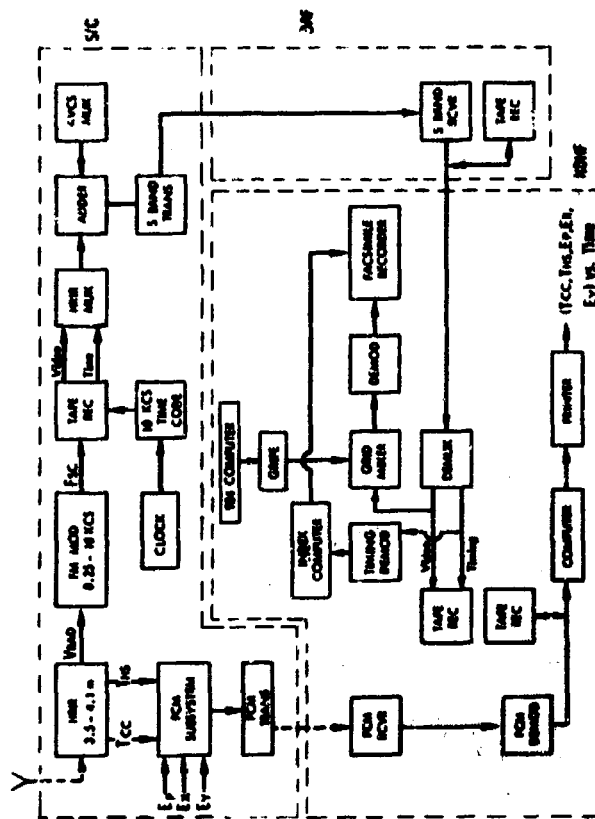
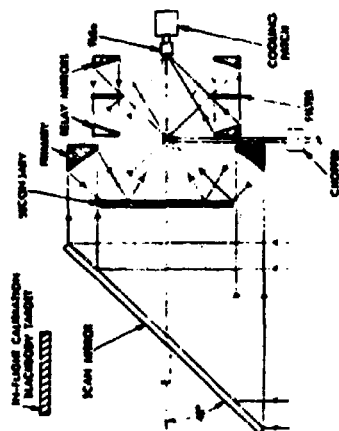


Figure 34b. Block Diagram of the Nimbus HRIR

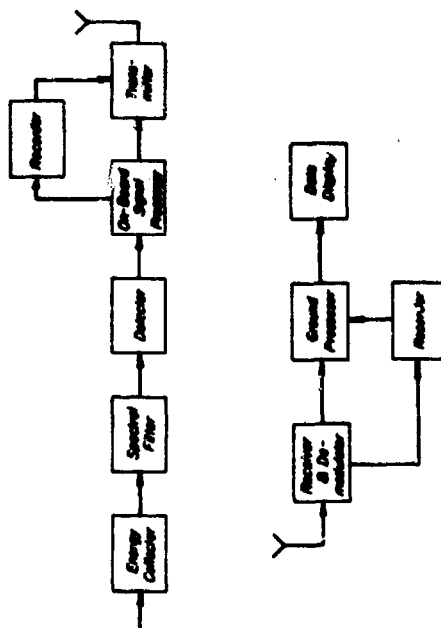


Figure 34a. Generalized Block Diagram of a Satellite Sensor System

Before being telemetered to a DAF, the HRIR signal is combined with the signals from another sensor on board the Nimbus I which is the Advanced Vidicon Camera System (AVCS). The combined signal is then transmitted by the S-band transmitter of the spacecraft.

At the ground, the telemetered data are received by an S-band receiver. The HRIR information, after electronic processing is recorded on magnetic tape. The recorded data can be used to generate a continuous strip analog picture on a facsimile recorder, or to produce digital values of the measurements.

From this simplified description of the data flow required for a single satellite sensor system, it may be seen that the components of the system can place constraints on the information obtained, as well as introduce degradation effects on the displayed data. The constraints and degradation effects of some of the more significant system parameters are discussed in the following sections.

6.2 Spectral Selectivity

6.2.1 Spectral Response

Geophysical targets and parameters exhibit spectral dependences in their radiation characteristics. For a given target element, there are spectral regions for optimum detection. As a consequence, some form of spectral selection is exercised in every remote sensor system. In the longer wavelength regions (such as the millimeter, centimeter and radiowave regions), spectral selection is achieved by electronic tuning of the detector system, completely analogous to the way an ordinary radio receiver is tuned to the desired station. In the optical regions of the visible and infrared, spectral selection is achieved by optical filters and the proper choice of detectors.

In either case, the parameter which can be used to specify the spectral selectivity of a sensor system is the effective spectral response function, ϕ_λ . ϕ_λ is simply the function of the incident energy, at each wavelength λ , which is actually measured. It is, therefore, defined as

$$\phi_\lambda = \frac{N_\lambda(\text{measured})}{N_\lambda(\text{incident})} \quad (95)$$

A given sensor system is an effective radiant energy detector only in those spectral regions in which ϕ_λ is significantly greater than zero.

Figure 35 shows the effective spectral response function of the HRIR Nimbus. It may be seen that the HRIR responds to (or measures) radiant energy only in the spectral interval extending from $\lambda \sim 3.3\mu$ to $\lambda \sim 4.2\mu$. This restrictive spectral response of the HRIR was chosen to meet the objectives of the system, which are to measure "surface" radiation, emitted in a narrow spectral interval centered at $\sim 3.8\mu$, where minimal atmospheric degradation effects can be expected. However, as it is often the case, spectral selectivity of the sensor is not complete. The energy measured by the HRIR could not be completely restricted to that which is emitted by the surface targets alone. The spectral regions, in the vicinity of 3.8μ , in which there is atmospheric absorption due to carbon dioxide and water vapor are shown in Figure 35 as dashed curves. The radiation measured by the HRIR, is therefore, contaminated by atmospheric absorption and emission.

Degradation effects can sometimes be reduced by narrowing the region where the spectral response function of the sensor is significantly greater than zero. In the case of the HRIR, for example, residual atmospheric effects might have been further reduced if the spectral response of the sensor were to be confined to a narrower spectral interval. However, as the spectral response of the sensor is made narrower, the energy incident on the detector is proportionately decreased. A point may be reached at which the signal energy is of the same order of magnitude as the noise generated by the detection system itself. The spectral response function of a sensor is, therefore, the result of trade off compromises between the ideal response and the energy available for detection.

6.2.2 Spectral Resolution

In most single channel radiometric or photometric measurements, the spectral response of the instrument also determined its spectral resolution. For such an instrument, the measured radiation may be specified as being within the spectral region defined by significant values of the spectral response function. No information on the spectral energy distribution within incremental parts of the overall region of the response can be derived from the measurements themselves. Simultaneous multispectral observations of a given feature can only be obtained by having a number of such sensors systems, each having a spectral response in different portions of the spectrum. Such multispectral measurements have been made, for example, by the Nimbus Medium Resolution Infrared system, which employs five separate channels and detectors.

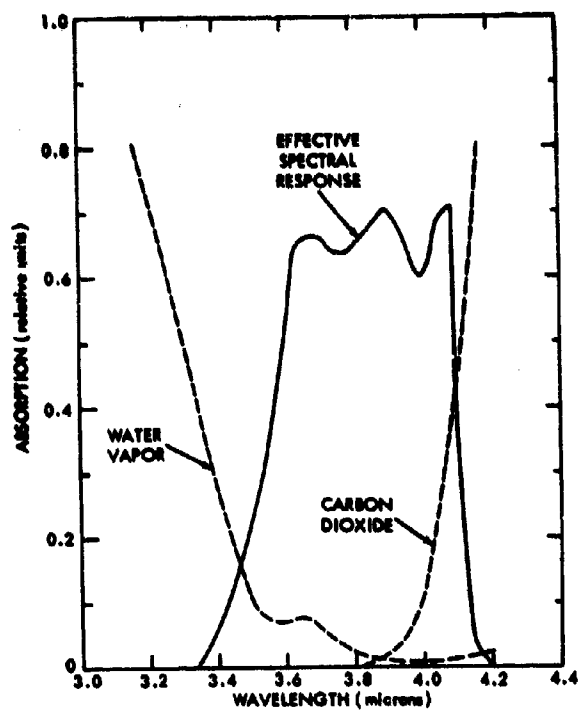


Figure 35. Spectral Response Function of the HRIR

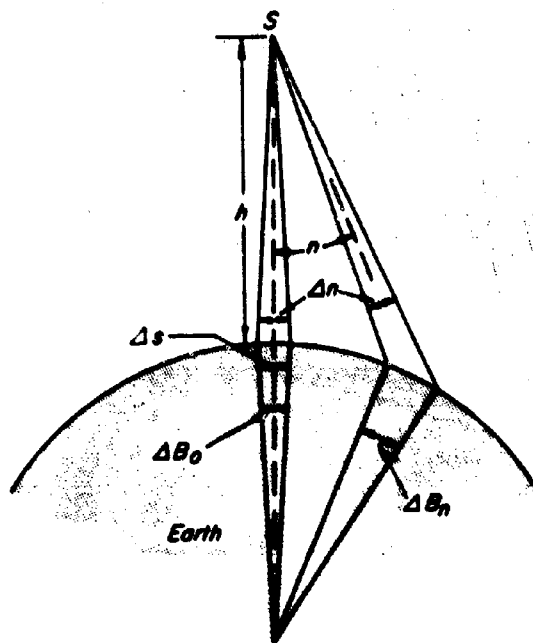


Figure 36. Variation of Resolution with Nadir Angle and the Effect of the Earth's Curvature

There are sensors which can spectrally resolve the radiation within the spectral interval defined by the overall spectral response function. A photographic camera using color film as a detector is a good example of such a sensor. The colors in the scene viewed by the camera are resolved in the image formed on the film. The spectral resolution of the camera is then dependent on the optics of the camera, as well as the emulsion of the film.

Other examples of sensors systems which can spectrally resolve the incident radiation are the spectrometer and the interferometer. These are standard laboratory optical devices which can be modified for satellite use.

6.3 Spatial Resolution and Geometric Distortions of Non-Imaging Systems

6.3.1 Spatial Resolution

It was stated previously that a satellite sensor has elements which define its spatial field of view at any given instant. In the HRIR sensor shown in Figure 34b, for instance, the optical elements in the radiometer housing limit its instantaneous field of view to a region of space lying in a one-half degree cone. Sources of energy lying outside this one-half degree field are not "seen" by the radiometer and are ineffective in producing detector output signals, although they may be scanned earlier or later. In the sensors operating in the longer wavelength regions, such as microwave radiometers and radars, the fields of view are similarly defined by their energy collection elements, which in these cases would be the receiving antennas.

In a non-imaging system, such as a radiometer, the instantaneous field of view of the sensor, in turn, defines its spatial resolution. The detector output of such a sensor, at any given instant, consists of a single value. If a target element totally fills the field of view of the sensor, and if it has uniform surface radiation characteristics, then the output signal is proportional to the target emitted (or reflected) energy. However, it is impossible to determine, from the measured data alone, whether this is indeed the case. A number of small target elements, of differing radiation characteristics, may produce an average emission or reflection which gives rise to the same detector output signal. It is seen therefore, that a non-imaging sensor can accurately measure variations of target energies which have spatial dimensions equal to or greater than that determined by the field of view of the sensor. But it is incapable of doing so when such variations are of a smaller

spatial scale. In other words, the spatial resolution of such a sensor is determined by its field of view, which, in turn, is determined by the design of its energy collection components.

The area on the surface of the earth intercepted by the field of view of a non-imaging sensor is defined as its ground resolution. Usually, the ground resolution is specified in terms of a linear measurement instead of an areal measurement. For example, the HRIR system, with its one-half degree field of view, has a ground resolution of approximately 8 km when the sensor views the surface of the earth at a nadir angle of zero degrees, and the satellite is at an altitude of 925 km. The dependence of ground resolution on sensor field of view and satellite altitude can be seen in Figure 36, if only the zero nadir part of that figure is considered for the moment. At the nadir, and assuming a flat earth, ground resolution Δs is given by

$$\Delta s \sim h (\Delta n) \quad (96)$$

where

Δs is the linear ground resolution
 h is the satellite altitude
 Δn is the field of view of the sensor

6.3. 1.1 The Effects of the Curvature of the Earth and Sensor Nadir Angle on Resolution

Equation (96) is only a simplification of all the factors effecting the resolution of a non-imaging sensor. The surface of the earth is not flat, and the sensor nadir angle will often not be zero degrees. These deviations from the idealized case represented by Equation (96) have further effects on the resolution of the sensor. In the following paragraphs, these effects are analyzed in terms of the ground resolution, ΔB , given as degrees in great circle arc. The great circle arc ground resolution is somewhat simpler to treat than the linear ground resolution Δs . On the earth's surface, one degree of great circle arc equals 60 n.mi.

From Equation (53) of Section II, the following relation can be derived:

$$\frac{dB}{dn} = \frac{\cos n}{\sqrt{\left(\frac{R}{R+h}\right)^2 - \sin^2 n}} - 1 \quad (97)$$

where

n = nadir angle,
 R = radius of the earth
 h = satellite altitude.

At the nadir ($n = 0$), dB/dn has an absolute value of (h/R) . dB/dn increases as n increases and, at the horizon where $\sin n_H = R/(R+h)$, $dB/dn = \infty$.

The resolution of a satellite sensor is often expressed in terms of its resolving capability along the ground, at zero nadir angle, for a given satellite altitude. Let Δn be the angular resolution of a satellite sensor (Fig. 36). Then the ground resolution, ΔB_0 , is given by

$$\Delta B_0 = 2 \left\{ \arcsin \left[\left(\frac{R+h}{R} \right) \sin \frac{\Delta n}{2} \right] - \frac{\Delta n}{2} \right\}, \text{ or} \quad (98a)$$

$$\Delta B_0 = \frac{h}{R} \Delta n, \text{ if } \Delta B_0 \text{ and } \Delta n \text{ are small.} \quad (98b)$$

The ground resolution, ΔB_n , at any other nadir angle, n , is then given by

$$\Delta B_n = \left(\frac{dB}{dn} \right)_n \Delta n, \text{ or} \quad (99a)$$

$$\Delta B_n = \left[\frac{\cos n}{\sqrt{\left(\frac{R}{R+h}\right)^2 - \sin^2 n}} - 1 \right] \Delta n \quad (99b)$$

as long as Δn is not too large.

If B , rather than n , is known, Equation (55), (Section II), can be used to find n .

NAVTRADEVCE 66-C-0031-1

The consequences of Equation (99b) can be illustrated using Table 3 (Section II). Assume a satellite height of 500 n.mi. and (because Table 3 uses 2° increments of nadir angle) a 2° angular resolution, Δn . ΔB_o , the ground resolution at the sub-point, is given approximately as 0.2° (of great circle arc). As nadir angle increases, it is seen that (at 500 n.mi. altitude):

n	ΔB_n (Deg, GCA)	ΔG_n (n.mi.)	$\Delta B_n / \Delta B_o$
0°	0.2°	12	1
15°	0.4°	24	2
39°	0.6°	36	3
46°	0.8°	48	4
49°	1.0°	60	5
56°	2.0°	120	10

It is obvious that resolution degrades with increasing nadir angle, and that the rate of degradation also increases with increasing nadir angle.

A second form of degradation due to increasing nadir angle occurs from the increasingly poorer perspective as the local zenith angle of observation increases. The effect is particularly significant if the area or conditions viewed have vertical relief, as in the case of a mountainous area or a field of scattered or broken clouds.

As one way of showing this, let Δn and ΔB_n be small enough to neglect the curvature of the earth's surface over the distance ΔB_n . In this case, simple trigonometry shows that the linear width of the sensor cone of resolution, N , taken perpendicular to the line of sight where it intercepts the earth, is given by

$$N = \Delta B_n \sin E \quad (100)$$

where E is the elevation angle, which can be determined from Equations (59), (60), and/or (61), and where ΔB_n is here expressed in units of length. The linear vertical width of the sensor cone of resolution, N_h , is then

$$N_h = \Delta B_n \sin E \cos E \quad (101)$$

From Equation (60)

$$N_h = \Delta B_n \left(\frac{R+h}{R} \right) \sin n \sqrt{1 - \left(\frac{R+h}{R} \right)^2 \sin^2 n} \quad (102)$$

Using the example of a 500 n.mi. satellite, a 2° angular resolution of the sensor, and $n = 39^\circ$,

$$N_h = (36)(1.14)(0.629) \sqrt{1 - (1.14)^2 (0.629)^2} = 18$$

$$E = 44^\circ$$

To illustrate two possible effects of this degradation on the signal reaching the sensor, consider a field of scattered cumulus cloud streets with the lines of clouds oriented perpendicular to the line of sight from the satellite. Assume the clouds have a vertical thickness of 5000 feet, and there are clear lanes between each cloud line which are 5000 feet wide. Analysis of such a situation for $E = 44^\circ$ shows that,

(1) Whether measuring reflected sunlight (albedo), or emitted infrared radiation in an atmospheric window, a very significant proportion of the radiation observed will come from the sides, rather than the tops, of the clouds.

(2) The ground will not be visible to the sensor in lanes between the cloud lines and, if there are no breaks along the individual cloud lines, the scattered-to-broken field of clouds will appear overcast.

From spatial resolution considerations alone, a sensor with a very restrictive field of view would be highly desirable. However, the field of view of most non-imaging systems results from trade off compromises between spatial resolution and the minimum energy level which can be detected by the detector. By narrowing the field of view, the target area viewed by the sensor is reduced. As a consequence, the sources of radiant energy contributing to the energy which is incident on the detector are similarly decreased. Depending on the target radiation characteristics and the detectivity of the detector, there is a limit to the spatial resolution which can be practically achieved.

Furthermore, in future advanced sensory systems, practical resolutions (when they can approach the order of 0.1 mile or better) may be limited by the increased quantities of data to be processed as resolution improves.

6.3.2 Distortions Introduced by Sensing and Recording Systems

In addition to the distortions and degradations introduced by the curvature of the earth, about which little can be done, there are additional distortions introduced by the sensing and recording systems for which corrections are often omitted. These can best be discussed by analyses of a few typical systems.

Several present and prospective satellite sensors operate by scanning, with a fixed angular field of view, at a constant angular rate around an axis which is parallel to the satellite roll axis. This method of observation increases the effective areal coverage of the sensor. Examples include the Nimbus High Resolution (HRIR) and Medium Resolution (MRIR) Infrared Radiometers. Various image dissectors which are now under development may have somewhat similar characteristics.

In such a system, it is to be noted that the scan line across the earth is perpendicular to the heading line, not to the subpoint track, (neglecting the usually negligible effect of the advance of the satellite during a single scan).

Figure 36 can be used in the analysis of this type of system. Equations (53) and (97) provide the relationships between B and n . Thus, Equation (99b) defines the degradation of resolution, in the direction parallel to the scan, as nadir angle increases.

Because the line-of-sight distance from the satellite sensor to the earth, ρ , increases with increasing nadir angle, there is also a (somewhat lesser) degradation of resolution in the direction parallel to the heading line and perpendicular to the scan. Figure 14 (Section II) shows that

$$\rho = \frac{Y}{\sin n} \quad (103)$$

and so, from Equation (65)

$$\rho = \frac{R \sin B}{\sin n} \quad (104)$$

If Δn is the angular resolution of the sensor, ΔB_0 is the ground resolution at the subpoint, from Equation (98); and Δb_n is the resolution in degrees of great circle arc in the direction parallel to the heading line, then

$$\frac{\Delta b_n}{\rho} = \frac{\Delta B_o}{h}, \text{ or}$$

$$\Delta b_n = \frac{R \Delta B_o \sin B}{h \sin n} \approx \frac{\Delta n \sin B}{\sin n} \quad (105)$$

To demonstrate the increase of Δb_n as n increases, note that when $n = 0$, $\rho = h$, and $\Delta b_n = \Delta B_o$. When $n = n_H$, Equation (49) (Section II) can be used to determine that

$$\begin{aligned} \Delta b_{n_H} &= \frac{R \Delta B_o \sin B_H}{h \sin n_H} = \frac{\Delta B_o R \sqrt{1 - \left(\frac{R}{R+h}\right)^2}}{h \left(\frac{R}{R+h}\right)} \\ &= \Delta B_o \sqrt{1 + \frac{2R}{h}} \end{aligned} \quad (105a)$$

$\sqrt{1 + \frac{2R}{h}}$ is obviously always greater than one.

Similarly, from Equation (104)

$$\rho_H = \sqrt{h^2 + 2Rh} \quad (105b)$$

demonstrating, as would be expected, that $\rho_H \geq h$.

When a sensor of this type is designed, it is customary to adjust the resolution and the scan rate, in association with the satellite ground velocity, v_g , so that there will be no overlap or underlap along the subpoint track. Let B_S be the distance (in degrees of great circle arc) along the subpoint track. Then

$$v_g = \frac{2 \pi R}{360} \left(\frac{dB_S}{dt} \right) \quad (106)$$

For no overlap or underlap at the subpoint, the scanner will complete one rotation when B_S changes by an amount ΔB_o , and the change of nadir angle of the scanner must be

$$\frac{dn}{360^\circ} = \frac{dB_S}{\Delta B_o} \quad (107)$$

Accordingly,

$$\frac{dn}{dt} = \frac{(360)^2 v_g}{2\pi R(\Delta B_o)} \approx \frac{(360)^2 v_g}{2\pi h(\Delta n)} \quad (108)$$

where

dn/dt is in degrees per second

Δn is in degrees

v_g is per second and in the same length units as h .

Obviously, from Equation (79), there is then increasing overlap between such scan lines as n or B increase.

When recording the data from such a scan,³⁴ one common practice is to use a flat-film which passes under a rotating scanner (which scans perpendicular to the film advance). The rotating scanner serves as an analog of the satellite sensor, and the moving film serves as an analog of the satellite motion over the earth.

Let

- X = distance measured across the film, from the centerline
- α = angle of rotation of the recording scanner, also measured from the film centerline
- Y = distance from the film plane to the axis of rotation of the scanner (a constant)

Then

$$\frac{X}{Y} = \tan \alpha \quad (109)$$

$$\frac{dX}{dt} = Y \sec^2 \alpha \frac{d\alpha}{dt} \quad (109a)$$

Using Equation (91) and letting $\frac{dB}{dn} = M = \frac{\cos n}{\sqrt{\left(\frac{R}{R+h}\right)^2 - \sin^2 n}} - 1$,

$$\frac{dB}{dX} = M \frac{dn}{dX} = M \left(\frac{dn}{dt} \right) \left(\frac{dt}{dX} \right),$$

or substituting for (dt/dX) ,

$$\frac{dB}{dX} = M \left(\frac{\cos^2 \alpha}{Y} \right) \left(\frac{dn}{dt} \right) \left(\frac{dt}{d\alpha} \right) \quad (110)$$

In practice, the satellite and recorder scanners are synchronized to scan at the same rate, and to be vertical at the same instant (i.e., $dn/dt = d\alpha/dt$ and $n = \alpha$). Then

$$\frac{dB}{dX} = M \left(\frac{\cos^2 n}{Y} \right) \quad (110a)$$

In a second common recording practice, a recorder stylus moves at a constant rate in the direction perpendicular to the advance of the recording paper. In this case,

$$\frac{dX}{dt} = K' \quad (\text{a constant})$$

Again, synchronization occurs giving

$$\frac{dB}{dX} = KM, \quad (111)$$

where

$$K = 1/K' (dn/dt) \text{ is a constant.}$$

In both Equations (110a) and (111), dB/dX is the scale of the recorded data in the direction perpendicular to the movement of the satellite (i.e., cross-track). Figure 37 shows how these recording systems compress the scale as nadir angle increases.

Figure 38 is perhaps a more vivid illustration. It is a 5° latitude-longitude grid³⁵ for one such sensor (Nimbus II HRIR/DRIR) prepared for the type of recorder where $dX/dt = \text{a constant}$. Note that the areas near the edges of the data are badly compressed (or foreshortened). A similar, although somewhat less, compression also occurs^{40, 34} for the recorder where $dX/dt = Y \sec^2 \alpha \, d\alpha/dt$.

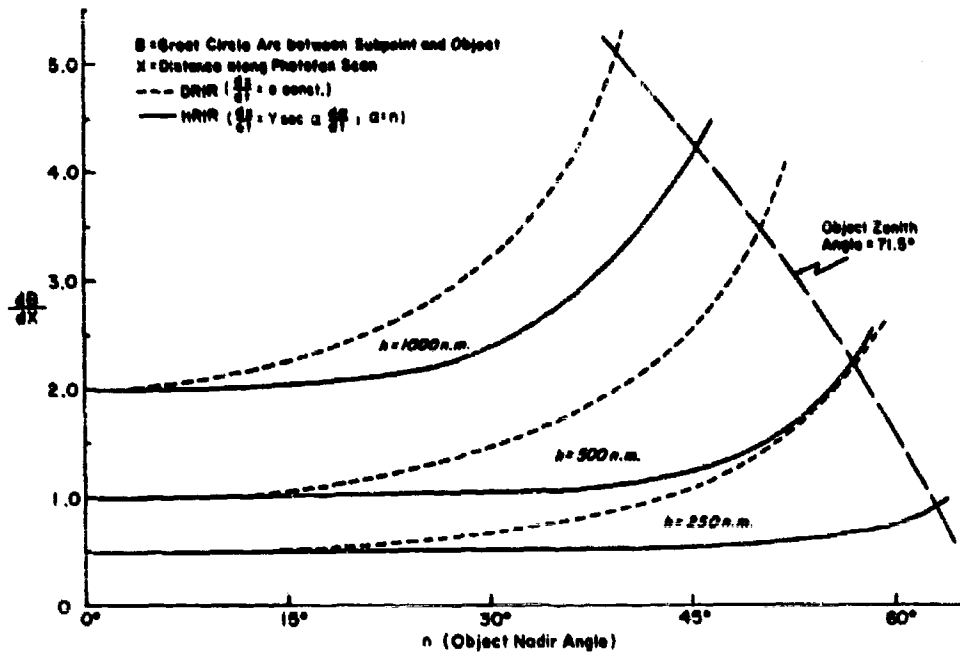


Figure 37. Derivative of Earth Scan with Respect to Recorder Scan (i.e., scale) as a Function of Object Nadir Angle, for Nimbus II

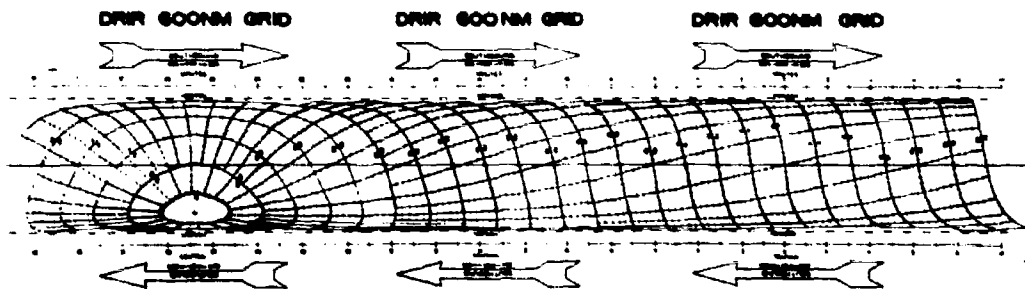


Figure 38. Reduced-Scale DRIR Latitude-Longitude Grid

Methods of rectifying the data from such satellite scanners during their recording can readily be developed.³⁴ Figures 39a and b show relatively crude rectifications of Nimbus I HRIR data, prepared by a simple photographic technique (the unrectified presentations are those for a system where $dX/dt = Y \sec^2 \alpha \, dn/dt$). Far better mechanical or electronic procedures for such rectifications have been proposed.

It is to be noted, however, that:

- (1) While rectification is highly desirable (since it provides a uniform scale, a better appearance, and congruency to standard map projections), it cannot improve the degradation in resolution with increasing nadir angles that are inherent in the satellite observing geometry.
- (2) Rectification can never be carried all the way to the horizon, since dB/dn becomes infinite at the horizon. A somewhat arbitrary cutoff point must be chosen. The cutoff at $\alpha = 71.5^\circ$ used in Figure 37 is based on experience with TIROS data, which indicated a 58° object nadir angle (at a satellite altitude of 400 n.mi.) to be a reasonable estimate of the limit of consistently useful data.

6.4 Imaging Systems

In imaging sensor systems, such as the AVCS and APT television systems of Nimbus and ESSA satellites, the sensor field of view does not determine its spatial resolution. It only determines its instantaneous coverage, i.e. the region of the earth over which simultaneous observations can be made at a given time.

In a photographic camera, the spatial resolution is determined by the ability of the lens system to image point sources onto the photographic film, and by the ability of the chemicals on the film to reproduce these imaged sources. However, in most satellite imaging sensors, the detectors on board the satellite are not photographic films since films must be physically retrieved. The more frequent form of a satellite imaging sensor is the television camera, such as those employed in the AVCS and APT systems. While a television camera employs an optical system similar to that of a photographic camera, its spatial resolution is generally not as good as that of a camera using similar optics and is not limited by the optics.

The reduced spatial resolution is due to the fact that with a television camera, the image is formed electronically on the face of a photoconductive tube such as a vidicon (Fig. 40). An electron beam, in the tube, then scans this image

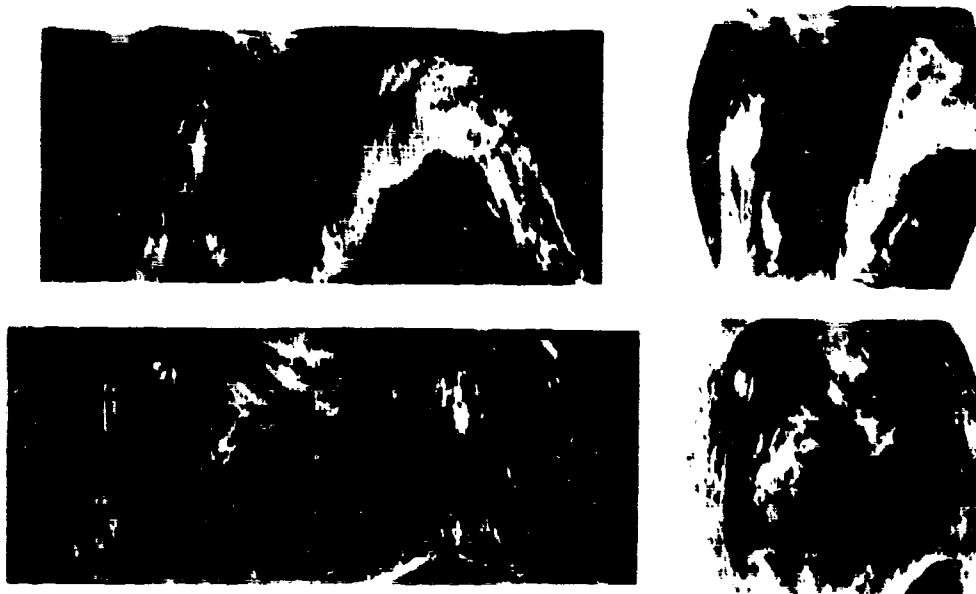


Figure 39b. Unrectified (Top) and Rectified (Bottom) Portions of Orbits 252 and 253, Nimbus I, HRIR

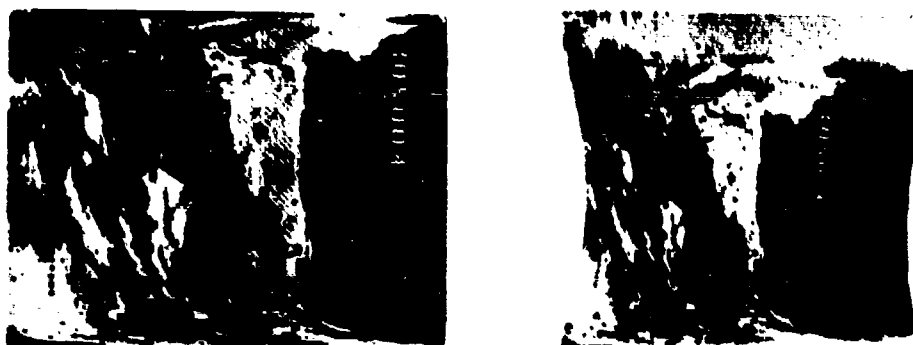


Figure 39a. Unrectified (Top) and Rectified (Bottom) Portion of Orbit 207, Nimbus I, HRIR

along discrete lines known as rasters (See Widger, ⁶ p. 71-76 for a fuller discussion). The electrical signal output of the tube is proportional to the instantaneous conductivity of a small area of the image defined by the resolution of scanning electron beam.[†] As a consequence, the resolution of a television camera is not limited by the optics, but by the scanning electronics. In addition, the resolution is a function of the position on the image relative to the optical axis of the systems. The significant resolution effects for a television system are discussed in the following paragraphs.

6.4.1 The Television Camera

To practically discuss the case of a television camera sensing system, operating from a satellite and viewing the earth, it is desirable to first choose a relatively simple case and to postpone the several probable additional complexities until later.

Figure 41 shows a camera whose optical axis is assumed vertical (whose sensitive surface is therefore parallel to the earth at the subpoint). It is also assumed that the camera has a perfect non-distorting lens. f , the distance from the lens to the sensitive surface, is the focal length of the camera system. Actually, $f \ll h$, but f is greatly exaggerated in the figure for clarity of illustration.

Let the sensitive surface be a square C units of length on a side. The cross-track and along track coverage provided by a single frame is then given by

$$\tan n_c = \frac{C}{2f} \quad (112)$$

where n_c is the nadir angle at the midpoint of a side of the image. Using Equation (54), B_c can be determined from n_c , and the coverage is $2B_c$.

Let the sensitive surface to be scanned along l parallel raster lines, at l points per line (a square raster). (Although the scan along any raster line is continuous, for convenience let it be made up of l discrete points.) If the resolution of the raster scan is ΔC ,

$$C = l \Delta C$$

[†] The resolution of this electron beam can be thought of as analogous to the resolution of the instantaneous field of view of a non-imagery scanning sensor.

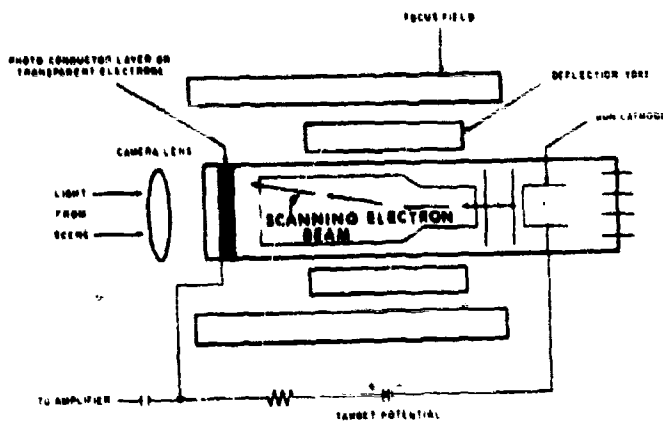


Figure 40. Schematic of a Television Camera System

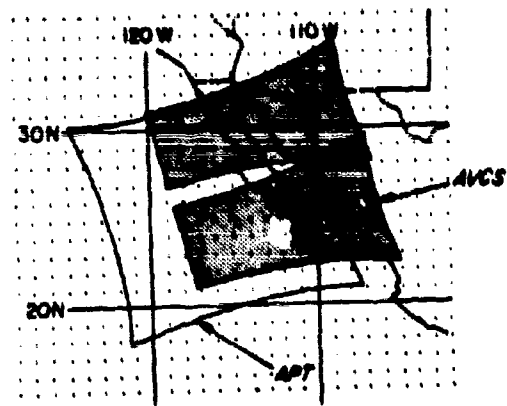


Figure 42. APT vs. AVCS Coverage

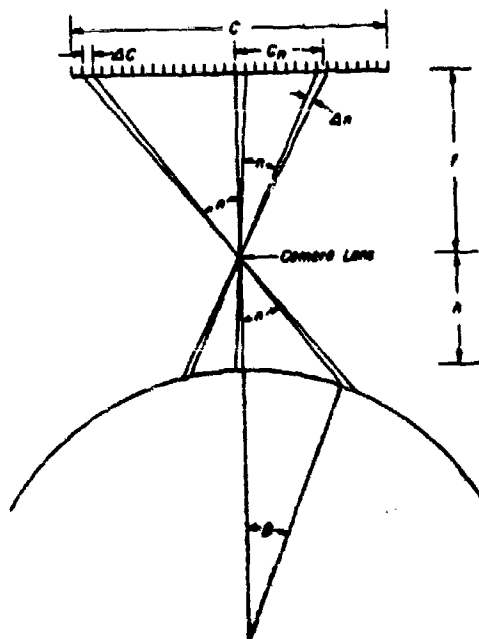


Figure 41. Television Camera Viewing Geometry

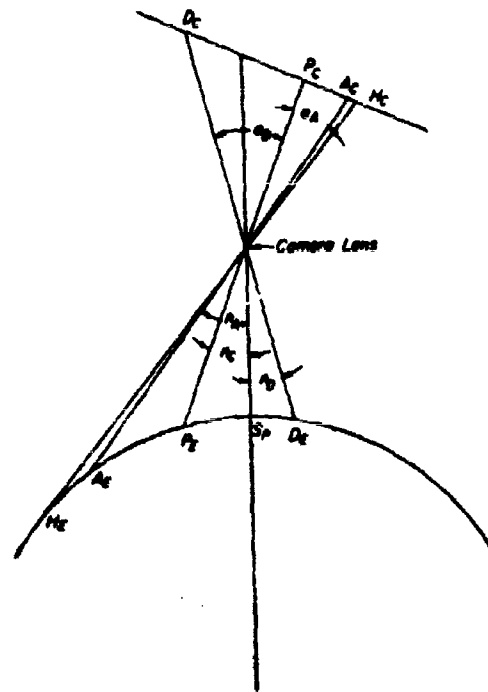


Figure 43. Geometry of a Television Camera Viewing at Nadir Angles other than Zero

f , C , ℓ , and ΔC are assumed to be design constants for any single camera system. Let it be assumed further that the scene imaged on the sensitive surface is reproduced without geometric distortion in subsequent parts of the television electronics, transmission, and recording system.

Figure 41 also shows that the distance of an image point on the sensitive surface from the center, C_n , is given by

$$C_n = f \tan n \quad (113)$$

or

$$dn = \frac{\cos^2 n}{f} dC_n \quad (114)$$

Let Δn be defined as the angular resolution of a ray corresponding to ΔC , then Equation (114) leads to

$$\Delta n = \frac{\cos^2 n}{f} \Delta C \quad (114a)$$

Since ΔC is a design constant, Δn decreases as n gets larger and the effect of the camera geometry alone would be to improve the resolution in the areas of the image farthest from the image center.³⁸

The overall resolution of the image can be determined by substituting Equation (114a) in Equation (99b) to obtain,

$$\Delta B_n = \left[\frac{\cos n}{\sqrt{\left(\frac{R}{R+h}\right)^2 - \sin^2 n}} - 1 \right] \frac{\cos^2 n}{f} \Delta C \quad (115)$$

The effect is tabulated on the next page, where a 500 n.mi. satellite is again assumed. However, instead of the $\Delta n = 2^\circ$ for $n = 0$ used previously, a $\Delta n = 0.2^\circ$ for $n = 0$ is used.

It is obvious that the effect of the camera geometry is to significantly decrease the rate of resolution degradation with nadir angle as compared to that for the scanner.

n	ΔB_n (scanner)	ΔB_n (camera)	ΔB_n (scanner)	ΔB_n (camera)
	(Degrees, Great Circle Arc)		(Nautical Miles)	
0	0.020	0.020	1.2	1.2
15°	0.040	0.037	2.4	2.2
39°	0.060	0.036	3.6	2.2
46°	0.080	0.039	4.8	2.3
49°	0.100	0.043	6.0	2.6
56°	0.200	0.062	12.0	3.7

To obtain the projection geometry of the recorded image, note that Equation (113) is the same form as Equation (109a) if $X = C_n$, $Y = f$, and $n = \alpha$. Since Equation (97) applies to any satellite viewing system, Equation (110a) can be used to determine the geometrical characteristics of the recorded picture, rewriting it now in the form

$$\frac{dB}{dC_N} = M \left(\frac{\cos^2 n}{f} \right) \quad (116)$$

where

$$M = \frac{\cos n}{\sqrt{\left(\frac{R}{R+h}\right)^2 - \sin^2 n}} - 1$$

C_n is measured as the radial distance from the center of the recorded image.

In general, the sensitive and recording surfaces are square, so C_n has its maximum value at the corners where

$$C_n \text{ max} = \frac{\sqrt{2}}{2} C \quad (117)$$

Because of the relationships shown in Equation (116) and (117), the area shown in the square image does not represent a square area on the earth's surface, but rather one with a pin-cushion shape, as is illustrated by the APT coverage in Figure 42. The large, unshaded area is that viewed by the Nimbus I APT, a camera oriented with its optical axis vertical.

The above discussions can be generalized to the case of a camera whose axis is at an angle to the vertical. In Figure 43

- $P_E P_c$ = camera optical axis
- P_E = camera principal point on earth
- P_c = camera principal point on image (image center)
- n_c = nadir angle of camera axis

From Equation (53) in Section II, it is obvious that the distance between S_p and P_E , B_p , is given by

$$B_p = \text{arc sin} \left[\left(\frac{R+h}{R} \right) \sin n_c \right] - n_c \quad (118)$$

A distance on the film from the principal point (picture center) in the plane of Figure 43, C_n , is given by Equation (115) as

$$C_n = f \tan a \quad (119)$$

Again in the plane of Figure 43, the object nadir angles are given by

$$\left. \begin{aligned} n_A &= a_A + n_c \\ n_D &= a_D - n_c, \text{ or} \\ n &= a \pm n_c \end{aligned} \right\} \quad (120)$$

For points other than those in the plane of Figure 43, it is obviously necessary to use still more complex relationships, but it is apparent that there is still a unique relationship between each point on the image and its counterpart on the earth.³⁷

Again constraining the analysis to the plane of Figure 43, Equations (63), (119) and (120) lead to the relationship

$$\frac{dB}{dC_n} = \frac{M}{f} \left[\cos^2 (n \mp n_c) \right] = \frac{M}{f} \left[\cos^2 n \right] \quad (121)$$

with more complex relationships applying outside the plane of Figure 43.

Still again staying in the plane of Figure 43, the resolution of points across the image can be determined by reference to Equation (115), which must be rewritten as

$$\Delta B_n = \left[\frac{\cos n}{\sqrt{\left(\frac{R}{R+h}\right)^2 - \sin^2 n}} - 1 \right] \frac{\cos^2 \alpha}{f} \Delta C \quad (121a)$$

Since the quantity in the brackets is a minimum when $n = 0$, while $\cos^2 \alpha$ decreases as α increases, the best camera resolution occurs when the camera is tilted so the satellite subpoint is in the foreground and recorded near an edge or corner of the image.³⁸

The shaded areas in Figure 42 show the areas on the earth imaged by a camera with a square sensitive surface and an optical axis nadir angle of 35° .

Horizons provide an excellent basis for determining attitude. This can be shown using Figure 43. Let $H_E - H_C$ be the ray from the horizon. Then,

$$n_H = n_c + \alpha_H$$

$$\tan \alpha_H = \frac{C_H}{f}$$

$$\sin n_H = \frac{R}{R+h}$$

$$n_c = \arcsin \left(\frac{R}{R+h} \right) - \arctan \left(\frac{C_H}{f} \right)$$

Since R , h , and f can be assumed to be known, a measurement of C_H (the distance from P_c to H_c) permits the nadir angle of the camera axis to be easily calculated.^{37c}

From the preceding discussions, it should be obvious that to determine the geographical positions (ϕ, λ) of all points on a satellite picture the following must be known:

Latitude of satellite subpoint, ϕ_o

Longitude of satellite subpoint, λ_o

Height of satellite, h

Nadir angle of camera optical axis, n

Asimuth of the principal line, α , which is the line joining the satellite subpoint and the intersection of the camera optical axis and the earth's surface (the principal point on the earth)

Camera focal length, f

Coordinates of points on the image, x and y .

From these data, the latitude, ϕ , and longitude, λ , of any point on the image can be determined. Or, conversely, the coordinates on the image of specified intersections of latitude and longitude can be determined, and a latitude-longitude grid can be constructed at the scale and perspective of the image. In either way, the data in the image can be related to its position on the earth, and to other data whose locations are known.

One set of expressions relating these parameters is given as Equation (122). For obvious reasons, such calculations are almost always made only with the aid of high speed computing equipment. Most commonly, the computers produce either:

- (1) a latitude-longitude grid drawn to the perspective and scale of the satellite image as recorded, or
- (2) an input to the recording equipment, which causes latitude-longitude grid points to be recorded at the appropriate positions on the image^{39, 40} (Figs. 39a and 39b provide examples, although for the scanning HRIR data rather than a television picture).

It is also obvious that, with appropriate ancillary mapping programs, the computers can also use expressions equivalent to Equations (122) to rectify satellite television signals to almost any desired standard projection. There are, however, other problems in rectification that are not discussed here; as a single example, the filling in of areas when rectification leads to a divergence of the parallel raster pattern of the original sensor scan.

For geographic location of satellite data when computers are not operationally available, the computers are used in advance to prepare sets of generalized grids which can be manually used in operational practice.^{41, 42, 35, 42} Figure 38 is such a grid.³⁵ Note that the longitudes are unlabeled and must be determined. In fact, when such a grid is placed on the data, the longitude lines on the grids will usually represent non-integral values of longitude. In another case (the system used during the early history of TIROS),^{41, 42} it was necessary to use a combination of a set of arbitrary Canadian grids drawn to the perspective of the satellite view, a related transfer grid, and a properly chosen base map of the same scale as the transfer grid.

(122)

$$x = f \left\{ \frac{\cos \phi \left[\cos (\lambda - \lambda_0) \left\{ -\sin \alpha \sin \phi_0 \right\} + \sin (\lambda - \lambda_0) \left\{ \cos \alpha \right\} + \sin \phi \left\{ \sin \alpha \cos \phi_0 \right\} \right]}{\cos \phi \left[\cos (\lambda - \lambda_0) \left\{ \cos \phi_0 \cos \eta + \cos \alpha \sin \phi_0 \sin \eta \right\} + \sin (\lambda - \lambda_0) \left\{ \sin \alpha \sin \eta \right\} + \sin \phi \left\{ \sin \phi_0 \cos \eta - \cos \alpha \cos \phi_0 \sin \eta \right\} - (R + h) \cos \eta \right]} \right\}$$

$$y = f \left\{ \frac{\cos \phi \left[\cos (\lambda - \lambda_0) \left\{ \cos \phi_0 \sin \eta - \cos \alpha \sin \phi_0 \cos \eta \right\} + \sin (\lambda - \lambda_0) \left\{ -\sin \alpha \cos \eta \right\} + \sin \phi \left\{ \sin \phi_0 \sin \eta + \cos \alpha \cos \phi_0 \cos \eta \right\} - (R + h) \sin \eta \right]}{\cos \phi \left[\cos (\lambda - \lambda_0) \left\{ \cos \phi_0 \cos \eta + \cos \alpha \sin \phi_0 \sin \eta \right\} + \sin (\lambda - \lambda_0) \left\{ \sin \alpha \sin \eta \right\} + \sin \phi \left\{ \sin \phi_0 \cos \eta - \cos \alpha \cos \phi_0 \sin \eta \right\} - (R + h) \cos \eta \right]} \right\}$$

Where,

x, y	film plane coordinates
f	focal length
h	satellite height
R	earth radius
ϕ_0	latitude of subpoint
λ_0	longitude of subpoint
α	azimuth of principal line, here taken as counter-clockwise from north
η	radial angle
ϕ	latitude of point in image
λ	longitude of point in image

6.4.2 Distortions and Degradations in a Television Camera System

In the previous section (6.4.1), the geometric factors of a perfect satellite television camera scanning the earth were investigated. This section will consider some of the more frequent and significant distortions and degradations that may occur in a real camera and/or in the electronics used to process, transmit, record, and display the image.

6.4.2.1 Optical Distortions

Optical distortions may occur at the television camera lens, or at the optical elements between the ground kinescope and the recording camera.

The most common optical distortion is the radial or symmetrical (about the optical axis) distortion. In such distortions, light rays entering the camera are bent by non-uniform amounts which vary as a function of the angle between the ray and the optical axis, n was set equal to α , where n is the nadir angle of view and α is the angle (inside the camera) between the ray and the optical axis. For radial distortions,

$$\alpha = f(n)$$

where $f(n)$ may be a relatively complex expression. Once the relationship is determined, however, it can be used to appropriately modify the relationships between the location of a point on the earth and its position on the image plane.

Radial distortions are usually unavoidable design characteristics of the lens system, and are normally encountered only in comparatively wide-angle lens. Non-radial distortions are usually due to defects in the lens system and must often be handled on a point-by-point basis rather than as a tractable analytical expression. Fortunately, they can usually be avoided by proper quality control in lens system selection and testing.

Optical distortions in satellite cameras are determined, prior to launch, by the photographing of suitable test pattern targets and analyses of these photographs. Optical distortions in the recording systems are determined by photographing suitable test patterns generated on the CRT of the recording kinescope. Furthermore, the ground recording systems are accessible if adjustments or replacements are found desirable.

The TIROS wide-angle cameras had a relatively distorting lens (Elgeet) with the distortion becoming appreciable (for operational purposes) beyond a radius from the center of the picture about halfway from the center to a corner, and rapidly increasing from there outward. The sense of the distortion was to make features near the picture edges appear more compressed in the radial direction, and closer to the picture center, than they would without distortion. One consequence of this distortion was to accentuate the curvature of the horizon when it appeared in the picture. The distortion of a typical TIROS wide angle lens⁴¹ is shown in Figure 44, where H is the actual distance from the center measured on a picture (of appropriate scale) and H' would be the distance of the same point in the absence of distortion. The insert shows how a rectangular grid becomes distorted when photographed through a typical TIROS wide angle lens.

Different lenses have, fortunately, been used in other meteorological satellite camera systems. They have been principally the Tegea Kinoptik (used in the TIROS medium resolution, the Nimbus APT, and the TOS (or ESSA) APT and AVCS cameras) and a 16.5 mm lens used on the Nimbus AVCS. These lenses are essentially non-distorting, with a distortion of only about 1-10% even near the limits of the image.

6.4.2.2 Electronic Distortions

Electronic distortions result from such causes as non-uniformity of the scanning deflections in either the satellite vidicon camera or the kinescope cathode ray tube, or wow and flutter in the tape recorders. The most common distortions include (see Fig. 45)

- Aspect ratio: One dimension of the image shorter than the other
- Keystoning: A compression of the image along one side
- Barrel: A compression of the corners of the image
- Pincushion: An expansion of the corners (or a compression near the middle of the sides) of the image
- Tearing: Some of the lines of the scan shifted to one side.

Distortion patterns far more complex than these can and frequently do exist. Combinations of two or more of the above patterns can occur. Images may be distorted in one area and not another, or in varying ways in different parts of the image. Minor or significant deviations of the scan patterns may be superimposed on parts or all of any primary distortion pattern.

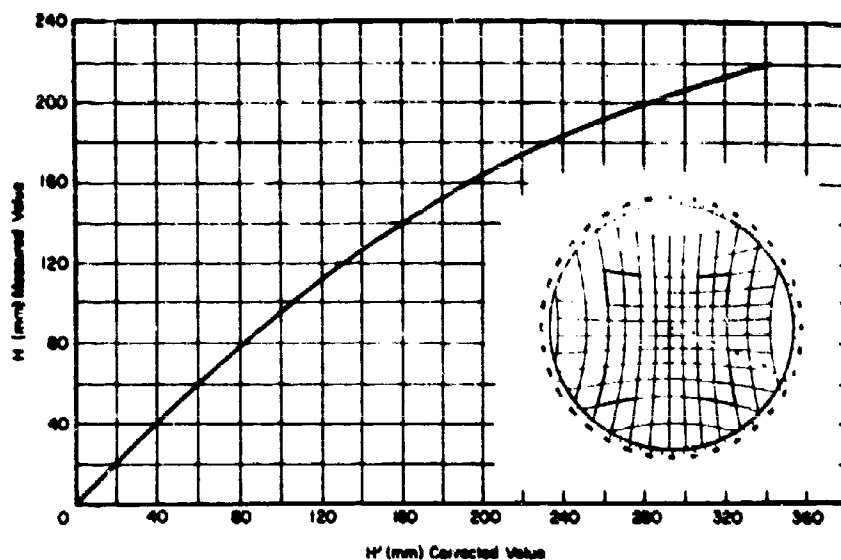


Figure 44. Correction for TIROS Lens Distortion

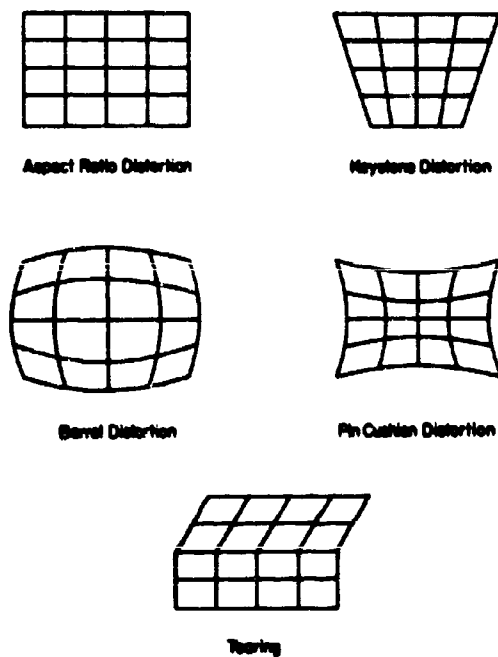


Figure 45. Types of Electronic Distortions

Fortunately, electronic distortions can be detected and determined from the fiducial marks. Fiducial marks are regular patterns of lines etched onto the sensitive surface and there merged with the image. Accordingly, any electronic distortions in the image are reflected in the positions in the image of the fiducial marks. (However, since the fiducial marks are behind the satellite optical system, they cannot be used to detect optical distortions in the satellite camera lens.)

Figure 46 shows the pattern of fiducial marks used on the AVCS and APT cameras.

The feasibility of and complexities in correcting for electronic distortions vary with their type, extent, and complexities. Linear distortions (aspect ratio and keystoneing) usually do not present an undue problem. Non-linear distortions frequently require complex processing and corrections, and would not be attempted unless the errors are extreme and/or the accuracy requirements are pressing. (It is to be noted, however, that there is seldom a valid reason for accepting significant electronic distortions in the first place, since they can almost always be prevented by suitable designs and/or adjustments of the equipment.)

6.5 Contrast Considerations

The interpretation of satellite data is based on the interpretation of the spatial variations in the parameter displayed. Depending on the display method, these variations could be variations in grey scale, as in the case of television pictures, or they could be voltage variations as shown on a recorder chart. The parameter displayed is proportional to the energy measured. While the term contrast is most appropriate in the description of the gradient of brightness on a photograph, it can be applied, as it is here applied, to rate of change in magnitude of any displayed parameter.

In an ideal situation, the contrast as exhibited in the displayed data should be directly related to the inherent contrast of the target elements at the time of measurement. However, even in the absence of atmospheric contrast degradation effects, which can be quite substantial, the various sensor system components introduce effects which can degrade the inherent contrast. In fact, a satellite sensor system, such as that shown in Figure 33, can be considered to be a series of consecutive transfer functions whereby a signal input in one form is converted into an output in another required form. The combination of the individual transfer functions corresponding to each of the components is the transfer function of the system as a whole. This system transfer function then determines the ability of the system to adequately reproduce the inherent contrast of the target.

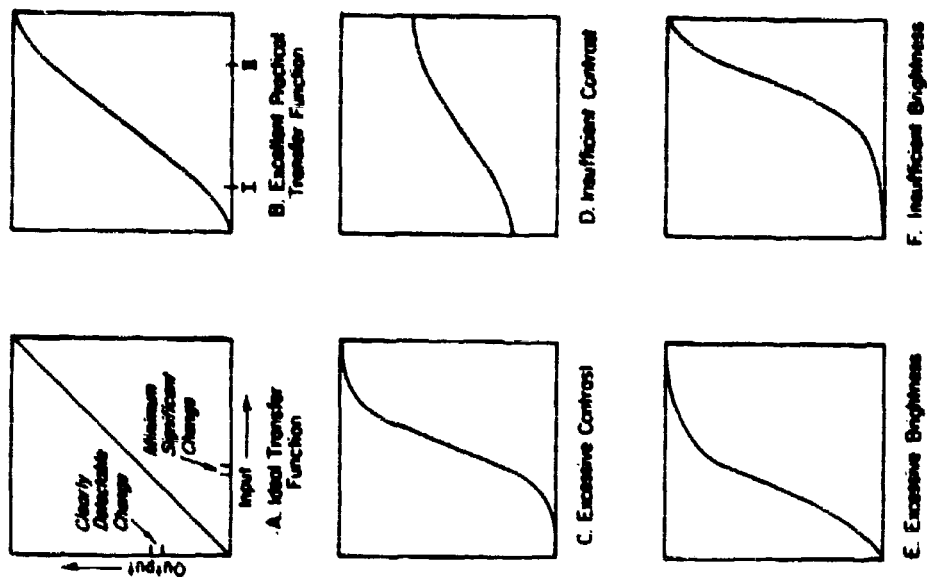


Figure 47. Transfer Functions

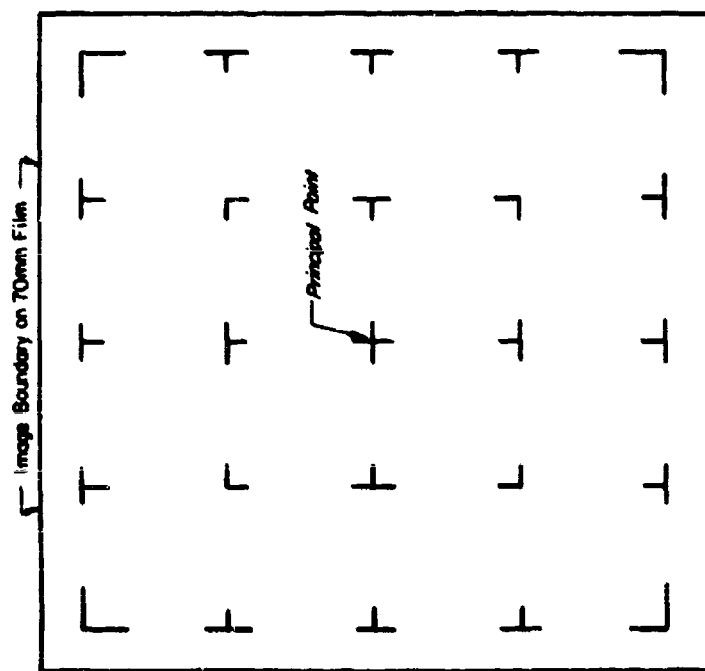


Figure 46. Nimbus AVCS Fiducial Matrix

In order to illustrate the relations between the transfer functions of a system and its ability to reproduce contrast variations, the case of a satellite television camera system is chosen as example.

The set of transfer functions in a satellite television observing system includes at least the following, where each successive output in the list becomes the input to the next stage:

1. Scene illumination, to
2. Electron density on sensitive surface, to
3. Camera output voltages, to
4. Transmission frequency or amplitude variations, to
5. Receiver output voltages, to
6. Kinescope CRT (cathode ray tube) illumination, to
7. Recording camera film response, to
8. Film density after processing.

A more complete list could be prepared by including:

- a. Voltages to magnetization of a recording tape, and vice versa, if one is used, between 3 and 4 and/or between 5 and 6.
- b. Each stage of electronic amplification between 3 and 4 and between 5 and 6.
- c. Successive photographic steps as prints or copies are made.
- d. As an alternate to 6, 7, and 8: Analog signal to digital input conversion if the data are to be computer processed.

An ideal transfer function would be linear over the entire range of interest, and any significant change of the input would produce a clearly detectable change in the output (see Fig. 47a). No practical system reaches this degree of perfection. Rather, the transfer function will have something of an S-shape (Fig. 47b). There will be a threshold level (lower left) below which increase in the input produces no detectable change in the output, and a saturation level (upper right) beyond which the output has little or no increase regardless of the increase of input. Excellent results can be achieved with a transfer function like that in Figure 47b, however, if the range of likely inputs can be limited to the essentially linear part of the curve, say between I and II in Figure 47b.

The slope of the transfer function curve (the rate of change of output to change of input) is known as its gamma. Ideal gammas are usually those near one, when appropriate units are used for the input and output.

Too large a gamma leads to excessive contrast (Fig. 47c), where most of the change of output occurs over a small range of input. The threshold and saturation levels extend over much of the input range and obliterate small input changes where the input level is low or high. Too small a gamma leads to insufficient contrast (Fig. 47d), with a large change in input leading to only a small change in output. For example, a photograph resulting from a system with a small overall gamma would be flat, with no areas either very dark or bright.

In some cases, a gamma which is somewhat too large (or small) in one stage of a system can be counteracted by a gamma with an opposite tendency (of appropriate magnitude) in a later stage.

Figure 47e shows a transfer function leading to excessive brightness in the output, with most of the upper range of the input leading to output saturation. Such a transfer function will obliterate details in an overcast layer, but may be used to intensify ground detail. Figure 47f illustrates the reverse situation, where the entire lower range of input is near or below the output threshold. This will usually obliterate ground detail and clouds of low brightness, but may be used to emphasize differences in cloud covered areas.

In a satellite observing system, the vital factor is the overall transfer function relating the scene observed to the recorded image. It is, of course, influenced and to at least some extent limited by each subsidiary transfer function. A poor transfer function at any one stage can seldom be completely compensated for at a later stage, especially when the output is below threshold or above saturation.

Proper transfer functions require:

1. Proper design and prelaunch setting of the satellite equipment
2. Proper design, and appropriate checking and adjusting of the ground electronics
3. Proper selection and control of the recording film and its processing.

Proper transfer functions are necessary for a good qualitative appearance of the image, and essential if any quantitative use is to be made of the image brightnesses. Reference 44 describes in some detail the steps that were necessary for quantitative analysis of the TIROS pictures.

As a considerable assistance to quantitative analysis, Nimbus incorporates a calibrated step-wedge gray scale in the AVCS vidicon system. This step wedge appears in each picture as a narrow band across the top. (See Fig. 48).

The grey scale has 15 steps of relative luminance in increments of $\sqrt{2}$, giving a potential dynamic range of $2^{7.5} = 175$. This is somewhat beyond the capabilities of the vidicon system to reproduce linearly. The actual behavior of the vidicon-modulator-demodulator chain is illustrated in Figure 49, which shows the voltages measured at the input terminals of the ground kinescope during scans across the grey scale wedges while Nimbus I was in actual flight. The three photographs in Figure 49 each provide the transfer function between the brightness scale of the grey wedge (abscissa) and the camera output voltage (ordinate).

Black is at the left (bottom), and white toward the right. At the end of a sweep, the retrace goes to "blacker than black," followed by a synchronization pulse and the beginning of the next sweep.

It is seen that the transfer functions over the grey scale range are hardly linear, although camera B (the center camera) does a surprising job with only a moderate knee in the middle of the grey, and with perhaps the three whitest steps confused. The other two cameras saturate at both ends. Camera C exhibits a distinct knee, resulting in effectively abbreviated dynamic range. It must be concluded that the dynamic range achieved is below the design potential, and, what is even more significant, that the transfer function is quite an individual property of each vidicon. As yet, no success has been achieved in obtaining data indicating the extent to which a transfer function shows the same sort of variation from one area to another of the same vidicon tube.

The noise level appears alarming in these oscilloscope traces. However, the eye readily averages it over several lines, as does the persistence of the kinescope. The result is that on the final film, the grey steps are clearly visible in the reasonably sloped parts of the transfer characteristics.

Actual picture reproduction from Nimbus was initially hampered by the use of an automatic camera-processor system not intended for maintenance of sensitometric quality standards. This has effectively resulted in a further diminution of the dynamic range. The camera-processor was pressed into service when the planned wide range system failed to materialize. It has produced excellent results on subjects within a narrow dynamic range, such as terrain features.

NAVTRADEVCEEN 66-C-0031-1

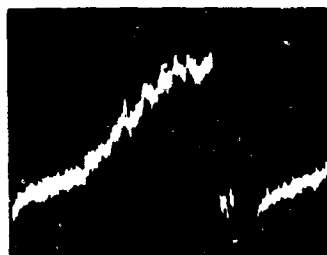


Grey scale wedge

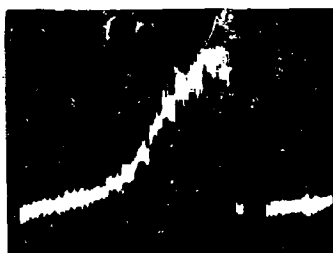
Figure 48. Nimbus AVCS Photograph with Grey Scale Wedge



Camera A



Camera B



Camera C

Figure 49. In-flight Calibrations of Transfer Functions of Nimbus I AVCS Cameras

Allied Research, under contract to NASA, has subsequently found suitable techniques for recording the full range of AVCS photography on film. They were aided in this endeavor by consultants from Itek. A sensitometrically controlled ground camera-processor system that will permit obtaining quantitative luminance values from Nimbus I and future AVCS photography has been established. The AVCS system will be used on Nimbus C, and on some of the TOS satellites. It may also appear on some of the ATS satellites.

While the above analysis of transfer functions was made in terms of a television system, the same type of analysis can be performed for any sensor system. With the HRIR sensor shown in Figure 34. For example, the primary input to the satellite radiometer is the effective radiance, \bar{N} . The calibrated output as received at the ground is converted to the Equivalent Blackbody Temperature, T_{bb} . Figure 50 shows the overall transfer function of the Nimbus I HRIR.

6.6 The Effects of Noise

One of the principle limitations to the sensitivity of a sensor system is noise. Noise may enter into a satellite system in a number of ways. It was shown in Sections IV and V that, depending on the types of measurements involved, radiation sources on the earth and in atmosphere can be significant sources of background noise. The effects of this type of noise can be minimized by spectral selection of the radiation measured by the sensor.

Noise can also be generated or picked up by the electronic components of the sensor system itself. Some of the more significant of these noise components are:

1. Electronic noise generated by the detector and the detection electronics due to random electron motions. This type of noise is probably what caused the broadening of the curves shown in Figure 49.
2. Natural or artificial radio noise signals acquired by the ground receiver. The TIROS I pictures frequently show noise bursts or lines (bright spots or lines on the image) due to the fact that the receiving antenna was near a public highway and would at times pick up radiation from automobile ignition systems.
3. Electrostatic or electromagnetic pickup. Many TIROS pictures show 60-cycle noise which leaked across from 60-cycle AC commercial power input. Sometimes this is loosely referred to as "cross-talk," which more properly refers only to leakage between similar transmission channels.

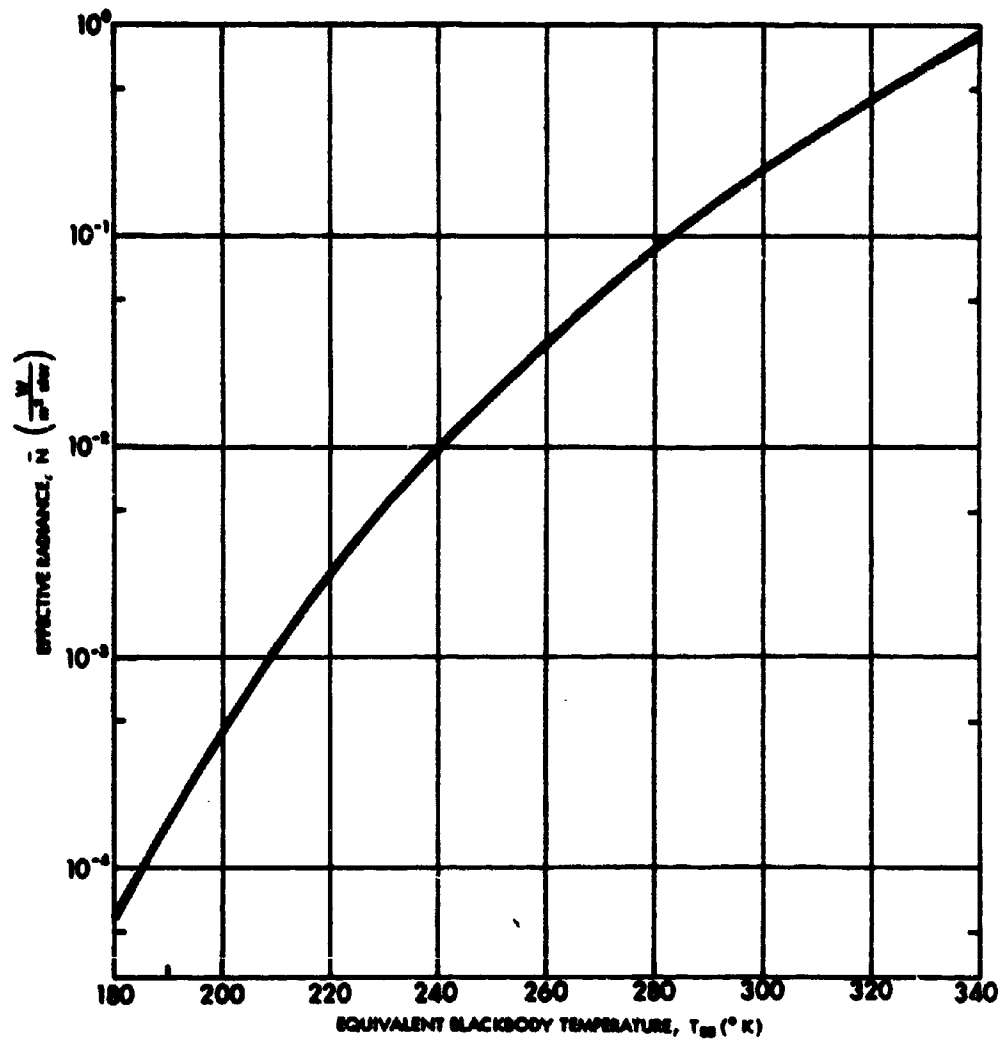


Figure 50. Calibration Curve of Nimbus HRIR

Signal cross-over within the spacecraft is also not uncommon. In their analysis of the data from the HRIR of Nimbus I, Fujita and Bandeen,⁴⁵ for instance, found that two types of noise are superimposed on the data. One was an oscillatory noise identified as a 200 cps, 500-millivolt peak-to-peak background level present on the HRIR power line in the spacecraft. The second was a periodic noise consisting of sharp spikes occurring at the rate of 16 per second. This second source of noise has not been identified but is suspected to originate on the spacecraft.

The effects of noise can be seen by examining the data analysed by Fujita and Bandeen. Figure 51a shows an analog trace of the HRIR output superimposed on the topography of the region over which the measurements were made. The HRIR measures surface temperature (see Section X). Accordingly, the amplitude variations in the analog trace should follow the variations in topography. Figure 51a shows, however, that the analog trace undergoes many more oscillations than can be accounted for by topographic variations. These additional variations in amplitude are due to the superimposed noise discussed earlier. It is seen, therefore, that noise can effectively degrade the data.

A technique often used to minimize the effects of this type of noise is to perform running means (or averages) of the data. Figure 51b shows a number of curves, each corresponding to a running mean using a different averaging interval (the intervals are in terms of degrees of scan angle of the HRIR system). It is seen that the curve using a one degree running mean represents the best compromise between the elimination of the oscillatory noise and preserving the real variations in the signal.

6.7 A Note On the Calibration of IR Sensors

Measurements obtained by satellite IR sensors are often specified in terms of a calibrated value known as effective (or equivalent) blackbody temperature, denoted by T_{bb} . Since the relation between T_{bb} and the radiant energy measured by the sensors is not immediately obvious, a short discussion of this relation is provided below.

A radiometer with a relatively narrow field of view essentially measures beam radiation, or radiance, propagating towards the sensor along its optical axis. In general, the radiance measured by such a sensor is given by

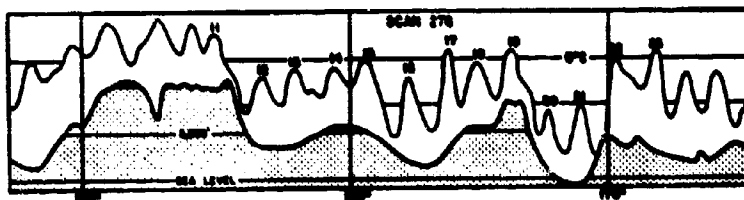


Figure 51a. Nimbus I HRIR Scan 276, Illustrating Oscillatory Noise Superimposed on the Data

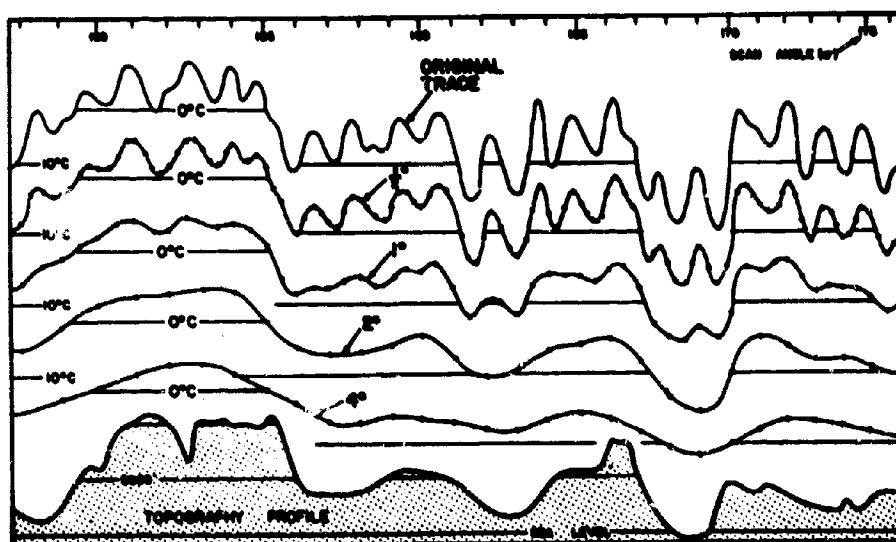


Figure 51b. Suppression of Oscillatory Noise by Computing Running Means

$$\bar{N} = \int_0^{\infty} N_{\lambda} \phi_{\lambda} d_{\lambda} \quad (123)$$

where

N_{λ} = spectral radiance of the energy incident on the sensor

ϕ_{λ} = spectral response of the sensor.

\bar{N} is known as the effective radiance measured by the sensor.

(NOTE: for a given distribution of N_{λ} , \bar{N} is dependent on ϕ_{λ}).

With the sensor viewing the earth from orbital altitudes, the spectral radiance received, N_{λ} , originates from a number of sources located in the atmosphere and on the surfaces of the earth. Consequently, it is often difficult to relate the effective radiance, \bar{N} , to any specific parameter.

It has been found convenient, especially in window measurements to express the measurement from orbit in terms of the temperature of a blackbody which, when it completely fills the sensor's field of view, would give rise to the same effective radiance. The relationship between effective radiance and blackbody temperature, for a given sensor, is unique. This may be seen by considering the form of Equation (123), appropriate to the case in which a blackbody completely fills the field of view of the sensor, given as follows

$$\bar{N} = \int_0^{\infty} N_{b\lambda}(T) \phi_{\lambda} d_{\lambda} \quad (124)$$

where

$N_{b\lambda}(T)$ is the spectral radiance of a blackbody at temperature T .

Since $N_{b\lambda}$ is uniquely related to temperature according to Planck's Law, and for a given sensor, ϕ_{λ} is fixed, \bar{N} is also uniquely related to the temperature of the blackbody viewed by the sensor. Consequently, it is possible to calibrate the output of such a sensor in terms of blackbody temperatures (see Fig. 50).

The measurements obtained by the sensor in orbit can, therefore, be specified in terms of these calibrated blackbody temperatures. Since a sensor in orbit does not measure blackbody radiation in general, the temperatures are known as effective or equivalent blackbody temperatures, T_{bb} . It may be seen from this

discussion that if the sensor in orbit views a surface target such that

- (1) The target completely fills the field of view of the sensor,
- (2) The target has uniform surface temperature and surface emissivity equal to one in the spectral interval of the response of the sensor,
- (3) The spectral response of the sensor is located in a perfect window,

then the effective temperature, T_{bb} , measured by the sensor would be the actual temperature of the surface viewed. While these conditions are never completely fulfilled in practice, measurements obtained in a number of so called IR windows sometimes approximate these conditions (see Section X) sufficiently so that the T_{bb} values obtained may be applied directly to the determination of surface temperatures.

6.8 The Effects of the Display Format on Satellite Acquired Data

Geophysical data acquired by unmanned satellites must be telemetered to the ground, and when acquired there is in the form of electrical signals. While the inherent information content of the data received is limited by the characteristics of the sensor system itself (and of the transmission link between the satellite and the ground receiving station), the format in which the data are presented to the user very largely determines the usefulness of the data in any given application.

Since the raw data are in the form of electrical signals, the data can be presented in a number of ways. However, consideration must be given to the fact that geophysical observations are generally useful only if

- (1) They are ultimately visually presented in a permanent format for analysis,
- (2) They are ultimately presented in such a way that the spatial variations of the observations are readily apparent.

With these considerations, it may be concluded that the actual formats by which the data can be usefully displayed are limited. For instance, data displays employing audio devices would seldom, if ever, be suitable. While such displays could be useful in the detection of the presence of specific types of targets, the actual geographical location of such targets could not be easily obtained from audio techniques. Furthermore, as stated previously, the interpretations of most geophysical observations are based on the analysis of the spatial variations of the measured or observed parameter over a large region of the globe. These spatial

variations must be simultaneously presented to the analyst. Consequently, the display must be visual. Of course, the data will often be machine processed, and at times partially objectively analyzed, before presentation to the human interpreter.

The most common formats used for the display of satellite acquired data are

1. Analog traces of the received signal presented on a strip chart,
2. Two dimensional analog pictures, such as television pictures and the photofacsimile presentations of IR data (the HRIR of Nimbus and the MRIR of Nimbus II),
3. Digitized mappings of the calibrated sensor output, with digital values specified at grid points.
4. Machine analyses of the digitized data, presented in map formats,
5. Manually prepared data formats based on the interpretation made of the data presented in any one of the previous formats. These include nephanalyses, such as those used in most operational analyses and dissemination of TIROS and ESSA data.

Not all of the above listed data presentation are of equal effectiveness in meeting the data user's requirements. For instance, while the analog trace display usually reproduces the details in the original data in the greatest fidelity, it is very inappropriate for recognition and for the two dimensional qualitative analyses which are quite often required in the field. A better format for this is the pictorial display, such as that employed for the APT and DRIR data. The loss in detail (detail beyond a certain level is not generally required anyway) is replaced by the ability of the display to present vividly, and dramatic, significant geophysical features.

Perhaps the best display format is to have the data displayed simultaneously both in the pictorial format and in the digitized format. The pictorial format can then provide "quick-look" identification of significant areas, after which detailed analysis can be performed of the digitized mapping.

It should be pointed out that not all of the above listed display formats are available to all users. The first two formats (analog traces and pictures), for instance, are generally available operationally only to those who have direct access to the originally recorded satellite signals, and the necessary data processing equipment. This limitation is due to the large bandwidth communication requirements necessary to transmit the data in near real time. The transmission of digitized mappings requires less stringent but still significant communications facilities, and

the processing procedures by which these mappings are obtained are time consuming and expensive. At present, such a data format is available on a real time basis only at the National Environmental Satellite Center (NESC). With the exception of the data obtained in the APT mode of transmission, most local stations can be expected to receive satellite data in the hand processed, annotated, format; or later as summarized forms of the digital displays. The exact formats available to Navy installations will depend on both the products disseminated from NESC and Naval management decisions as to the transmission of these products to various Navy units.

6.8.1 Examples of Some Common Display Formats

An example of the analog trace display format was shown in Figure 51a. Figure 52 shows a similar analog record of the data obtained by the HRIR of Nimbus I over the Philippines. The record shown covers nearly two scan cycles of the sensor. In a complete scan cycle, the detector views, in turn, an in-flight blackbody calibration target (which is part of the radiometer housing), outerspace, then the earth. The in-flight calibration portions of the scan are identified in the figure. The space portions of the scan can be identified by its characteristically low equivalent blackbody temperature. These two portions of the scan provides an in-flight check of calibration.

A calibration scale in terms of equivalent blackbody temperatures has been superimposed on the data. Using the time scale shown at the bottom of the trace record, it is then possible to determine the spatial variations of the measured equivalent blackbody temperature on the earth along the line scanned by the radiometer.

It may be seen from this illustration that this format of data display is highly unsatisfactory as far as two dimensional qualitative analyses of the data are concerned, in spite of the high fidelity with which the data is presented.

Figure 53a shows the data from the same sensor as displayed by a photo-facsimile recorder. The facsimile recorder converts the radiometer output signals into a continuous strip picture, line by line, on film. Blanking circuits in the recorder reject unwanted sections of each line scan. Only the earth portion of the scan and, for calibration purposes, very small portions of the space scan are recorded on the film strip. The shades of grey depicted in the figure correspond to variations in the measured equivalent blackbody temperature with darker shades corresponding to warm temperatures. In the current scheme only 10 signal levels are displayed in grey shades of the picture while 100 levels are contained in the original signal, representing a loss in fidelity.

NIMBUS I HRIR

170 170 325
SEP 16, 1964
EAST OF PHILIPPINES

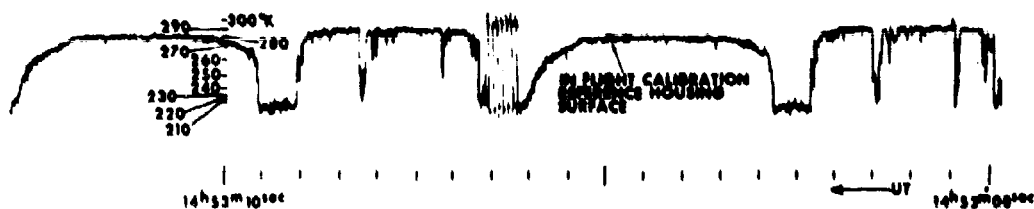


Figure 52. Nimbus I HRIR Analog Trace

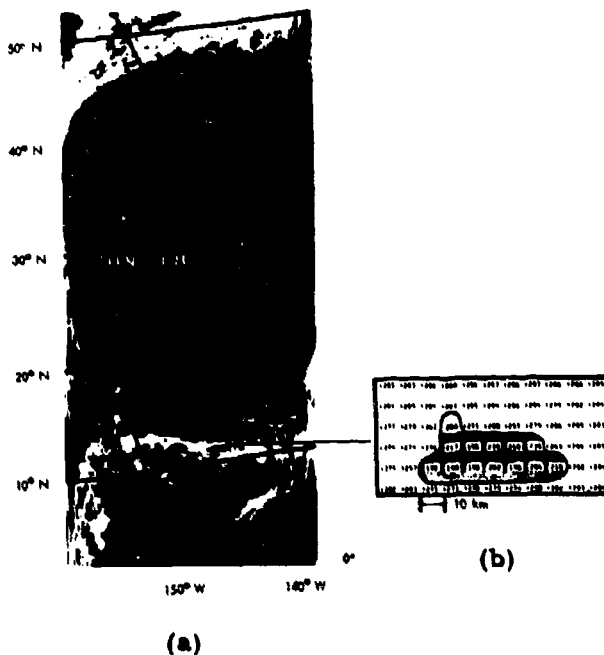


Figure 53. (a) Photofacsimile Display and
(b) Digital Display

However, the ability of this display format to reconstruct the data from an essentially non-imaging sensor to form a two dimensional picture is an invaluable aid for qualitative analyses of the data. In Figure 53a for instance, the white areas represent cold equivalent temperatures, and therefore clouds (see Section X). Consequently, areas of cloud cover are vividly outlined for easy recognition. Other features are also recognizable in this picture. For instance, the warm waters of the tropical Pacific Ocean can be recognized in the dark area near the bottom of the picture in contrast to the somewhat cooler temperatures of the North Pacific Ocean just north and south of 40°N .

Figure 53b shows another method by which the same data can be displayed. In this case, the original analog signals have been digitized with full fidelity and the digital data processed by a computer where calibration and geographic referencing is applied automatically. The result is a two dimensional mapping of the data with numerical values of the measurements specified at grid points.

Figure 54 shows yet another method by which the data from the same sensor can be displayed. Figure 54b shows the photofacsimile depiction of Typhoon Sally as seen by the HRIR of Nimbus I. In Figure 54a is shown a computer analysis of the same data.

The examples shown to illustrate the different display formats have been all taken from the HRIR sensor. However, the techniques involved can be applied to other sensors as well. Figure 55, for instance, shows an example of the photofacsimile display of the data obtained by the medium resolution infrared radiometer of Nimbus II. This radiometer has five separate channels, with each channel measuring in a different portion of the spectrum. The data from all the channels are displayed in one picture together with a grey scale and a geographic reference grid.

In the case of television pictures, the data are logically displayed in the two dimensional grey scale pictorial format. Many examples of these pictures are found in Section IX.

It should be noted that the displays so far discussed have included those which are automatically produced. No subjective interpretation of the data is involved. Such is not the case when the data are displayed, for instance, in the forms of nephanalyses in which the data are reduced to a format suitable for facsimile transmission. Examples of nephanalysis displays are shown in Figures 56 and 57. In Figure 56b is shown the nephanalysis prepared from the photofacsimile presentation of the HRIR data shown in Figure 56a. Figure 57a shows the television picture of cloud cover from which the nephanalysis in Figure 57b was prepared.

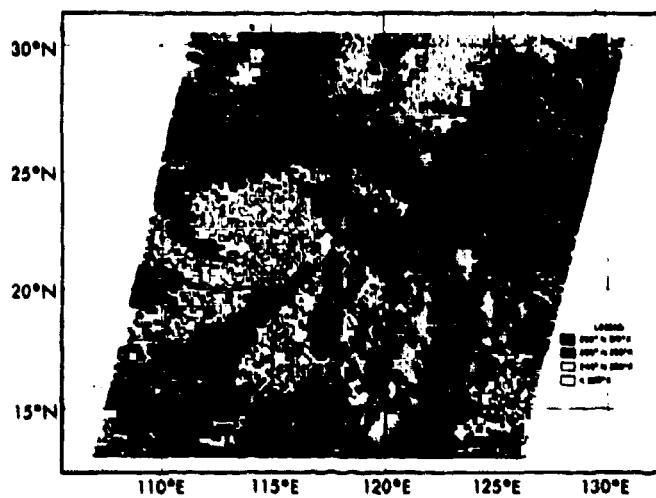


Figure 54a. Computer Analysis Display of Typhoon Sally



Figure 54b. HRIR Photofacsimile Depiction of Typhoon Sally



Figure 55. Pictorial Display of Nimbus II MRIR Data

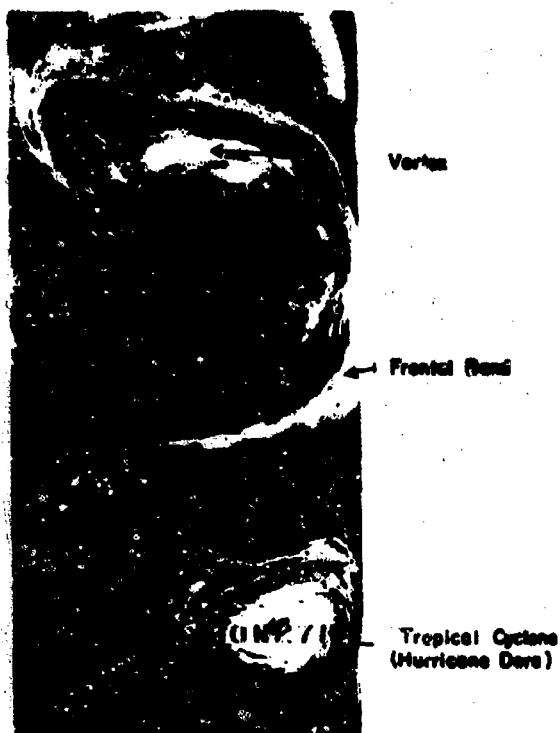


Figure 56a. HRIR View of a Cloud Vortex, a Frontal Band and a Hurricane

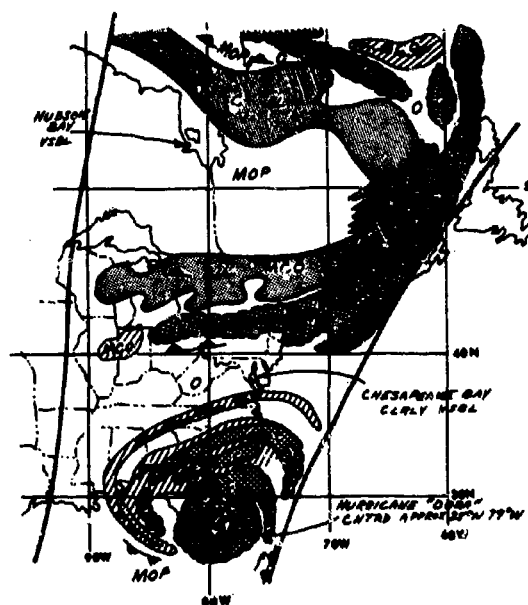


Figure 56b. Nephanalysis Prepared from Figure 56a.



Figure 57a. TIROS VII Television Mosaic

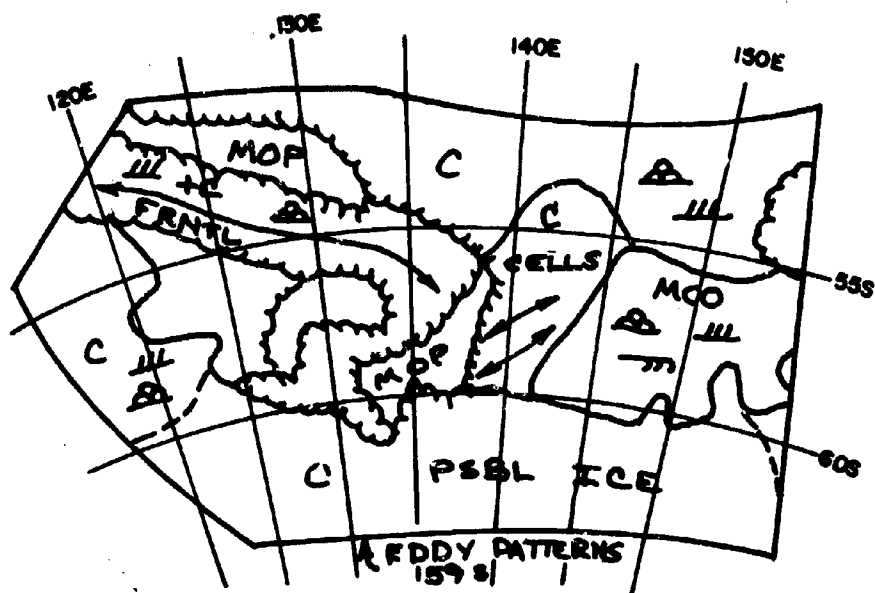


Figure 57b. Nephanalysis Prepared from Figure 57a

NAVTRADEVGEN 65-C-0031-1

Other manually produced display formats can also be prepared from satellite data. The appropriateness of a format obviously depends on the data requirements of the user. However, if the data is to be effectively applied, the user must understand the basic limitations of the particular format or formats of the data which he has to deal with and their relationships to the information content of the originally received analog signals from the satellite sensor.

SECTION VII

EARTH-SYNCHRONOUS SATELLITES

7.1 Introduction

At an altitude of approximately 35,880 km (19400 n.mi.), the period of a satellite in circular orbit is exactly twenty-four hours, the rotational period of the earth. Accordingly, a satellite in an equatorial (0° inclination) orbit at this altitude will appear to remain fixed over a given point on the equator. Such a satellite is referred to as earth-synchronous, and often merely as synchronous. Syncom, Early-Bird, and most recently ATS-B demonstrate the capability to put a satellite in such an orbit.

From such a position, a satellite can continuously view approximately 25% of the globe, with the area centered on the satellite subpoint. Figure 58 shows the local object zenith angles of points within the range of a synchronous satellite located over 150°W , the position planned for NASA's ATS-B. Figure 59 shows the perspective of the earth as seen from ATS-B.

The great advantage of an earth-synchronous satellite is its ability to provide observations of all or parts of the area within its field of view as frequently and as repetitively as its communications bandwidth and power supply permit. In fact, this is perhaps its sole advantage, since the great distance from a synchronous satellite to the earth creates significant problems as to the linear resolution, on the earth, of features observed. Cooper⁴⁷ has shown that, except from the viewpoint of the continuous observations of an area made available from a synchronous satellite, there would appear to be little point in operating meteorological satellites at altitudes much above 4000 miles. While coverage and uniformity of linear resolution (for a given sensor angular resolution) improve somewhat with increasing orbit altitude, linear resolution degrades with altitude. An optimum compromise of these factors appears to exist near 4000 miles. (It is to be noted, however, that these optical factors are only a fraction of the factors that must be optimized in the final design of any meteorological satellite system.)

As Widger⁶ has discussed, satellites with orbital periods of twenty hours could also be placed in inclined and/or eccentric orbits to provide special observational capabilities. As far as is known, however, such orbits are not at present under active consideration.

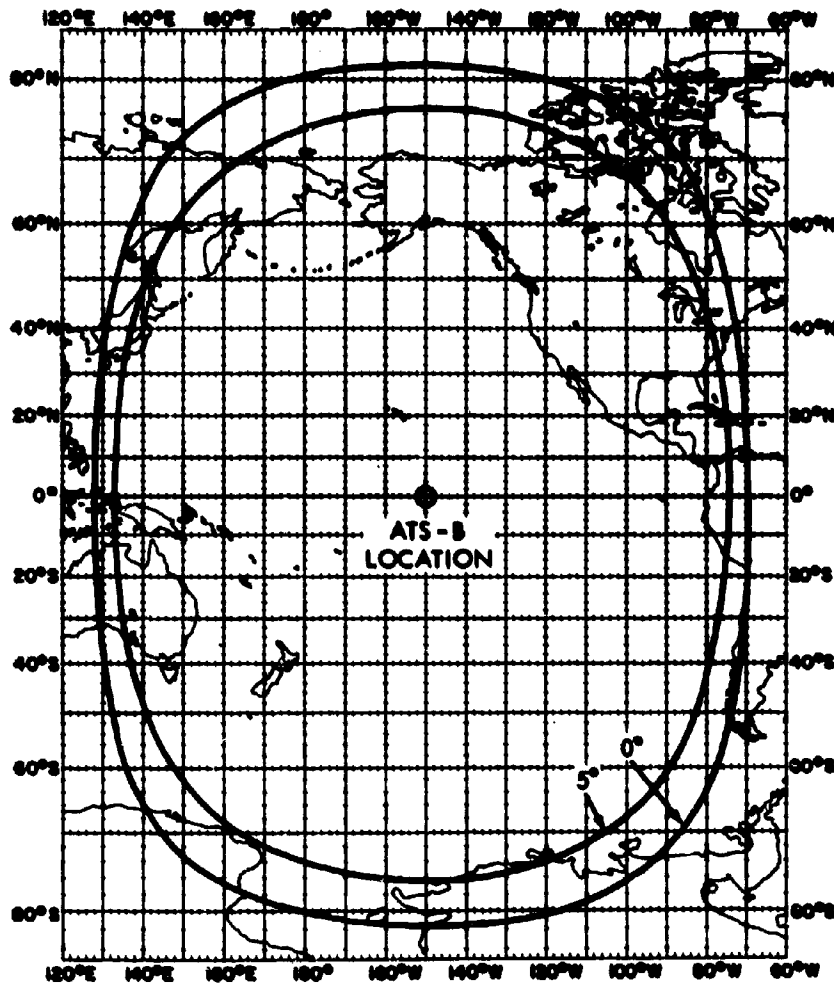


Figure 58. Local Object Zenith Angles of Points Within Range of ATS-B

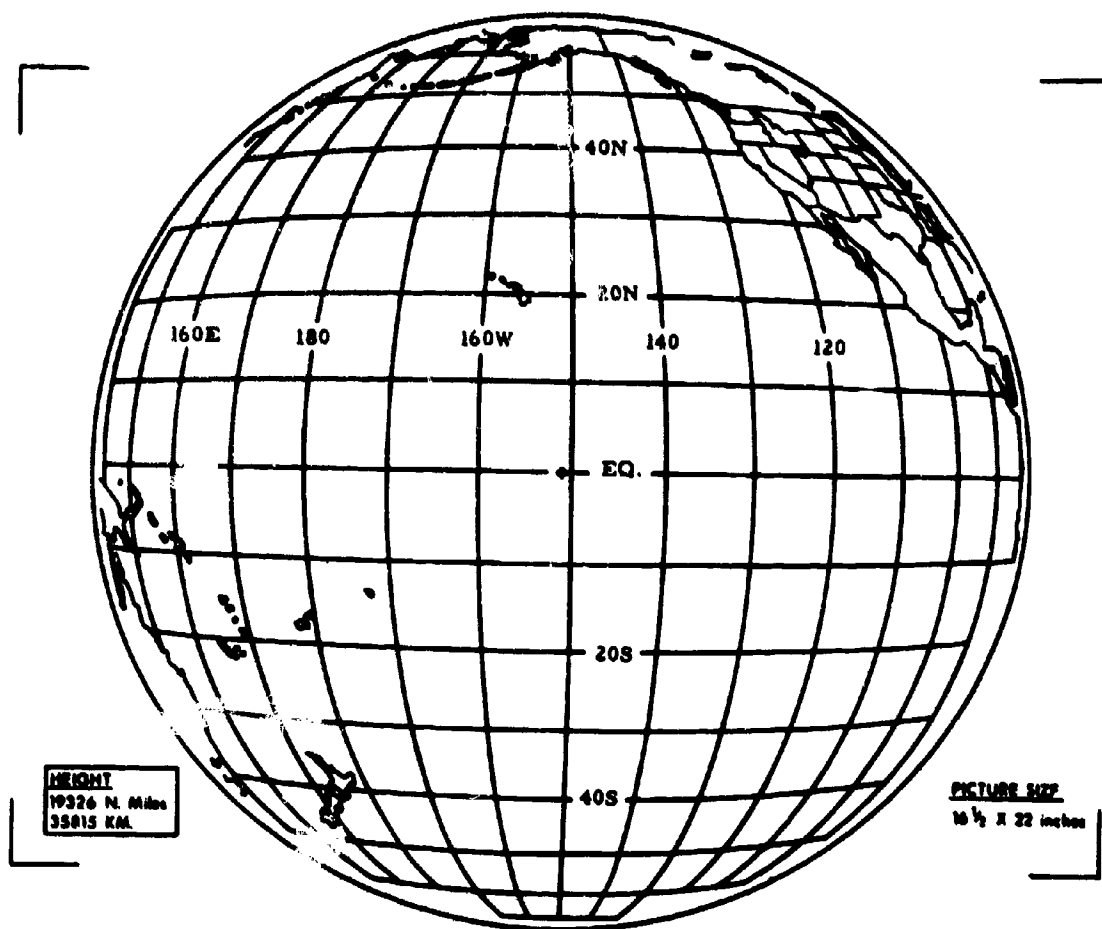


Figure 59. Unrectified ATS-B Geographic Grid

7.2 Problems Associated with Sensor Resolution from Synchronous Altitudes

A major problem in the design and operation of a synchronous satellite is the (angular) sensor resolution required for adequate linear resolution on the earth or in the atmosphere. Table 10 shows the linear resolution, ΔB_o , at the sub-satellite point of a synchronous satellite for several angular sensor resolutions, Δn .

Table 10
Linear Resolution at Subsatellite Point of a
Synchronous Satellite

Δn (Deg)	ΔB_o (Deg. GCA)	ΔB_o (n.mi.)
0.01	0.056	3.4
0.05	0.282	16.9
0.1	0.564	34
0.5	2.82	169
1.0	5.64	340

For comparison, the average angular resolutions of some satellite sensors flown to date are:

TIROS Narrow Angle Camera	0.018°
Nimbus AVCS	0.046°
APT (Nimbus or ESSA)	0.11°
Nimbus HRIR	0.5°

From a synchronous satellite, the earth is only some 17.3° in diameter, and so the maximum useful sensor nadir angle is less than 8.6°. As a consequence of the small apparent diameter of the earth and the large satellite altitude, small differences in nadir angle, n , lead to large differences in the area observed, and the linear resolution on the earth still degrades rather rapidly with increasing nadir angle. Table 11 illustrates this point for a few chosen nadir angles and angular sensor resolutions, Δn , where ΔB is the resolution on the earth and B is the distance along the earth from the sub-satellite point.

It is obvious from Table 11 that sensor resolutions of about 0.01 degrees, and preferably better, are required for most useful observations from the synchronous altitude. Furthermore, sensor attitude must be known to the same order of accuracy if the observations are to be located with useful precision.

155

n (Deg)	Deg. GCA	n.mi.	dB/en	Δn (deg) 0.01		Δn (deg) 0.05		Δn (deg) 0.1		Δn (deg) 0.5	
				ΔB GCA	n.mi.	ΔB GCA	n.mi.	ΔB GCA	n.mi.	ΔB GCA	n.mi.
0	0	0	5.53	0.056	3.4	0.282	16.9	0.546	34	2.82	169
2	11	660	5.80	0.058	3.5	0.290	17.4	0.560	35	2.90	174
4	24	1440	6.45	0.065	3.9	0.312	18.7	0.645	39	3.12	187
6	38	2220	8.12	0.081	4.9	0.406	24.4	0.812	49	4.06	244
8	60	3600	13.9	0.139	8.4	0.695	41.7	1.39	84	6.95	417
8.5	70	4200	28.8	0.288	17.3	1.44	86.5	2.88	173	14.4	865

As mentioned above, the real advantage of a synchronous satellite will be its capability of very frequent observations, and so its observations of rather small scale changes (since there is a high correlation between the lifetime of a meteorological feature and its geometric scale). It is estimated that, for maximum use, a synchronous satellite should possess a resolving capability (over programmable areas of limited size) of about 0.1 n.mi. This implies the need of a sensor resolution of at least the order of 0.0003° , and of one somewhat better than even that if the useful field of view is to extend far from the subpoint. If it is assumed this would be provided by a camera system with the order of a 1000 raster line capability, this implies a total camera field of view of only about 0.3° (about 100 n.mi. near the subpoint). This will also require that the sensor attitude be controllable to at least the order of 0.03° , and be determinable to at least the order of 0.003° , if real use is to be made of the camera capabilities.

While TV sensor resolutions of the order suggested above do not appear to present an undue problem, attitude control and determinations of this order do and are very likely to require some form of star tracking.

Infrared sensors with linear resolutions of even as good as a few miles also present a real problem. As noted above, this implies sensor resolutions of the order of 0.01° . The best infrared sensor resolution presently available on meteorological satellites is 0.5° (Nimbus HRIR), and even this was a compromise from the original goal of 0.15° . Appropriate infrared sensors of better resolution exist only in the classified domain, if at all. Accordingly, present synchronous meteorological satellite (SMS) plans are considering the use of infrared sensors from principally the heat balance, rather than the cloud observation viewpoint.

Sensor resolution problems for synchronous altitudes are even less hopeful when detectors operating at longer wavelengths (microwave radiometers, spheres, radar, etc.) are considered.

The present concept of employment of an operational synchronous meteorological satellite is large area (the whole disk of the earth or a significant fraction thereof), moderate (a few miles) resolution surveys about once or a few times an hour. On the basis of these and any other available data, specific small (order of a few hundred mile diameter) areas of significant weather (squall lines, hurricanes, etc.) would be monitored every few minutes at high resolution. This might be done by either a single Zoomar type camera (which increases the flexibility as to area size

NAVTRADEVCE 66-C-0031-1

and resolution, but may present lubrication and other reliability problems), or by an array of fixed focal length cameras of different resolving capabilities (which is less flexible, but does provide redundancy).

Visual spectrum observations from a synchronous satellite also introduce such problems as:

1. The need for night, as well as day, observing capabilities, which introduces the sensitivity, dynamic range, and night air-glow problems discussed in more detail in Sections V and VI. Unless these are solved, a synchronous satellite's efficiency will be reduced by at least 50%.

2. The illumination contrasts at the terminator, which require either a very wide dynamic range or some form of variable density, gray wedge filtering matched, as a function of time, to the position on the image of the terminator.

A further problem is that of station-keeping (maintenance of subpoint position), especially if the desired subpoint is not one of those at which a synchronous orbit is stable.

7.3 A Note on ATS-B

The ATS-B (Applications Technology Satellite) was successfully launched in December 1966. It subsequently drifted to a position with subpoint located at approximately 151°W. While it is not strictly a geophysical satellite, it carries two meteorological experiments; (1) the Suomi camera and (2) WEFAX. The WEFAX experiment is to demonstrate the utility of a satellite as a transmission link in the transmission of meteorological charts and analyses. A detailed discussion of this use of satellites is included in Section XIV. The Suomi camera makes observations of cloud cover. High quality pictures taken with this camera have already been received.

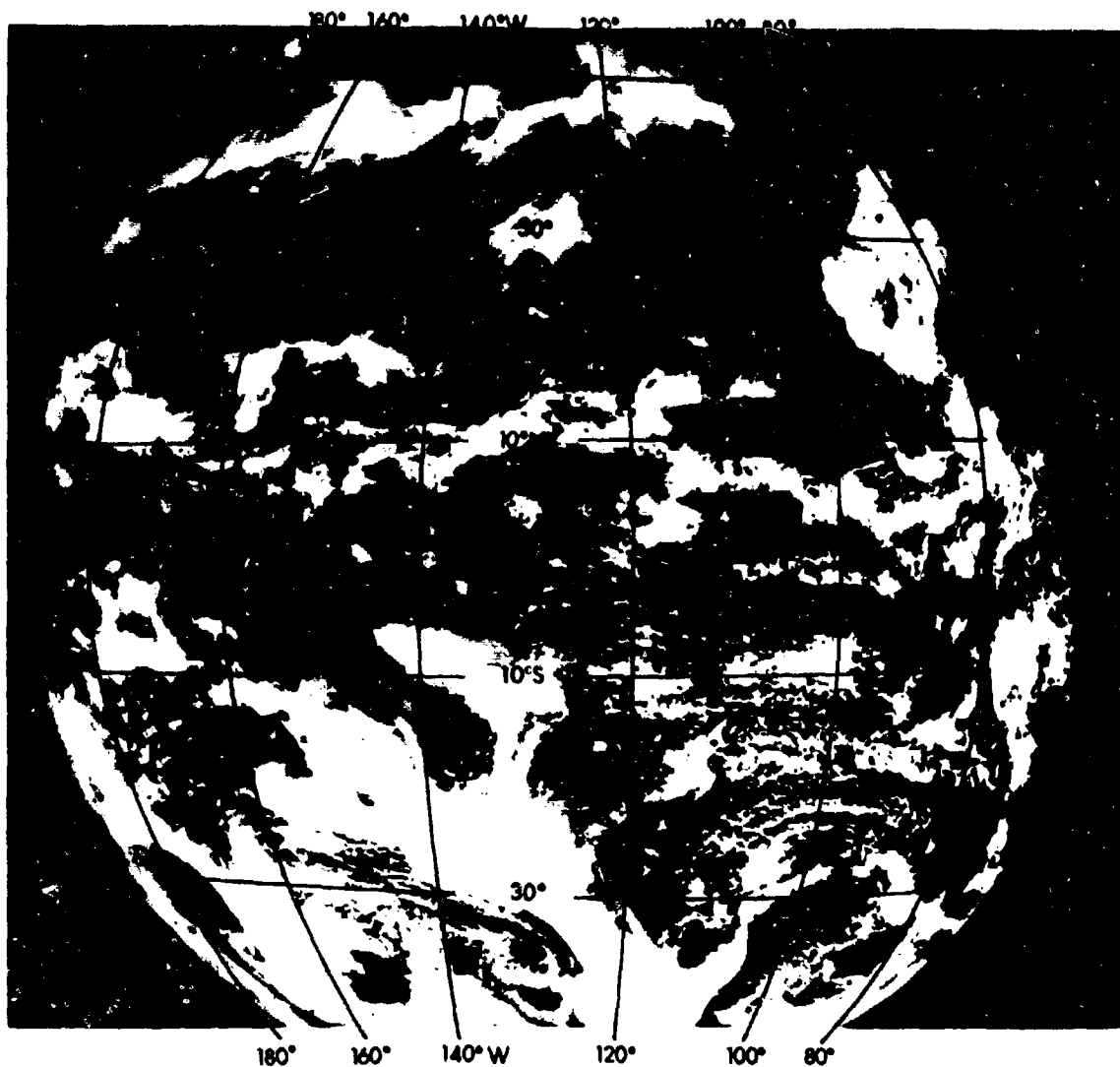
Unlike a television camera, the Suomi camera is not an imaging device. It consists of a photo-multiplier looking through a telescope to a mirror. The spin axis of the satellite is held in the north-south direction so that the telescope, looking out of the side of the satellite, scans across the earth in the direction roughly parallel to the equator. At each spin the position of the mirror will be altered slightly so that the next scan is slightly displaced from the previous one. The spin rate is 100 rpm and a scan of the earth of about 50° north to 50° south will be

NAVTRADEVCEEN 66-C-0031-1

completed in 2000 spins, or twenty minutes. Synchronization of scan is achieved by use of a sun sensor. Readout on the ground is through a very precise photo-facsimile device capable of 2000 line resolution.

The system has a ground resolution of approximately two miles near the equator with resolution decreasing away from the subsatellite point due to the increasing sensor nadir angle (See Section VI).

The pictures so far obtained show amazing detail. Not only are the cloud formations over the Pacific clearly depicted, but a number of geophysical features along the coast of California and Mexico can also be seen (see Fig. 60).



The northern hemisphere contains a frontal network east of Kamchatka, USSR, an organized cloud area off of the lower California and Mexican coasts and a rain producing system over the eastern section of the United States. Oriented east-west off of northwest South America lies the Intertropical Convergence Zone. The southern hemisphere displays phenomena common to this area: large north-south frontal bands; a low pressure area located near the Antarctic icecap; and the Andes mountains outlined by clouds.

Figure 60. Cloud Photograph from Synchronous Altitude

SECTION VIII

A BRIEF SURVEY OF SATELLITE OBSERVATIONS

This section provides a brief survey of (1) the more significant geophysical parameters and features observable from satellites, (2) the spectral regions or regions in which such observations are made, and (3) the basic techniques employed to obtain the observations.

8.1 Surface Temperature

The temperatures of the surface of the earth, including sea surfaces, can be obtained by satellite sensors having spectral responses located in atmospheric windows in either the IR or microwave regions of the spectrum. The ability of such sensors to measure surface temperature is based on the relationship between (1) the radiance emitted by the surfaces and (2) temperatures and emissivities of the surface (Sections III and IV). It is necessary that such measurements be made in an atmospheric window to minimize the effects of atmospheric absorption and emission (Section V).

In the IR, surface temperatures can only be made over regions free from cloud cover, since clouds are generally opaque to IR radiation. In the microwave region, however, surface temperature observations can be made even in the presence of cloud cover (Section V).

Surface temperature measurements have been made by a number of satellite sensors, including the window Channels (Channel 2) of the scanning radiometer of TIROS and of the Medium Resolution Infrared Radiometer (MRIR) of Nimbus II, and the High Resolution Infrared Radiometer (HRIR) of Nimbus I and II. These sensors all operate in the infrared. Microwave radiometers have been test flown on balloons and aircraft and it is expected that a microwave radiometer will be flown in a satellite in the near future.

8.2 Atmospheric Temperature

IR and microwave radiation measurements confined to an absorption band of an atmospheric gas are related to:

1. The vertical distribution of the absorbing gas.
2. The vertical temperature structure of the atmosphere.

If the vertical distribution of the absorbing gas is known, it is then possible to deduce the temperature structure of the atmosphere.

The techniques used to obtain the temperature data from absorption band measurements are not as straight forward as that used in obtaining surface temperature measurements. In general, it may be stated that, in order to obtain a complete vertical profile of atmospheric temperature, simultaneous, or nearly simultaneous, measurements must be made in a number of spectral intervals within an absorption band of one of the well-mixed gases such as CO_2 (or at a number of nadir angles using a single spectral interval). Such multispectral measurements have not yet been made from satellites. The instruments, spectrometers and interferometers needed to make such measurements are being developed, have been test flown on balloons, and are expected to be flown in the near future.

While no satellite measurements of the vertical distribution of atmospheric temperatures have been made, the mean temperatures of a deep layer in the lower stratosphere have been measured from satellites. These measurements have been made using a single radiometer with a fixed bandpass located in the 15μ absorption band of CO_2 . The relationships between the effective temperature measured by such a radiometer and the mean temperature of the stratosphere are, again, somewhat complex. A full discussion of these measurements can be found in Section X.

It should be pointed out that IR radiometric measurements of atmospheric temperatures can be seriously hindered by the presence of clouds. For instance, temperature profiles cannot be obtained below cloud top altitudes. Microwave techniques can, however, be used (at least in principle) to make atmospheric temperature measurements in and below clouds.

8.3 Humidity (Atmospheric Water Vapor)

Atmospheric humidity measurements have been obtained by satellite IR radiometers (the scanning radiometer of TIROS and the MRIR of Nimbus II) with spectral responses located in the 6.3 μ water vapor absorption band. These measurements are again based on the fact that radiation measured in a water vapor absorption band are related to both the concentration of water vapor in the atmosphere and to the vertical distribution of atmospheric temperature. Techniques have been developed whereby the mean relative humidity of the upper troposphere can be determined from these measurements, provided that concurrent IR window temperatures are also available.

If simultaneous measurements in a number of wavelength intervals within a water vapor absorption band are made concurrent with measurements of the vertical distribution of atmospheric temperature, it is possible, in theory, to derive the vertical distribution of water vapor.

8.4 Clouds

Satellites are most useful for the observation of clouds. The generally high albedo contrasts between clouds and surrounding clear area render them easily detectable by satellite sensors which operate in the visible portions of the spectrum. Such sensors would include television cameras, photographic cameras, radiometers and photometers as well as a host of exotic devices.

Cloud detection by IR sensing techniques is also possible. This is due to the fact that clouds act as blackbody radiators in the IR. Consequently, an IR window sensor can measure the temperatures of cloud top surfaces. Since cloud top temperatures are generally cooler than the temperatures of surrounding surfaces, it is possible to delineate areas of cloud cover in an analyzed field of IR window temperature measurements.

The ability of IR window sensors to detect the presence of cloud cover is independent of solar illumination. As a consequence, these sensors can provide cloud cover data during nighttime portions of the orbit (when visible sensors such as television cameras are generally inoperative) provided the cloud tops are high enough for their temperatures to be measurably cooler than the underlying surface.

Cloud cover observations using both visible and IR techniques, have been made by a number of satellite sensors. The visible sensors include the television cameras of TIROS, Nimbus and ESSA satellites; the photographic cameras used by the astronauts in the manned space flights; and the reflectance channels of the scanning radiometer of TIROS and of the MRIR of Nimbus II. IR observations of cloud cover have been made by the window Channels of the radiometers of TIROS and of the MRIR of Nimbus II, as well as by the HRIR of Nimbus II.

A problem found in the cloud observation techniques, discussed previously, is their inability to detect the presence of thin clouds. The application of the laser as an active technique for the detection of such clouds has been suggested. In such a technique, a pulse of laser light would be transmitted from the satellite in the direction of the earth. A sensor also located in the satellite would measure the energy scattered back by air molecules and by the particulates in the atmosphere. The presence of a thin cloud along the propagation path of the pulse would be revealed by a sudden increase in the measured back scattered energy. This technique would be essentially the same as that employed in microwave radars.

8.5 Storms, Hurricanes, Fronts, and Synoptic Patterns

A number of meteorological systems, such as extratropical storms, tropical storms, and hurricanes and frontal systems, have characteristic cloud cover patterns. It is, therefore, possible to detect their presence by analyzing the cloud cover observation obtained by satellites.

8.6 Sea State

Sea state has been found to be a very difficult parameter to measure from satellites. The most promising technique seems to be the use of side-looking radars, in which the observed backscattered patterns can, hopefully, provide a measure of the sea state. There is currently insufficient experimental information to allow for a proper evaluation of this technique. Some rough measure of sea state can be obtained from the size and intensity of observed sunglint in visible measurements.

8.7 Hydrological Features (Rivers, Lakes, Glaciers, Snow Cover, Ice Floes)

Many of these features have been observed in satellite television pictures. They are manifested in these pictures by the brightness contrast which they exhibit. For instance, water surfaces such as lakes have characteristic low albedos. Consequently, they appear in television pictures as dark areas. On the other hand, snow and ice have characteristic high visual albedos. They, therefore, appear as bright areas in these pictures.

In at least one case, the presence of a large ice floe has been detected in IR window measurements. This was due to the fact that the ice floe had a colder temperature than the surrounding water. Similarly, the presence of rivers and lakes can often be detected in IR measurements, due to the temperature contrast between these features and surrounding regions.

The use of a microwave radiometer to detect and track icebergs has been suggested. The use of microwave radiometers in such a scheme appears to be attractive, since microwave measurements are not affected by clouds and the effective temperature contrast between ice and water is high (due to the low emissivity of ice in the microwave region).

8.8 General Surface Observations

From the discussions of the attenuation effects of the atmosphere presented in Section II, it is seen that surface observations of such features as deserts, swamps, coastal features and others, should be made in an atmospheric window region. It was also shown in Section IV that such windows exist in the visible, IR, and microwave parts of the spectrum. The choice of the window to use would depend on the nature of the targets to be observed. The spectral region chosen should obviously emphasize the contrast between the target and its surroundings. Furthermore, better detection can often be achieved by making simultaneous observations of the same feature in a number of spectral intervals within a given window, or in a number of windows. Such multispectral measurements take advantage not only of the intensity contrast in a given spectral interval between the target and its surroundings, but also of the spectral contrast.

More detailed discussions of the applications of satellites in surface reconnaissance are presented in Sections IX and X, in which details of the observational techniques in the various spectral regions are discussed.

8.9 Summary of Sensor/Data Systems

A summary of the sensor/data systems applicable to satellite acquisitions of geophysical data is provided in Table 12. The table includes a number of sensor-parameter combinations not specifically discussed in the brief survey presented above. In addition, observations and measurements using data telemetered from buoys and balloons have been included.

It should be noted that the technical feasibility of a number of the sensor-parameter combinations included in the table remains to be demonstrated.

167

Data Types		Positive Techniques				Active Techniques				Toluntary Techniques			
Subject Area	"Photography" or Television	Infrared Radiometer	Calibrated Radiometer	UV Spectral Radiometer	Nitrogen Radiometer	Laser Illumination	Laser Rangefinder	Laser Lidar	Microscopic Imager	Sensor Based	Controlled Environment	Fluorescing Probe	Visual Probe
Geography:													
Sea Bed	X	X	X		X				X	X		X	X
Sea Surface Temp.													
Sea Surface Temp., Salinity, Density	(X)												
Sea Surface Currents													
Sea Surface Currents		X							X	X		X	X
Sea Profile	X	X							X	X		X	X
Sea Depth	X	X							X	X		X	X
Coastal Geography	X	X	X						X	X		X	X
Coastal Ecology	X	X	X						X	X		X	X
Marine Biological Studies	X	X	X						X	X		X	X
Tide Measurements		X							X	X		X	X
Microscopy:													
Atmospheric Temperature		X	X		X								
" Humidity					X								
" Pressure					X								
" Wind					X								
Cloud Systems													
Micro-Tropical Storms	(X)	X	X		X				X	X		X	X
Tropical Storms	X	X	X		X				X	X		X	X
Precipitation	X	X	X		X				X	X		X	X
Small Scale Storm Storms	X	X	X		X				X	X		X	X
Lightning	X	X	X		X				X	X		X	X
Geophysical Phenomena (General):													
Albedo													
Sea Level													
Sea Level													
Lower Landmass		X	X		X								
Cloud Reflection		X	X		X								
Geography (Littoral Region)													
Land Features, Modification	X	X			X				X	X			
Vegetation	X	X			X				X	X			
Hydrological Features	X	X			X				X	X			
Shore, Lake	X	X			X				X	X			
Sea Cover	X	X			X				X	X			
Military Intelligence													
Ship Movement	X	X			X				X	X			
Strategic Structures	X	X			X				X	X			
Beacon	X	X			X				X	X			
Fuel Tanks	X	X			X				X	X			
Construction Areas	X	X			X				X	X			

SECTION IX

OBSERVATIONS AND MEASUREMENTS IN THE VISIBLE

9.1 Introduction

It was noted in Section V that the visible portion of the spectrum represents a broad atmospheric window in which atmospheric gaseous attenuation of radiation is minor. Consequently, it would appear that visible observations and measurements would be highly useful in the surveillance of the surface features of the earth.

It was also noted, however, that clouds are opaque to visible radiation. In the presence of cloud cover, the surfaces of the earth cannot be seen from satellite altitudes. Clouds, on the other hand represent a significant class of meteorological targets. From observations of the extent of cloud cover, the cloud patterns, cloud types and other cloud parameters, meteorologists are able to deduce a large quantity of information relating to the concurrent meteorological processes. Cloud observation, is therefore, an important aspect of satellite geophysics. Indeed, the television cameras of the TIROS, ESSA and Nimbus series of satellites have been designed primarily for the purposes of making global cloud cover observations. Such observations have provided the meteorologist with information for the preparation of neph-analyses. Even as early as 60 days after the launch of TIROS I, a nephanalysis based on satellite television pictures of cloud cover was prepared and disseminated. Since then, satellite television data, have become an important tool in meteorological analysis and forecasting.

In spite of the fact that these television cameras were primarily designed for cloud observations, a number of surface features in cloud free areas have been noted in the pictures. In addition, the color photographs made by the astronauts of the Mercury and Gemini manned space flights have demonstrated the potentials of multispectral, high resolution, visible observations from spacecraft in the areas of surface surveillance.

In addition to these satellite observations made by imaging sensors, a large body of radiometric data has been collected by the visible channels of the scanning radiometer of TIROS and of the Medium Resolution Infrared Radiometer (MRIR) of Nimbus II. These radiometric measurements are ideally suited for the determinations of the albedos of the different surfaces of the earth and of cloud surfaces, and have been used in energy balance studies.

9.2 A Note on the Application of Visible Observations from Satellites to Surface Surveillance

As noted previously, the television cameras on the current geophysical satellites are designed primarily for the observations of cloud cover. In these television pictures, areas of cloud cover appear white against a darker background of the surfaces of the earth, and of the oceans. However, a number of surface features of interest have been observed and identified in cloud free regions of these photographs. These have included such quasi-meteorological features as the extent of snow cover, the presence of sea and lake ice, and a number of geological features. Examples of these features, as observed in satellite televisions are shown in a later section.

These television pictures have been obtained by sensors which measure radiation in the broad spectral interval from ~ 0.5 to $\sim 0.9\mu$. Colors within this broad spectral interval are not resolved in the photographs. The color photographs obtained by the astronauts of the manned orbital flights have demonstrated the potentials of multispectral observations (and increase resolution) in surface surveillance. In the following paragraphs, the factors which might render the interpretation of visible observations difficult are discussed.

The delineation and identification of surface targets or features in satellite imagery is primarily based on contrast variations observed in the measured data. The contrast may be in intensity or brightness alone (as in the case of a black and white photograph or television picture), or it may be a combination of spectral and intensity contrast (as in color photographs). In any case, for a target to be detected, it must exhibit contrast from its surrounding, or background. Clouds, for instance, have generally higher reflectivities than the surrounding surfaces. As a consequence, they are often contrasted against a darker, less reflective, background.

At the level of the target, the target exhibits a contrast from its background which may be given as

$$C_o = \frac{N_T - N_B}{N_B} \quad (126)$$

where

N_T = radiance of the target
 N_B = radiance of the background
 C_o is known as the inherent contrast.

Since in the visible portion of the spectrum, the radiance propagating from a surface is dependent on the solar irradiance on the surface and on the reflectivity of the surface, under identical solar irradiance conditions, the inherent contrast between a target and its background is then simply related to the differences in the reflectivity of the target and its background. The larger this difference, the greater is the contrast, and the easier it becomes to detect the target.

It was noted in Section IV that reflectivities of surfaces are spectrally dependent. Consequently, the inherent contrast between a given pair of target and background is also spectrally dependent. Obviously, an optimum detection system for that target element would be one in which the wavelength chosen for the measurement would maximize the contrast in reflectivity. However, it should also be noted that the same target element might exist over a variety of background surfaces having different spectral reflectivity properties. As a consequence, it is not always possible to design a sensory system which can always observe a given target under maximum contrast conditions.

In addition to the problems related to inherent contrast, the atmosphere also has an influence on the interpretability of the observations. In spite of the fact that the visible portion of the spectrum is a relatively clean window as far as gaseous absorption is concerned, visible radiation propagating through the atmosphere is attenuated by the process of scattering by molecules and by dust particles. These scattering processes tend to reduce the inherent contrast. This may be seen by considering the change in contrast at the level of the satellite. Let the contrast at the satellite be given by C_{∞} . From the definition of contrast, this may be written as

$$C_{\infty} = \frac{N_{T\infty} - N_{B\infty}}{N_{B\infty}} \quad (126a)$$

where

$N_{T\infty}$ and $N_{B\infty}$ are respectively the radiance arriving at the satellite sensor from the target element and from the background.

It was noted in Section V that scattering reduces the transmissivity of the atmosphere so that $\tau \neq 1$. Furthermore, scattering also introduces "non-image" forming light into the beams of radiation originating from the surfaces of the earth. As a consequence, $N_{T\infty}$ and $N_{B\infty}$ can be written as

$$N_{T\infty} = N_T \tau + N_s$$

$$N_{B\infty} = N_B \tau + N_s$$

where

τ is the transmissivity of the atmosphere

and

N_s is the radiance added by atmospheric scattering.

The contrast at the satellite sensor is then given by

$$C_{\infty} = C_0 \left[\frac{1}{1 + \frac{N_s}{N_B \tau}} \right] \quad (126b)$$

Since the term in the brackets is always less than 1, the contrast at the satellite sensor is always less than the inherent contrast.

In Section V, it was noted that molecular scattering, which is always present in the atmosphere, increases in significance with decreasing wavelength. Consequently, atmospheric effects in the degradation of inherent contrast can also be expected to increase with decreasing wavelength. This is one of the principle reasons why satellite television cameras have spectral responses designed with short wavelength cutoffs at $\sim 0.5\mu$. As an indication of the contrast degradation of the atmosphere and its dependence on wavelength, Table 13 has been constructed.

Table 13

Contrast Degradation of the Atmosphere

λ	Background	% Transmission of Contrast
4050 Å	Grass Turf	~ 5
4920	Desert Sand	~ 45
6430	Desert Sand	~ 85

A number of experimental and theoretical studies have been performed of the optimum spectral intervals for surveillance from satellites. Perhaps most significant of these is the experiments made by Astronaut Cooper on space flight MA-9.⁴⁸ During the course of the flight, Astronaut Cooper made a number of photographs

with a Hasselblad Camera. The camera had a filter holder which held three filters side-by-side so that simultaneous photographs at three wavelength intervals were obtained. The spectral intervals used were: $6600 - 9000\text{\AA}$, $7300 - 9000\text{\AA}$, $7900 - 9000\text{\AA}$.

From the analyses of the resulting photographs, it was concluded that

1. Contrast between clouds and water, and land and water is high in the $6600 - 9000\text{\AA}$ region.
2. Contrast is low between clouds and land covered by green vegetation in the same spectral region.
3. Observations of cloud cover can best be made in the $5000 - 7200\text{\AA}$ as a compromise between the adverse effects of scattering by aerosols and molecules at shorter wavelengths, and low contrast effects of clouds over land at near infrared wavelengths.

From this short discussion, it may be concluded that simultaneous measurements made in a number of spectral intervals should provide better observations of surface features. From the experiments of MA-9 for instance, it may be seen that if simultaneous measurements are made in $6600 - 9000\text{\AA}$ and $5000 - 7000\text{\AA}$ intervals, it may be possible to better differentiate clouds from surfaces and vegetated areas from unvegetated areas than currently possible with the satellite photographs.

9.3 Examples of Some of the Visible Observations Made from Satellites

9.3.1 Determination of Cloud Altitudes

An experiment was performed on Gemini-Titan 5 to determine cloud top altitudes.⁴⁹ The instrument used was a compact grating spectrograph camera which records simultaneously a photograph of the cloud and its spectrum from 7500\AA to 7800\AA in the vicinity of the oxygen "A" line. The principle of deducing cloud-top heights from such measurements is discussed in detail by Wark and Mercer.⁵⁰ Briefly, it requires measurement of the fractional transmittance at a suitable wavelength in the absorption band of oxygen. This transmittance is determined from the height of the cloud and the local zenith of the sun and the observers. That is, the transmittance depends on the effective amount of oxygen in the optical path above the cloud. Since oxygen is a well mixed gas, its effective amount above a cloud top is determined by the height of the cloud top.

NAVTRADEVGEN 66-C-0031-1

The results of this experiment are summarized below:

Cloud Identification	Cloud Top Altitude	
	From Experiment	Actual
Stratus	980 mb	950
ITC	440 mb	-
"Doreen"	320 mb	(350-220)

It is seen that such measurements can provide estimates of cloud top heights.

9.3.2 Observations of Surface Features

In spite of the fact that the television cameras of the TIROS, Nimbus and ESSA series of satellites were not designed to observe surface features, a number of significant surface features have been noted in the pictures obtained. In particular such features as coastlines, ice fields, snow cover, deserts, water bodies such as inland lakes and rivers, oceanic islands and atolls are regularly observed in the television pictures. Examples of these features as depicted in satellite television pictures are shown in Figures 61a, b, c, and d.

In addition, studies by Morrison, et al.⁷⁷ and others have demonstrated the utility of these photographs in geological investigations.

The sunglint depicted in the pictures shown in Figure 61b should be noted. When the sea surface is calm, and the sun is at an angle which gives rise to specular reflection, the sea surface increases in reflectivity, resulting in an area of enhanced brightness in a satellite photograph. Observations of sunglint effects can be used to determine sea state. However, its usefulness is rather limited due to the low probability of its occurrence.

9.3.3 Meteorological Observations

A large amount of meteorological information can be deduced from satellite photographs. First of all, satellite photographs depict the extent of cloud cover, the cloud patterns, and cloud types. From these basic cloud data, meteorologists are able to determine the locations of significant meteorological systems and the



**Ice Fields and Ice Packs
(Antarctic Region) (N)**

Admiralty
MT. Range



**Ice Floes and Ice Bergs
(Antarctic Region) (N)**



**Lake and Mountains with Snowfield
(USSR) (N)**

Lake Retba

Lake
Issik-Kul



**Lake and Mountains with Snowfield
(USSR) (N)**

Tien Shan
MT. Range

Figure 61a. Selected Terrestrial Features

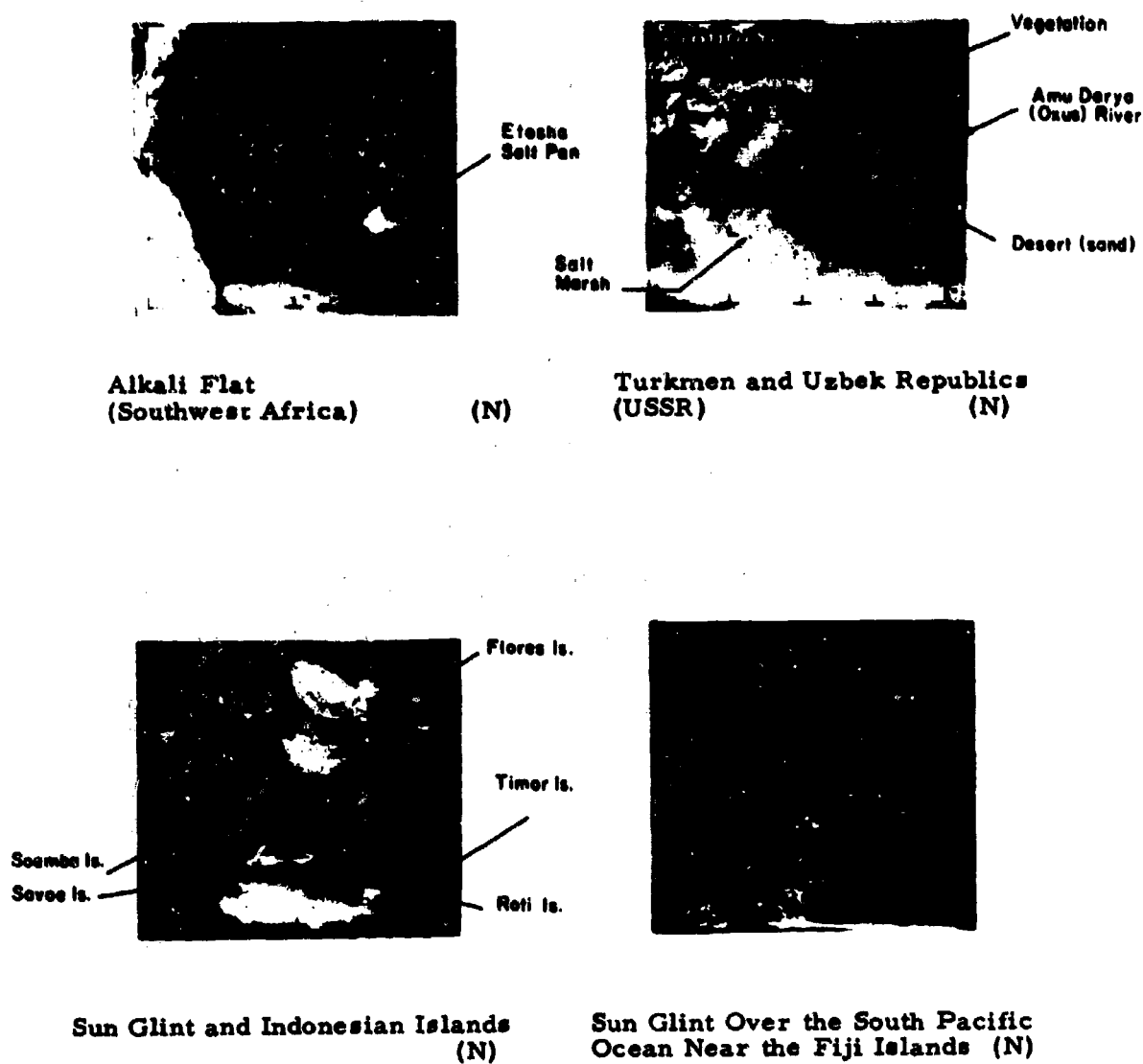
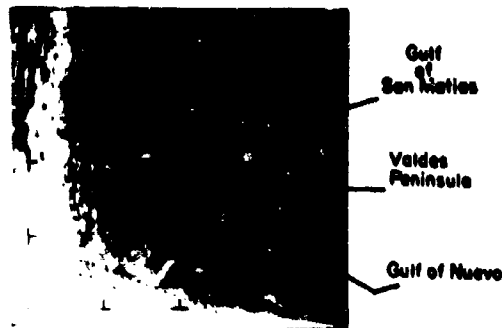
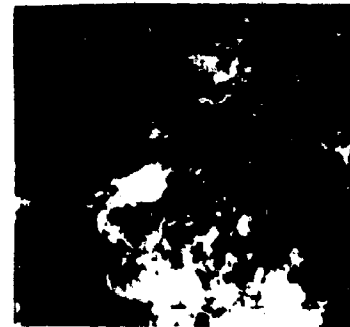


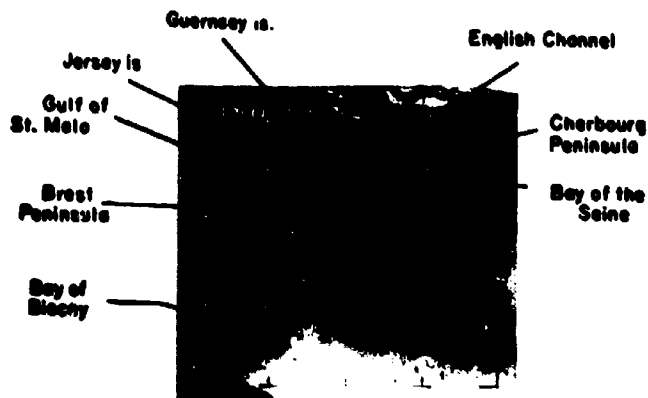
Figure 61b. Selected Terrestrial Features



Coastline of Argentina (N)



Islands and Atolls
Tuamotu Archipelago (N)

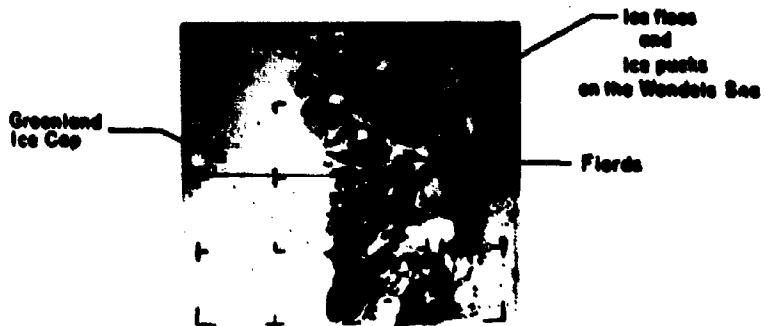


Coastline of Northwest France (N)



Canadian Rocky Mountains
(Snowfield) (N)

Figure 61c. Selected Terrestrial Features



Ice Cap and Florida
Northeast Greenland (N)



Ice Cap
Southern Greenland (N)

Figure 61d. Selected Terrestrial Features

processes by which the cloud formations might have been produced. The relationships between the cloud fields as observed in satellite photographs and meteorological processes form one of the principle areas of investigation in satellite meteorology. This field of study is by no means complete. However, the study performed by Widger et al.⁵¹ essentially summarizes the state of the art in the meteorological interpretation of satellite photographs.

Among the more obvious meteorological uses of satellite photographs are the identifications, in terms of characteristic cloud cover patterns, of storms and frontal systems. Figure 62 shows examples of satellite photographic depictions of various tropical storms and typhoons. Figure 63 shows cloud pictures of several cyclones in various stages of development from the open wave stage to the occluded, to the decay stage.

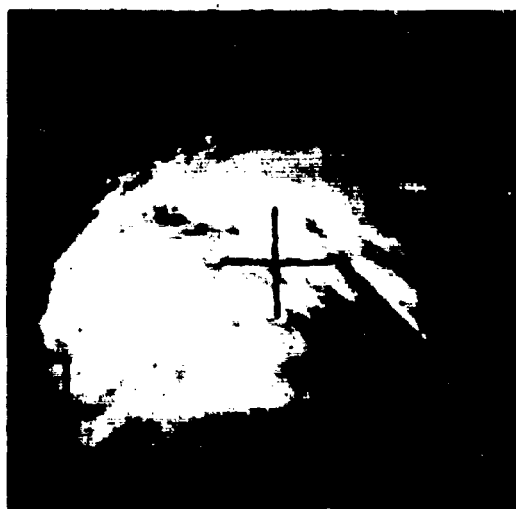
However, much more detailed information of meteorological processes, both on the synoptic scale and on the mesoscale, can be deduced from these pictures. Meteorological parameters such as the fields of motion, the probability of precipitation and others can be and have been, determined from cloud pictures. The reader is referred to Reference 51 for detailed discussions of the interpretation techniques in the use of satellite photographic data.

Figures 64 and 65 have been included to demonstrate the increase in detail between the photographs obtained by astronauts on manned space flights and television photographs. Figure 64 shows a photograph taken from Gemini 10 over the northeast coast of South America. The details observed in this photograph (even when reproduced in black and white) can be compared with the photograph taken by Nimbus II of the same region some three hours later (Fig. 65).

In addition to the satellite photographs, it was noted that visible satellite observations have included radiometric measurements of the energy reflected from the surfaces of the earth, sea surfaces and cloud top surfaces. These measurements have been used to deduce the albedos of the various types of surfaces. Studies^{53, 54} of energy balance of the atmosphere have also made use of such data. Greaves et al.⁵⁵ have also found such measurements useful in the delineation of clear from cloud areas.



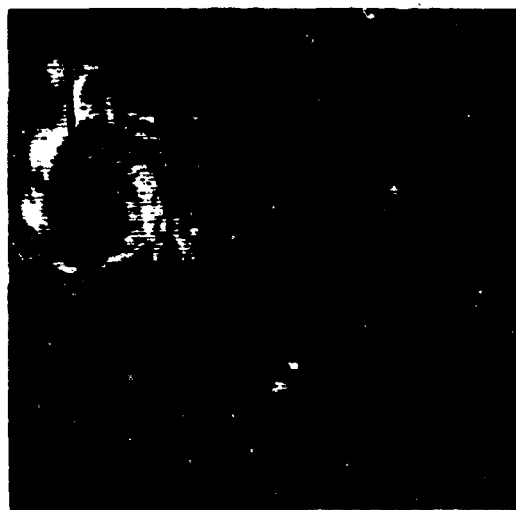
Intense Tropical Storm



Typhoon



Hurricane



Dissipating Tropical Storm

Figure 62. Satellite Depictions of Tropical Storms and Cyclones



Figure 63. Satellite Depictions of Cyclones at Various Stages of Development



Figure 64 Gemini X Photograph of the Northeast Coast of South America

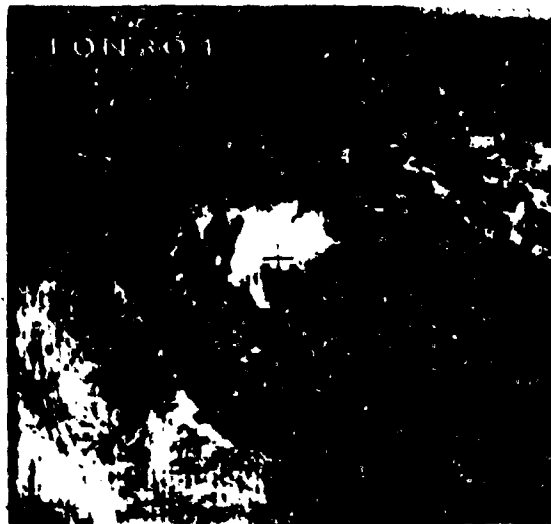


Figure 65. Nimbus Photograph of the Northeast Coast of South America

9.4 Applications of Optical Lasers to Geophysical Observations from Satellites

9.4.1 Introduction

With the advent of the laser as a useful source of energy in the optical and near infrared regions, the possibilities of making radar-like measurements at optical frequencies have been investigated by a number of investigators. Some of these possibilities and the technical difficulties in their realization are discussed below.

9.4.2 Lasers

A laser probing system is an "active" system requiring a transmitter and a receiver with the sampled portion of the atmosphere separating the two. In satellite operations, the transmitter and receiver must, of necessity, be coaxial or near coaxial with both transmitter and receiver beams pointing in the same direction. Consequently, only those techniques which measure the information content of the back-scattered energy are appropriate to satellite operations.

Of the available laser types (rod, gas, injection or solid state), the one that now seems most appropriate to satellite operations in terms of its capability of delivering high beam energy density over a long transmission path is the Q-spoiled giant pulse ruby rod laser. The unmodified pulse from a ruby laser is composed of a random series of spikes of energy spread out over 200 to 500 μ secs. In order to achieve high power output, the energy is concentrated in a single pulse of short duration (\sim tens of nanosecs) by means of Q-spoiling techniques where the optical resonance cavity of the laser is formed for only a few nanosecs. The usual method of Q-spoiling or Q-switching employed has been the use of a rotating prism or mirror to form one end of the resonant cavity. Other methods such as a combination of a Kerr Cell and Wollaston prism have been used.

When operated in the giant pulse mode, a laser sounding system is essentially a pulse radar in the optical frequencies. "Target" information is contained in the characteristics of the backscattered energy. Range or the "target" is derived from the measurement of the time lapsed between the emission of the transmitted pulse and the reception of the signal. Unlike microwave pulsed radar, a pulsed ruby laser system cannot now be operated in a scanning mode due to the low pulse repetition rate presently available (on the order of one pulse per minute). This

limitation is imposed on the ruby laser by the methods used in optical pumping and heat dissipation. When operated in this mode, the ruby laser has a power efficiency of only 0.1%. With the limited power available in a satellite a laser system would be probably limited to single pulse operations over selected "targets."

The advantages of a laser radiation source over other sources in the optical frequencies are its intensity, monochromaticity and coherence. Beam divergence can be limited only by diffraction. Divergence on the order of 1 foot in 190 miles has been achieved.

The coherence of the transmitted light permits, in theory, coherent detection schemes which would reduce background noise to the spectrum occupied by the signal. Unfortunately, the state-of-the-art is such that it is not yet possible to take operational advantage of this mode of detection. There is at present no sufficiently stable local oscillator which could provide the difference in frequencies needed for the RF region at which amplification filtering and other signal processing is possible.

The high frequencies at which optical lasers work would make them ideally suited to measurements of small velocities by Doppler techniques. However, Doppler measurement techniques have to await the development of high energy lasers that are truly frequency stabilized. There is also the technique of photo-mixing which would have to be perfected.

9.4.3 Obscurations and Targets

If "obscurations" are defined as those objects or phenomena which attenuate the transmitted beam so as to reduce its maximum range, then certain classes of "obscurations" form also the "targets" of interest. Electromagnetic energy is attenuated by absorption and scattering. Absorption is effected by the gaseous components of the atmosphere as well as by suspended solid particles. Gaseous absorption is localized in frequency in terms of absorption lines and bands.

The telluric absorption spectrum has been extensively studied. The possibility of lasers in communications has spurred further interest in the telluric absorption spectrum especially in the visible and near infrared, the region in which laser emission lines are located. The studies of Long⁷⁸ provide valuable information concerning the absorption of laser radiation in the atmosphere.

The scattering of energy from the transmitted beam is by the air molecules themselves, suspended particles (aerosols), clouds and any object within the transmitted beam which has a scattering cross-section. The theory of scattering for spherical scatterers has been extensively treated in the literature. A comprehensive treatment of both the limited theory of Rayleigh and the general theory of Mie are presented in the work by Van de Hulst.⁷⁹ Tables of scattering functions for a Rayleigh atmosphere are available.⁸⁰ Scattering functions for a non-Rayleigh atmosphere are also available for certain wavelengths based on the aerosol distributions of Junge.⁸¹

Scattering functions of clouds of selected cloud droplet distribution have also been computed by many authors. In principle, it is possible to calculate the scattering function of any object for any wavelength by the application of the scattering theory of classical electromagnetics.

It must be pointed out that scattering, which attenuates the beam, is also the mechanism which provides the ultimate information in any laser probing technique.

There is one form of "obscuration" which does reduce the maximum range of a laser system independent of the parameter to be sampled. This is the background noise level. There is present in the atmosphere, especially during daylight hours, a certain D. C. level of light intensities. This is mainly the results of scattered solar energy. This background noise reduces the signal-to-noise ratio for any detection system, thus limiting the maximum range or sensitivity. Background levels for various conditions have been measured by many research groups. A summary of the contributions from such sources as the moon, clouds, the earth's surface and airglow is given in a report by Boeing.⁸²

9.4.4 Laser Probing Systems in Use

There is at present no satellite-borne laser probing system. Some ground-based laser systems for atmospheric work have been built. These are of two types. The first type is essentially a ranging system for the location of cloud layers and aerosol layers in the atmosphere. The other type attempts to measure the concentration of a gaseous (e.g., water vapor) component of the atmosphere. The second type depends on the thermal tuning of a ruby laser and the coincidence of a water vapor absorption line with the ruby line.

In the simple ranging technique, a cloud layer or an aerosol layer is presented as a region of enhanced return (spikes). The range or altitude of the layer is derived from the angle of the beam and the time lapsed between the emitted pulse and the reception of the signal similar in nature to the radar "A" or "R" scope presentation. This similarity has led to the rise of the term "lidar" (light detection and ranging) for this laser application.

Some qualitative statements have been made of the size distribution of the scatterers based on assumptions made of the nature and shape of the scattering particles. Scattered returns from over 130 km have been detected, making it obvious that lidar is an excellent candidate for observation from orbit.

The measurement of water vapor method is based on the differential absorption of energy at two adjacent wavelengths. The difference in the measured backscattered energy between a pulse in an absorption line or band and one just outside of the band should provide the information necessary to deduce the water vapor structure in the atmosphere, provided a knowledge of the band absorption coefficient is known.

All of the ground-based systems described use a pulsed ruby laser in the Q-switch mode as transmitter and a low noise high gain photomultiplier as detector. The photomultiplier with an S-20 surface is still the best detector in the frequency region. Methods for computing signal-to-noise ratios for such a system are well developed. Optical components for such systems have also been well investigated.

Other proposed laser measurements suitable for satellite applications are:

Resonance Scattering

Delgano⁸³ has pointed out that the backscattered cross-section in the peak of resonance line of a gas should increase by many orders of magnitude due to the anomalous nature of the index of refraction at resonance. They have derived the equation for the scattering cross-section at resonance. Since the total scattered cross-section is a function of the number density of the gas, it should be possible to measure gas concentrations in the atmosphere by using a laser which operates in a frequency corresponding to a resonance line of the gas whose concentration is desired.

No experimental systems based on the technique have been reported. Calculations of scattered cross-sections at resonance are available only for sodium. Such calculations are not exceptionally difficult to perform and should not be a

scattering block. The main problem is the availability of lasers operating in frequencies corresponding to resonance lines which would produce a scatter cross-section large enough as not to be masked by the process of normal Rayleigh and Mie scattering.

Doppler Measurements of Velocities to Infer Temperature

The method of temperature sounding by means of Doppler measurements of the velocity distribution of the gas molecules has been proposed by Schotland, et al (1962).⁸⁴ The theory presented is based on the relation between the velocity distribution and the kinetic temperature of a gas given by the Maxwell-Boltzmann equation. System characteristics for both a pulsed and CW laser needed for such measurements are presented in the cited reference. The present state-of-the-art cannot meet these requirements. The problem of a local oscillator for RF superheterodyning has also to be solved.

Possible Laser Applications

<u>Parameter</u>	<u>Technique</u>
Cloud top heights	Simple ranging
Multilayer clouds	Simple ranging
Aerosol layers	Simple ranging
Temperature	Doppler
Water vapor and other gas constituents	Differential absorption and resonance scattering
Micro-structure of clouds	Ranging and scanning
Sea surface slope	Ranging
Sea state	Returned signal processing

9.4.5 Presentation of Data

Since a laser system is an analog of a microwave radar in the visible frequencies, the methods of presentation of radar data may be adopted for laser measurements. For simple ranging measurements an analog of the radar A-scope presentation is used. If a permanent record of the returned signal is needed, a photographic reproduction of the scope trace is made or the data can be recorded on an oscillograph. In an A-scope type presentation the amplitude of the trace is proportional to the magnitude of the backscattered energy and the distance swept out by the trace, when synchronized with the emitted pulse, is proportional to the

range. In order to minimize the length of the sweep and yet not lose the details in the regions of interest, a variable time delay mechanism may be built into the oscillograph - laser system such that the sweep is initiated at a predetermined interval after the emission of the pulse, the "R" scope. The sweep rate can also be made variable. This method of data presentation is the one in use at present by the ground based systems cited previously.

Similarly, for Doppler measurements by laser, when it becomes possible, the techniques presently in use by Doppler radars for data presentation may be adapted.

SECTION X

INFRARED OBSERVATIONS AND MEASUREMENTS

10.1 Introduction

It was pointed out in Section III that, at the range of temperatures characteristic of the earth and atmosphere, the radiation emitted is spectrally concentrated in the infrared region. Remote measurements made in the infrared are, therefore, usually related to the thermal properties of the earth and atmosphere.

Before proceeding to an analysis of the geophysical parameters deducible from IR measurements, it might be well to first relate the IR radiation arriving at a satellite sensor to the various sources on the surfaces of the earth and in the atmosphere. These relationships can best be described in terms of the radiation transfer equation which is developed below. On the basis of this equation, it is possible to delineate the major types of IR observations.

From the discussions of the sources of IR radiation presented in Sections IV and V, it is seen that the radiance, N , arriving at a satellite sensor, in general, consists of contributions from the surface and from the atmosphere. Consequently, N , can be written as

$$N = N_s + N_a \quad (127)$$

where

N_s = radiance contributed by the surface

N_a = radiance contributed by the atmosphere.

In the IR regions in which reflected solar radiation is not a significant contributing source (i.e. $\lambda > 4\mu$), the surface contribution term in Equation (127) can be explicitly given as

$$N_s = \epsilon_s N_b(T_s) \tau_a \quad (128)$$

where

ϵ_s = surface emissivity

T_s = surface temperature

N_b = blackbody radiance

τ_a = transmissivity of the total atmosphere

(It should be noted that the spectral dependence of the terms in Equations (127) and (128) though not explicitly indicated, is assumed).

In order to evaluate the atmospheric contribution term, N_a , let the atmosphere be stratified into n layers as shown in Figure 66. The radiance emitted by the layer (n) at the top of the atmosphere is given by Equation (93) (Section V) as

$$N_n = \epsilon_n N_b(T_n) \quad (129)$$

where

ϵ_n = emissivity of the n^{th} layer

T_n = mean temperature of the n^{th} layer

$N_b(T_n)$ = blackbody radiance at temperature T_n

Since, it has been assumed that no atmosphere exists above this layer, N_n reaches the satellite unattenuated, i.e.,

$$N'_n = N_n$$

where

N'_n = radiance received by the satellite from the n^{th} layer
(see Figure 66).

An expression similar to Equation (129) may be derived for the next layer, i.e., the $(n-1)$ layer as

$$N_{n-1} = \epsilon_{n-1} N_b(T_{n-1}) \quad (129a)$$

However, the radiance emitted by this layer must propagate through the n^{th} layer before reaching the satellite. Consequently the radiance contribution from this layer, N'_{n-1} , is given by

$$N'_{n-1} = \tau_n N_{n-1}$$

where

τ_n is the transmissivity of the n^{th} layer.

or

$$N'_{n-1} = \epsilon_{n-1} N_b(T_{n-1}) \tau_n$$

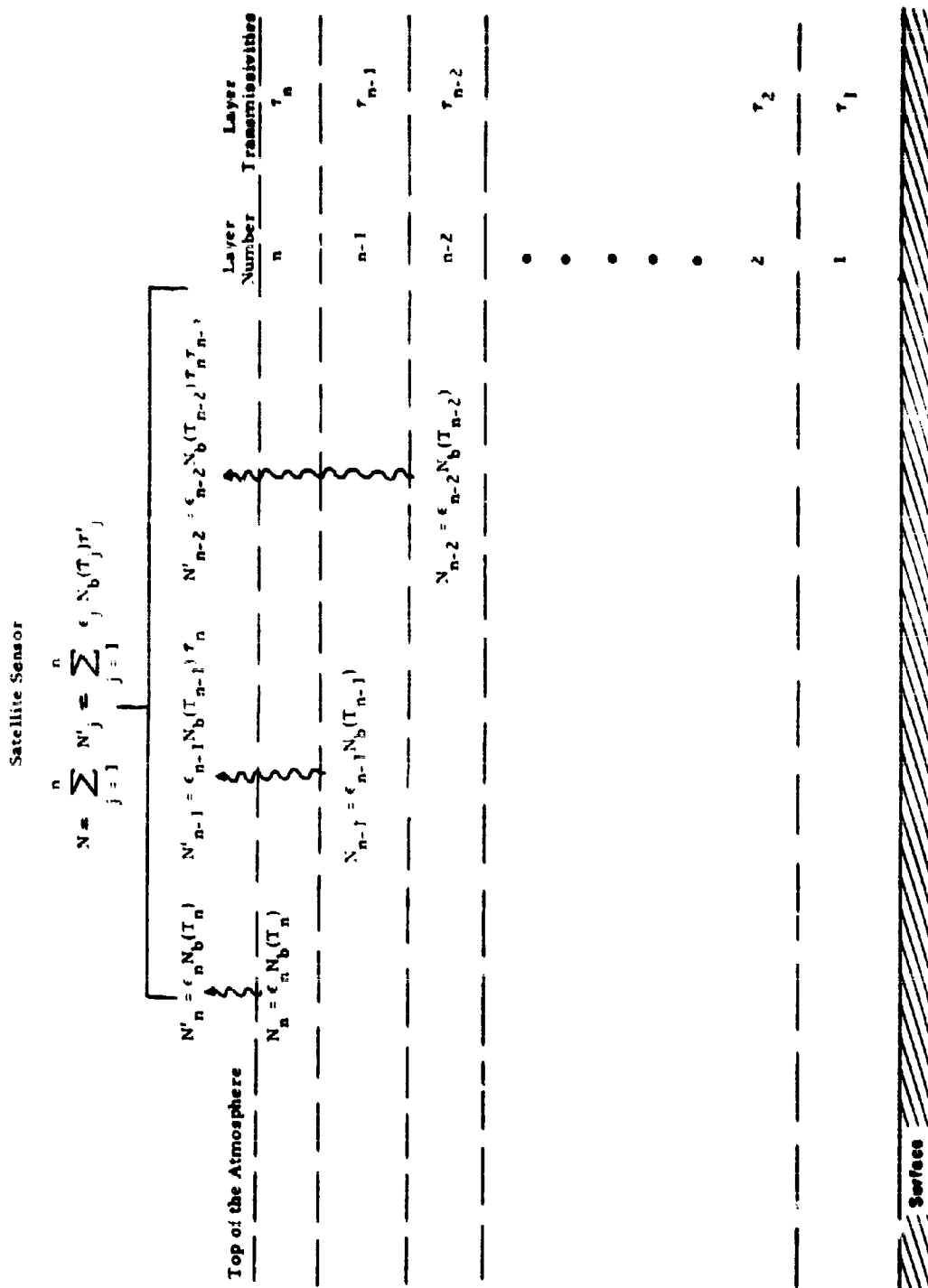


Figure 66. Schematic of Stratified Atmosphere

By applying this argument to each of the layers in succession, the radiance contribution, N'_j , of the j^{th} layer is given by

$$N'_j = N_j \times \tau_{j+1} \times \tau_{j+2} \times \dots \times \tau_n \quad (130)$$

where

$\tau_{j+1}, \tau_{j+2}, \dots, \tau_n$ are the transmissivities of the atmospheric layers above the j^{th} layer, and

$\tau_{j+1} \times \tau_{j+2} \times \dots \times \tau_n$ is the transmissivity of the total atmosphere above the j^{th} layer.

The mathematical form of Equation (130) can be simplified by letting

$$\tau_{j'} = \tau_{j+1} \times \tau_{j+2} \times \dots \times \tau_n.$$

Then

$$N'_j = \epsilon_j N_b(T_j) \tau_{j'} \quad (130a)$$

It is seen, therefore, that the contribution from each layer in the atmosphere depends on (1) the emissivity and the temperature of the layer itself, and (2) the transmissivity of the atmosphere above the layer.

Using Equation (130a) the total atmospheric contribution to the radiance received at the satellite is then the sum of the contribution from each of the layers, i. e.,

$$N_A = \sum_{j=1}^n N'_j = \sum_{j=1}^n \epsilon_j N_b(T_j) \tau_{j'} \quad (131)$$

Combining Equation (131) with Equation (128), Equation (127) becomes

$$N = \epsilon_s N_b(T_s) \tau_s + \sum_{j=1}^n \epsilon_j N_b(T_j) \tau_j \quad (132)$$

(NOTE: $\tau_s = \tau_1 \times \tau_2 \times \dots \times \tau_n$)

Equation (132) relates the IR radiation received at a satellite sensor to the sources of radiation on the surface and in the atmosphere. Since thick clouds absorb all incident IR (Section V), it may be concluded that in the presence of extended cloud cover, the surface emission term in Equation (132) should be replaced by the emission from cloud top surfaces. Consequently, for cloud covered situations,

$$N = \epsilon_c N_b(T_c) \tau'_a + \sum_{j=n'}^n \epsilon_j N(T_j) \tau_j \quad (132a)$$

where

- ϵ_c = emissivity of cloud top surface
- T_c = temperature of cloud top surface
- τ'_a = transmissivity of the total atmosphere above cloud top
- n' = first atmospheric layer above cloud top.

Recalling that atmospheric gas absorption and emission are spectrally dependent, it may be concluded that the significance of each of the terms in Equation (132) is also spectrally dependent. Consequently, there are three basic types of IR observations. The first type is made in an infrared window region, in which the surface term dominates. The parameters deducible from these measurements are related to surfaces - the sea surface, the surface of the earth, or cloud surfaces - within the field of view of the sensor. The second type is made in absorption bands of one or more of the optically active gases of the atmosphere. In such measurements, the atmospheric contribution terms dominate. Parameters deducible from these measurements are characteristically related to the structure of the atmosphere itself. The third type of measurement is made over a very broad spectral region in the infrared. These measurements provide information on the total infrared radiation leaving the earth-atmosphere system as a whole.

In the following sections, a study is made of the significant geophysical parameters deducible from each of these types of IR measurements. Discussions of the geophysical degradation effects are also included.

10.2 Infrared Window Observations

In a perfectly clear window (i.e., a spectral region in which the atmosphere does not exist or absorb radiation). Equation (131) or Equation (132a) reduces to

$$N = \epsilon_s N_b(T_s) \text{ (in the absence of clouds)} \quad (133)$$

or

$$N = \epsilon_c N_b(T_c) \text{ (in the presence of clouds)} \quad (133a)$$

Furthermore, it was shown in Sections IV and V that the IR emissivities of most surfaces can be approximated by 1. Equations (133) then reduce further to

$$N = N_b(T_s) \quad (134)$$

or

$$N = N_b(T_c) \quad (134a)$$

It is seen therefore that the radiance measured in a perfect IR window is the radiance emitted by a blackbody at the temperature corresponding to the temperature of the surface viewed by the IR sensor. Because of the unique dependence of blackbody radiance on temperature (Section II), the measured radiance is then uniquely related to the temperature of the surface viewed.

10.2.1 Geophysical Degradation Factors in Infrared Window Measurements

The prime geophysical parameter of interest in infrared window measurements is a surface temperature. The extent to which a sensor can detect this temperature depends on the degree to which following assumptions, made in the derivation of Equations (134), are fulfilled in practice

1. Perfectly clean atmospheric window
2. No reflected or scattered energy from extraterrestrial sources
3. The surface within the field of view of the sensor is uniform, and may be characterized by a single temperature, T .
4. Within the spectral region specified by the response of the sensor, the emissivity of the surface may be considered to be equal to 1.

To the extent that these assumptions are not completely fulfilled, there will exist a difference between the measured effective blackbody temperature, T_{bb} , and the actual temperature of the surface being measured. In the following paragraphs, these effects are analyzed.

10.2.1.1 Atmospheric Absorption Effects

In Section V, it was shown that the infrared windows are not perfectly clean. The 8 to 13 μ window, for instance, spans a spectral region containing an ozone absorption band centered at 9.6 μ , and residual absorption due to water vapor and carbon dioxide. These residual gaseous absorptions have the effect of reducing the radiance measured by the sensor and, therefore, lower the measured effective temperature. In order to compensate for these attenuation effects to arrive at corrected surface temperatures, the atmospheric terms in Equations (131), though small, must be evaluated.

However, as pointed out in Section V, the inclusion of these terms require a knowledge of the vertical distribution of the absorbing gases in question. The distributions of ozone and water vapor are variable in both time and space. It would be impractical to attempt to compute corrections for each individual satellite measurement, even if the necessary data were available for the computations.

Wark, et al⁵⁷ devised a method of estimating these correction factors. A detail discussion of the procedure may be found in their report. In summary, they applied the equation of radiation transfer, to 103 atmospheric soundings having various typical but different distributions of temperature, moisture and ozone. The effective temperatures which would be detected by the radiometer under these different sets of conditions were then computed for various nadir angles. From plots of the computed effective temperatures, and the corresponding surface air temperatures of the soundings, they derived an empirical relationship relating the magnitude of the temperature correction to the effective temperature measured by the sensor, the sensor nadir angle and a moisture parameter which is dependent on the total precipitable water in the atmospheric column. Although their results are strictly applicable only to the window channel of the scanning radiometer of TIROS II, it is instructive to examine the magnitude of the errors introduced by atmospheric gaseous absorption in this broad window. For this reason, the empirical equation derived by Wark, et al, was solved for a range of effective temperatures for nadir angles = 0° and 45°. The results of these computations

are shown in Figure 67. Along the ordinate is plotted the total precipitable water in the atmosphere (in centimeters). The abscissa values are the temperature corrections which must be added to the effective temperatures. The satellite measured effective temperatures are shown as curve lines in the graph.

The magnitude of the effect of attenuation on surface temperature measurements depends, of course, on the intensity of the residual gaseous absorption in the spectral region of the response of the sensor. The Nimbus HRIR (High Resolution Infrared Radiometer), for example, operates in the 3.4μ window region where residual gaseous absorption is less intense than in the 8μ to 13μ region (Section V). Kunde⁵⁸ has made computations using the magnitude of the temperature correction for this particular radiometer. These are reproduced in Figure 68. Comparison of these curves with those shown in Figure 67 reveals that, on the whole, atmospheric attenuation is less significant in this spectral region than in the broader window.

Based on the same argument, measurements made in a narrower spectral interval near the center of the 8μ to 13μ window, but away from the 9.6μ O_3 absorption band, should also reduce the magnitude of the gaseous attenuation effect. In fact, this has been done in the medium resolution infrared radiometer (MRIR) of Nimbus II. At the time of this report, the digitized data from this particular radiometer were not available for evaluation so that no assessment of the improvement can be made here.

10.2.1.2 Particulate Attenuation

Another source of significant atmospheric degradation of infrared window measurements appears to be the presence of "invisible" clouds. Attenuation of infrared energy by atmospheric aerosols, due to absorption and scattering, is normally insignificant. However, when such aerosols exist in large concentrations their usual effect is, again, to lower the measured effective temperature.

It has been postulated that a layer of very tenuous cirrus clouds are often present in the atmosphere, although "invisible" to ground observers and satellite television cameras. There is currently, no practical way to handle these attenuation effects. For a detailed discussion of these problems, the reader is referred to the study performed by Hale, et al.³¹

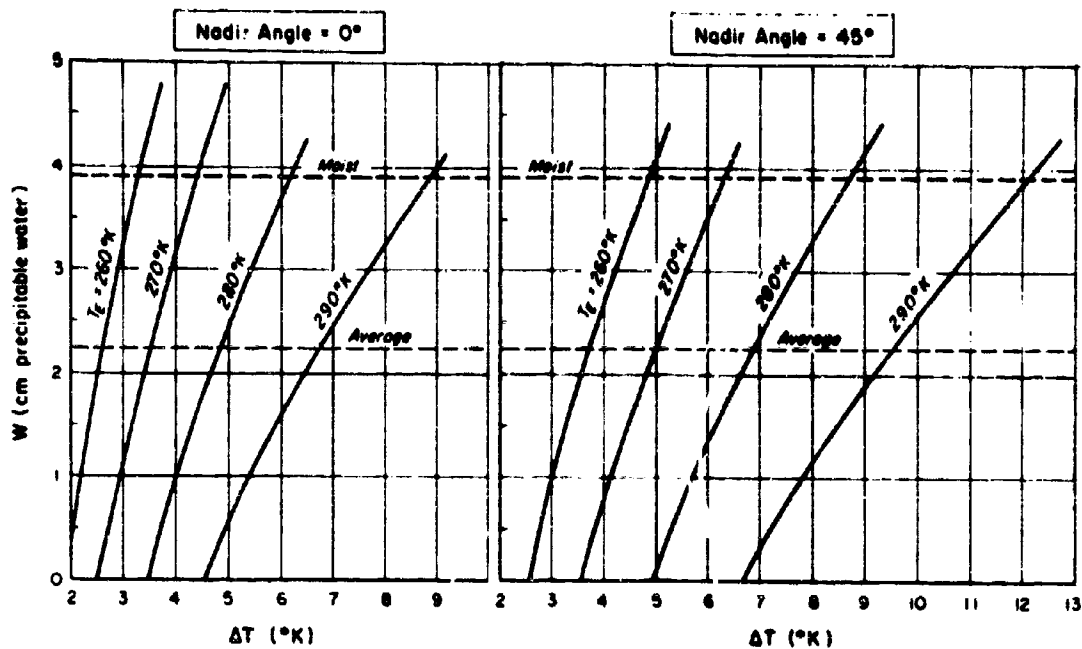


Figure 67. Clear Sky Temperature Corrections for Window Channel of TIROS VII

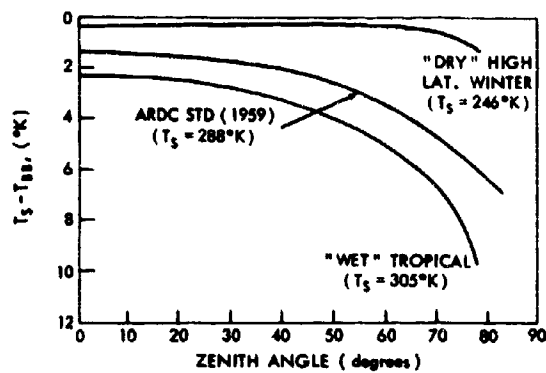


Figure 68. Clear Sky Temperature Corrections for Nimbus HRIR

10.2.1.3 Solar Contamination Effects

Nighttime infrared window measurements are generally free from reflected radiation. Daytime measurements, in the shorter wavelength infrared windows, are contaminated by reflected solar radiation. This has been clearly evident in the measurements made by the Nimbus HRIR (3 μ to 4.5 μ region). Reflected solar radiation is still quite significant at these wavelengths. Wexler³⁴ has computed the degradation effects of solar radiation on measurements made by this particular radiometer, based on the assumption of isotropic reflection. The parameters he used to make his computations are solar zenith angle, and the albedo of the reflecting surfaces. The results of his computations are shown in Figure 69. It should be noted that the corrections are negative, i.e., reflected solar radiation adds to the measured effective radiance or the equivalent blackbody temperature. As a result, the measured temperatures are higher than what they should be.

In the 8 μ to 13 μ window region, solar irradiance is insignificant, and it has not been found necessary to correct for reflected radiation even in daylight measurements. Consequently, 8 μ to 13 μ window measurements are as effective during daylight hours as at night.

10.2.1.4 Non-Uniformity of the Surface Viewed

The spatial resolution of an infrared sensor has finite dimensions. The possibility exists, therefore, that different portions of the surface area viewed by the sensor have different characteristics. Neglecting the problem of non-uniform emissivity, there is still the possibility of non-uniform surface temperatures. In many instances, the gradient of surface temperatures are insignificant when compared with the sensitivity and resolution of the sensors. However, there are some very significant cases in which the non-uniformity of the surface temperature within the field of view may lead to problems of data interpretation. The most common of these are those cases in which the field of view of the sensor is partly filled by high cold clouds and partly filled by the warmer surface below the clouds. The measured effective temperature then corresponds neither to that of the cloud top nor that of the surface below. A similar situation exists when the sensor views the edge of a cloud with vertical development. The area of the cloud viewed by the sensor then has a temperature gradient of the order of magnitude of the mean vertical lapse rate of the atmosphere ($\sim 6.5^\circ \text{K/km}$). The resulting measured effective temperature is again difficult to interpret.

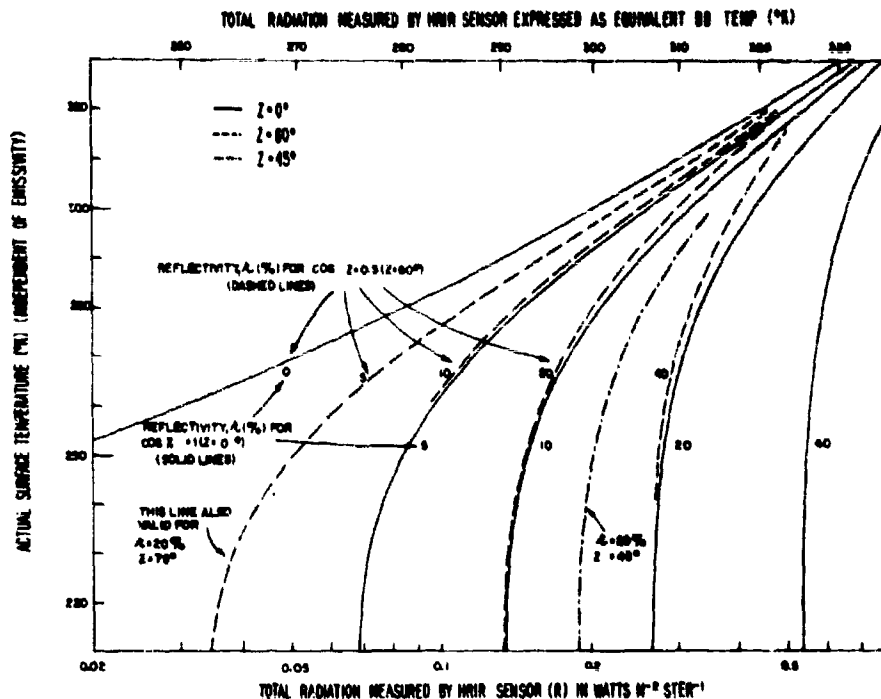


Figure 69. Quantitative Relationships Between Temperature of a Radiating Surface, Total Radiation as Measured by HRIR, and Solar Reflectivity

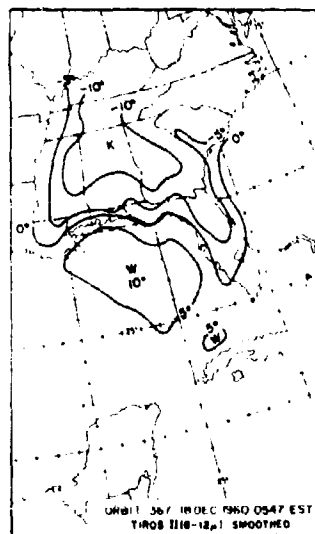


Figure 70a. Field of Effective Temperatures from TIROS II, Orbit 367 at 0547 EST, 18 December 1960

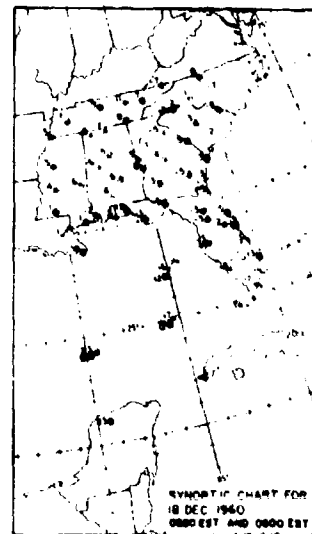


Figure 70b. Synoptic Chart for 0500-0600 EST, 18 December 1960

10.2.1.5 Emissivity Effects

In most instances, the assumption of blackbody emissivity ($\epsilon = 1$) has not been found to be the most significant source of error in the determination of surface temperatures for the two prominent infrared window regions (i.e., 3.4 μ to 4.0 μ and 8 μ to 13 μ). Even for a ground resolution as good as 8 km, (the resolution of the Nimbus HRIR), no case has been found where the measured effective temperature variations could be clearly identified with variations in surface emissivity. Nordberg et al.⁵⁹ state that effective detection of surface features by means of emissivity differences, from spacecrafts, will only be possible if the spatial and spectral resolutions of current infrared window sensors are improved by several orders of magnitude.

10.2.2 Geophysical Parameters Deducible from IR Window Measurements

10.2.2.1 Surface Temperatures

The primary geophysical parameter deducible from IR window measurements is surface temperature. In the absence of cloud cover, the measured equivalent blackbody temperatures, when properly corrected for degradation effects, should correspond to the actual surface temperature. Even when correction factors are not available, the patterns of surface temperatures should be deducible from such observations.

In an early study of data obtained by the IR window sensor of TIROS II, Roa and Winston⁶⁰ found that the uncorrected equivalent blackbody temperatures obtained over a clear area corresponded quite well with the concurrently obtained surface air temperatures. Figures 70a and 70b, taken from their study, illustrates this point. The analysis of the equivalent blackbody temperatures measured by the satellite is shown in Figure 70a. The concurrent synoptic chart for the region is shown in Figure 70b. Clear sky conditions prevailed over the region at the time of the satellite observations. When the analysis of equivalent blackbody temperatures is compared with that of surface air temperatures, the correspondence between the two is quite apparent.

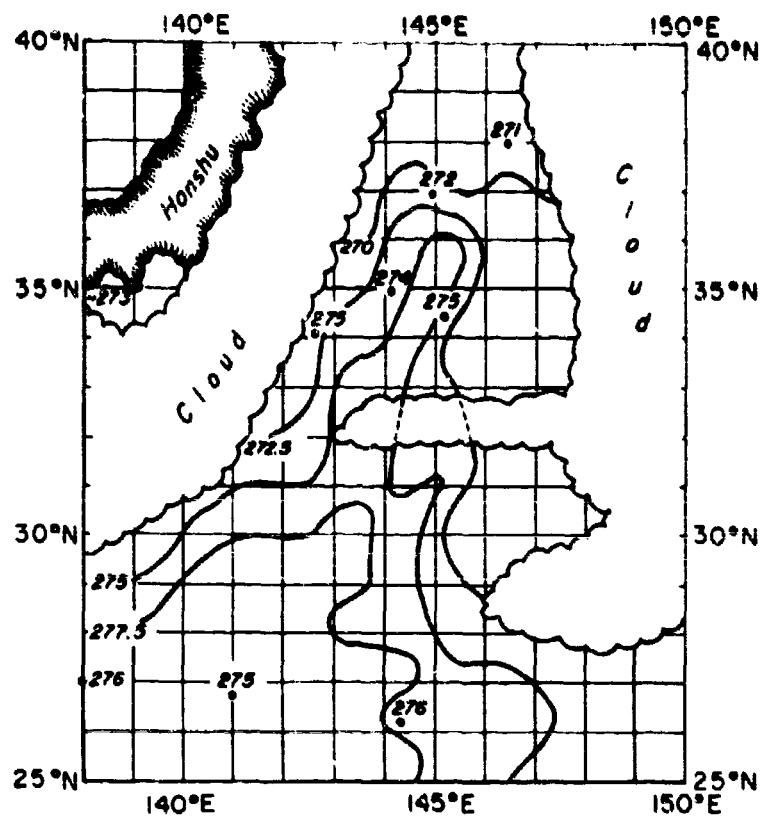
Greaves, et al.⁵⁵ studied the feasibility of applying satellite IR window measurements to the determination of sea surface temperatures. The satellite data they used were those obtained by TIROS VII. Their efforts were hampered by a number of factors, including (1) frequent lack of concurrent satellite television picture data, or conventional surface observations over the oceans for determining clear sky conditions, and (2) the inadequacy of ship reports of sea surface temperatures for comparison. In spite of these difficulties, they demonstrated that while it may be difficult to obtain absolute measurements of sea surface temperatures using the IR window data from satellites, good measurements of the gradients of sea surface temperatures can be obtained.

An example of one of the cases studied by Greaves, et al. is shown in Figure 71. The area investigated is in the vicinity of the Kuroshio Current. The isotherms drawn in the figure are for 0.5°K increments of equivalent blackbody temperature. The absolute values of the isotherms shown have been adjusted to fit concurrent ship reports of sea surface temperatures. However, the gradient of the equivalent blackbody temperatures have not been changed.

It may be seen in this analysis that the gross outlines of the warm Kuroshio current can be seen to the southeast of Japan. The usual north-south temperature gradient in this region for the month of August (the IR data were obtained on 11 August 1963) is from 294 to 301°K, or a difference of about 7°K, which is in agreement with the temperature gradient as analyzed from the IR data.

No detail study of the applicability of the data obtained by the HRIR of Nimbus to surface temperature determinations is available. Preliminary analysis of limited samples of the data performed by Nordberg and Samuelson⁵⁹ indicates, however, that better correlations between the equivalent blackbody temperature as measured by this sensor and the actual surface temperature can be expected.

One of the major problems in the use of satellite IR window data in the determination of surface temperatures is in the delineation of adequately cloud free areas. This problem is particularly acute when concurrent satellite television pictures, or ground observations of cloud cover are not available. While it is possible to use the IR window data themselves to delineate cloud cover areas (see Section 10.2.2.2), ambiguities quite often exist in cases involving scattered or broken clouds, thin clouds, low clouds, fog and haze, and snow covered regions. Widger, et al.³⁴ in their detailed study of the IR window data obtained by the HRIR of Nimbus I, concludes that the only real proof that an area is clear, is the visibility



• Normalized Ship Reports

Figure 71. Sea Surface Temperature Pattern as Observed by TIROS VII, Orbit 779, in the Vicinity of the Kuroshio Current

of identifiable landmarks in the IR data. For a full discussion of the problems involved in cloud covered-clear area discrimination using satellite data, the reader is referred to Reference 34.

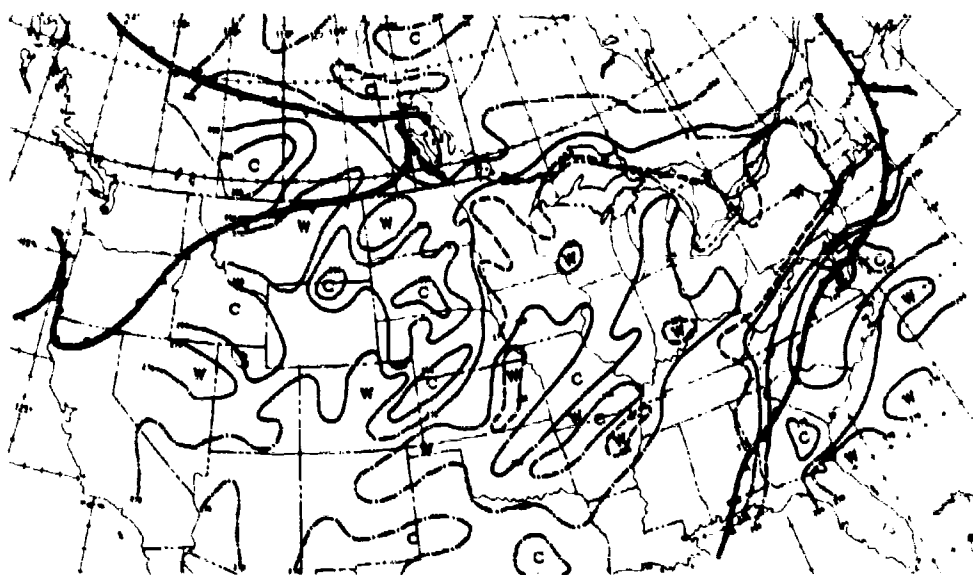
It should also be kept in mind that the HRIR of Nimbus has its spectral response located in the 3.4 to 4 μ region in which solar contamination, is a significant degradation factor in daytime measurements. Consequently, the data obtained by this sensor during daylight portions of the orbit cannot be applied to the determination of surface temperatures.

10.2.2.2 Cloud Cover

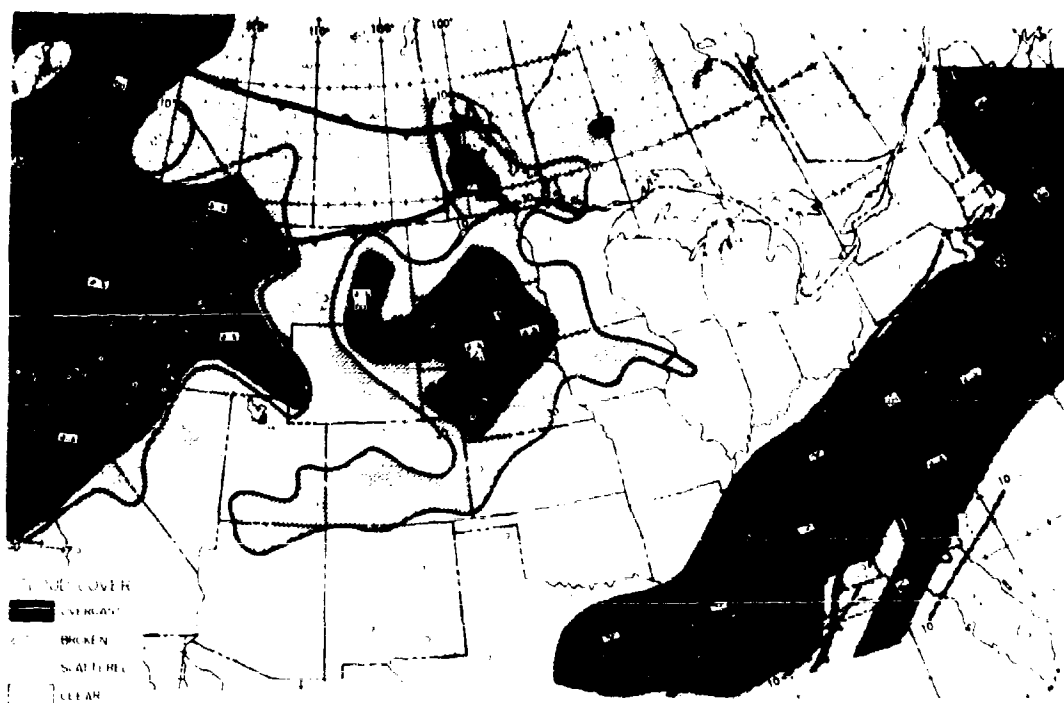
Over cloud covered regions, a satellite IR window sensor measures the temperature of the cloud tops. Since cloud top surfaces are generally colder than the surfaces of surrounding clear areas, it would be possible to delineate cloud covered areas from cloud free areas in an analyzed field of IR window equivalent blackbody temperatures. To a first approximation, areas observed to have relatively warm temperatures are likely to be clear (exceptions exist in polar regions and for fog and low clouds). Areas with colder temperatures are likely to be cloud covered. Areas of abrupt temperature gradients in the data can usually be assumed to indicate the boundaries between clear and cloudy areas, or between areas with high and low clouds, except when boundaries between land and water bodies are observed.

The reader must be warned that while these criteria are useful, the difficulties and ambiguities in the use of IR data for the delineation of cloud cover noted in Section 10.2.2.1 must be kept in mind, when these criteria are applied. (Examples of some of the problems involved are shown in Figures 76 and 77.)

The use of IR window sensor measurements in the determination of cloud cover is shown in Figures 72a and 72b. The radiation data is from TIROS II. The analyzed T_{bb} temperature field (without atmospheric absorption corrections) is shown in Figure 72a, which also includes the locations of surface fronts determined from conventional data. It may be seen in this figure that a band of low T_{bb} values, extending in a northeast-southwest direction, is located in the eastern part of the United States with lowest temperature about 240°K. The T_{bb} values, over the



i



central United States is fairly uniformly high ranging from 280° to 285° K. Based on what has been said of the relation between T_{bb} values and the surface emitting temperatures, the band of low equivalent temperatures along the east coast of the United States should be associated with a band of high cloud overcast straddling the surface frontal zone, and the region of high T_{bb} 's in the central United States should correspond to a generally clear area. This general pattern of cloud cover derived from the radiation data, is confirmed by the nephanalysis shown in Figure 72b.

The ability of IR window sensors to discriminate between cloud covered and cloud free regions makes them highly useful observational tools especially at night when present satellite television cloud cover pictures are not available. One of the principal motivations in the development of the Nimbus HRIR was to provide cloud cover observations to complement the television coverage available only during daylight portions of the orbit.

Besides having a higher spatial resolution, the data obtained by the HRIR are presented automatically, in a photofacsimile format in which the measured effective temperatures are displayed in 10 shades of grey, with warm temperatures represented by the darker shade of grey, and cold temperatures represented by lighter shades. Since the effective temperatures measured over cloud covered regions are generally colder than those obtained over clear regions, clouds are represented in the photofacsimile presentation in lighter tones, with the highest (and therefore coldest) clouds appearing as white. This format of data presentation eliminates the tedious process of analysis needed to derive cloud cover information from the measured effective temperatures.

Examples of cloud cover as depicted by this format have been shown in previous sections of this report. Other examples are shown in Figures 56a, 73a, and 73b, which are respectively (a) cloud vortex, a frontal cloud band, and a hurricane, (b) cloud pattern associated with a well developed shortwave, (c) cloud cover pattern associated with lee waves. An example of the technique used to depict cloud cover over a large region is shown in Figures 74 and 75. The photofacsimile data obtained by the satellite on adjacent orbits have been assembled together to form a mosaic. Figure 75 shows the concurrent NMC 500 mb analysis and frontal analysis superimposed on the HRIR data mosaic.

Examples of ambiguities in cloud cover determinations in IR window measurements are shown in Figure 76a and in Figure 76b. In Figure 76a, the isothermal analysis of the equivalent blackbody temperatures obtained by TIROS II is shown

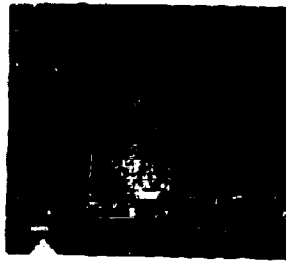


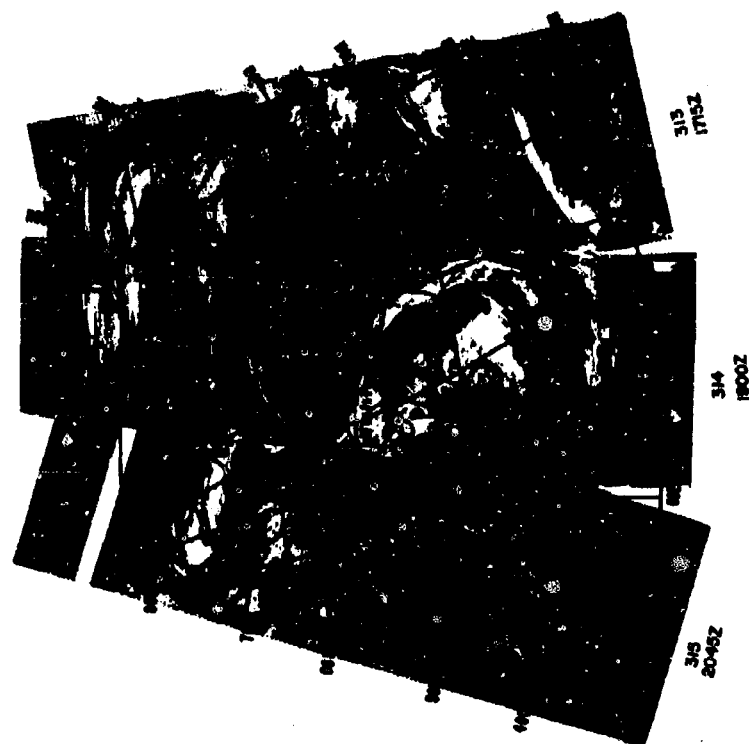
Figure 73a. HRIR View of a Well Developed Short Wave Trough



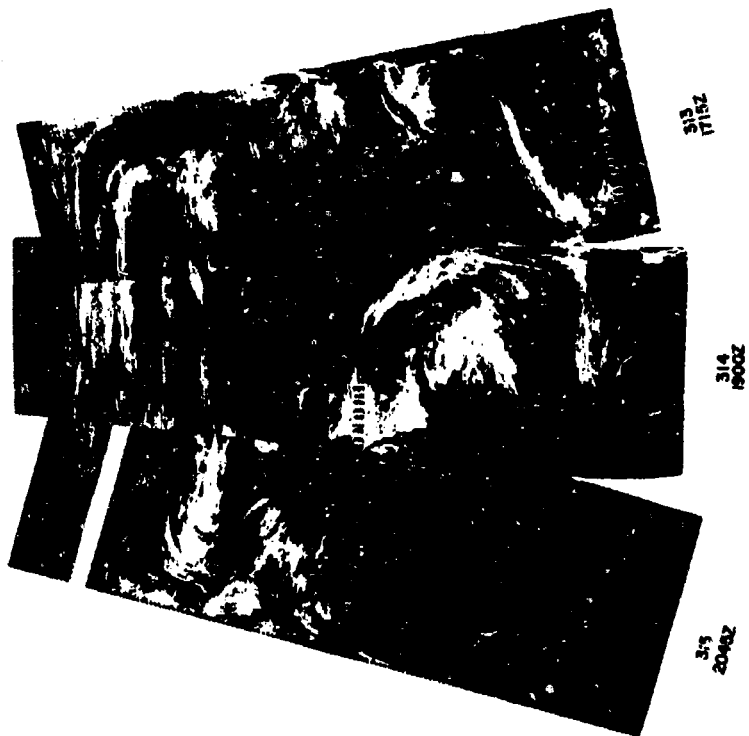
Jet Stream
Cirrus Band

Lee Wave Clouds

Figure 73b. Lee Waves as Observed in the HRIR (near 39°N, 239°E)



18 SEPT, 1964



18 SEPT, 1964

Figure 75. Mosaic with NMC 500 mb Analysis and Russian Frontal Analysis, both for 0000 GMT, 19 September 1964

Figure 74. HRIR Mosaic for 18 September 1964

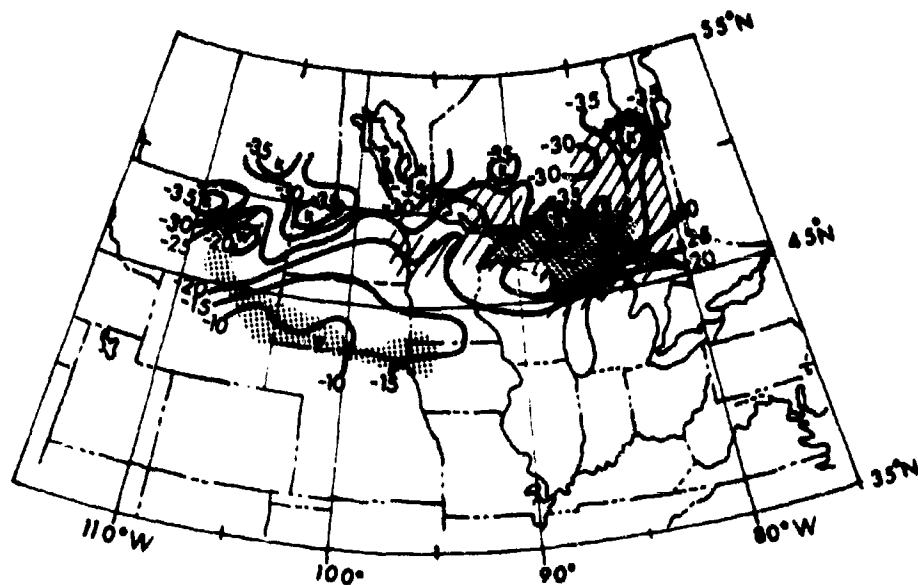


Figure 76a. Field of Effective Temperatures from TIROS II, Orbit 406 at 2150 CST, 20 December 1960, Superimposed on Cloud Cover Analysis. (Hatched area is scattered and dotted pattern is broken or overcast)

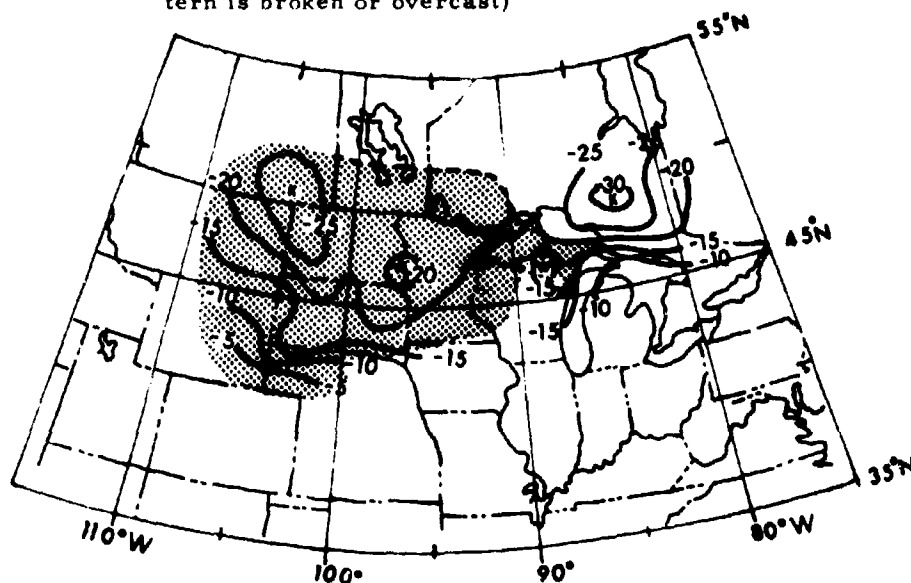


Figure 76b. Surface Air Temperature and Reported Snow Cover (dotted pattern), 2100 CST, 20 December 1960

superimposed on the cloud cover analysis based on conventional data. Very low equivalent temperatures were observed over the United States-Canadian border. Except for the cold center over Lake Superior, associated with substantial cloudiness, these low equivalent temperatures were obtained over cloud free surfaces. Examination of the snow cover map shown in Figure 76b, reveals that the region reported snow cover at the time of the IR measurements. Apparently, the surface temperature of snow cover was colder than the temperatures of some of the cloud tops. Here is a case in which the cold equivalent temperatures measured over a snow covered region can be mistakenly identified as having originated from the tops of clouds.

Figure 77 shows an example of the effects of the general equator-to-pole temperature gradient. In the figure, the area over Quebec and Labrador is significantly colder (a lighter grey in the HRIR photofacsimile presentation) than a concurrent area of low overcast over the Ohio River valley. Yet the region with the coldest equivalent temperature was noted to be definitely clear. The observed cold temperatures over this region is simply due to the general equator-to-pole temperature gradient.

Numerous examples of such ambiguities in the case of IR window data to delineate cloud cover may be found in Reference 34.

10.2.2.3 Cloud Top Height Determinations

It has been shown that when an IR window sensor views a cloud-covered region and a uniform cloud fills the instantaneous field of view of the sensor, the equivalent blackbody temperature measured by the sensor should correspond to the temperature of the cloud top surface. If the temperature in the troposphere decreases monotonically with altitude, and if the clouds do not penetrate into the stratosphere in which the temperature generally increases with height, the blackbody temperatures measured can be used to determine cloud top heights if concurrent temperature-height profiles of the area are available. However, radiosondings of atmospheric temperature is generally unavailable over data sparse areas such as the world oceans. Approximate methods must be employed based either on climatological estimates of temperature lapse rates appropriate to the regions of interest or on radiosondings of temperatures at the nearest reporting stations.

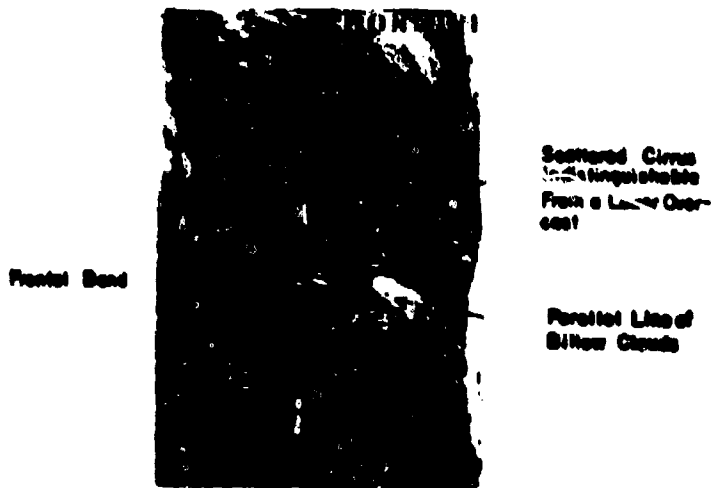


Figure 77. Illustrations of the Effects of Latitudinal and Frontal Temperature Gradients on HRIR Data

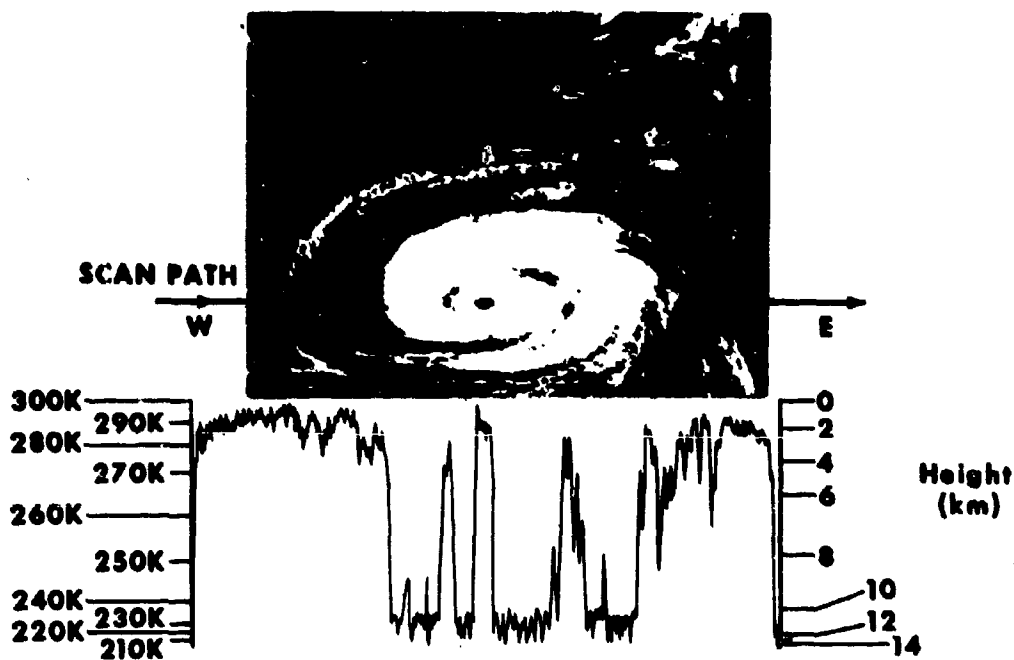


Figure 78. Cloud Top Height Determination Using HRIR Data (Hurricane Gladys)

An example of cloud top height estimation based on IR window temperatures is shown in Figure 78, which shows the photofacsimile picture of the cloud formation over Hurricane Gladys, obtained by the HRIR of Nimbus I. (Note the characteristic spiral band pattern of the clouds). At the time of the IR observation, the hurricane was located at approximately 26°N , 66°W . Also shown in the figure is the single analog trace through the eye of the hurricane along the west to east scan path indicated in the photofacsimile depiction. A scale of equivalent blackbody temperatures, determined from the calibration of the HRIR, is shown to the left of the analog trace, while to the right, a height scale, corresponding to these temperatures, has been constructed based on the nearly concurrent radiosounding of atmospheric temperature taken at Kindley Air Force Base, Bermuda.

It may be seen that the heights of the cloud top surfaces along the scan line shown can be easily determined from the analog trace using the scales provided. While such detailed IR data (i.e. in analog trace format) are seldom, if ever, available to the general data user, the case shown in Figure 78 provides a rather graphic demonstration of the basic technique in the determination of cloud top heights from IR window measurements.

An example of cloud top height determination on a larger scale is shown in Figure 79. The analysis shown in this figure is based on the IR window data shown previously in Figure 72a. The three-dimensional temperature field needed for the extrapolation of cloud top heights was constructed from the analyzed temperature fields on constant pressure charts produced by the National Meteorological Center. From these data, a temperature-height curve for every location in the region of analysis can be obtained.

Using the technique illustrated in Figure 78, cloud top heights over the whole region were determined, and the isolines of cloud top heights (in thousands of feet) are shown in Figure 79. Comparison of the analysis shown in this figure with the cloud contour chart shown in Figure 72b, shows that the cloud top heights obtained are quite reasonable. Pilot reports of observed cloud top heights also confirmed these estimates.

It should be pointed out that while the photofacsimile format of data presentation cannot be used for detailed estimates of cloud top heights, gross approximations may be made based on the relationship between grey scale steps and temperature, and therefore altitude. In most instances, such gross approximations are sufficient.

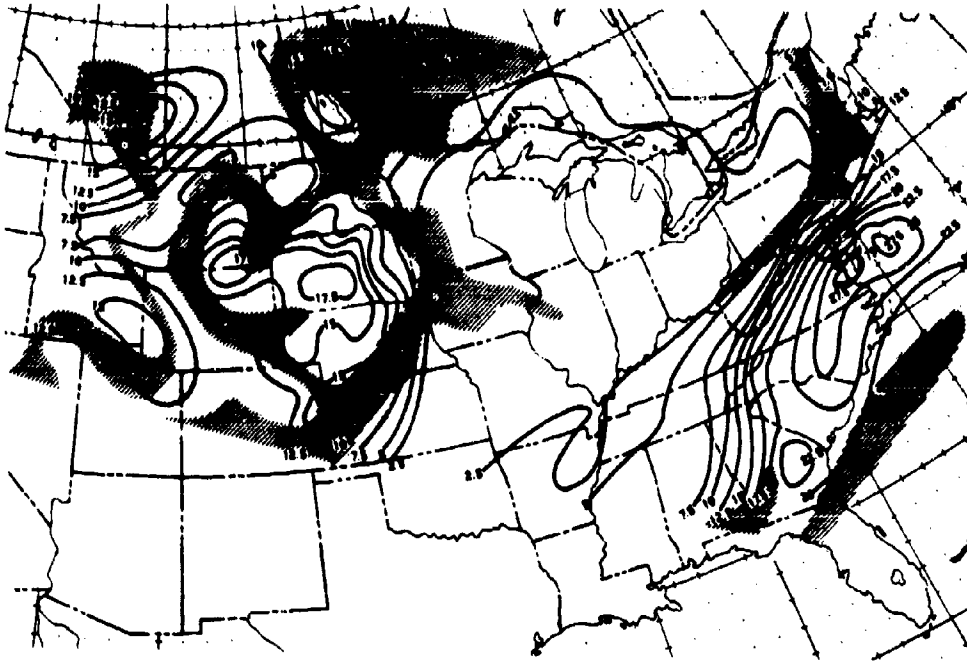


Figure 79. Height of Cloud Tops (Thousands of Feet), 1800 GMT, 23 November 1960, as Estimated from TIROS II Radiation Measurements. Hatched Areas are Broken Clouds and Dotted Areas are Scattered Clouds

When the instantaneous field of view of the sensor is filled by broken or thin clouds, the energy reaching the sensor comes in part from the warm earth and in part from the colder clouds. The resulting radiometer reading is thus a value between that for clear skies and that for an overcast at the level of the thin or broken cloud cover. For instance, a partial cloud cover with tops at 15,000 feet might produce a temperature equivalent to that from an overcast with tops at perhaps 8,000 feet. If the data were to be used to determine cloud top heights, an error of 7,000 feet would result. Similar problems exist when the field of view of the sensor is filled by clouds with tops at different levels, or when the sensor views the edge of cloud with vertical development.

The atmospheric temperature lapse rate itself may introduce problems in cloud height determinations from IR window data. For instance, Figure 80 shows a radiosounding of atmospheric temperature. The temperature curve shows a subsidence inversion layer located between 800 and 700 mb. The concurrent IR window sensor temperature measured by TIROS VII over the region was 269°K. It may be seen from the sounding that, due to the inversion, the top of the cloud can be placed at three levels — 800 mbs, 785 mbs or 680 mbs.

It may be concluded from this discussion that the determination of cloud top heights from IR window data can be erroneous. Synoptic climatological considerations or rapid, small scale variations in the IR data as the sensor scans across an area may be helpful in detecting such errors. As is so often the case with all types of satellite data, the integration of satellite and available conventional information leads to the best interpretation.

10.2.2.3.1 A Note on the Application of Daylight IR Measurements Made in the 3.6 μ to 4.1 μ Window

It has been pointed out that reflected solar radiation is a significant contributor to the radiance measured in the 3.6 to 4.1 μ window during daylight hours. This component of the measured radiance renders interpretation of daylight observations made in this window difficult to interpret. The HRIR of Nimbus uses this spectral interval for its observations. In the following paragraphs, the difficulties in, and limitations to, the application of daylight data obtained by this sensor are summarized.

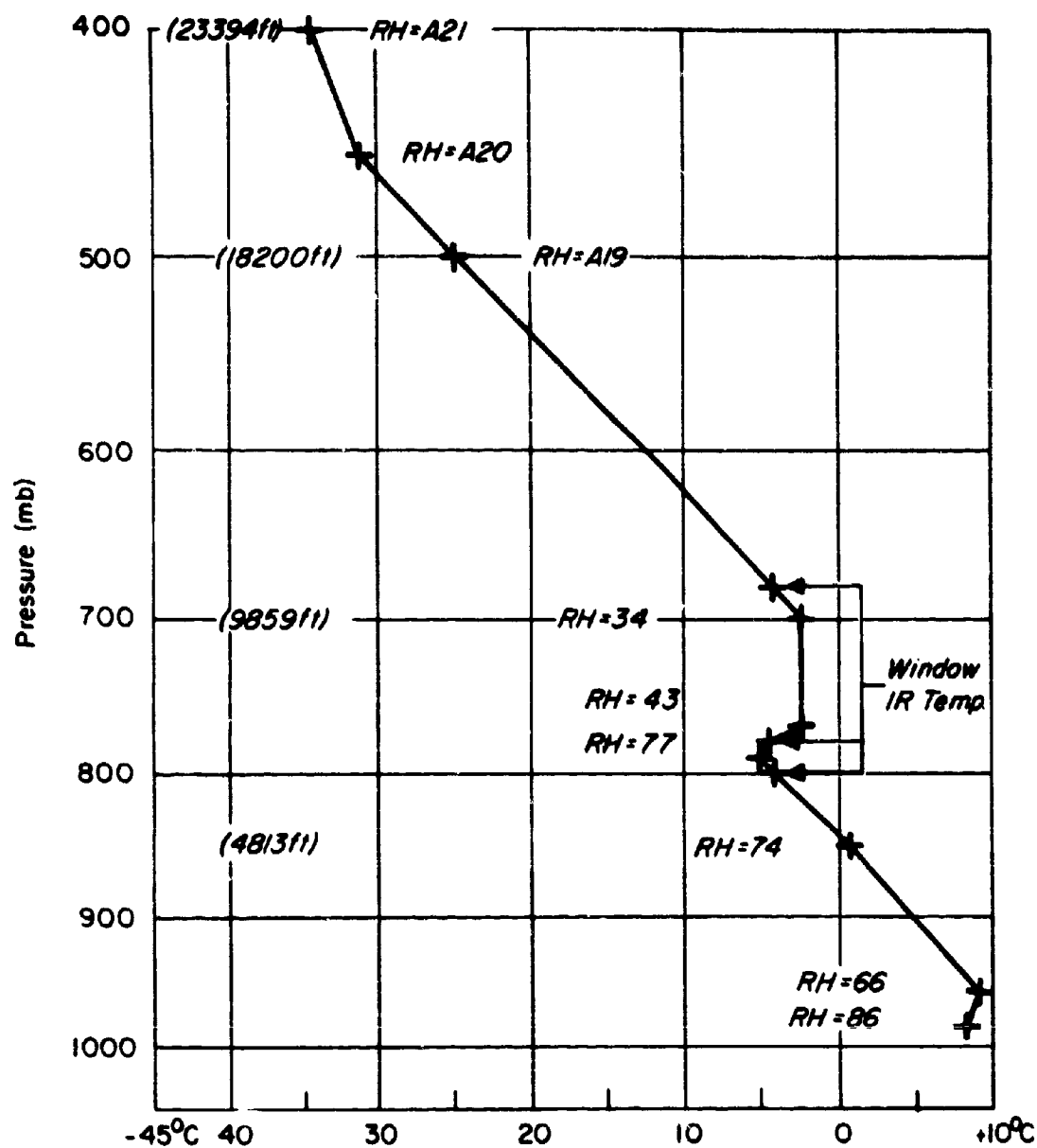


Figure 80. Comparison Between Cloud Top Height Determined from Radiosonde Data and that Deduced from Satellite Radiation Data in the Presence of Subsidence Inversion

Although HRIR was designed primarily for operation at night, it has been at times used under daylight conditions and, in the absence of TV cloud pictures, can provide useful data not otherwise available. Because of the spectral interval used (3.6 to 4.1 μ), however, the sensor responds to reflected solar radiation as well as to emitted infrared energy. In these wavelengths, the amount of radiant energy from these two sources is of the same order of magnitude. The combination of the two sources of energy may make quantitative interpretation virtually impossible, and often complicates qualitative interpretation.

In order to use the daylight HRIR data or to compare them with TIROS or AVCS pictures, it is desirable to print the HRIR so the majority of the clouds (areas of relatively intense radiation) are white. For the daylight HRIR, where solar reflectivity usually exceeds thermal emission, this is, of course, the reverse of the most effective photographic polarity for presentation of the night HRIR data (in both cases, it is desirable for the clouds to be depicted as whiter than the background). Presentation of the clouds as white is vital to ease of interpretation, whether or not comparisons with other data are to be made. This has been noted by several groups besides the Geophysics Division of Allied Research which tried and often discarded attempts to work with TIROS pictures in negative form.

Comparative analyses of daytime HRIR data and approximately concurrent TIROS pictures have left no doubt that, over the oceans, daylight HRIR would be of significant value in the absence of TV pictures. Even small details within a common cloud pattern can often be identified in both the TIROS pictures and the HRIR data (see Figs. 81a and 81b).

In the daytime the HRIR signal is, of course, a combination of reflected sunlight and thermal emission. In this situation, there is apparently little variation in the reflection term with cloud top height, but there is a rapid decrease in the emission term, thus causing high clouds to appear less bright in HRIR than lower clouds (Fig. 81b, where the stratus west-southwest of Baja California is lower than much of the cloudiness to the east and southeast). This is, of course, a reversal of the usual relationship between cloud brightness and cloud top height as seen in the TIROS TV pictures, or in the nighttime HRIR. As a consequence, brightness often tends to be inversely related to significance.

Over land, the thermal emission of the relatively warm land appears to be high enough to prevent significant contrast between clouds and the land surface; it is difficult to even detect the clouds (Fig. 81b). The value of daytime HRIR over



Figure 81a. Nimbus I HRIR Daylight View of Western Europe and the Mediterranean



Figure 81b. Nimbus I HRIR Daylight View of the Western United States and Eastern Pacific Ocean

land is highly questionable. This is because the higher temperatures and lower reflectivities of the land normally are approximately equivalent in total radiation (at the wavelengths to which the HRIR is sensitive) to the radiation resulting from the lower temperatures and higher reflectivities of the clouds.

10.2.2.4 Applications of IR Window Observations to Meteorological Analysis

The ability of IR window sensors to depict the extent of cloud cover, cloud patterns, and other properties of cloud fields, makes it possible to deduce from the measured data many aspects of the existing meteorological condition. In this regard, IR observations of cloud cover serve a function similar to television pictures in meteorological analysis.

A number of studies have been performed of the meteorological data content in IR window observations. In view of the fact that, at least in the near future, the only IR window data available directly to local data users will be those obtained by the HRIR (transmitted in the Direct Readout mode), the study performed by Widger et al.³⁴ is, perhaps, the most appropriate. In their study, detailed analyses, illustrated with case studies, were performed of the meteorological interpretation of the HRIR data. While the IR data used in the study were taken from HRIR measurements, the conclusions reached in the study may be applied, in most instances, to similar data obtained in other IR windows or by other sensors. In the following paragraphs, a short summary of results of their investigation is presented. For details, the reader is referred to the original report.

This summary covers the following significant topics:

1. Frontal analysis
2. Cloud vortices
3. Clouds outlining high pressure areas
4. Mesoscale observations
5. Antarctic analysis, and
6. Tropical analysis.

1. Relationships of Extratropical HRIR Data to Mid-Tropospheric as Compared to Frontal Analyses

Prominent extratropical cloud patterns shown by the HRIR data have been found to be relatively cold and so reaching well into the middle or upper troposphere. These are in general far better related to the mid-tropospheric (500 mb) flow patterns than to frontal analyses. Essentially all extratropical areas of cold clouds of significant size, as seen in the HRIR, can be satisfactorily explained in terms of areas of cyclonic vorticity or vorticity advection, or as clouds formed in such an area and subsequently advected from it. Reasonable patterns of day-to-day continuity usually present fewer problems when viewed in terms of these explanations.

While there is often a good correlation between cloud bands or areas and analyzed fronts, it can usually be noted that, in the absence of upper level support, such clouds seldom extend to significant heights. Furthermore, in many cases it appears difficult to establish a reasonable continuity, from one day to that of the next, for the frontal analyses, or for the cloud bands and areas when it is attempted to explain them and their continuity primarily on the basis of frontal concepts. Since frontal analysis is often highly subjective, this is not entirely unexpected.

It should not be inferred from the above that fronts do not exist, or that they are always insignificant. Rather, it would appear that their effects are more constrained to the lower levels (those where the clouds appear light grey or darker in the HRIR). A usually necessary and at times a sufficient condition for the clouds to extend to higher levels (where they appear white in the HRIR) is mid-tropospheric flow patterns which produce significant upward vertical velocities at the synoptic scale, or permit them at the meso or convective scales.

As an illustration of these matters, it may be helpful to consider the so-called "back door" cold front of New England, a front that comes in principally from the north rather than from the west. Such fronts usually are associated with significant temperature contrasts at low levels, and often there is adequate moisture in the warm air. Under classical frontal concepts, one might expect considerable weather with such fronts, but this is seldom the case. This is because they usually lack upper air support and are often under the weather suppressing influence of northwest flow aloft.

At least three types of frontal band clouds have been noted. These may be classified as (a) frontal bands with only low level clouds, (b) low level frontal cloud bands with higher level scattered-to-broken cloudiness, and (c) frontal cloud bands with extensive high level cloudiness.

An example of a frontal situation with clouds only in the lower atmosphere is shown in Figure 83, near 72°N , 110°E . Figure 82, near 65°N , 110°E , shows an example of low level frontal cloud bands with higher level scattered-to-broken cloudiness, while in Figure 83 (near 54°N , 120°E) is shown an example of a frontal cloud band with extensive high level cloudiness.

2. Cloud Vortices

Cloud vortices are well depicted in the HRIR data, and can usually be recognized without difficulty (Fig. 56a). The overall shapes of the high and low cloud patterns as depicted in the HRIR are basically the same as those made so familiar by the TIROS pictures. The HRIR-detected temperature variations, however, clearly reveal differences in cloud top heights which are far from obvious in the TIROS pictures. The cloud top height distributions correspond well to those found by Sherr and Rogers,⁶² using integrated analyses of TIROS cloud picture and IR data. Furthermore, the HRIR data reveal significant details that are often poorly visible, if at all, in the TIROS IR data.

The relationships between cloud vortices and the stages of cyclonic development are clearly seen in the HRIR data. As an example, the high cloud spirals observed in mature cyclones, while apparently the result principally of advective processes, appear often to be modulated by mesoscale of varying vertical velocities (Fig. 56a). In areas where the air moves poleward, the clouds often broaden and brighten, presumably due to intensified upward motion. Conversely, areas of equatorward movement are those where the clouds thin and darken, suggesting some degree of downward motion. This, of course, agrees with vorticity and thermal advection concepts since warm thermal and/or cyclonic vorticity advections most commonly exist in poleward moving air. It seems likely that this type of cloud top height detail, which only an HRIR system seems likely to supply, may often be significant. In several cases, it has been possible to relate the details in the vortex cloud patterns to small short wave perturbations superimposed on cyclonic circulations (Fig. 56a).



Figure 82. IRIR Mosaic with NMC 500 mb Analysis (0000 GMT, 17 September 1964 West of about 110°E; 1200 GMT, 16 September to the East), and Russian Frontal Analysis for 0000 GMT, 17 September 1964.

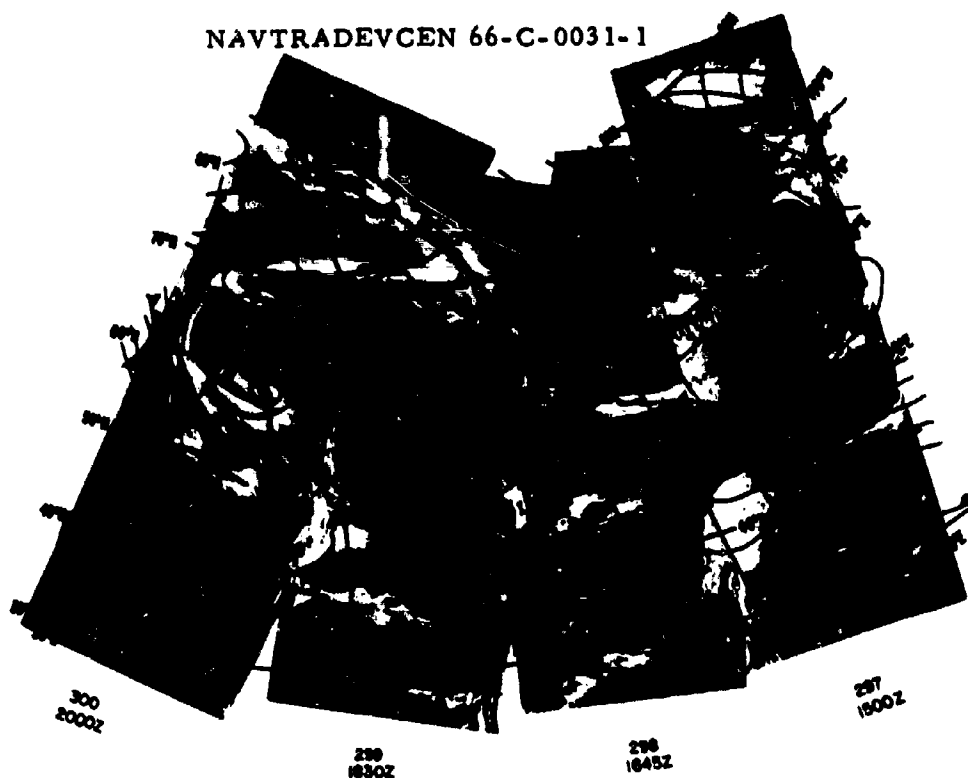


Figure 83. Mosaic with NMC 500 mb Analysis (0000 GMT, 18 September West of about 120°E; 1200 GMT, 17 September to the East), and Russian Frontal Analysis for 0000 GMT, 18 September



Figure 84. HRIR Observations of Cloud Vortices and Frontal Cloud Bands

3. Clouds Outlining a High Pressure Area

Apparently persistent cloud patterns often outlined at least the western edge of a major high pressure area, especially in the case of an Ω -block when such cloud bands conform to at least much of the western part of the Ω flow pattern (Figs. 82 and 83).

It appears that one source of these cloud patterns is a series of cloud bands or areas which are formed in areas of upward vertical velocity to the west of the high or the Ω flow. At first these clouds move eastward in a more or less normal westerly flow. When they begin to come under the influence of the high or of the Ω flow, this both reduces further eastward motion and tends to dissipate any portions of the cloud bands which do move further eastward. Thus, a series of cloud bands which moves into the western edge of a major ridge leads to the appearance of a persistent cloud outlining at least the western portion of the ridge.

A second source of the cloud band outlining such ridges is cloudiness formed in areas of significant upward motion adjacent to the western part of the ridge, as in the cutoff low typically found just west of an Ω -ridge, and subsequently advected along the flow pattern around the ridge.

In one case, it has been possible to relate the changes in such cloud bands to the partial breakdown and transformation of an Ω -block over Eurasia. It appears that similar cloud bands exist in other blocking situations, and that their patterns, movements, and changes may aid in deducing the establishment, persistence, transformation, and dissipation of Ω -blocks and other major high pressure areas. It further seems probable that a similar mechanism may occur with late spring and early summer squall lines over the eastern United States, which often appear to form in and move eastward from a trough in the Mississippi Valley, and to dissipate as they come under the influence of the Bermuda High, at times before reaching the east coast.

4. Mesoscale Observations

There appears to be a rather pronounced tendency for very white (cold) areas in the HRIR to be associated with general areas of present or very recent past precipitation. At least one exception, that of cirrus clouds, does appear to exist, however. Outside of this exception, the correlation between the white (cold) HRIR areas and areas of precipitation appears far better than the rather poor correlation found between bright TIROS clouds and concurrent precipitation. More study of this relation is still needed.

Many of the bright, narrow cloud bands seen in the HRIR are, or include, jet stream cirrus bands. These bands and their orientations often seem to conform to the concurrent upper level analyses. In some cases, however, these bands cut across the jet streams as analyzed, even over areas of adequate data. In such cases, they may correspond to the area of cirrus that often exists downstream from an area of confluence between two converging jet streams.

Frontal bands often exhibit a texture in the HRIR, with scattered-to-broken higher clouds over a lower overcast. This texture is often in the form of mesoscale bands, generally parallel to the overall orientation of the frontal band. Sizes and spacings suggest they may be associated with the mesoscale wave-type motions of approximately 70 km apart, that Elliott and Hovind⁶³ have identified in frontal zones approaching the California coast. If so, these scales of motion appear to be frequent and to be found in other parts of cyclonic vortices than along the cold or occluded front. For example, a similar scale of structure can be noted on the west side of many of the HRIR observed cloud vortices (Fig. 56a).

There are indications that certain more or less V-shaped cloud patterns, may be characteristic of certain types of squall or convective lines. Patterns of the same general shape were identified in TIROS pictures of squall and convective lines. Further study will be required to determine what significance (if any) there may be to this possibly characteristic pattern, and the dynamic factors that lead to its formation.

Small details, such as lee wave clouds, are often clearly visible in the HRIR data (Fig. 73b). The altitudes that lee wave clouds sometimes attain (up to 12,000 feet above the terrain) may explain their visibility in the HRIR data as compared to the frequent loss of visible structure of cellular clouds of apparently similar dimensions.

5. Antarctic Analysis

Studies of a several day series of HRIR observations over the Antarctic Ocean have demonstrated that the principles developed for HRIR analysis in the northern hemisphere are equally applicable in the southern hemisphere.

In most aspects, those weather systems which were observed, conformed with previously published discussions of the synoptic climatology of the region. It does appear, however, that the circulation in the area just north of the Antarctic continent is more complex, and so the zonal circulation is significantly more disturbed, than

is usually shown on conventional analyses of the area. Consequently, it is more appropriate to use the HRIR data to develop improved analyses for these data deficient areas than it is to attempt to use the conventional data to confirm the Antarctic area HRIR observations.

Because the HRIR data are most useful and most easily interpretable at night, they will be particularly valuable during the Antarctic winter months, when the extended periods of darkness permit longer periods of HRIR observations within each day. During this season, the conventional data are even more sparse than during the Antarctic summer.

Comparative studies of the HRIR and the TIROS TV data show that the cellular cloud patterns to the rear of cyclones, as seen in the HRIR, are of a larger scale than often apparently similar patterns as seen by TIROS. Usually, when the cellular patterns are seen in the TIROS pictures, the area will appear as only a solid, grey, low cloud mass in the HRIR. Accordingly, it is unlikely that the principles developed by Merritt and Rogers⁶⁴ for determining low level winds from such TIROS convective patterns will be applicable to HRIR data. The procedures developed for the use of the TIROS data were based on a convective cloud layer sufficiently shallow for significant changes in wind direction to be improbable; the cellular cloud pattern as seen in the HRIR are usually cases where the cumulus clouds appear to extend through a relatively deep layer.

Studies with the HRIR data, and with comparative TIROS and AVHRR data, indicate that it is nearly impossible to detect cloudiness over the Antarctic continent by any present type of satellite observation. The few exceptions are only cases where the clouds from systems off the coast can be traced for a short distance inland. It is possible to detect cloudiness over the ice pack which normally surround the continent, using the HRIR, providing the clouds are sufficiently high and cold. It may often be difficult to determine from the HRIR alone where the edge of the ice pack is, or exactly which areas are clouds and which are ice. In the TIROS pictures however, the edge of the pack ice can usually be seen. Since the edge of the pack ice normally moves only slowly from day to day, this gives a reliable indication of where ice is to be expected in an HRIR observation, even if the TIROS and HRIR data were a day or so apart. Accordingly, the combination of the two types of data often gives a reliable indication of where cloudiness exists above the ice pack.

The HRIR data are also applicable to ice surveys in the Antarctic area, since ice-free areas and "breaks" in the pack ice are often visible. In some cases, as in the vicinity of the Balleny Islands, the presence of, absence of, or size of such openings in the ice pack (or their changes from day to day) may be useful indications of the approximate direction of the surface wind.

6. Tropical Analysis

In the tropics, the principles used for TIROS picture analysis are also found to be generally applicable to the HRIR data. Because the early stages and further development of tropical disturbances appear to be related to the extent and organization of active convective areas where cumulus extend to comparatively great heights, the cloud height information that is provided by the HRIR data is at least as valuable in the tropics as at higher latitudes.

Cases studied over the Pacific have shown that the HRIR data permit significant improvements in the conventional operational analyses, which are almost always based on an inadequate number and density of observations. Joint use of the HRIR data, and either AVCS or TIROS pictures, provides twelve hour continuity, whereas only 24 hour continuity is normally possible using either data type alone.

The HRIR data also provide previously unavailable information on small scale details of tropical cloud systems which appear to be significant to an understanding of tropical weather mechanisms. For example, in a case studied, the HRIR data showed that the initial cloud formations associated with one upper level cyclone occurred as narrow bands of cold (high) cloud around the periphery of the cyclonic circulation. These bands appear to be related to vertical motions produced by small scale relative vorticity advections on the cyclonic side of a peripheral wind maximum.

10.2.2.5 Applications of IR Window Measurements to Surface Surveillance

One of the applications of infrared remote sensing techniques from satellites is surface surveillance of geophysical features or man-made targets. The ability of an IR sensor to detect specific surface features or targets depends on the relative intensity and spectral characteristics of the radiation emitted by the targets as compared to the background, the attenuation characteristics of the atmosphere, the size of the target elements relative to the resolution capability of the sensor, and the spectral response of the sensor. From the previous discussions of the attenuation effects of the atmosphere, it is obvious that for surface surveillance, IR windows should be used.

This principle may be applied to man made target detection. For example, if a target is of such a nature that it can cause the environmental temperature over a large region to increase sufficiently above the normal background temperature, the possibility of detecting such a target may exist.

10.2.2.5.1 Examples of IR Surface Surveillance

The resolutions of the IR window sensors of TIROS and Nimbus satellites are not capable of resolving man made targets. However, large geophysical targets and features have been observed.

Figure 85 made by the HRIR of Nimbus I over the western part of the U.S. shows a number of geophysical features in the cloud free areas. These include Death Valley, Lake Tahoe, the Grand Canyon, and the outlines of the continental boundary. It is apparent that the identification of these features in the picture is dependent on "ground truth." These geophysical features stand out in the pictures in darker shades due to their higher temperatures as compared with the surface temperatures of the surrounding regions. In the case of the outlining of the continental boundary, the ocean waters are warmer than the adjacent land areas. Consequently, the sensor is able to depict the boundary between the land surface and the warmer ocean.

Figure 86 shows the depiction by the HRIR of Nimbus I of the same iceberg as that shown previously in the AVCS picture in Figure 61b (Section IX). Figure 87 shows the Salar de Atacama dry salt lake bed clearly outlined in the HRIR data.

These are but a very small sample of the geophysical features which have already been observed in satellite IR measurements.

The problem of non uniqueness of target signatures in IR window measurements has led to proposals of specific systems to detect specific targets. As in the case of visible observations, multispectral measurements within a single window or in a number of windows might provide better identification of specific types of targets or features. However, as Colwell⁶⁵ has pointed out, many problems remain to be solved in the area of target surveillance using satellite IR sensing techniques.



Figure 85. HRIR Ocean and Terrain Temperatures over the Southwestern U.S. on 30 August 1964

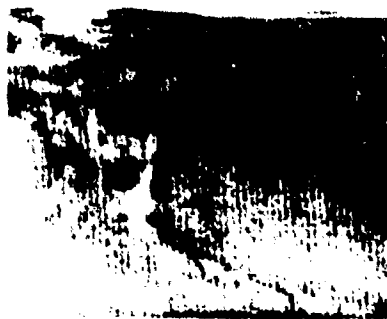


Figure 86. HRIR Photograph of an Iceberg

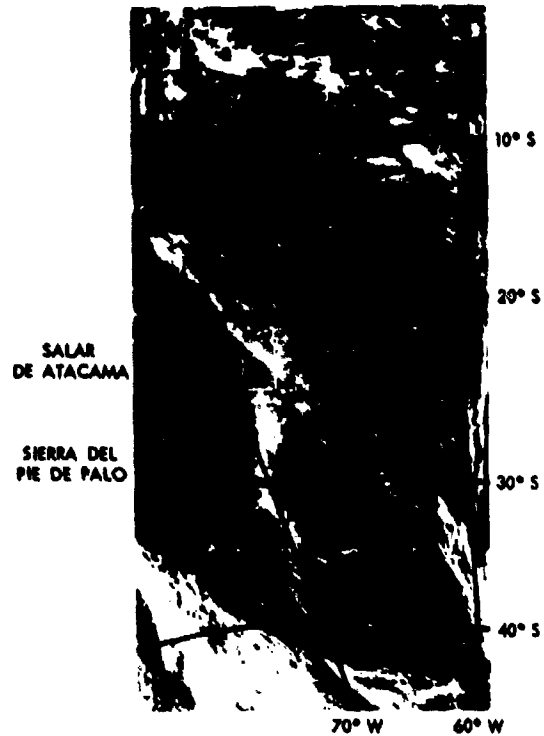


Figure 87. HRIR Observations over South America, 14 September 1964

The detectability of any target in an IR window is based on the same principles as those involved in the detectability of thick clouds. First of all, the target must have emission in the spectral region of the sensor such that it is distinguishable from the background. For example, clouds are detectable in IR window measurements due to the fact that generally they are colder and the radiance emitted by the clouds is less than the background. Accordingly, a contrast in intensity exists between the cold target and its background. Unlike measurements made in the visible by photographic techniques, in which shadow effects are often used to detect targets, the only "identifier" in infrared techniques is intensity contrast. It is often impossible, for instance, to detect the presence of cloud cover over snow covered surfaces by IR techniques, due to the lack of contrast.

It should be pointed out that target detectability does not guarantee target identifiability. If the shape of the target is not unique, or if the target is so small that its shape is not resolved in the measured data, the only signature of the target measured is the intensity contrast, which is not unique. The identifiability of the target may then depend on the experience of the data analyst and his foreknowledge of the probable existence and locations of targets of interest.

Targets of sizes smaller than the resolution of the sensor may be detected provided that their intensity contrast is sufficiently high. Consider the case illustrated in Figure 88. In the absence of the target, the power measured by the sensor may be approximated by

$$\begin{aligned}
 P(\text{no target}) &\approx P_B + P_a \\
 &= \tau N_B A_s \frac{A_r}{R^2} + P_a
 \end{aligned}
 \tag{135}$$

where

- P_B = power from the background surface
- P_a = power contributed by the atmosphere
- τ = transmissivity of the atmosphere to the surface
emitted radiation
- N_B = radiance emitted by the background surface
- A_s = area resolution of the sensor at the surface
- A_r = effective aperture of the sensor
- R = distance of the sensor from the surface.

$P(\text{no target})$ then defines the background condition.

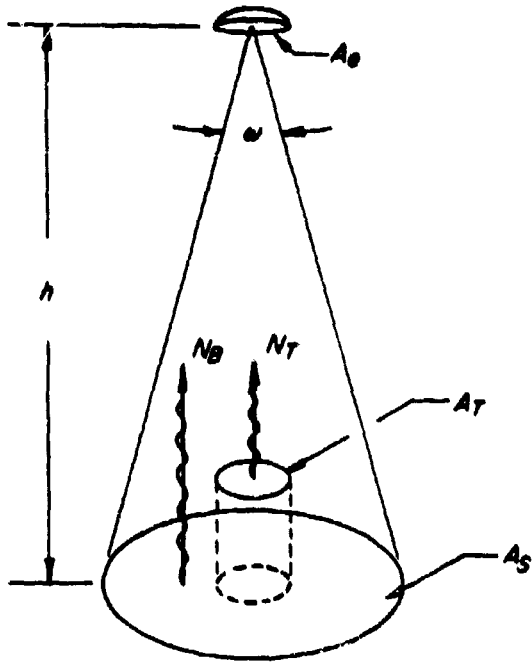
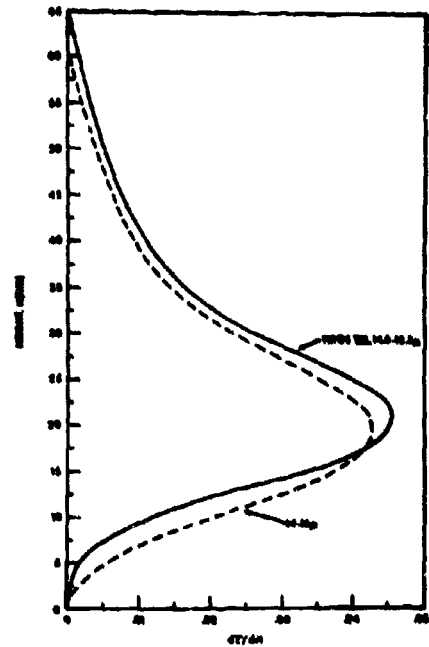
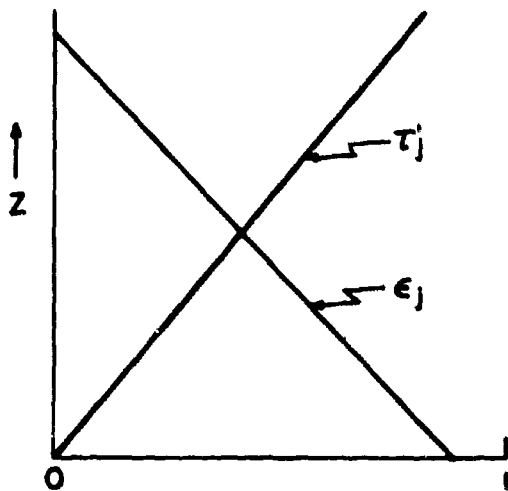
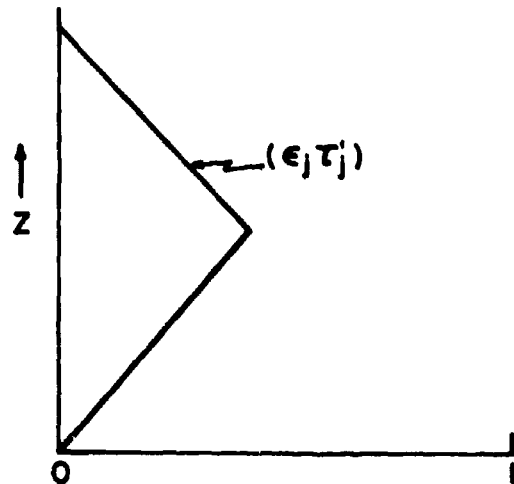


Figure 88. Geometry for Target Detection


Figure 89. Vertical Profile of $(\epsilon_j \tau_j')$ for 15u Channel of TIROS VII

Figure 90a. Schematic of the Vertical Profiles ϵ_j and τ_j' for a Well Mixed Gas

Figure 90b. Schematic of the Vertical Profile $(\epsilon_j \tau_j')$ for a Well Mixed Gas

If now a target of effective emitting surface area, A_T , and radiance, N_T , is inserted into the beam (with $A_T < A_s$), the power measured by the sensor is then approximately P (with target) $\approx (N_B(A_s - A_T) + N_T A_T) \tau A_r / R^2 + P_a$.

In an atmospheric window, the contribution from the atmosphere, P_a , is generally insignificant and can be neglected. The percentage change in the measured power as a result of the presence of the target may be obtained from the following:

$$\begin{aligned} & \frac{P(\text{with target}) - P(\text{without target})}{P(\text{without target})} \\ &= \frac{N_B(A_s - A_T) + N_T A_T - N_B A_s}{N_B A_s} \\ &= \frac{(N_T - N_B) A_T}{N_B A_s} \end{aligned} \quad (136)$$

Since N_B and A are fixed, it is obvious that the ratio as defined in Equation (136) will increase or decrease depending on the magnitudes of A_T and N_T . For a given sensor system, there is a threshold value (i.e. minimum value) of this ratio below which the sensor is incapable of resolving. If the target size, A_T , is fixed, its detectability is then determined by the magnitude of N_T relative to N_B . When N_T is sufficiently larger or smaller than N_B for the absolute value of the difference $(N_T - N_B)$ to be large enough to produce a ratio above the threshold, then the target may be detected. If $(N_T - N_B)$ is large enough, a target may be detected even if $A_T < A_s$.

When $A_T < A_s$, a target will be detected, at best, as a single warm or cold spot, and its identification will be difficult or may even be impossible.

There is a class of targets, both man made and natural, which may be detected by the effects which they have on their environment. For example, the courses of rivers have been traced in the HRIR nighttime data of Nimbus I even though the widths of the rivers were many times smaller than the resolution of the sensor. It has been postulated by Nordberg and Samuelson⁵⁹ that the prominence of these rivers in the data is due to the fact that the heat capacity of the ground along these rivers is increased, over the adjacent land areas, by the presence of moisture. The increase in heat capacity causes the soil to retain the heat absorbed during the daylight hours longer than the adjacent drier regions. As a consequence, the regions along the banks of the rivers are warmer than the surrounding land, providing a signature for the identification and location of the rivers in the nighttime data.

10.3 Measurements in Atmospheric IR Absorption Bands

10.3.1 Introduction

At present, satellite IR absorption band measurements have been limited to those made in the 6.3μ H_2O band and in the 15μ CO_2 band. These measurements have been made by fixed band pass radiometers. From the 6.3μ data and corresponding 8- 12μ window, mean upper tropospheric relative humidities have been obtained.⁶⁶ The 15μ CO_2 data have provided mean lower stratospheric temperatures.⁶⁷ Merritt⁶⁸ has also made use of the 15μ data of TIROS III in synoptic studies.

The potentials of IR absorption band measurements are, however, much greater. The vertical sounding of atmospheric temperatures by means of measurements in different spectral intervals in the 15μ CO_2 band originally proposed by Kaplan,⁶⁹ may soon become a reality. King,⁷⁰ in his study of the potentials of remote sounding, has shown that, besides the vertical distributions of atmospheric temperature, the distributions of mixing ratios of the optically active gases and a number of other meteorological parameters are also deducible from measurements in IR absorption bands. Bandeen⁷⁴ has suggested the possibility of obtaining cloud top altitudes by comparing simultaneous measurements made in an atmospheric window and in an atmospheric absorption band.

The possibility of deducing the various atmospheric parameters from IR absorption measurements are dependent on the proper interpretation of the measurements. The interpretation of the measured data is based on the physical processes giving rise to the measured radiation. These physical processes are expressed in the radiative transfer equation approximate to IR absorption band measurements.

For measurements made in an IR absorption band such that the atmosphere is opaque to surface emitted radiation, the equation of transfer (i.e., Eq. (132)) becomes

$$N = \sum_j \epsilon_j N_b(T_j) \tau_j' \quad (137)$$

where the subscript j indicates the contribution from the j th layer in the atmosphere. In the most general case, not only are the contributions from each of the layers in the atmosphere unknown, but the individual terms in Equation (137) pertaining to each layer are also unknown. The $N_b(T_j)$ term is dependent on the temperature of

the layer; the ϵ_λ term is dependent on the amount of the absorbing gas in the layer, and the τ'_j term is dependent on the amount and vertical distribution of the absorbing gas above the layer. (see Section VI). If all the terms remain unknowns, there is no way to solve for any of the desired atmospheric parameters.

Fortunately, there are certain species of atmospheric gases which are well "mixed" and so have total concentrations which are stable in time and place. Atmospheric CO_2 is such a gas. Furthermore, CO_2 has a relatively intense absorption band at 15μ . Consequently, the vertical distribution of the $(\epsilon_j \tau'_j)$ part of Equation (137), for any wavelength in the 15μ CO_2 band, should be relatively independent of geographic location and time, and can be determined from existing conventional meteorological data.

Many investigators have studied the absorption characteristics of this 15μ CO_2 band as a function of concentration, total pressure, and temperature. These investigations have included both theoretical calculations (most notably by Elsasser⁷¹ and Goody⁷²) and actual laboratory measurements (Howard, Burch and Williams⁷³ etc). For detailed discussions of their methods, the reader should refer to the original articles. Based on these studies, tables are available which permit the computation of the vertical distribution of $\epsilon_j \tau'_j$ for any wavelength in the 15μ CO_2 band. The usual method adopted is to stratify the atmosphere into a finite number of thin layers similar to that shown in Figure 66. The effective amount of carbon dioxide in each layer is then computed. The transmissivities corresponding to that amount of CO_2 can then be determined. Finally, the product $(\epsilon_j \times \tau'_j)$ for each layer is computed based on these calculated values of transmissivities. When these values are plotted versus height (or atmospheric pressure), the results are curves showing the vertical distributions of the function $(\epsilon_j \tau'_j)$. An example of such a curve is shown in Figure 89. It is the mean curve for the wavelength interval $14-16\mu$, which is the spectral response of the 15μ channel of the scanning radiometer of TIROS VII.

Notice that the curve has a single peak at ~ 20 km. This is due to the characteristic vertical distribution of CO_2 . As in the case of atmospheric density, the amount of carbon dioxide in a unit volume falls off with altitude. Since the emissivity term increases with increasing amounts of the absorbing gas, while the transmissivity term decreases with increasing amounts of the gas, the vertical distributions of each of these terms should be opposite, i.e., an ϵ_j curve would have a maximum near the surface and decrease upwards, while the transmissivity

term τ'_j should have a minimum near the surface and increase upwards. This is illustrated schematically in Figures 90a and 90b. The curve representing the products of these two terms should, therefore, have a single maximum value.

Examination of Equation (137) shows that the contribution of any layer to the total measure radiance may be considered to be the blackbody radiance emitted by the layer, at the temperature of the layer, "weighted" by the product $(\epsilon_j \tau'_j)$ for the layer. This product has often been called the weighting function. From an examination of the weighting function, it is possible to infer the levels in the atmosphere from which the greatest percentage contribution to the measured radiance is expected to originate for a given wavelength or band of wavelength. In the case of the 15μ CO_2 channel of TIROS VII, it is seen from Figure 89 that over 60% of the measured radiance is expected to come from the layer between 15 km and 25 km. Computations of the vertical distributions of the radiance contributions for various "standard" atmospheric temperature lapse rates have been made by Bander et al. for this particular radiometer. These are shown in Figures 91a, b and c. It is seen from these figures that the layer of maximum contribution to the measured radiance, for each of the curves, remains at the level of the lower stratosphere.

The vertical distribution of the weighting function $(\epsilon_j \times \tau'_j)$ is dependent on wavelength. In a relatively intense portion of the 15μ CO_2 band, the peak of the curve is near 25 km. On the other hand, in less intense portions of the band, the peak shifts downwards towards the surface. Figure 92, taken from Wark and Fleming,⁷⁶ shows the weighting functions for six wavelengths in the 15μ CO_2 band. The altitudes of the peaks of these curves shifts downwards from A to F. Curve A is for $\tilde{\nu} = 669\text{cm}^{-1}$, which corresponds to the most intense parts of the 15μ band.

It is to be noted that while the location of the peak of the weighting function for a wavelength in the 15μ CO_2 absorption band is dependent on the wavelength in question, this location is more or less invariant for the given wavelength. This is not the case with the peaks of weighting functions in absorption bands of variable gases such as water vapor and ozone. It is not possible to specify the location of the peak of the weighting function for these gases from a specification of wavelength alone. Knowledge of the total amount and the vertical distribution of the absorbing gas is required. Consequently, it is not possible to specify the layer or layers in the atmosphere which contribute most significantly to the measured radiance. It is seen, therefore, that interpretation of these measurements is inherently more difficult than the interpretation of CO_2 absorption band measurements.

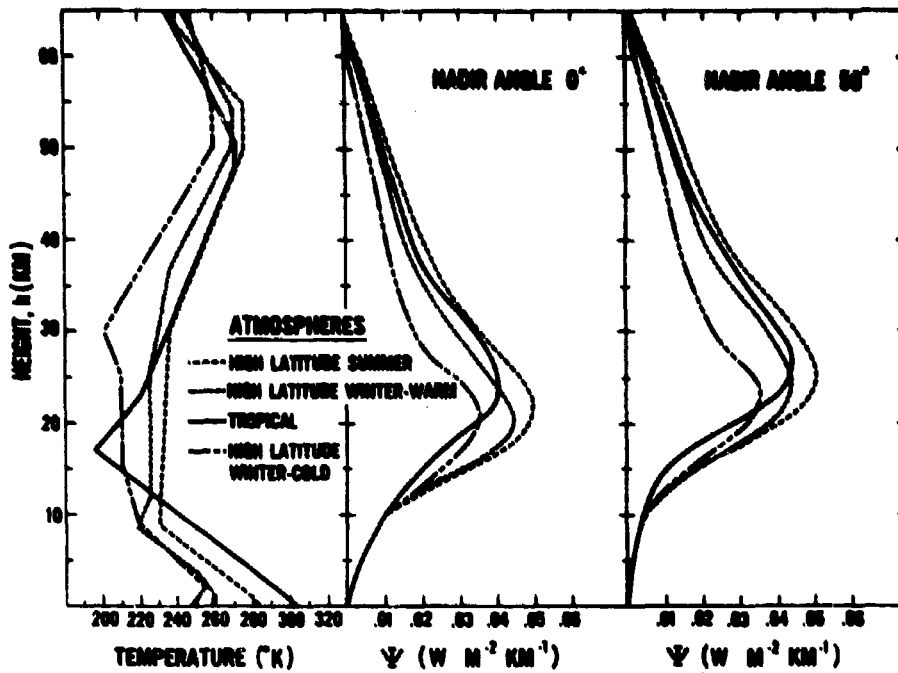


Figure 91. Weighting Functions for the 15μ Channel of TIROS VII

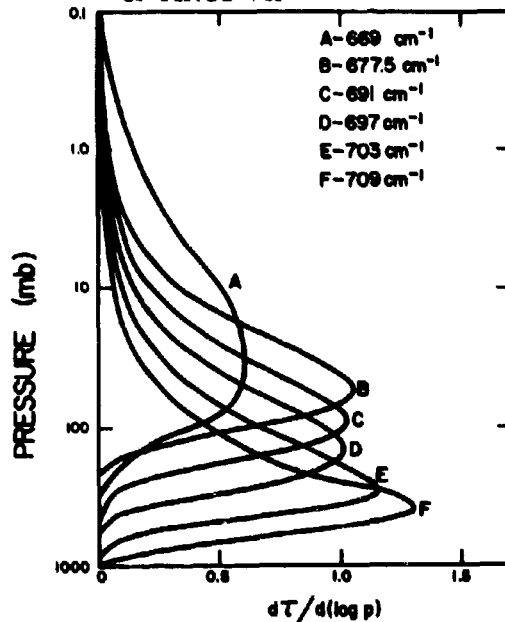


Figure 92. Weighting Functions at Six Spectral Intervals in the 15μ Band

As was pointed out earlier, IR measurements in the 6.3μ band of H_2O have already been obtained. A technique for the interpretation of these measurements has been developed. The use of these data based on this technique is discussed and illustrated in a later section.

10.3.2 Geophysical Factors Degrading Absorption Band IR Measurements

The discussion of the effects of atmospheric particulates on IR window measurements in general, apply also to IR absorption measurements with the exception of clouds. It was stated previously that although thin and tenuous clouds degrade window measurements, thick clouds represent a significant class of targets or parameters in window measurements. In the case of absorption band measurements, clouds, even thick clouds, do not generally form a class of targets of interest. Their presence in the field of view often make interpretation of the data difficult.

The reasoning behind this may be understood as follows: If the vertical distribution of the absorbing gas and the intensity of the absorption are such that an appreciable amount of the measured radiance may be expected to originate from below cloud top levels, the presence of a cloud prevents the radiation from these levels from reaching the sensor. As a consequence, information from below cloud top levels is lost. Furthermore, if the radiation emitted by the cloud top surface is less than that which would have been emitted by the layer below cloud top altitudes in a clear atmosphere, the measured effective blackbody temperature would appear to be colder.

The significance of cloud contamination to absorption band measurements depend on the shape of the weighting function. The 15μ channel of TIROS VII, for example, had a weighting function which showed that very little of the measured radiance can be expected from below 6 km. Consequently, clouds with tops below 6 km would not be expected to significantly degrade the measurements. On the other hand, clouds with tops above 6 km have been found to lower the measured effective temperature. Merritt has estimated the effects of high clouds on measurements made by this radiometer based on the assumption that the total field of view of the sensor was filled with a cloud deck with a uniform top. He found that a degradation on the order of $1^\circ - 4^\circ K$ can be expected with cloud tops at 6-8km, and higher degradations on the order of $4^\circ - 10^\circ K$ with cloud tops at 8-15 km.

Obviously if the weighting function of a particular radiometer is such that it normally "sees" into the warmer regions of the troposphere, the cloud contamination would be more significant, not only in magnitude, but also in frequency. Such is the case with the 6.3μ water vapor channel of TIROS and Nimbus II. For the range of mean relative humidities between 5% and 100%, the peak of the weighting function is located at approximately 7 km. Much of the measured radiance can, therefore, be expected to originate below this peak. The probability of clouds in the field of view of the sensor with tops above these regions is much higher than that for the 15μ channel. As a consequence, this channel shows the degradation effects due to clouds much more frequently. Comparisons of the simultaneous measurements made by the 15μ channel, the window channel, and the water vapor channel dramatically reveals this fact. An example of this effect is given in Section VI, using the pictorial analog data obtained by the MRIR of Nimbus II.

The method of estimating the effect of clouds on IR measurements is essentially that of determining the effect of a specific target on a uniform background. This was treated in Section 10.2.2 for the case of window channel measurements. However, the method may be modified to cover the cases of absorption band measurements by using the full equation for IR radiation transfer. It is obvious that quantitative estimates of cloud contamination effects cannot be obtained unless the cloud top altitudes are known. Consequently, it is often possible to recognize only that a measurement has been contaminated by clouds.

10.3.3 Parameters Deducible from IR Absorption Band Measurements

10.3.3.1 Mean Stratospheric Temperature

It was shown in Section 10.3.1 that by confining the measurements to a relatively intense portion of the 15μ CO_2 absorption band, the peak of the weighting function is located in the lower part of the stratosphere. Consequently, the greater part of the measured radiance can be expected to originate from the lower stratosphere and upper troposphere. The equivalent blackbody temperatures, T_{bb} , measured can then be interpreted as the mean temperature of the lower stratosphere.

The scanning radiometer of TIROS VII and the medium resolution radiometer of Nimbus II each had a channel designed to measure these temperatures. From the data obtained by the radiometer of TIROS VII, global maps of lower stratospheric temperatures for the various seasons have been obtained.⁶⁷

Merritt⁶⁸ has performed a study of the use of such observations in synoptic analysis, and concludes that they provide a potential basis for inferring significant information related to the thermodynamical and dynamical processes which occur during the formation and development of tropospheric cyclonic activity. Among the synoptic uses of the data investigated by Merritt are:

1. Upper tropospheric trough location and relative intensity.
2. Tropopause contour patterns and relative temperatures
3. Upper tropospheric and lower stratospheric isotherm patterns
4. Areas of large scale vertical motions associated with cyclonic developments.

While the measurement of mean stratospheric temperatures is significant in itself, it is obvious that the potential utility of the measurements lie in the area of synoptic analysis. Currently, studies are being performed to extend the initial findings of Merritt in establishing relationships between tropospheric processes and the temperature patterns as determined by measurements in the 15μ band of CO_2 .

10.3.3.2 Vertical Profiling of Atmospheric Temperature

Figure 92, in Section 10.3.1, shows the vertical distributions of the weighting functions in six wavelength intervals within the 15μ CO_2 absorption band. It was also noted that the altitude of the peaks of these curves shift downwards from A to F (See Fig. 92) with A representing the peak of the weighting function for the most intense portion of the 15μ band. From what has already been said concerning the relationships between the layer in which the peak of a weighting function is located and the equivalent blackbody temperature measured, it may be concluded that if simultaneous measurements were made in a number of spectral intervals within the 15μ band, it would be possible to deduce the temperature structure of the atmosphere.

This is indeed the basis of the techniques proposed to obtain vertical profiles of atmospheric temperature from satellites. The actual techniques by which the temperature data are to be extracted from the radiance measurements required sophisticated mathematics and will not be gone into here. However, it may be seen that basically, the inversion problem (i.e. the extraction of temperature from measured radiance) involves the solution of a set of n simultaneous equations for $(n - 1)$ values of temperatures. Each of the n equations is of the form given by Equation (132) and

correspond to a radiance measurement made in one specific wavelength interval within the 15 μ absorption band. The methods by which these equations can be solved to provide a unique temperature profile of the atmosphere have occupied many investigators. Most recently, Wark and Fleming⁷⁶ have shown that by a suitable approximation of the Planck radiance, the resulting set of equations is amenable to numerical solution. However, they also noted that the solutions obtained are unstable and require smoothing techniques. For a detailed discussion of the techniques involved, the reader is referred to the original article.

It is more instructive, however, to examine the results which they obtained based on their technique. From radiosonde observations of atmospheric temperatures (extrapolated to 0.1 mb), the expected effective radiances measured in the six wavelength regions shown in Figure 92 were computed using a transfer equation similar to Equation (132). In other words, the satellite data were simulated. The inversion technique was then applied to the simulated data. The computed temperature profiles are shown in Figure 93 together with the actual temperature profiles as obtained by radiosondes.

It should be noted that no vertical profiling of atmospheric temperatures has been made from satellites. However, the instrumentation necessary to achieve simultaneous multispectral measurements is being developed and tested in balloon flights. It is expected that such measurements will be obtained from satellites within the near future.

Another method which has been proposed for obtaining vertical distribution of temperatures is the so-called angular scan method. This method is based on the limb darkening effect. Radiation measurements are made at a single wavelength interval, but at a series of nadir angles. As the nadir angle of the measurement is increased, the radiation from any given level in the atmosphere will have to propagate through a longer pathlength of the absorbing gas before reaching the satellite. Consequently, the τ'_j term for any atmospheric layer decreases with increasing nadir angle. This produces the same effect on the weighting function as the changing of wavelengths in the wavelength or frequency scan method. Measurements at a high nadir angle correspond to measurements made in a more intense portion of the absorption band.

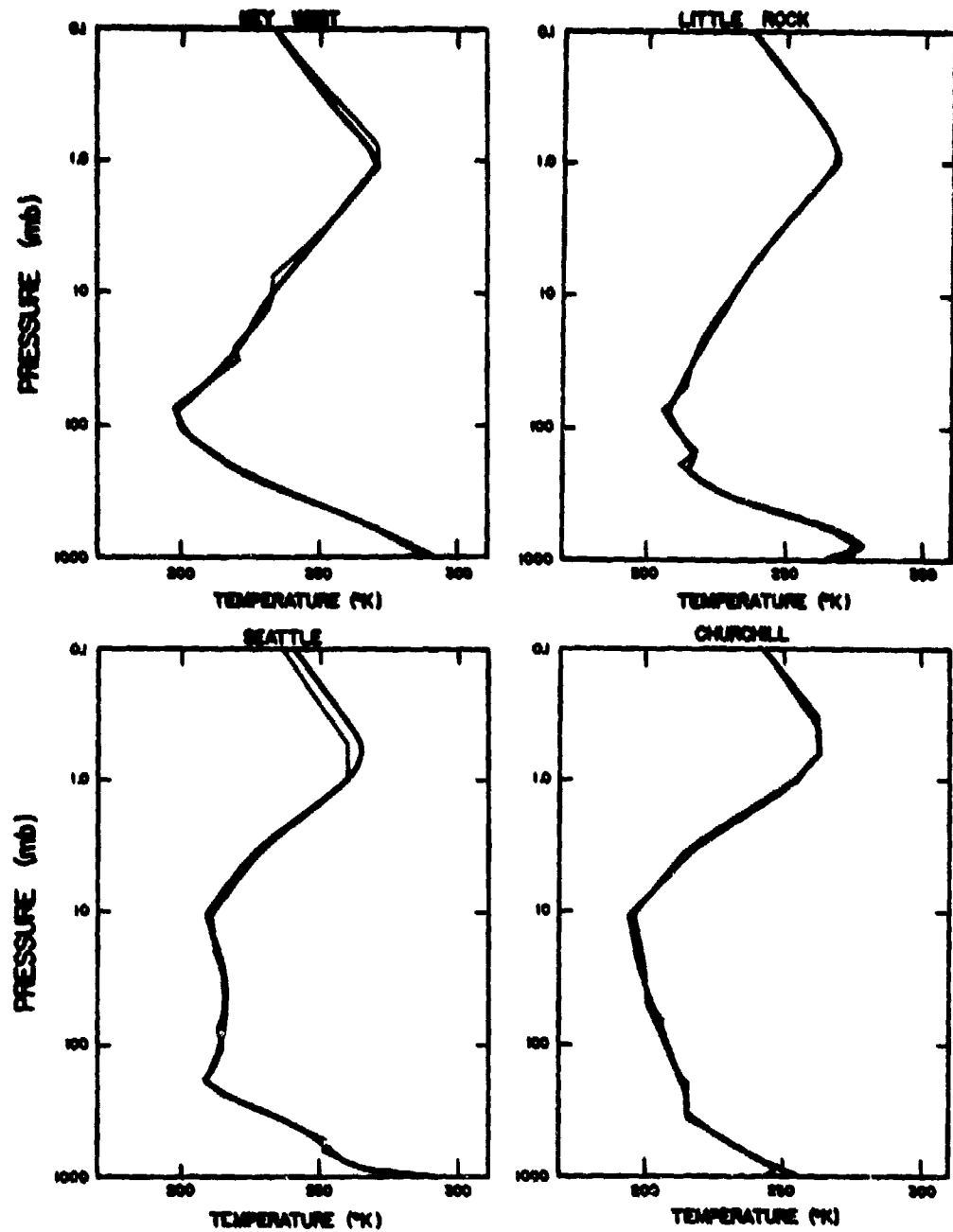


Figure 93, Solutions to the Temperature Inversion Problem for Four Selected Radiosonde Observations

This angular scan method is not presently being pursued as intensively as the frequency scan method. Data from the 15μ channel of the scanning radiometer of TIROS VII did not show a limb darkening effect sufficient to give the degree of temperature resolution desired. If the frequency scan method proves to be successful (as now seems likely), it is doubtful that the angular scan method will be further pursued for geophysical measurements, although it has been used for planetary exploration (the Mariner II radiometer observations of Venus).

10.3.3.3 Atmospheric Water Vapor

Measurements in the 6.3μ water vapor absorption band have been made by the scanning radiometer of TIROS and the MRIR of Nimbus II. These measurements do not lend themselves to easy interpretation due to the reasons stated in Section 10.3.1. From a measurement made in a single wavelength interval in the 6.3μ band of H_2O , it is impossible to separate the effects of water vapor content to the measured effective radiance from the effects of temperature. However the equivalent blackbody temperature so obtained can provide a qualitative estimate of the relative "moistness" of the troposphere. This may be seen by considering the fact that in a perfectly dry atmosphere, the equivalent blackbody temperature measured would correspond to the surface temperature (similar to that obtained in an IR window). However, if the tropospheric relative humidity is increased, the peak of the weighting function would be shifted upwards where the temperatures are lower. Consequently, the equivalent temperature measured would also be lower. As a first approximation, lower T_{bb} values may be considered to have originated from a more moist atmosphere, while warmer T_{bb} values would correspond to a drier atmosphere. Figure 94a taken from Moller and Rasche,⁶⁶ shows the weighting functions for the 6.3μ channel of TIROS VII. The curves were obtained based on an assumption of no variation of relative humidity with height in the troposphere. It is seen that the peaks of the curves shift quite significantly with the temperature regime as well as the moisture required. In general, however, the peak shifts upwards (towards colder temperatures) with increasing mean tropospheric relative humidity.

Based essentially on this argument, Moller and Rasche have constructed "evaluation" diagrams by which the mean relative humidity in the troposphere can be obtained from measurements made in the 6.3μ band and simultaneous measurements

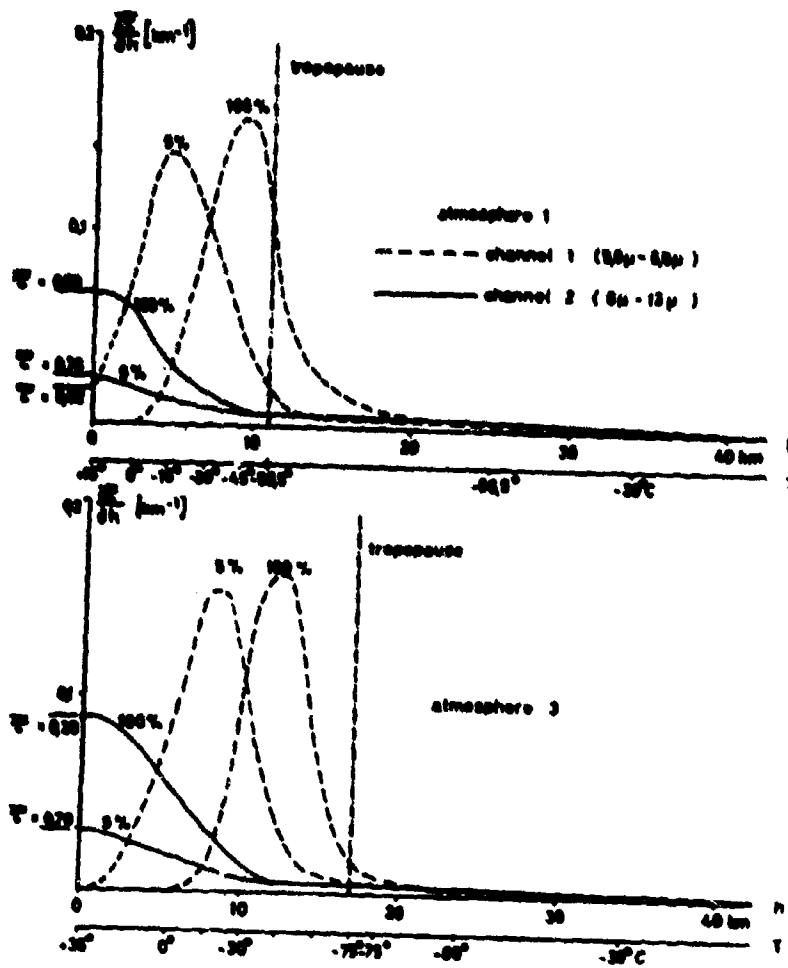


Figure 94a. Weighting Functions of TIROS Radiometer

in an atmospheric window. While their study was confined to the evaluation of data obtained by the scanning radiometer of TIROS II, it should be noted that the same technique can be applied to the evaluation of data from similar radiometers.

Figure 94b shows the evaluation diagram as derived by Moller and Rasche. The dashed curves in the figure are the equivalent blackbody temperatures measured by the water vapor channel. The solid curve lines are the equivalent blackbody temperatures measured by the window channel. The abscissa values, corresponding to the intersection of a water vapor T_{bb} with a window T_{bb} , is the mean relative humidity of the troposphere. The ordinate values are the surface temperatures (i. e., window channel Temperatures corrected for water vapor, similar to Figure 67 shown previously).

The utility of the evaluation diagram of Moller and Rashke has been tested only climatologically, i. e. the evaluation of the global distribution of moisture averaged over a period of time. Examples of these evaluations will be given in Section 10.3.4.

As yet, no significant attempts have been made to apply the water vapor channel measurements to synoptic scale studies, although Bandeen⁸⁵ has made use of the water vapor data in a study of Hurricane Anna. However, Glaser and Milford⁸⁶ in an early study (prior to the launch of TIROS II) based on simulated satellite data, noted that the patterns of equivalent blackbody temperatures as measured in the 6.3 μ water vapor band should provide indications of the fields of vertical motion in the troposphere. In particular, they noted the relationships between the patterns of simulated temperatures and the position of the jet stream. These initial findings are currently being pursued by the scientists at Allied Research Associates, Inc.

Single channel measurements in the 6.3 μ H₂O absorption band cannot provide information on the vertical distribution of atmospheric water vapor. Even simultaneous measurements in a number of spectral regions within the 6.3 μ band cannot provide sufficient information to deduce the water vapor structure. This, again, is due to the fact that in order to separate the effects of water vapor from the effects of temperature on the measured radiance, the temperature structure of the atmosphere at the time of measurement must be known.

In the light of this requirement, it is seen that successful implementation of the scheme to obtain vertical distribution of atmospheric temperatures from satellites can provide the necessary temperature data for the interpretation of multispectral H₂O absorption band measurements for the vertical distribution of atmospheric water

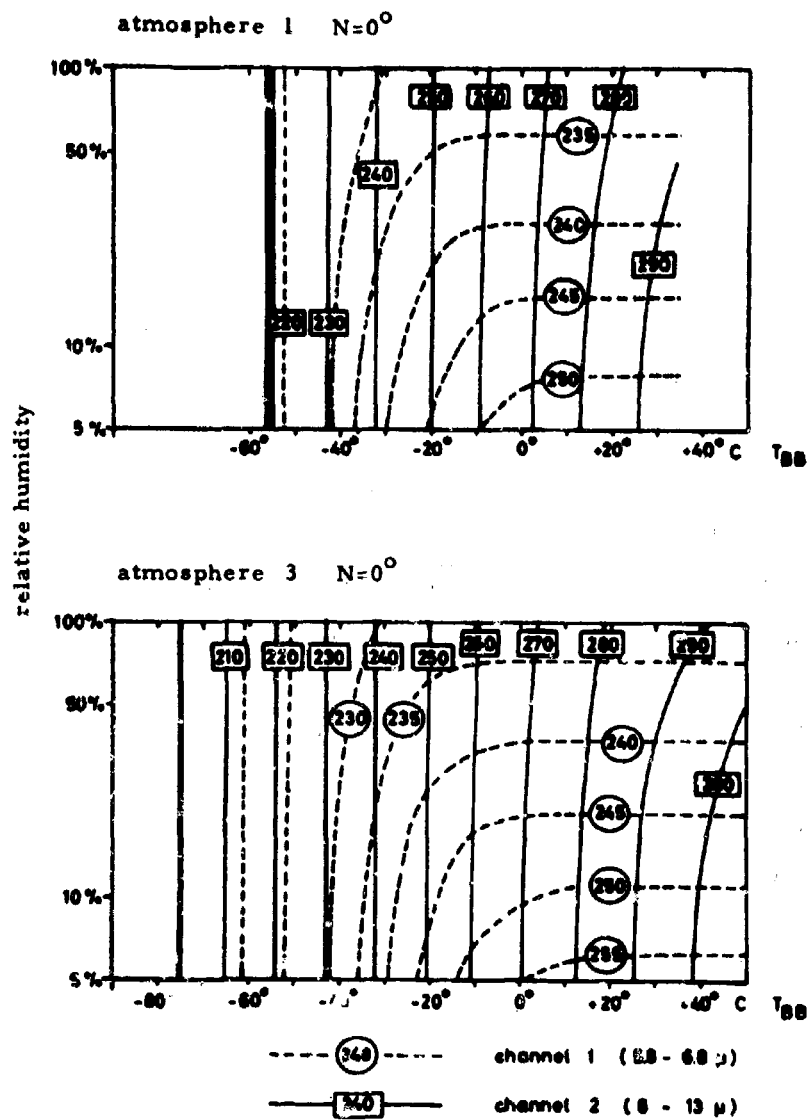


Figure 94b. Moller Diagram for the Evaluation of Relative Humidity from Satellite Radiation Measurements

vapor. Hanel⁸⁷ has suggested the use of a single interferometer as sensor for obtaining multispectral measurements in both the 6.3μ absorption band of H_2O and the 15μ band of CO_2 . The data can then be used first to determine the temperature structure of the atmosphere, then the vertical distribution of water vapor.

10.3.4 Examples of Satellite Measurements in IR Absorption Bands

It was noted previously that absorption band measurements from satellites have been limited to those made in the 6.3μ H_2O band and the 15μ CO_2 band.

From the 15μ measurements, quasi-global maps of the mean stratospheric temperatures for all seasons have been obtained. These maps agree quite well with similar maps constructed from conventional data. Figure 95, for instance is the mapping of lower stratospheric temperatures constructed from measurements made by TIROS VII over the period 19-25 June 1967. Notice the general south to north increase in the measured effective temperature which is the characteristic direction of the temperature gradient in the lower stratosphere. Figure 96 shows the reversal of this gradient in the winter as measured by TIROS VII.

Besides providing a climatological atlas of lower stratospheric temperatures, the measurements of TIROS VII also reveal the rapid changes in stratospheric temperatures associated with sudden stratospheric warmings.

Figure 97 shows one of the first mappings of mean relative humidity in the upper troposphere using the 6.3μ measurements obtained by TIROS IV. The interpretation of the measured T_{bb} values in terms of mean relative humidity was based on Moller's technique described previously. It can be seen from this figure that the distribution of moisture is characteristically depicted in the 6.3μ measurements. For instance, the moist tropical region is delineated by mean relative humidities in excess of 60%. The high pressure area over the Atlantic with its associated dry air is shown to have low relative humidities.

For a better depiction of IR absorption band measurements, the reader is referred to Figure 55 of Section VI in which the measured values of the 15μ and 6.3μ channels of the MRIR of Nimbus II are simultaneously displayed with data obtained by the other channels. It may be seen from this figure that the use of simultaneously obtained data at various wavelength intervals can be extremely helpful in the determination of cloud contaminations in IR absorption band measurements. The data from visible channel (during daylight portions of the orbit) and the IR window channel can be used to delineate the areas in which possible cloud contamination can be expected.

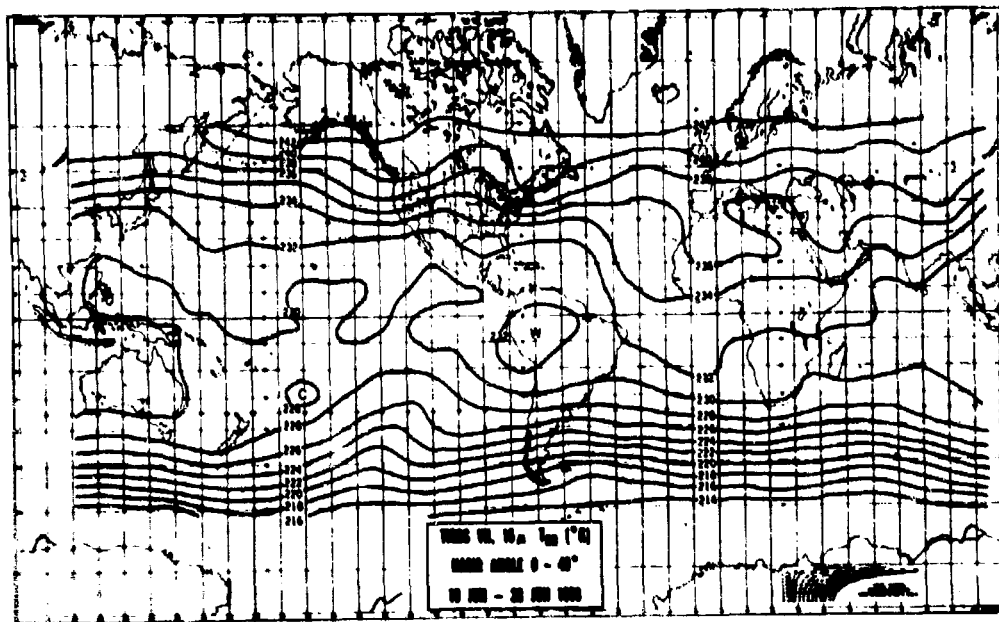


Figure 95. Mean Stratospheric Temperatures for 19-28 June 1963, as Determined by TIROS VII

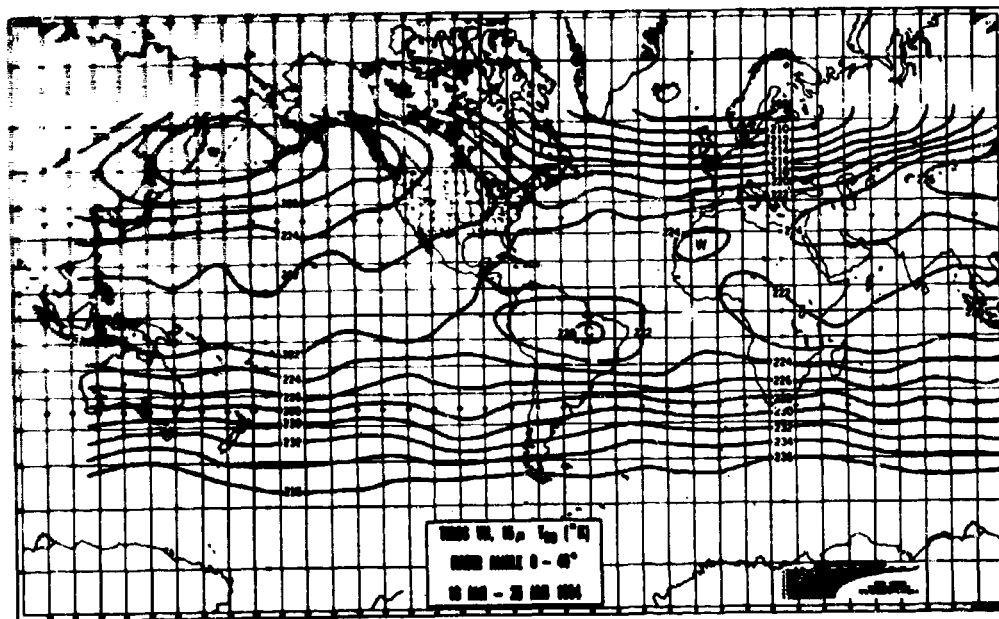


Figure 96. Mean Stratospheric Temperatures for 16-25 January 1964, as Determined by TIROS VII

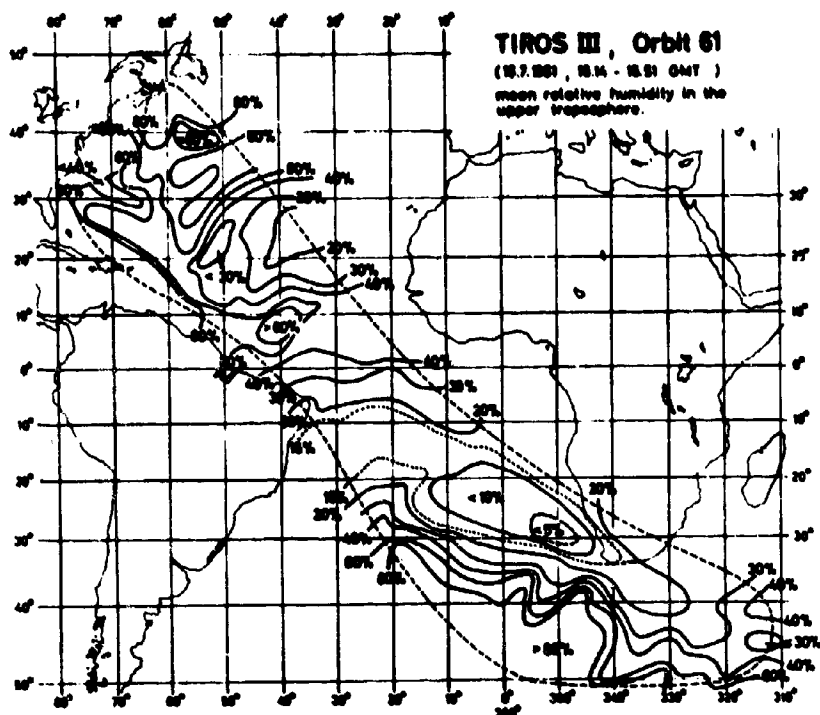


Figure 97. Mapping of Mean Tropospheric Relative Humidity Based on TIROS III Channel 1 Data (Orbit 61)

10.4 Measurements of Total Outgoing Radiation

The net radiation balance, i. e. the input solar radiation and the radiation loss (due to both reflection and emission) by the earth and atmosphere to space and their variation with space and time is an important parameter in the determination of available atmospheric energy. As a consequence, it is of interest to measure the total radiation emitted from the earth and atmosphere to space. This is a parameter ideally suited to satellite measurements, since the satellite is well above the layers of the atmosphere from which radiation losses may be expected.

Since, at the temperatures characteristic of the earth and atmosphere, the emitted radiation is significant only in the infrared region, the total outgoing radiation would best be measured by an infrared sensor having a response function over the total infrared spectrum. Such broad band measurements have been made by the TIROS satellites as well as by Nimbus II. The spectral response of these instruments typically covers the broad spectral region from approximate 7μ to 32μ .

Since the purpose of these measurements is to deduce the total radiation flux leaving the atmosphere, all radiation components and processes in the atmosphere, with the exception of reflected solar radiation, are of significance. With the short wavelength cutoff of the spectral response at $\sim 7\mu$ reflected solar radiation does not enter into the measurements. Consequently, there are no geophysical degradation effects, of the type discussed previously, to these measurements.

It should be pointed out, however, that difficulties do exist in the interpretation of the measured values. As Wark et al.⁵⁷ have pointed out, the parameter of interest is the total flux, i. e., the radiation energy leaving the atmosphere, per unit area, in all directions. With the instrumentation currently available, the parameter that is measured is the energy leaving in a particular direction — in the direction of the satellite sensor. When considering the total infrared radiation leaving the atmosphere, the assumption of isotropic emission no longer applies and the limb darkening effect (as a function of angle) must be taken into account. Consequently it is essential to be able to deduce the angular distribution of the radiation leaving the atmosphere from the measurement of the radiation leaving in a single direction.

Wark et al, has devised a method of estimating the angular function $I(\theta)$ from measurements made at a single angle. The method is again based on computations made from 106 model atmospheric soundings of temperature, moisture and ozone. The equation of radiation transfer is applied to these models and the outgoing intensities at different values of nadir angle are computed. The limb darkening

effect is then estimated from these computed values, resulting in a semi-empirical relationship which permits the derivation of the total outgoing flux from an intensity measured in a given direction. For Channel 4 of TIROS III, for example, the equation given by Wark et al is:

$$A = I(\theta = 0) A + CI(\theta = 0)$$

where

$I(\theta = 0)$ = intensity measured at nadir.

A and C are numerical constants derived from their computations.

10.5 Importance of Simultaneous Multispectral Measurements in the IR

The importance of multispectral observations, with regard to photographic techniques, and observations made in the near IR using reflected solar radiation as the source of energy, was pointed out, in Section IX. In general, when simultaneous multispectral measurements are available, there is an increase in information.

This fact applies equally or with greater force to the medium IR spectral regions. Experience has shown that the interpretation of IR measurements is greatly facilitated when simultaneous observations are also available in the visible portions of the spectrum. For example, Greaves et. al.⁵⁵ when studying the applicability of the window channel measurements of TIROS to the determination of sea surface temperatures, found that it was necessary to make use of simultaneous measurements made by the reflectance channel, or by TV cameras, to determine the boundaries between clear and cloud covered regions.

As a second example, certain crucial aspects of cloud patterns are easier to see in the infrared than in the television pictures. On the other hand, low level clouds can often not be definitively observed in the infrared, making a combination of the television pictures and the infrared data highly desirable. Investigations have shown that even relative cloud top altitudes often cannot be reliably estimated from the TIROS pictures alone, but that these altitudes are clearly revealed by the infrared data. This added information about the vertical structure of the vortical cloud patterns has turned out to be crucial to understanding the processes forming the satellite observed cloud vortices.

Measurements made in the different spectral region of the IR are also often used jointly. The feasibility of vertical sounding of atmospheric temperature is based

on the interpretation of essentially simultaneous measurements made in different spectral regions in an absorption band. Moller's evaluation diagram for humidity (Fig. 94b) is an example of the joint use of measurements made in two different bands within the IR. The determination of mean relative humidity and corrected surface temperature, using the method established by Moller, requires the comparison of the window measurements with the measurements made by the water vapor channel.

In the application of satellite acquired data to synoptic analyses, the independence on simultaneous multispectral measurements is even greater. Many examples of this can be found in References 34 and 51.

SECTION XI

MICROWAVE OBSERVATIONS AND MEASUREMENTS

Microwave observations logically divide into two classes - those made by passive radiometric techniques, and those made by microwave radars. In the following paragraphs, each of these two classes is separately discussed.

11.1 Microwave Radiometry

11.1.1 Introduction

Both infrared and microwave radiometers measure energy thermally emitted by the surface, clouds, or the atmosphere. The microwave radiometer, however, can "see" through clouds at wavelengths greater than 3 cm. Thus, microwave radiometry offers the potential for true "surface" observations.

However, it should be noted that a number of difficulties exist in the interpretation of microwave observations. Most significant of these is the fact that emissivities of surfaces in the microwave cannot be approximated by unity, and are dependent on the polarization of the radiation measured by the radiometer. Furthermore, as a consequence of the low emissivity, the reflectivity of the surface becomes proportionately significant. The radiation propagating from the surface may therefore consist of an emitted and a reflected component. As a consequence, a unique temperature comparable to the true surface temperature may be impossible to obtain.

In summary, the radiation measured by a microwave radiometer is affected by contributions from the following:

- a. Thermometric temperature of the source
- b. Emissivity/reflectivity of the source
- c. Physical state of the source
- d. Wavelength of observation
- e. Polarization effects from the source, intervening medium, and antenna
- f. Intervening medium

- g. Noise generated by the receiving antenna
- h. Noise from the receiver
- i. Interfering non-thermal signals from lightning, radars, harmonics of communication signals, etc.

It should also be noted that while in the infrared, the energy emitted by a blackbody is proportional to the fourth power of its temperature, in the microwave regions, the energy emitted is only proportional to the first power of temperature. This implies that microwave radiometers must measure energy at very low levels. As a result of the necessity of making low energy level measurements, another restriction is placed on satellite microwave applications. This is the time-resolution problem leading to equivalent interpretation problems. The observational scatter has been expressed by the Dicke equation

$$\sigma_T = K \frac{(T_a T_n)}{(B\tau)^{1/2}} \quad (137)$$

where

- σ_T = Standard deviation of a measurement
- T_a = Apparent temperature of the radiation measured ($^{\circ}\text{K}$)
- T_n = Equivalent input noise temperature of the receiver ($^{\circ}\text{K}$)
- B = Frequency bandwidth of radiation (cps)
- τ = Observation time (or integration time) (sec)
- K = Modulation factor.

Equation(137) implies that the error in the measurement of the apparent temperature decreases as the square root of the observation time. Because of satellite scan motions, observation time is directly related to spatial resolution. Thus a basic trade off exists between spatial and temperature resolution which can be only partially resolved by use of giant receiving antennas.

11.1.2 Equation of Transfer

In many aspects, the equation of transfer for microwave radiation is similar to that for IR radiation. However, as it has been noted, the energy emitted by a blackbody at microwave wavelengths is directly proportional to the temperature. As a consequence, the notation can be greatly simplified.

Figure 98 shows a schematic of the various components which combine to give rise to the measured apparent temperature. From this figure, it may be seen that the equation of transfer for microwave radiation may be expressed as

$$T_a = T_v \epsilon_r r_w + \Sigma L_v^2 (1 - \epsilon_w) + P_w \epsilon_w L_v + T_v \epsilon_v$$

where

- T_a = Apparent temperature measured by the radiometer
- T_w = Temperature of the surfaces viewed by the radiometer
- ϵ_w and r_w are respectively the emissivity and reflectivity of the surfaces view.
- Σ = Absolute temperature of the sky above the atmosphere
- L = Absorption due to the atmosphere
- T_v = Apparent temperature of water vapor clouds

11.1.3 Parameters Deducible from Microwave Radiometric Measurements

Even with all the attendant problems, numerous applications have been proposed for satellite-borne microwave radiometry, but as yet no earth directed experiments have been launched into orbit. (One is planned for Nimbus B or D.)

11.1.3.1 Sea State

Vivian⁸⁸ suggests that sea state can be derived from the difference in emissivity between different polarizations at several different frequencies.

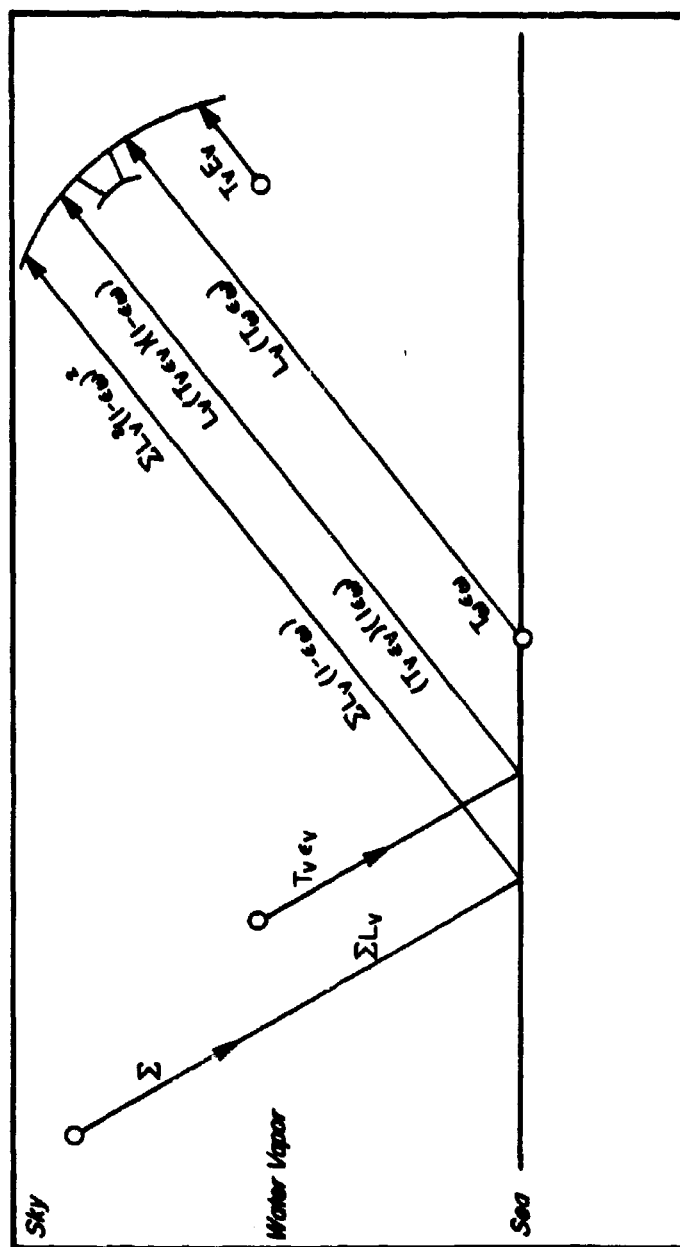


Figure 98. Schematic of Microwave Radiation Transfer

11.1.3.2 Ice Floes

Conway and Mordon⁸⁹ describe how the difference in microwave emissivity between sea water and ice could be used to map ice areas. Since these measurements can be at wavelengths longer than 3 cm, cloud cover interference occurring with IR and visual observations would be eliminated. This application seems one of the more immediately feasible of those suggested to-date.

11.1.3.3 Atmospheric Temperature

In Section V, it was noted that a number of oxygen absorption bands are located in the microwave region. Like CO₂, oxygen is a well-mixed gas. Consequently, the IR technique of temperature sounding by either spectral scanning or angular scanning can also be applied to the microwave region.

11.1.3.4 Sferics Detection

This application for microwave radiometry has already been noted in Section VIII.

11.2 Radar Observations from Satellites

11.2.1 Introduction

The concept of using radar aboard satellites is more than ten years old and was first proposed by Wexler⁹⁴. The concept remains an intriguing one in the areas of surface surveillance and detection of precipitation. However, there are serious hurdles and stumbling blocks in the implementation of radar satellite techniques.

For instance, the entire question of the feasibility of meteorological radar for precipitation detection aboard a satellite has been explored at considerable length by Dennis⁹⁵. Dennis' conclusions are rather pessimistic and may be summed up by this quotation from his report:

"In summary, a meteorological satellite radar, assuming it were technically successful, would be an extremely complex means of acquiring crude estimates of the instantaneous rainfall rate, a rapidly fluctuating function which is only loosely correlated with the prevailing synoptic situation. Such data would be of negligible importance to weather forecasters dealing with either local or large-scale systems, and would be too crude to provide reliable inputs to research programs involving climatology or the general circulation."

Although the ground-based K_A band radars such as the TPQ-11 are capable of detecting most clouds, it must be expected that because of the R^2 effect either the power requirements would have to be increased by a factor of 10 or only about half of the clouds detected from the ground would be detectable from the satellite. At best, power requirements are likely to be excessive even at the lower satellite altitudes.

Dennis also seriously questions in principle the feasibility of the use of a side-looking radar from a satellite. Since this type of radar is basically a Doppler system, Dennis believes that ambiguities in target range, azimuth bearing, height and radial velocity would prove very difficult if not impossible to resolve.

The most valuable information in terms of coverage would be provided by some form of scanning radar capable of monitoring a strip several hundred miles in width on each orbit. Dennis' analysis indicates that a phased antenna array would be required for such a function necessitating a complex scanning system.

In spite of the numerous hurdles and stumbling blocks the possibilities of a successful satellite radar system are so far-reaching that repeated objective assessments of the problem at intervals are called for. Eventually the state of the radar technology will permit the feasibility of an operational satellite system.

11.2.2 Display Techniques

Techniques of display from satellite radar have not yet been considered in detail. However the adaptation of certain techniques from ground-based and airborne radars are indicated as solutions. The form of display considered most suitable for adaptation to satellite uses is the time-height indicator (THI). This is the type of indicator currently used with fixed-beam radars, generally vertical-pointing, of which the K_A band AN/TPQ-11 is an example.

As used with the TPQ-11, the indicator consists of a facsimile-type strip recorder on which the vertical sweep of the radar beam is continuously recorded. On such a record, height is the ordinate, time the abscissa. For satellite radar use, a similar form of display could be utilized for a vertically-pointing (downward) radar on an earth-oriented vehicle. By using the proper PRF (pulse repetition frequency) and gating the signal so as to accept only that portion containing weather information (below 70,000 ft) and expanding the scale, a detailed vertical cross-section of the significant weather immediately below the vehicle might be obtained. Experience and the fact that there is approximately a 10 to 1 ratio of cloud to precipitation indicates that the choice of the high frequency K_A band might prove to be a wise one. This could be expected to detect much of the cloudiness directly below the spacecraft in addition to the precipitation and would be attenuated only in the relatively rare encounter of heavy showers and thunderstorms directly below. In addition, data on cloud composition and height would provide valuable information in the interpretation of satellite cloud photos.

The radar data would presumably be stored aboard an unmanned satellite, then transmitted during periods of acquisition. Since this type of data lends itself readily to quantizing and digitization, on-board storage should not be a serious problem.

In a modified form of the THI, the fixed antenna points sideways but depressed below the horizontal. A radar of this type, the AN/UPD-1 (Project MICHIGAN) had been used successfully according to Scheps⁹⁰ aboard aircraft to map the earth's surface in the form of a strip. Excellent resolution has been obtained even with a small antenna by taking advantage of the motion of the aircraft to create a synthetic "aperture" many times the size of the antenna.

The choice of wavelength for satellite radar must be made by considering the antenna size, beam width and attenuation. At shorter wavelengths the beam widths are narrower, giving greater resolution, for the same antenna size. The backscattering cross-section of cloud and precipitation also increases with decreasing wavelength; however, attenuation by cloud and rain increases. X band (3 cm) airborne radar has produced satisfactory results for mapping areas of ice, and for providing information on the state of the sea and for geodetic surveys. At K band (near 1 cm), attenuation may at times prevent the obtaining of such information. However, this may be satisfactory for the detection of cloud and precipitation, particularly for a vertically pointed (downward) radar. Although heavy rain may attenuate the signal so that precipitation near the ground may not be detected,

nevertheless, K band should satisfactorily delineate the areas of precipitation. Attenuation, when it occurs, can be recognized and used to advantage to indicate the presence of heavy rain. The use of K band radar would also have the advantage of smaller power requirements than radar at longer wavelengths.

The type of display to be used for a side-viewing radar would probably also take the form of a facsimile strip chart feeding at a rate such that the dimensions of the mapped area and the chart would be kept in scale with a minimum of distortion.

11.2.3 Terrestrial Applications of Spacecraft Radars

Apart from the meteorological use of satellite borne radar in the detection and location of areas of precipitation, a number of terrestrial applications have been proposed. Some of the more significant of these applications are discussed below.

11.2.3.1 Terrestrial Mapping

As early as 1948, Smith⁹² demonstrated the mapping capabilities of airborne radars. With the advent of the side looking radar, radar mapping has received increasing attention. At present at the University of Kansas, GIMRADA, Ohio State University and a number of other institutions, evaluations are taking place of sophisticated multi-frequency, polypolarization, coherent imaging systems for geoscience purposes. These studies in effect rest on the successes of multispectral photography and infrared measurements in surface surveillance. In the same manner, a multispectral and polypolarization radar system can take advantage of the spectral and polarization dependences of the scattering properties of the different surfaces of the earth. It is the hope that a substantial information gain can be achieved by these techniques, permitting the separation of individual target elements.

Among the specific areas in the geosciences in which spacecraft radar mapping would be useful are Glaciology: in the definition of the mass budget of the Antarctic and Greenland ice sheets, and in the measurements of sea and lake ice; Geology: in the mapping of flood plains, interior and coastal dune fields and other structural features.

11.2.3.2 Oceanography

Perhaps the application of spacecraft borne radar in the field of oceanographic measurements is most significant to the Navy. Pierson et al⁹³ has suggested that the sea state can be determined by radar if the angular dependence of the backscatter from the sea on the roughness of the sea surface is taken advantage of. They noted that for a given material, the "smoother" the surface, the more the scatter increases near the horizontal and the more rapidly it falls off with angle near the vertical. Thus, a smooth sea gives a stronger echo near the vertical than a rough sea, but at angles of 10^0 or so it falls off to a lower value than that for rough sea. They suggested that one observation every eighty nautical miles over the ocean would provide a detailed picture of the heights of the waves.

They also suggested by using a satellite radar as an altimeter, the slope of the sea surface, storm surges, tsunamis and heights of tides can ultimately be detected from satellites.

SECTION XII

DATA COLLECTION SATELLITES

12.1 Introduction

A major limitation of meteorological and geophysical satellites is their inability to make ambient measurements of the atmosphere (except its extreme outer fringes), the oceans, and the earth's surface. Information reaching a satellite is limited to that transmitted by electromagnetic radiation.

This can be overcome by the use of a series of appropriate observing platforms or stations in the atmosphere, or oceans, and/or earth which are radio-interrogated by the satellite as it passes over them. If the platform is mobile (a balloon or a drifting buoy), the satellite would also determine the geographical position of the platform. The geophysical observations and the geographical location information would be recorded by the satellite and telemetered to the ground at a CDA station, where the data would be processed and the observations transmitted to the using agencies. The movement of a balloon or a drifting buoy would provide, respectively, wind or ocean current information.

In order to prevent interference between interrogations of different platforms, each platform would be assigned a unique address to which it and only it would respond when this address is transmitted by the satellite. In some of the systems presently under study, the satellite would repeatedly cycle through all addresses, with a pause between each successive address to receive the response when the platform is within radio range. While this approach is in some ways the simpler, it limits the number of platforms that could be concurrently in use (or interrogated on a single frequency), since an address cycle must be completed within about one minute if at least two (and preferably at least three) interrogations necessary for location (unless the Omega system, discussed below, is used) are to be completed during each satellite pass within range of the observing platform.

In other systems, a specific program of discrete addresses, to be transmitted by the satellite at specified times, would be transmitted to the satellite (and recorded in it) each time the satellite passed over a CDA station. The program would cause an address to be transmitted only when the satellite is expected to be within range

of the corresponding platform, and when the relative satellite-platform positions were expected to be optimum for the interrogation and location operations. This system obviously increases the number of platforms that can be serviced by a single satellite. One disadvantage is that the platform locations must be forecast with some reasonable degree of accuracy; this may be a problem with balloons, which will normally drift at speeds of 30 - 100 knots or more. Experience has indicated that predicted future positions are likely to be in error by 25% or more of the length of the trajectory over the period of prediction, although the data to be expected from the balloons themselves may lead to improved trajectory forecasts.

12.2 Methods for the Location of Moving Platforms

Two methods for determining the geographical positions of moving platforms have been proposed: (a) range circle intersections, and (b) Omega.

In the first method, the range from the satellite to the platform is determined by the time it requires a radio signal to travel from the satellite to the platform and back, and by phase comparisons between the transmitted and received signals. The intersection(s) of two or more such range circles, and the known positions of the satellite, provide the platform position. An ambiguity may exist if the platform is close to the satellite subpoint track; otherwise, it can usually be resolved by the use of three range circles and the curvature of the subpoint track, or by the previous history of the platform's positions and movements. In the case of rapidly moving platforms (especially balloons in or near the jet stream), the movement of the platforms over the few minutes between successive range determinations may be a source of significant error. It would, however, appear feasible to develop techniques for significantly reducing this source of errors by re-cycling successive approximations of the platform positions and the derived winds.

A further disadvantage of the range intersection approach is that it appears to be inapplicable to earth synchronous satellites, thus limiting interrogations and position determinations to those few short periods each day when a low altitude satellite orbits near a platform of interest.

An alternative approach now being considered would make use of proposed (Navy) Omega long range, world-wide, navigation system. Omega is somewhat like Loran in that it is based on the intersection of hyperbolae established by the transmissions from fixed stations, but uses a very long wave (about 15 kc) transmission

frequency. If Omega were to be used, the platforms would merely receive the Omega signals and relay them, in a transponder mode, to the satellite for recording. All data processing would occur on the ground after readout of the data stored in the satellite. Since the only interaction between the satellite and the platforms is that of interrogation, the Omega approach could apply to satellite altitudes as high as those of a synchronous satellite.

The possible disadvantages of Omega include:

1. The equipment required to receive and transpond the Omega signals may be excessive for use on balloons compatible with aircraft safety.
2. Because the Omega signals are surface propagating, and the propagation velocity varies somewhat with the type of surface, there may be questions as to the accuracy of the position fix.
3. Because of budgetary problems, it is not certain just how soon a world-wide, operational Omega system will be implemented.

Once the platform positions were obtained (by either approach), the velocities of either constant level balloons or drifting buoys would be obtained from position differences over an interval of one orbit or more (1-1/2 hours or more). If the range intersection method is used, positions on previous and subsequent orbits can almost always be obtained and used in those cases where the platform is near the subpoint track and there is a position ambiguity.

A very significant set of observing platforms in such a system would be an extensive network of super-pressure constant-density-level balloons. If these balloons are to float at the levels where the data would be of greatest operational use, the balloons, their transponder electronics, and any sensors must be so light-weight and frangible as to provide no hazard in the event of a collision with an aircraft. It is generally felt that the IRLS (Interrogation, Ranging, and Location System), to be flown on Nimbus B as a first actual test of the data collection satellite concept, cannot meet this requirement. This restriction will also limit the number, type, complexity, and accuracy of the sensors that could be used on the balloons, but it is generally felt that even if only winds could be determined (from the balloon position displacements), the worldwide data so obtained would be of sufficient value to justify the system. It is felt the balloons can also measure pressure altitude, temperature, and possibly humidity.

Before such a network of satellite-tracked balloons can be implemented, it will be necessary to obtain international concurrence to their flight through the airspace of all nations.

Except for whatever hazards to shipping larger size drifting buoys might be felt to constitute, the amount of surface and subsurface meteorological and oceanographic data obtainable from either anchored or drifting buoys would be limited only by:

1. Buoy size and capacity
2. Sensor capabilities
3. Buoy power
4. Buoy-satellite bandwidth and information rate limitations.

Naval interest will center on buoy-acquired data, such as sonar or other underwater sound; oceanographic data on temperatures, salinity, sea state, and sea life; and conventional meteorological data. The treatment of much of this data may be unaffected by the unconventional mode of transmission.

The critical links in a buoy-data collection system are the buoy-satellite and satellite-buoy paths, since high gain antennas cannot be employed for the large area coverage required. Considerations of galactic noise, ionospheric attenuation and reflection, transmitter and receiver efficiency and cost, and international frequency allocations, indicate communication frequencies in the 400 to 500 megacycle region.

Telemetry of information (from the buoy) such as temperature, pressure, wind and wind direction, can be accomplished with an information rate equivalent to approximately 1 kilobit/sec. Sonar information, broadcast in its entirety, would vastly increase the data rate. However, the large power requirement necessary for the wideband transmission of sonar "imagery" will probably result in the inclusion of decision circuits in the buoy to filter out only the significant "events" for transmission.

Studies of data-collection satellite systems assume the above information rates are transmitted in the 400 mc band with a transmitted power of approximately 10-20 watts from the buoy. At the ranges of interest, the bit error rate (assuming digitized sensor information) is predicted to be 10^{-5} or less. Hence, we need not concern ourselves with the simulation of errors due to thermal noise under normal operating conditions.

Of more serious concern are data transmission dropouts such as would be experienced in the presence of "noise" bursts radiated from ships, airplanes, island transmitters and the like. Another source of signal dropout occurs in rough seas when shadowing occurs (waves between buoy and satellite) or when the buoy is pitched sufficiently to raise the hemispherical antenna pattern of the buoy above the satellite. Multipath and associated fading presents a potential problem where the reflecting surface of the sea is close to the broad coverage antenna pattern.

Communications dropouts will result in both erratic data and a complete absence of portions of the data which can reduce the reliability of information thus acquired.

12.3 Training Problems

Until such time as engineering and management decisions regarding the various possible approaches to an operational data collection satellite reach far more of a consensus than is currently the case, it would be pointless to consider in any detail the simulation and training that such a system will require. At present, it seems unlikely that an operational data collection satellite system and its ancillary platforms will come into being prior to 1970, and even this may be an unduly optimistic estimate. Thus, time should be readily available for simulation and training designs, assuming the progress of subsequent engineering and management decisions is adequately monitored.

Skills that such a system are likely to require of Navy personnel might include:

- a. Determination and preparation of interrogation programs to be transmitted to the satellite, including the possible necessity of forecasting drifting buoy and balloon trajectories and future positions.
- b. Processing and reduction of the data acquired, including position determinations, wind or ocean current determinations, and observation decoding.
- c. Sorting and distribution of the various data obtained. As read-out from the satellite, the data will consist of a random array of several types of observations from several types of platforms. Few users will be interested in all the data from all the platforms. A sort and distribution in terms of user requirements (both as to types of observations and geographical areas) will be required.

d. Data interpretation. While some of the data characteristics will be similar to those of standard meteorological and oceanographic data, there will also be significant differences. The observations from balloons and drifting buoys will obviously not be at fixed locations. The times of the observations will not be synoptic (except possibly when earth synchronous satellites are used), but will be related to the satellite orbit parameters; for example, observations collected by sun-synchronous satellites would cluster at or near fixed local times. The position observations of balloons and drifting buoys will for the first time permit analyses in Lagrangian (particle trajectory) terms; meteorological and oceanographic flow patterns are now analyzed almost solely in Eulerian terms (fluid velocities at fixed points).

SECTION XIII

SATELLITE TRANSMISSION OF FACSIMILE
WEATHER CHARTS (WEFAX)

13.1 Introduction

The use of meteorological satellites to transmit facsimile weather charts (both analyses and prognoses) or other graphic material is an obvious concept, and has been nicknamed WEFAX. The successful operation of the APT systems (TIROS VIII, Nimbus I, ESSA II) leaves little question of the feasibility, especially since standard weather charts require no grey scale discrimination. For other graphic material, it would only be necessary to insure that (1) the scanning unit has an appropriate grey scale capability, (2) the material can be fitted in the available transmission times, and (3) the sizes of any characters or symbols are sufficient to be legible after transmission and recording.

At local weather stations, the charts would be received using the standard APT receiver-recorder, or a similar unit. (For material transmitted via an earth-synchronous satellite, the receiving antenna would not need to be remotely controllable since the satellite position would change only slowly, if at all. Accordingly, a separate receiving unit might be feasible and would avoid having to miss transmissions concurrent with passes of lower-level APT satellites.)

Three modes of transmission can be visualized:

1. Full time, real time relay via an earth-synchronous satellite.
2. Part time (shared use) real time relay via an earth-synchronous satellite.
3. Transmission to and recording in a low-level satellite (at a QDA station), with the charts played out and transmitted along the orbit and with chart areas phased to the areas of transmission. In this mode, it is most probable that these chart transmissions would share the APT transmitter and be interspersed between APT pictures, but with no significant loss of the area coverage provided by the APT pictures.

Part-time transmissions from an earth-synchronous satellite are planned on an experimental basis from the NASA ATS-B satellite. After other experimental projects planned for the ATS-B are completed, the time available for WEFAX may be expanded from the original 20-25 minutes every six hours which is presently scheduled. It might even become essentially full time.

WEFAX transmissions interspersed between APT pictures are being considered by NASA for Nimbus D (1968 launch).

13.2 Types and Numbers of Charts Available from WEFAX

The types and numbers of charts which might be available from WEFAX are discussed in some detail below. (For a complete analysis of the potential uses of WEFAX see Ref. 93).

WEFAX transmissions in the time intervals between APT pictures (during daylight) or in otherwise unused night periods (in the absence of DRIR transmissions) from sun-synchronous (i.e., low level) satellites can provide a global distribution of a significantly useful number of the most critical weather charts. A similar capability exists for earth-synchronous satellites whose WEFAX transmissions are limited to a small fraction of a day; in this case, of course, the degree of global capability depends on the number and geographical positions of the concurrently operating earth-synchronous satellites.

In contrast, most land-line and radio facsimile transmissions operate on an essentially continuous schedule which occupies nearly the full 24 hours of each day. This permits the transmission of a wide variety of charts at such recurrent intervals as are made appropriate by the scheduled synoptic hours of observation (the intervals are usually six or twelve hours), and by the relative operational significance of the different types of charts. There is apparently a significant operational demand for each and every one of these charts, since a major controversy ensues following any proposal to delete an existing chart in favor of a new one. (In this regard, recall the difficulties that existed in obtaining time for satellite nephanalysis transmissions during the first several years of the TIROS programs.) In fact, the demand for chart variety and frequency is so great that the U.S. Weather Bureau operates two concurrent land-line facsimile circuits within the continental United States; one to all stations and the other to provide additional charts to major forecast centers.

With this background in mind, it seems unlikely that a limited WEFAX capability (such as would be available from charts interspersed between APT pictures, or limited transmissions from earth synchronous satellites) can ever

be competitive with land-line or radio facsimile where sufficient communications exist, or for nations which are able to consider the costs of reasonably adequate weather information dissemination as secondary to the need for obtaining and distributing the data.

On the other hand, if a capability for full time WEFAX transmissions from earth-synchronous satellites were to be implemented, it would often be fully competitive with land-line or radio facsimile systems. This would certainly be true in most of the remote or less developed areas of the world. Even in the continental United States, such a system would merit full consideration, especially if an additional facsimile circuit, or major equipment replacements over an existing circuit, were contemplated.

The WEFAX capability, even when very limited in the number and variety of charts it can disseminate each day, can particularly benefit the smaller, remote weather stations whose professional manning may range from a single forecaster to no more than one forecaster per shift. To a greater or lesser degree, such a station will receive weather observations for its immediate vicinity - say a radius of the order of 500 miles - by existing conventional communications. It can use to significant advantage regional analyses and prognoses prepared by an adequately staffed center, and covering an area surrounding the station and of the order of 5-10 million square miles. In many cases, existing communications do not provide such analyses, or provide them only in forms requiring laborious reception and decoding procedures. The WEFAX charts would supplement the local area information and would improve the reliability of the forecasts issued by such stations, especially in the period of 24 to 48 hours.

Figure 99 shows the numbers of, and areas covered by, charts that could, at a maximum, be received by a station at 40°N from a single low-level (750 n.mi.) satellite, operating only during daytime with WEFAX transmissions interspersed between APT pictures.

The following tabulation indicates the charts that could be received each day from 20-25 minute transmission periods from an earth-synchronous satellite.

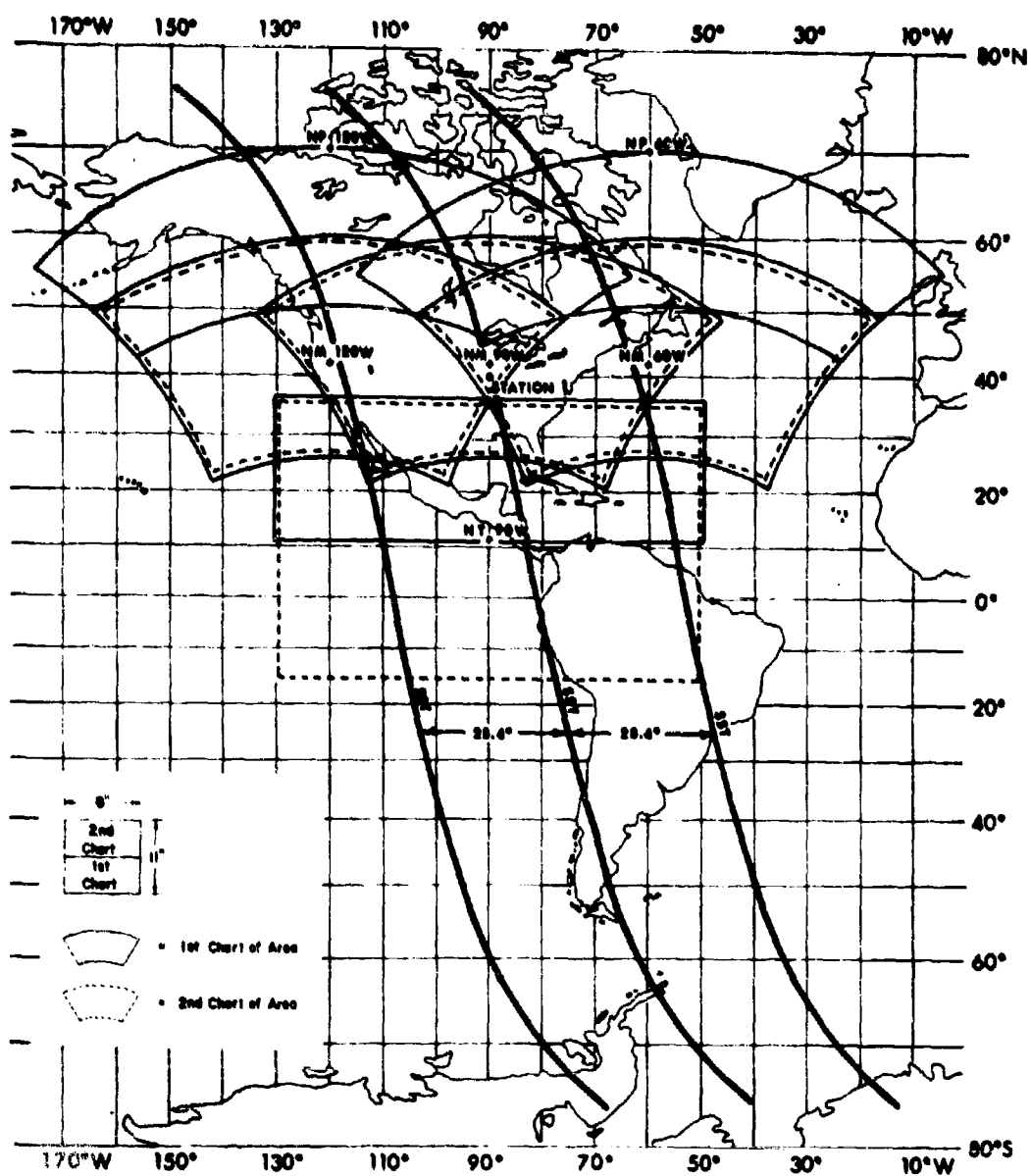


Figure 99. Maximum WEFAX Coverage (on overhead pass) that Would be Acquired by a Station at 40°N from a Sun-Synchronous Transmission

NAVTRADEVCE 66-C-0031-1

First Transmission Period

NPMW	Composite Surface & 500 Millibar Analysis
NPME	Composite Surface & 500 Millibar Analysis
TROP	Surface Analysis
SPM (or SPMW & SPME)	Composite Surface & 500 Millibar Analysis

Second Transmission Period

NPMW	Composite Surface & 500 Millibar 36 Hour Prognosis
NPME	Composite Surface & 500 Millibar 36 Hour Prognosis
TROP	200 Millibar Analysis
SPM (or SPMW & SPME)	Composite Surface & 500 Millibar 36 Hour Prognosis

Third and Fourth Transmission Periods

The transmissions in the third and fourth periods would be the same as those in the first and second periods, respectively, except that the times of the charts would be twelve hours later.

The above cycle would be repeated each day.

The meaning of the capital letter chart designators is summarized below:

Earth-Synchronous Satellite WEFAX Chart Designators

NPMW	Northern Polar and Mid-Latitude Chart-Western Section 1 : 30,000,000 Polar Stereographic
NPME	Northern Polar and Mid-Latitude Chart-Eastern Section, 1 : 30,000,000 Polar Stereographic
TROP	Tropical Chart; 1 : 40,000,000 Mercator
SPMW	Southern Polar and Mid-Latitude Chart-Western Section 1 : 30,000,000 Polar Stereographic
SPME	Southern Polar and Mid-Latitude Chart-Eastern Section 1 : 30,000,000 Polar Stereographic
SPM	Alternative Southern Polar and Mid-Latitude Chart; 1 : 60,000,000 Polar Stereographic

Table 14 indicates the average numbers and types of WEFAX charts that could be available, under one plan, to a station at 40°N, from transmissions from various numbers of limited-transmission earth-synchronous and APT-interspersed low level (750 n.mi.) satellites.

13.3 Training Requirements

From the viewpoint of training, the WEFAX capability would present little or no new problems. The operation of the weather station receivers would require a part of exactly the same procedures as those required for acquiring APT data (determination of antenna angles, and receiver operation). The charts, once received, would be used the same as any other conventional weather charts received by land-line or radio facsimile, with the exception that some minor modifications might result from:

1. Limitations to the number, coverage, and/or variety of charts of the WEFAX mode is either the part-time earth synchronous, or the low-level APT interspersed.
2. The possibility of some changes in the chart scales.

Table 14

**Average Number and Types of Weather Charts
Received Daily by a Station at 40°N Latitude**

ONE EARTH-SYNCHRONOUS SATELLITE			ONE SUN-SYNCHRONOUS SATELLITE		
Number of Different Periods	Chart Area	Type of Chart	Number of Different Areas	Chart Area	Type of Chart
2	NPMW	Sfc & 500 Anal	1/2	NP	Sfc Anal
2	NPMW	Sfc & 500 36 Hr Prog	1/2	NP	Sfc & 500 36 Hr Prog
2	NPME	Sfc & 500 Anal	3	NM	Sfc & 500 Anal
2	NPME	Sfc & 500 36 Hr Prog	3	NM	Sfc & 500 36 Hr Prog
2	TROP	Sfc Anal	1	NT	Sfc Anal
2	TROP	200 Anal	1/2	NT	200 (or 500) Anal
2	SPM	Sfc & 500 Anal			
2	SPM	Sfc & 500 36 Hr Prog			

TWO SUN-SYNCHRONOUS SATELLITES			ONE EARTH-SYNCHRONOUS SATELLITE & ONE SUN-SYNCHRONOUS SATELLITE		
Number of Different Areas or Periods	Chart Area	Type of Chart	Number of Different Areas or Periods	Chart Area	Type of Chart
1/2	NP	Sfc Anal	1/2	NP	Sfc Anal
1/2	NP	200 Anal	1/2	NP	Sfc & 500 36 Hr Prog
1/2	NP	Sfc & 500 36 Hr Prog	3	NM	Sfc & 500 Anal
1/2	NP	300 Anal	3	NM	Sfc & 500 36 Hr Prog
3	NM	Sfc & 500 36 Hr Prog	1	NT	Sfc Anal
3	NM	Sfc 72 Hr Prog	1/2	NT	200 (or 500) Anal
3	NM	Sfc & 500 Anal	1	NPMW	Sfc & 500 Anal
3	NM	200 Anal	1	NPMW	Sfc & 500 36 Hr Prog
1	NT	Sfc Anal	1	NPMW	200 Anal
1	NT	Sfc 36 Hr Prog	1	NPMW	Sfc 72 Hr Prog
1/2	NT	200 (or 500) Anal	1	NPME	Sfc & 500 Anal
1/2	NT	700 (or 850) Anal	1	NPME	Sfc & 500 36 Hr Prog
			1	NPME	200 Anal
			1	NPME	Sfc 72 Hr Prog
			1	TROP	Sfc Anal
			1	TROP	200 Anal
			1	TROP	700 Anal
			1	TROP	Sfc 36 Hr Prog
			1	SPM	Sfc & 500 Anal
			1	SPM	Sfc & 500 36 Hr Prog
			1	SPM	200 Anal
			1	SPM	Sfc 72 Hr Prog

SECTION XIV

THE GROUND COMPLEX REQUIRED TO SUPPORT A SATELLITE

14.1 Introduction

Any geophysical satellite must be supported by a very significant ground complex, and this is particularly true of an operational system. The functions of this complex may be summarized as

1. Tracking
2. Data acquisition
3. Data processing and dissemination

14.2 Tracking

A satellite in orbit must be tracked and its position in space (at known times) determined frequently at a number of points suitably spaced over the earth. These tracking data are essential to the geographic location of the observations made by the satellite, and to the prediction of the areas of feasible data coverage, the times and sites at which data acquisition is possible.

The tracking is performed by a network of tracking stations. Examples of such networks include the NASA STADAN (formerly known as Minitrack) and the Navy SPASUR. The tracking data obtained by the individual stations are communicated to a central point where they are processed by high speed computers to provide orbital ephemerides at frequent intervals (no less than at weekly intervals). These orbital data are then communicated to (1) data processing centers where the satellite's positions in space and time are determined to permit geographic referencing of the observations transmitted by the satellite; and (2) satellite control centers where they are used to predict the areas of coverage, the times and stations at which data acquisition is possible, and consequently the programs to be communicated to and executed by the satellite.

14.3 Data Acquisition

In general, geophysical data are of greatest value if data for the entire world, or at least significant fractions thereof, are concurrently available at a single center for analysis. This requirement dictates that the global satellite observations be stored in the satellite and readout to a minimum number of data acquisition sites (as the satellite passes within their range) for processing and/or transmission to a central processing site. The readout stations are frequently referred to as Command and Data Acquisition (CDA) stations or Data Acquisition Facilities (DAF). While in theory a single CDA at either pole could intercept all passes of a satellite in a quasi-polar orbit, the practicalities of logistics and communications dictate two or three CDA's for any orbit inclination except a quasi-equatorial orbit. Since communications must then be provided to assemble at a central point the global data acquired by all CDA's, it may then be appropriate to locate the central data processing facility at a different site than one of the CDA stations; for example, at a point of easiest access to other sources of geophysical data and/or at an existing central communications terminal as regards dissemination of the processed data.

A typical CDA station will include

1. A high gain antenna, usually a 60-85 foot parabolic dish or an equivalent phased array
2. Computers to point the antenna at the predicted position of the satellite, and auto-tracking antenna controllers
3. Radio receivers and demodulators to amplify the satellite signals and separate the data from their carrier
4. Multiple speed tape recorders, to permanently record the data and to permit their playback at slower speeds as may be required for subsequent processing and/or transmission. In the event of loss or degradation of the data during subsequent transmission, these recordings provide the desired high quality data for archival processing.
5. Displays and/or photographic recording and processing equipment for quality control checks, and as a source of "hard-copy" data for analysis and facsimile transmission in the event of failure of the broadband surface transmission lines.

6. Terminal equipment for the surface transmission lines.
7. A command console, transmitter, and antenna for sending commands and future programs to the satellite.

Figure 100 is a highly simplified block diagram of a Nimbus DAF.

14.4 Data Processing and Dissemination

The transmission of the largely unprocessed data, from the CDA station to the central data processing facility, requires wide bandwidth reliable communications on a full time basis. The bandwidth must be at least sufficient to transmit a full orbit's data in less than an orbital period; since not all orbits can be interrogated and the satellites are usually designed to store at least two orbit's data, sufficient bandwidth to transmit two orbit's data within a single orbital period is desirable to avoid a temporary backlog of perishable weather data.

To provide this capability, Nimbus has full-time use of a 96 kcs (Telpak B) line from Fairbanks to Washington.

A complex man-machine interfacing facility is also required at the data processing central. The facility used for ESSA's National Operational Meteorological Satellite System is outlined in block diagram form in Figure 101.

To the left, the data enters the terminal equipment from the Telpak B lines. Control of the data flow and all the processing units is exercised by the semi-automatic control terminal and the system operator, shown at the bottom left. The data are immediately recorded on a magnetic tape, both to preserve them in case of a malfunction and to allow playbacks at varying speeds where the processing equipments require it. The pictures are gridded in the Data Merging Equipment with the gridding computations performed in a CDC 6600 computer, which is the heart of the NOMSS Data Processing System.

The tape on which the AVCS pictures are recorded is played-back at one-eighth the recording speed. The picture signals and the grid data (prepared by the computer from satellite orbital and attitude data) are sent to a grid-mixing unit. The pictures are gridded while they are still electrical signals.

The computer calculates where each point on the grid lines will fall in the TV scan, and sorts the points in that order. When the grid mixer sends the picture signals to a kinescope-recorder, it counts until a grid point is reached. It then suppresses the picture and inserts a grid-line dot. The mixer then continues the

NOMSS DATA PROCESSING SYSTEM

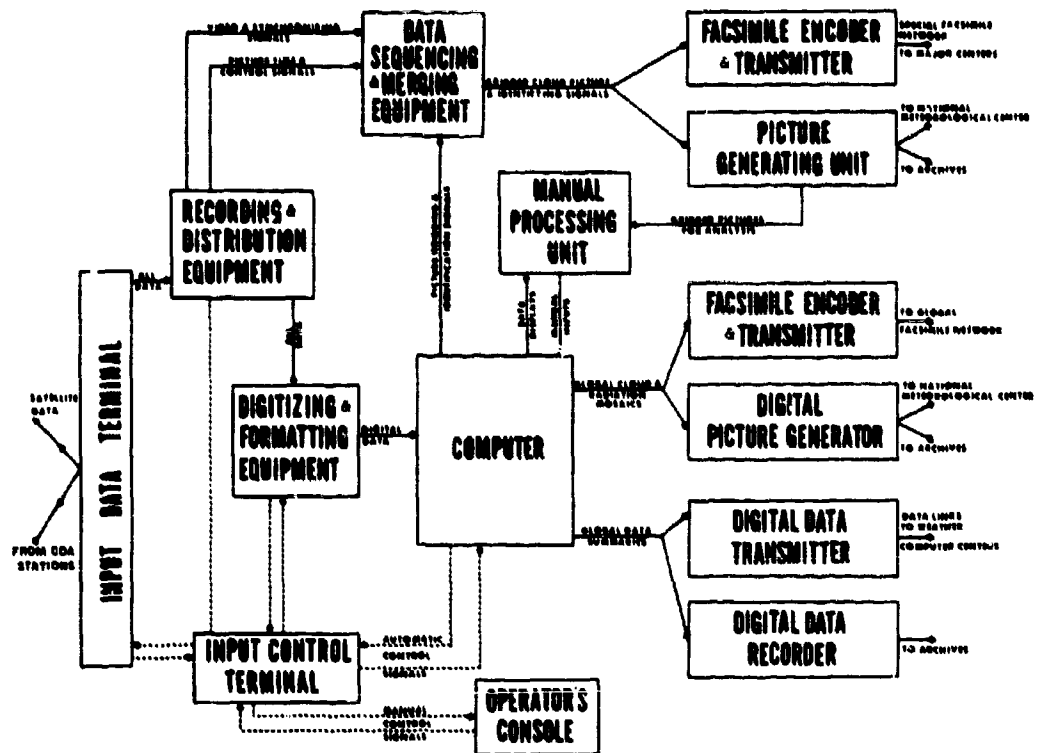


Figure 101. Block Diagram of NOMSS Data Processing System

the picture signals and counts to the next grid line point. The entire picture is played-out, combined with the proper grid to show the location of the clouds. This process requires only about thirty minutes for 96 pictures.

The gridded pictures are photographed on a kinescope, and are immediately developed to provide high quality films for operational analysis at the National Meteorological Center and for research. In parallel with this kinescope recording, pictures of selected areas are processed for transmission, by a special facsimile circuit, to major weather centrals in the United States. Similar processing, presentation, and distribution can also be used for the HRIR data.

The pictures and radiation signals are also converted into digital formats by the CDC 6600. This is done in the Digitizing and Formatting Equipment, which also loads the digitized data into the CDC 6600 Computer.

The computer is aided by analysts, who indicate areas which are snow and might be mistaken as clouds, and who perform other interpretation functions. Later, the computer may take over additional interpretation functions, but it will be a long time before the human analyst is obsolete. For this reason, the NOMSS processing system is a coordinated man-machine complex.

One function the computer can perform well is rectification (making the digitized data fit standard map projections). It can also summarize the digitized data; providing average values for small areas of cloud cover, cloud brightness, and cloud top height. With such compaction, the data fit facsimile limitations. At first, the human analysts will identify cloud types, cloud line orientations, etc.; later, the computer may handle these as the state-of-the-art improves. These compacted data, with manual annotations, may later serve as improved nephanalyses for transmission over the world. Other copies of these data go to the NMC for use in analysis and forecasting, and into the archives for research and climatology.

The digital output of the computer can be sent directly to other computers, both at the NMC and at other computer-equipped weather centrals. There, the data may be used for machine-made weather forecasts as rapidly as applicable techniques can be developed. Stored on tape or film, they can later be used by still other computers for research and climatology.

In summary, the outputs of the NOMSS Data Processing Center include:

1. Geographically Located and Gridded Cloud Pictures to:
 - a. National Meteorological Center
 - b. Major Weather Centrals, for selected areas
 - c. Weather Data Archives for R & D

2. Nephanalyses (eventually) Rectified, Digitized, and Annotated Pictures to:
 - a. Weather Stations, worldwide
 - b. National Meteorological Center
 - c. Archives
3. Rectified and Digitized Pictures to:
 - a. National Meteorological Center
 - b. Archives
4. Picture Data in Digital Form to:
 - a. NMC Computers
 - b. Computers at other weather centrals
 - c. Archives for research and climatology

The reduction, processing, and analysis of the data is a complex operation. Because of the perishability of weather data, each orbit's data must be processed before the next one comes in. A backlog cannot be tolerated.

A major restriction to the dissemination of the satellite data is the fact that transmission of the data in their full fidelity requires the full time use of several tens of kilocycles per second of communications bandwidth, while nearly all operational weather communications are no more than 3 kcs, and other geophysical communications are usually no greater. This requires that the data be analyzed and interpreted at or near the processing center, and converted into either analyzed schematics suitable for facsimile transmission or alphanumeric teletype messages. The consequent loss in detail, resolution, and information is illustrated in Figure 56a and 56b (Section VI).

SECTION XV

BRIEF ANALYSIS OF TRAINING REQUIREMENTS
FOR NAVY PERSONNEL

15.1 Introduction

To be effective, training devices must be designed in the context of personnel training requirements for the performance of specific tasks. In a total system for the processing and application of satellite acquired data (from the point of ground reacquisition of the data through processing, interpretation, display and utilization), many tasks of various types and at various levels of difficulty must be performed by the personnel involved. Some of these tasks are of a simple manipulative nature, requiring little more training than repetitive practice, while others demand high levels of interpretive skill specific to a given type of data. Still others require a broad training of the analyst, as for example in duties requiring proper conjoint use and interpretation of many types of data, both satellite acquired and "conventional," and their applications to a variety of Navy missions. Even these highly generalized discussions make it obvious that training simulators and aids cannot be designed without specification of the tasks for which training requirements exist, or will exist.

The definitions of tasks can be fully accomplished only after the total system has been defined. In the context of satellite sensing and naval operations the total system consists of many different equipments and functions, including the orbiting satellite or satellites, the satellite sensory systems (and therefore the types of data available), the data retrieval and data processing methods (and, therefore, the data display modes that will be used), the products arriving at a ship or shore station, and the processing, display and use of the data at the station itself. The operational requirements to which the data must be applied should also be included in this definition of the total system. The problems of properly formulating the system and analyzing it in terms of task performance requirements are complex at best, even for a system in which the components are well defined. The problems, as faced in this study, are further complicated by the fact that (1) many of the sensory systems are in various stages from conceptual design through actual development, and (2) the actual vehicles on which these advance sensors are to be flown, as well as the data telemetry and processing modes, are not defined. Furthermore, the roles of the Navy in either present or possible future geophysical satellite systems are not yet well established.

A satellite data flow chart depicting the current scheme of meteorological satellite operations has been constructed. A simplified form of this flow chart is shown in Figure 101a. All of the satellite acquired data (except the APT, Automatic Picture Transmission, pictures) are stored on tape on board the satellite, and are read-out when the satellite is within acquisition range (a radius of some 1500 miles) of either of two Command and Data Acquisition (CDA) stations, on command from these stations. From the CDA stations, the data, in their "raw" form are transmitted over wide-bandwidth communication to the National Environmental Satellite Center (NESC) where they are processed. Of the different types of data so far available from satellites, the only kind which is processed in "real time" and is available for operational use is the television pictures. Infrared radiation data are not currently being acquired by any operational satellite; in fact, the only IR data that will be available in the near future will be that from the Nimbus series.

The satellite pictures are in general available only to meteorological units at and in the immediate vicinity of the NESC processing center, due to the limited bandwidths of most weather communications. Montages of the pictures are prepared and made available to NMC and the Navy's Project FAMOS (also located at Suitland). FAMOS uses them to prepare and transmit, to the Fleet Numerical Weather Facility, Monterey, modifications to the conventional analyses which are suggested by interpretations of the pictures (see below).

At the processing center, nephanalyses are also prepared based on analyses and interpretations of the television pictures and other conventional data. These nephanalyses are transmitted to users by means of landline and radio facsimile. The broadcasts may be picked up by fleet units operating in the Atlantic, and constitute one of the forms of satellite data currently available to part of the Navy. A few shore-based Navy stations in the continental U.S. may also have access to the landline-transmitted facsimile nephanalyses.

At Monterey, global conventional meteorological data, as well as conventional oceanographic data, are used in high speed computers to prepare conventional meteorological and oceanographic analyses and prognoses, tailored to meet Navy requirements. In the current experimental scheme satellite acquired data are used only to modify the analyses or input data used by the high speed computers to prepare these products. The modifications are deduced at FAMOS, and are sent to Monterey as suggested numerical adjustments to grid point, computer input data. Consequently, the satellite data themselves are not part of, nor are they incorporated directly into,

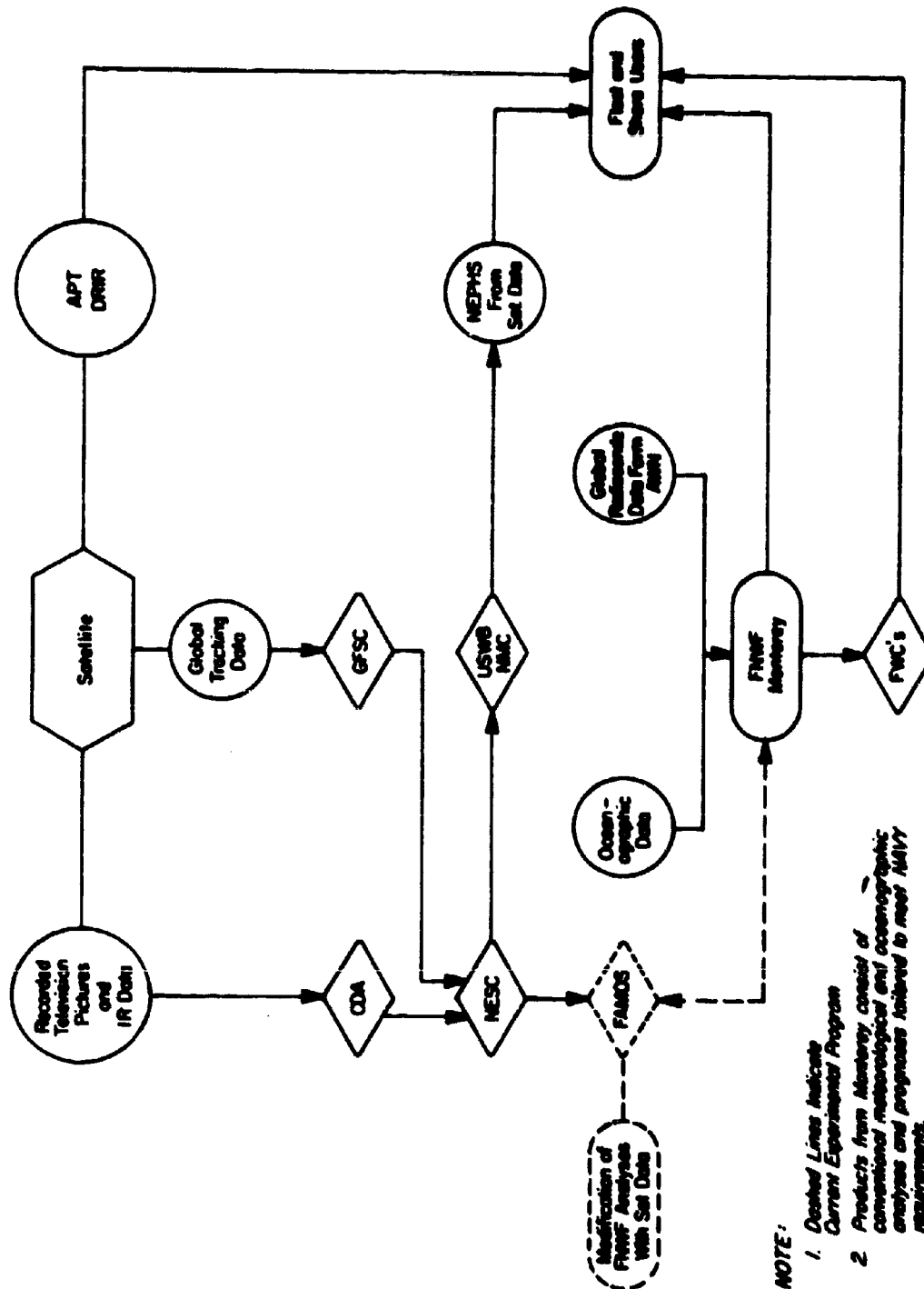


Figure 101a. Simplified Satellite Data Flow Chart

the products available from Monterey and transmitted to the various Naval installations throughout the world. Nevertheless, the modifications derived from the satellite data have been found to provide significant and consistent improvements in the FNWF prognoses.

However, these installations, as well as major units of the fleet, may acquire satellite data directly by means of the APT (Automatic Picture Transmission) system.

15.2 Delineation of the Areas Requiring Training

Based on this simplified analysis of the current scheme of satellite data flow to the Navy, it is seen that there are at least four areas in which Navy personnel training requirements exist for the proper handling and application of the satellite data. These are as follows:

1. Interpretation and use of the nephanalyses, presently received on the facsimile transmissions from Suitland by some Navy units.
2. For a limited number of Navy personnel, interpretation of the satellite pictures and montages, and their use in modifying the input grid-point used by FNWF.
3. Operation, interpretation and utilization of the APT mode of direct satellite data read out.
4. Background training in general satellite geophysics, to provide a source of Navy personnel capable of dealing with future satellite systems whose characteristics are presently rather uncertain.

15.2.1 Nephs

Nephanalyses, prepared from the satellite television camera pictures, are transmitted by means of landline and radio facsimiles from Suitland. Fleet units operating in the Atlantic (and possibly some continental U.S. shore units) which have suitable receiving equipment can receive these nephs. Even though Navy personnel are not directly involved in the ground acquisition, reduction, and analysis of the satellite data required to prepare nephs, it is obvious that they should be familiar with the format of the original data, their limitations and degradation effects, the processes whereby the nephs are produced from the original television pictures and the additional data degradations (or, for that matter, enhancement effects)

introduced by the processing. Familiarity with these processes and effects is essential to the proper and prudent interpretation and use of the nephs in operations. Accordingly, training requirements in this instance appear to go beyond simple training in interpretation of the final facsimile data. It should also include a familiarity with the data reduction processes involved in the generation of the nephanalyses. This can best be achieved if the trainees are given at least limited training and practice in the actual preparation of nephanalyses from the satellite picture themselves.

The training in the interpretative skills required for both the preparation and the use of nephanalyses are susceptible to simulation. Enough samples of real data exist so that the data themselves need not be simulated. However, the operational requirements for the data, as well as the operational environments in which the data must be interpreted and used, should also be simulated for training purposes.

15.2.2 Modifications to FNWF Input Data (Project FAMOS Functions)

The interpretative skills required here include many of those required for an understanding of the processes used in preparing nephanalyses or in the meteorological interpretation of the APT data. The major difference lies in the use of the analyses to modify numerical grid-point data. This requires an understanding of the relationships between the satellite-observed cloud patterns and such atmospheric parameters as pressure-surface heights, temperatures, and vorticity centers. Furthermore, a rather complete comprehension of the uses of the input data at FNWF, and of the consequences of recommended modifications, is required to avoid modifications that degrade, rather than improve, the FNWF prognoses.

Again, sufficient samples of real satellite data are readily available. Some method of feedback, to demonstrate the consequences of various types and degrees of modifications, will be highly desirable.

15.2.3 APT Mode of Data Acquisition

The other major area in which there exists a current training requirement is in the APT mode of data acquisition. This is one mode of data acquisition in which Navy personnel performs many operational tasks as well as interpretive tasks and in which the "raw" satellite data is available to Navy personnel in real time.

The APT system is essentially a satellite television camera system employing a vidicon tube as the sensor. The unique feature of this system is that the image is transferred to a second surface in the vidicon tube, on which it can be stored for a length of time without degradation. Consequently, the image on the second surface may be scanned electronically at a relatively slow rate, and the transmission of the data can be achieved over a narrow bandwidth. Furthermore, the system is programmed to read out automatically, with a new picture taken and read out at predetermined time intervals. The slow rate of data read out makes it possible to use receiving equipment on a comparatively modest scale of complexity and cost. The system is therefore ideally suited to local station reception. Some units of the fleet as well as some land installations are already equipped to handle the APT mode of data transmission.

A properly equipped station can receive APT pictures under the following conditions:

1. There is an operating APT satellite in orbit (NESC plans to keep at least one such ESSA satellite in operation at essentially all times).
2. The satellite is within line-of-sight to the station (with a radius of some 1500 miles for the 750 n.mi. altitude ESSA satellites).
3. The receiving antenna is pointed properly to track the satellite passage.

Furthermore, before the picture can be properly received and recorded, the satellite transmitted signal must be properly synchronized, and for the picture to be useful at all, geographical referencing must be performed.

In view of these requirements, the following tasks must be performed prior to interpretive analyses of the pictures:

1. Interpretation of the orbital message originated by NESC.
2. Plotting of the expected sub-orbital track and the times of satellite passage on a specially designed tracking board.
3. Determining the antenna azimuth and elevation angles, and pointing of the antenna to track the satellite as it passes near the station.
4. Operation and adjustments of the receiver, as required.
5. Gridding of the pictures, using the orbital data and the appropriate longitude and latitude grids.

All these functions are manually performed and the necessary skills can be demonstrated and practiced using simulation techniques. The design of such a simulator is discussed in Section XVII.

15.2.4 Background Training in the Fundamentals of Satellite Geophysics

Perhaps the most significant type of training is in the areas of fundamentals of satellite geophysics. Personnel well versed in the fundamentals would require a minimum of retraining to cope with the data received from a new satellite or a new satellite sensor.

Such fundamental training should cover the areas of (1) satellite orbital parameters, their meaning and their constraints on remote sensing as well as on the collection of data measured by buoy and balloon sensors; (2) the basic relationships between the radiation measured by a satellite sensor and the radiation processes of the earth and atmosphere; (3) the general techniques of remote observations; and (4) the basic methods of data processing and display and their effects on the measured data.

In the following sections, possible techniques and devices for the training in the areas outlined above are discussed. In particular, the use of an APT receiver simulator in training is emphasized. Such a simulator can provide the necessary training not only in the operation of an APT set but it can be effectively used in providing training in the interpretation of satellite data, the preparation of nephanalyses, and even in the basic aspects of satellite orbital constraints to the acquisition of data. The most important aspect of the training simulator is that it can provide the trainee opportunities to practice his basic skills and knowledge under conditions which simulate those he will face in the field.

SECTION XVI

SIMULATION AND TRAINING TECHNIQUES

16.1 Introduction

Two of the principal areas of concern in this study are (a) investigation of the possibility and techniques of simulating satellite acquired geophysical data for training purposes, and (b) the analysis of techniques for the training of naval personnel in the many aspects of satellite geophysics, possibly with the aid of training devices and simulators. The discussions in the preceding sections provide the necessary information for an investigation of the simulation and training aspects of satellite geophysics. In particular, the discussions of the various techniques by which satellite observations are made, and the geophysical and instrumental factors which effect such observations, provide the necessary information for the investigation of data simulation techniques. The discussions, and examples, of satellite data interpretation and processing, are useful for the analysis of training techniques. In the following paragraphs, the results of these investigations are presented.

16.2 Simulation of Satellite Data

16.2.1 Available Space - Acquired Data

The volume of data available for use in simulations for training purposes is large. The TIROS TV and IR data are enormous. A recent estimate of TIROS photography indicates there are some 500,000 good photographs available. The IR data are not as voluminous, but there are several thousands of minutes of measurement presently available on magnetic tape.

In addition to TIROS, Nimbus I and II have provided high resolution photographs, on the order of one-half mile, and high resolution infrared "window" data. (Nimbus I alone, has provided some 25,000 photographs and over 6000 minutes of HRIR data). Nimbus II carried a Medium Resolution Infrared Radiometer (MRIR) in addition to the HRIR and television camera. While the data obtained by this radiometer (6.4 - 6.9 μ , 10-11 μ , 14-16 μ , 5-30 μ and 0.2-4.0 μ) are limited, they are particularly

useful for training purposes because of the format by which they are displayed. The measurements from each of the channels are simultaneously displayed in a grey scale pictorial format. An example of this was shown in Section VI.

With the advent of ATS-B, data from synchronous altitude became available for the first time.

These data obtained by geophysical satellites can be augmented by the numerous color photographs made by astronauts of the Mercury and Gemini Manned Spaceflights. These color photographs are especially useful in providing guidelines in the simulation of higher resolution and multispectral observations which might become available from unmanned satellites in the future.

With the inclusion of observations from rockets, the whole altitude range of earth-directed observations from space, extending from ~90 km to synchronous altitude is covered by the currently available space-acquired data.

Table 15 provides a summary of all known unclassified space observations, both manned and unmanned, as of 1965, which would be of value in data simulations. The data, especially those obtained by the geophysical or meteorological satellites, probably include nearly every situation of attenuation, transmission, orbital constraint, and interpretation difficulty. It should be possible to use them to achieve good data simulation.

For the purposes of training personnel in the interpretation of these data, it would be necessary to select, from this voluminous data file, cases appropriate for training purposes. This selection of cases can be facilitated by reference to research studies performed using satellite data. More will be said of this topic in Section 16.3.

16.2.2 Computer Simulation of Satellite Data

In terms of the possible observation techniques discussed in previous sections, and summarized in Table 12, the current file of satellite acquired data and imageries is limited. While they are useful for data simulation in terms of current sensor systems, and those expected to be flown in the immediate future, these data cannot be applied directly to the simulation of data by more advanced sensor systems, or by sensor systems which operate at different wavelengths or employ basically different techniques. They are useful, however, in serving as a guide to development of synthetic simulation.

Table 15
Summary of Geophysical Observations from Space

Vehicle/Spacecraft	Launch Date	Instrument Packages	Altitude (ac. mi.)	Area Coverage	Operational Lifetime (Days)
V-2	1946	35 mm Motion Picture Camera	86	SW U.S.A.	-
V-2	1947	K-25 Aircraft Camera	115	SW U.S.A.	-
Aerobee and V-2	1946-1950	K-25 Aircraft Camera 35 mm Motion Picture Camera 16 mm Cinecolor Camera	69-92	SW U.S.A.	-
Viking 11 and 12	1954-1955	K-25 Aircraft Camera	Up to 182	SW U.S.A.	-
Atlas	1959	16mm Time Lapse Camera	Up to 265	Atlantic Ocean SE	-
Aerobee	1960	Maurer 220.70 mm Aerial Camera	54-161	North Central Canada, Hudson Bay	-
TIROS I	April 1960	2 TV Camera Systems	432-467	55°N - 55°S	88
TIROS II	November 1960	2 TV Camera Systems 5-Channel Scanning Radiometer	306-454	55°N - 55°S	70
Mercury MR-1	December 1960	Maurer 220G, 70 mm Camera	Maximum over 150	Florida, Bahama Islands	-
Mercury MA-3	April 1961	Maurer 220G, 70 mm Camera	Low Altitude Abortive Flight	Dubrovnik	-
Mercury MR-3	May 1961	Maurer 220G, 70 mm Camera	116	Florida, Bahama Islands Mostly Cloud Covered	-
TIROS III	July 1961	2 TV Camera Systems 5 Channel Scanning Radiometer	461-597	55°N - 55°S	111
Mercury MA-4	September 1961	Maurer 220G, 70 mm Camera	99-142	First Orbit Flight Path, Atlantic Ocean, North and Central Africa	1 Orbital Passes
Mercury MA-5	November 1961	Maurer 220G, 70 mm Camera	99-142	SE U.S.A. West Coast of Mexico, North Africa	2 Orbital Passes
TIROS IV	February 1962	2 TV Camera Systems	442-525	55°N - 55°S	125
Mercury MA-6	February 1962	Anasco Autoset 35 mm Camera	100-162	Florida, North Africa	3 Orbital Passes
Mercury MA-7	May 1962	Robot Recorder 35 mm Camera	100-167	West Africa, Atlantic Ocean and Other Areas	3 Orbital Passes

Table 15 cont'd.

Vehicle/Spacecraft	Launch Date	Instrument Package	Altitude (ft. mi.)	Area Coverage	Operational Lifetime (Days)
TIROS V	June 1962	2 TV Camera Systems	367-603	65°N - 65°S	321
TIROS VI	September 1962	2 TV Camera Systems	426-442	65°N - 65°S	399
Mercury MA-8	October 1962	Hasselblad 500 C, Modified 70 mm Camera	100-176	Western U.S.A., Mexican Gulf Coast, South Atlantic Ocean	6 Orbital Passes
Mercury MA-9	May 1963	Hasselblad 500 C Modified 70 mm Camera Modified Robot Camera	100-166	South-Central Asia, Philippine Islands, Pacific Ocean, Middle- East and North Africa	22 Orbital Passes 34 hours
TIROS VII	June 1963	2 TV Camera Systems 5-Channel, Scanning Radiometer	386-403	65°N - 65°S	Still Operative
TIROS VIII	December 1963	2 TV Camera Systems	435-569	65°N - 65°S	Still Operative
Nimbus I	August 1964	2 TV Camera Systems 1 High Resolution Infrared Scanning Radiometer	263-580	Pole to Pole	26
TIROS IX	January 1965	2 TV Camera Systems	436-563	Pole to Pole	Still Operative
Gemini 3	March 1965	Hasselblad 500 C Modified 70 mm Camera	98-140	Atlantic Ocean, Mexico, Africa and Others	5 hours
Gemini 4	June 1965	Hasselblad 500 C Modified 70 mm Camera Two-Color Photographs of the Earth's Limb Synoptic Photographs of cloud tops and Weather Systems Synoptic Terrain Photography with Particular Reference to Geological Features.	100-180	Areas Along Orbital Paths	4
TIROS X	July 1965	2 TV Camera Systems	459-521	Pole to Pole	Still Operative
Gemini 5	August 1965	Celestial and Space Object Radiometry Basic Object Photography Surface Photography Zodiacal Light Photography Synoptic Terrain Photography Synoptic Weather Photography Cloud-Top Spectrometer Study Hasselblad 500 C Modified 70 mm Camera	100-215	All Areas Along Orbital Paths	8

For instance, as a result of the analyses of current and past satellite acquired data, much has been learned of the effects of orbital and communications constraints on satellite data acquisition in general. This knowledge can be usefully applied to the synthesis of data to be expected from satellite sensors in the future.

In this regard, the usefulness of observations and measurements made from aircraft or balloon altitudes should not be overlooked. A number of the sensors which are ultimately flown on spacecraft are tested, in prototype, in aircraft or balloon flights. The development of a microwave radiometer for spacecraft applications, is an example. A number of microwave radiometers, of various designs and configurations, have made geophysical observations from aircraft altitudes. This is also the case with radar. The results of these studies can provide the basis for the preparation of synthetic satellite acquired data by extrapolation to satellite altitudes.

The manned spaceflight program has given impetus to a number of studies for the simulation of the geophysical system as viewed from space. However, the schemes proposed or being used are generally not applicable for the purposes of training personnel in the interpretation of geophysical data acquired from satellite altitudes, since they generally involve the simulation of the visual view of the earth as the manned spacecraft orbits about the earth.

For the purposes of this study, it is felt that the best method by which satellite data can be simulated, for those sensor systems for which no actual data exist, is computer simulation. This technique has been successfully used and is in fact being used in the generation of synthetic data. Glaser and Milford⁸⁶ for instance, synthesized limited samples of IR absorption band data prior to the launch of TIROS. On the basis of the synthetic data, they were able to deduce a number of useful conclusions on the possible interpretations of IR data.

Synthetic simulations of data are based on the best estimates of the nature of the original information field in the geosphere, the effects of interfering factors, and the spectral response of the sensor. These data then form the inputs to the equation of radiation transfer, appropriate for the spectral region in question. A number of these equations have been derived in this study. Equation (132) in Section X, for instance, is a form of the equation of transfer appropriate for the simulation of IR data. It is seen from this equation that the required inputs are, among others,

- (a) The emissivity of the surface viewed by the sensor.
- (b) The temperature of the surface viewed by the sensor.
- (c) The absorption and emission of the gases in the various layers in the atmosphere.

All of these parameters must be specified for the wavelength or wavelength interval in which the sensor is expected to operate. In the case of the simulation of IR data, they may be obtained by first specifying the nature of the surfaces or targets to be simulated, the surface temperature field, the three dimensional temperature field of the atmosphere over the region in which simulation of the data is desirable, and the vertical distribution of attenuating gases over this region. Using available data or the emissivities of various types of surface materials, and the absorption and emission characteristics of atmospheric gases in the various spectral regions of the IR, the input data necessary to solve Equation (132) can be obtained at various grid points. The density of the grid points would depend on, among other things, the expected spatial resolution of the sensor.

The equation of transfer is then solved at each of the grid points and plotted and analyzed. Since digital values are available at each of the grid points, the method of displaying the simulated data can be made to simulate the anticipated method of displaying the actual data when they become available.

The solutions to the equations of transfer can best be achieved by computer techniques. When a large field of values are to be simulated, hand computations become tedious, if not altogether unmanageable. Computer programs for the solutions of these equations can be written. A number of such programs exist, especially for the solutions of Equation (132). In these programs, the absorption and emission characteristics of atmospheric gases are expressed analytically, thus avoiding the tedious process of extrapolating these factors from tabulations.

It should be noted, however, that computer simulation of data are often not precise. This is especially true in those instances in which the factors affecting the data are not completely understood or known. However, for the purposes of training in the interpretation of gross scale features in the data, computer simulation should be sufficient.

Figures 102a and 102b⁹⁵ show an example of the effectiveness of this technique in the simulation of satellite data. Figure 102a shows a map of simulated IR "window" effective temperatures over the U.S., on 6 March 1959. The data for this simulated map were taken from conventional radiosonde observations. Figure 102b shows the concurrent surface chart showing the locations of the frontal systems. The high clouds associated with the frontal system are well simulated in Figure 101a, by the cold effective temperatures over the northeastern part of the U.S.

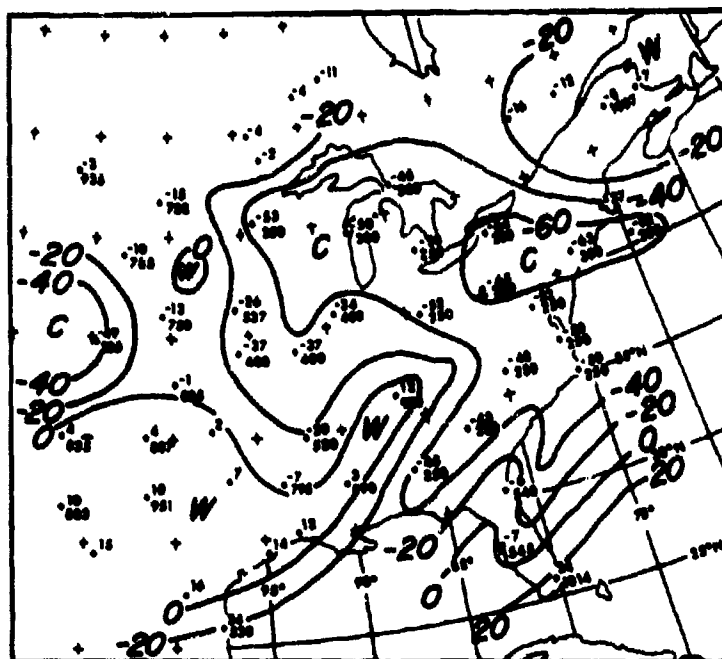


Figure 102a. Map of Simulated IR Window Effective Temperatures over the U.S., 0000 GMT, 6 March 1959

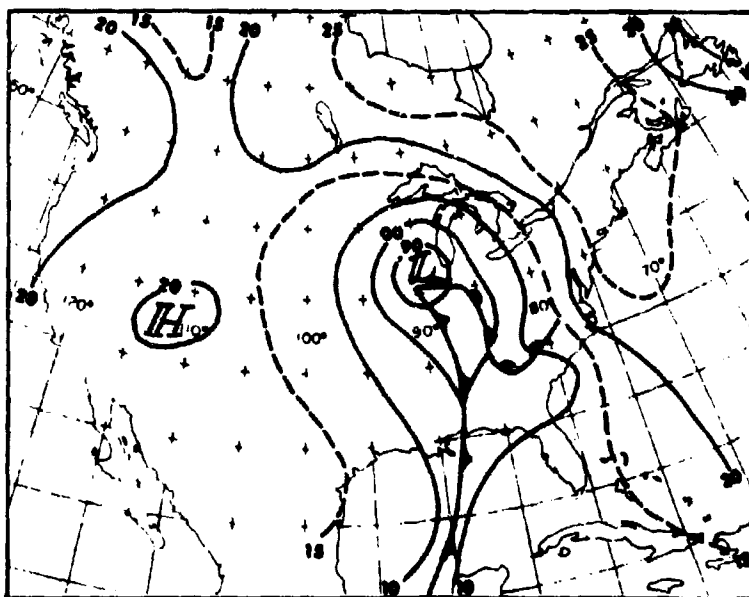


Figure 102b. Surface Map, 0000 GMT, 6 March 1959

16.3 Training Techniques and Devices Pertinent to Interpretation of Satellite Data

16.3.1 Introduction

The conception and design of training aids or devices that can be useful in programs concerned with the interpretation and application of satellite data are not straight-forward. The reasons for this include:

- a. The interpretations that can and must be made, and the procedures by which they are made, are seldom objective or quantitative in any major sense. Rather, at least at the present state of the art, they are highly subjective.
- b. The interpretations are based on the non-linear interactions of a wide variety of features, patterns, keys and clues. As yet, no systematized procedure (or check lists) to be followed when making the required interpretations have been developed. In this, the problems to be faced and the skills to be taught have much in common with conventional synoptic meteorology. Furthermore, the training should emphasize the joint, integrated use of satellite and conventional data and not the interpretation of satellite data alone.
- c. The interpretation is not a strictly real-time, instantaneous function, in the sense of the functions that must be performed when recognizing and/or tracking a fleeting target. On the other hand, the operational analyst is usually working under stringent limitations of time, manpower, and required outputs, which thereby prohibit the relatively leisurely study possible in a research situation. Nevertheless, the interpretation function is in many ways highly analogous to a research analysis in the sense that small apparently insignificant details may be critical to the proper interpretation of actually different, but superficially similar, situations.

As a consequence of these factors, the dilemma exists that:

1. The material to be assimilated by the trainees is voluminous (at best of the order of 400 pages of illustrated text) and mere assimilation of a written exposition of the state of the art is really only a preliminary to actual interpretive practice, extended practice being the key to operationally significant skill.
2. Demonstrative models (whether dynamic or static) and projector-displayed illustrations or examples appear to be helpful only (a) During the

preliminary stages of professional level training and (b) In training at sub-professional levels (enlisted observers) etc., where the objective is more to instill background rather than ultimate operational skill.

Yet the interpretive skills are probably more crucial, and are certainly required by a far greater number of personnel, than the objective skills discussed in other parts of this report for which training devices and procedures are far easier to design.

For personnel in formal training environments (i.e., Lakhurst, Navy Postgraduate School, etc.), the best solution would seem to be to:

1. Provide and use demonstration models and displays for sub-professional and non-professional level training, and for the appropriate preliminary levels of professional training.

2. Develop and provide practice kits for trainee use. The kits would provide cases, to be analyzed and interpreted, of progressively increasing complexity. The training situation would be made increasingly more realistic in terms of amount and variety of material provided, departure of cases from model situations, pressures of time, requirements to be satisfied, conversion from individual to coordinated group activity, actual or simulated interaction with external sources of information or constraints, etc. In the later stages of the practice sessions, at least some analyses and interpretations of local, concurrent situations should be called for, although the use of historical situations will still be required to provide a necessary degree of geographical and seasonal diversity. The local, concurrent cases require a capability for the local reproduction of sufficient copies of the basic materials, at a rapid rate, from the forms of data normally available to a weather station (i.e., facsimile charts, APT pictures, teletype data, etc.).

16.3.2 Sources of Interpretation Practices and Procedures

The following list provides the major reports and publications which can be used as sources of the interpretation practices and procedures which should be taught. It must be recognized that such a list becomes obsolescent as soon as it is prepared, and that training organizations must be continually on the alert for significant new sources, which can be found in the scientific literature and in R and D technical reports. Most of such technical reports are abstracted by DDC and/or NASA's STAR.

NAVTRADEVCEEN 66-C-0031-1

Perhaps the most comprehensive report on the interpretation of satellite data which presently exists is:

Widger, W.K., Jr., P.E. Sherr, and C.W.C. Rogers, 1964: Practical Interpretation of Meteorological Satellite Data, Final Report, Contract No. AF 19(628)-2471, ARACON Geophysics Company (reprinted as Air Weather Service Technical Report 185).

In somewhat more than a year since the publication of Practical Interpretation, significant progress has been reported in the techniques of interpretation for a number of topics. Publications covering these matters include:

Tropical Cyclones

Timchalk, A., L.F. Hubert, and S. Fritz, 1965: Wind Speeds from TIROS Pictures of Storms in the Tropics, Meteorological Satellite Laboratory Report No. 33, National Weather Satellite Center, U.S. Weather Bureau.

Extratropical Storms and Vortices

Sherr, P.E., and C.W.C. Rogers, 1965: The Identification and Interpretation of Cloud Vortices Using TIROS Infrared Observation, Final Report, Contract No. Cwb-10812, ARACON Geophysics Company. (This report provides a significantly improved hypothesis as to the factors producing cloud vortices, and how they can be interpreted.).

Jet Stream Cloud Bands

Oliver, V.J., R.N. Anderson, and E.W. Ferguson, 1964: "Some Examples of the Detection of Jet Streams from TIROS Photographs," Monthly Weather Review, 92(10), pp. 441-448.

Infrared Data

Widger, W.K., Jr., J.C. Barnes, E.S. Merritt, and R.B. Smith, 1965: Meteorological Interpretation of Nimbus High Resolution Infrared (HRIR) Data, Final Report, Contract No. NAS 5-9554, ARACON Geophysics Company.

Nimbus (Higher Resolution Television Data)

Boucher, R.J., 1965: The Meteorological Content of Nimbus I AVCS Data, Technical Note No. 6, Contract No. NAS 5-3253, ARACON Geophysics Company.

Sea Surface Temperature

Greaves, J.R., R. Wexler, and C.J. Bowley, 1965: The Feasibility of Sea Surface Temperature Determination Using Satellite Infrared Data, Final Report, Contract No. NASW-1157, ARACON Geophysics Company.

Semi-Quantitative Estimates of Mid-Tropospheric Temperatures

Merritt, E.S., and G.W.C. Rogers, 1965: Meteorological Studies of Mid-Latitude Atmospheric Circulations, Final Report, Contract No. N 62306-1584, ARACON Geophysics Company.

Terrain Features

Bird, J.B., A. Morrison, and M.C. Chown, 1964: World Atlas of Photography from TIROS Satellites I to IV, NASA Contractor Report CR-98.

Morrison, A., and M.C. Chown, 1964: Photography of the Western Sahara Desert from the Mercury MA-4 Spacecraft, NASA Contractor Report CR-126.

Nordberg, W., and R.E. Samuelson, 1965: "Terrestrial Features Observed by the High Resolution Infrared Radiometer," Observations from the Nimbus I Meteorological Satellite, NASA SP-89, pp. 36-46.

Popham, R., and R.E. Samuelson, 1965: "Polar Exploration with Nimbus," Observations from the Nimbus I Meteorological Satellite, NASA SP-89, pp. 47-59.

Conover, J.H., 1965: "Note on the Flora and Snow Cover Distributions Affecting the Appearance of Northeastern United States as Photographed by TIROS Satellites," Monthly Weather Review, 93(10), pp. 644-646.

Taggart, C.I., 1965: "Interpretation of Geological Features on a Satellite Photograph," Nature, 207(4996), pp. 513-514.

Cloud Plumes Created by Some Ships in Certain Meteorological Conditions

Anon., 1965: "Picture of the Month," Monthly Weather Review, 93(8), p. 504.

Meteorology Laboratory, AFCRL, 1965: "Curious Cloud Structure," OAR Research Review, 4(10), pp. 29-30.

Applications of Satellite Data to Numerical Weather Prediction

McClain, E. P., M. A. Rusecki, and H. J. Brodrick, 1965: "Experimental Use of Satellite Pictures in Numerical Prediction," Monthly Weather Review, 93(7), pp. 445-452.

Mountain Waves

Fritz, S., 1965: "The Significance of Mountain Lee Waves as Seen from Satellite Pictures," Journal of Applied Meteorology, 4(1), pp. 31-37.

Interpretation by Sub-professional Personnel

Widger, W. K., Jr., P. E. Sherr, and R. J. Boucher, 1966: Guide to the Operational Interpretation and Application of Meteorological Satellite Data for the Army, Volume I, Meteorological Interpretation. Technical Report ECOM-02173-5, Contract No. DA28-043-AMC-01273(E), ARACON Geophysics Company.

In a few topics, there exist somewhat more extensive discussions than those included in AWSTR 185 that may be of assistance to instructors, or provide additional examples for use in preparing training aids. Cases in point include:

Conover, J. H., 1962-63: Cloud Interpretation from Satellite Altitudes, CR Research Note No. 81 (and Supplement 1 hereto), Air Force Cambridge Research Center.

Whitney, L. F., Jr., 1963: "Severe Storm Clouds as Seen from TIROS," Journal of Applied Meteorology, 2(4), pp. 501-507.

Wark, D. Q., and R. W. Popham, 1962: Ice Photography from Meteorological Satellites TIROS I and II, Meteorological Satellite Laboratory Report No. 8, U.S. Weather Bureau.

National Weather Satellite Center, 1965: "Picture Interpretation," APT Users Guide, Environmental Science Services Administration, pp. 34-74.

Hopkins, M. M., Jr., 1965 (revised 1966): "Classification of Data Content," Section 5 of Design Plan for the Nimbus C Data Utilization Center, Technical Report No. 4, Contract No. NAS 5-3253, ARACON Geophysics Company (included in Nimbus II Users' Guide).

Staff Members, Aeronomy and Meteorology Division, 1965: Nimbus I High Resolution Radiation Data Catalog and Users' Manual, Volume I, Photofacsimile Film Strips, NASA, Goddard Space Flight Center.

Aeronomy and Meteorology Division, 1965: Nimbus I Users' Catalog: AVCS and APT, NASA, Goddard Space Flight Center.

16.3.3 Demonstration Devices

The following discussions concern demonstration devices that might be provided for classroom use. In general, it would appear that slides (or film strips), display or briefing charts, and perhaps in a few cases motion pictures will provide adequate means of conveying the desired information. Where typical sequences of the transition or development of meteorological systems require illustration, this can best be portrayed in such forms as: (1) a series of slides or charts, (2) several successive pictures on a single slide or chart, or (3) motion pictures (either schematics or manufactured sequences, since real sequences at adequately frequent frame intervals cannot be expected until a synchronous meteorological satellite is actually in operation).

It should be obvious that the classroom demonstrations must be supplemented by illustrated texts for independent study. In this regard, it must be noted that an integrated text in satellite meteorology does not presently exist. The best that is presently available would be a combination of Widger, et al: Practical Interpretation of Meteorological Satellite Data; and Widger: Meteorological Satellites; supplemented by appropriate copies of or extracts from some of the above listed and other reports. A suitable, integrated text would obviously include discussions of operationally significant orbital and viewing geometry factors, summary functional descriptions of equipment functions, geographical locations of data, etc., in addition to matters directly pertinent to data interpretation.

16.3.3.1 Cloud Types

Most of the significant cloud types identifiable from a satellite are discussed in Chapter 4 of AWSTR 185. The demonstrations should include typical, and later somewhat atypical, examples of each type, with accompanying examples of the same types of clouds as seen from the ground or aircraft. Where pertinent, accompanying synoptic maps should illustrate the conditions in which such clouds are found.

In a number of cases, the same cloud types appear significantly different at different resolutions. (For example, small scattered cumulus can be seen individually at Nimbus AVCS resolutions of a few tenths of a mile, but appear only as a uniform to slightly mottled dimly grey area at TIROS and ESSA resolutions of a few miles.) Such differences as occur over the range of operational resolutions must be demonstrated.

In those few cases where the high resolution infrared data permit cloud type identification examples of HRIR data should be included.

16.3.3.2 Key Features

A general survey of key features observed in the satellite data (as discussed in Chapter 5 of AWSTR 185, and or in the Nimbus C Design Plan) should precede the detailed discussions of each type of feature. The examples should include a variety of cases (first typical, and later more anomalous) of each significant type of feature (including both low and high resolution infrared examples) where appropriate; (see Ref. 34), accompanying surface and upper level synoptic charts, and the appearance in operationally disseminated nephanalyses.

16.3.3.3 Extratropical Vortical

The material to be presented is discussed in Chapter 6 of AWSTR 185, in the report by Sherr and Rogers referenced above, and in Reference 34. Examples should be shown of (1) vortices developing from frontal waves, (2) vortices developing from short wave troughs, and (3) other vortex types, usually associated with upper level systems. Examples both of typical stages of development and of typical and anomalous development sequences must be illustrated. The illustrations should include satellite photographs, high and low resolution infrared depictions, concurrent surface and upper level conventional synoptic analyses, and depictions in operational nephanalyses.

16.3.3.4 Fronts and Other Extratropical Synoptic and
Mesoscale Features

The material to be presented is discussed in Chapters 7 and 8 of AWSTR 185, and in Reference 34, as augmented by more recent findings cited above. Satellite pictures, infrared depictions (where applicable), synoptic analyses, and operational nephanalyses must be illustrated.

16.3.3.5 Tropical Systems

Tropical cloud bands, perturbations, and vortices are discussed in Chapter 11 of AWSTR 185, and as cited previously. Pictures, infrared depictions, synoptic analyses, and operational nephanalyses must be illustrated. Typical and anomalous sequences of the development of tropical perturbations and vortices should be shown.

16.3.3.6 Non-and Quasi-Meteorological Features

These are discussed in Chapter 9 of AWSTR-185, and in other references cited above. A variety of satellite pictures of each type feature, satellite infrared data, surface or aerial photograph, and topographic and/or geological maps must be used.

16.3.3.7 Examples

The following examples of the demonstrations discussed above are taken directly from the existing literature. Other similar examples abound in the literature, in both the documents cited above and in the other references cited in them. It seems obvious that even better demonstrations could easily be prepared if they were initiated with training as their specific objective, and were matched to the training sequence and syllabus to be employed.

Figure 103 shows a TIROS picture of lee wave cumulus and stratocumulus, and several essentially concurrent aircraft views of the same situation. The fields of view of the aircraft photographs are outlined on the TIROS picture.



342N



349N



367N



363N



373N

AIRCRAFT PICTURES 1907 - 1944Z (E-W)

363N 349N
373N 367N 342N



TIROS PICTURE 1857Z

Figure 103. Comparison Between Aircraft and Satellite Views of Clouds

Figure 104 shows a number of different perspectives on a case which included a mature extratropical vortex, a frontal band, and a hurricane: (a) conventional surface analysis; (b) 500 mb analysis; (c) HRIR view; (d) nephanalysis prepared from HRIR data; (e) mosaic of TIROS pictures and (f) operational nephanalysis showing area of extratropical vortex.

Figures 105 through 109 show TIROS pictures, TIROS infrared data, and conventional surface and 500 mb analyses during the development of a major extratropical vortex and of a secondary system that formed on the frontal band associated with the primary vortex: Figure 105, developing stage of primary vortex; Figure 106, mature stage of primary; Figure 107, early dissipating stage of primary; Figure 108, frontal wave (secondary development) to south of primary at time of Figure 106; Figure 109, occluding stage of secondary, at same time as Figure 107.

16.3.4 Case Studies for Laboratory Practice

Each case study kit for use in student training sessions should simulate, to a greater or lesser degree, conditions to be encountered under actual operational conditions. In the early stages of the training, the cases would be designed primarily to illustrate fundamental concepts and procedures, with operational simulation secondary. As student proficiency increases, the cases should be more and more oriented toward operational reality. In all stages of training, the emphasis should be on optimum joint use of all available data, not on just the satellite data.

In general, the cases and kits will differ from those previously used in synoptic meteorological training laboratories only by the addition of the satellite data and perhaps by the provision (in silent area situations in relatively advanced stages of the curriculum) of far less conventional data than would constitute a useful case in the absence of the satellite data.

It is suggested that the use of cases and kits including satellite data begin with the first cases used in the first synoptic laboratory (using relatively simple and straight-forward situations), since the satellite data provide a view of the real atmosphere that is seldom duplicable with only conventional data and analyses. It may, however, be desirable to include some cases without satellite data in later phases of training, since such situations are likely to be encountered in operational practice.

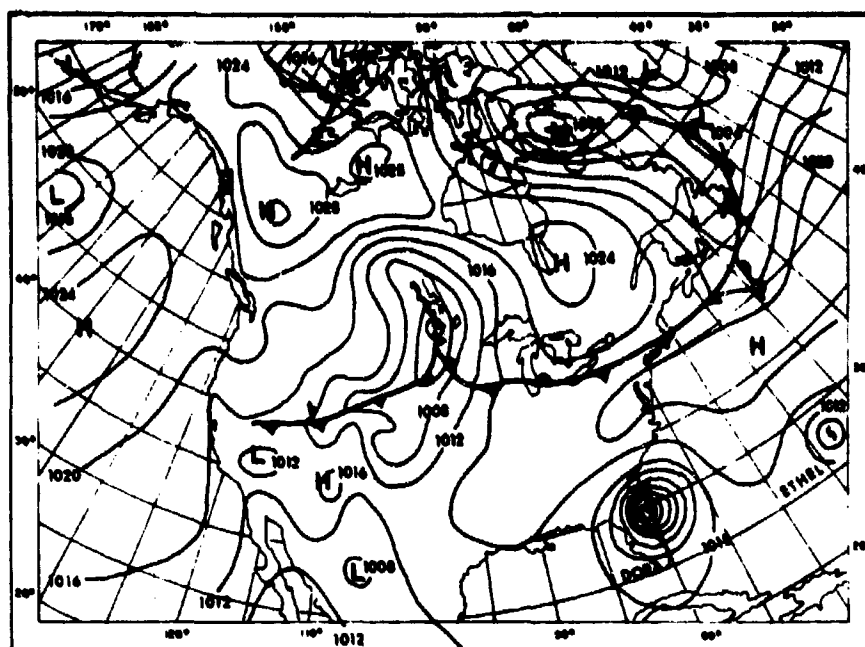


Figure 104a. Conventional Surface Analysis, 0600 GMT, 9 September 1964

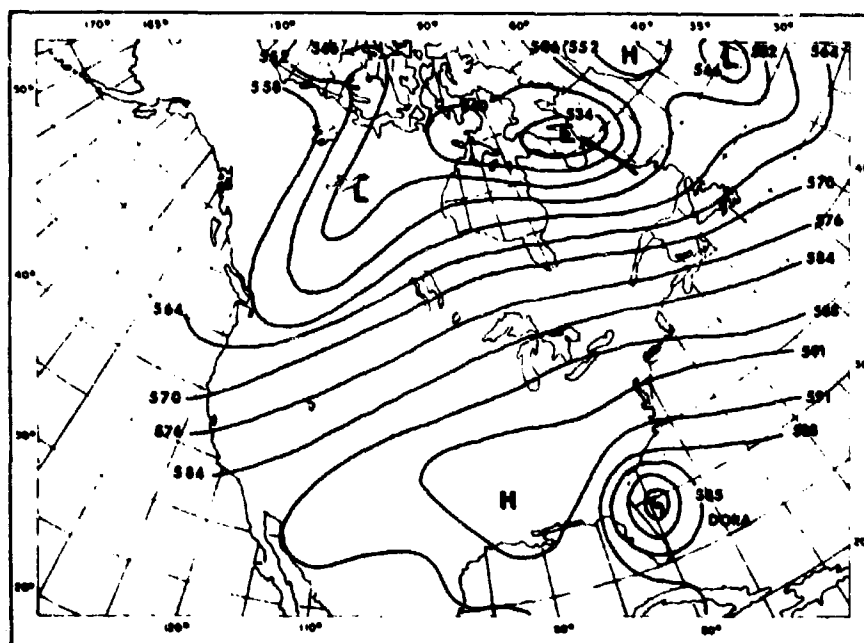


Figure 104b. NMC 500 mb Analysis, 1200 GMT, 9 September 1964

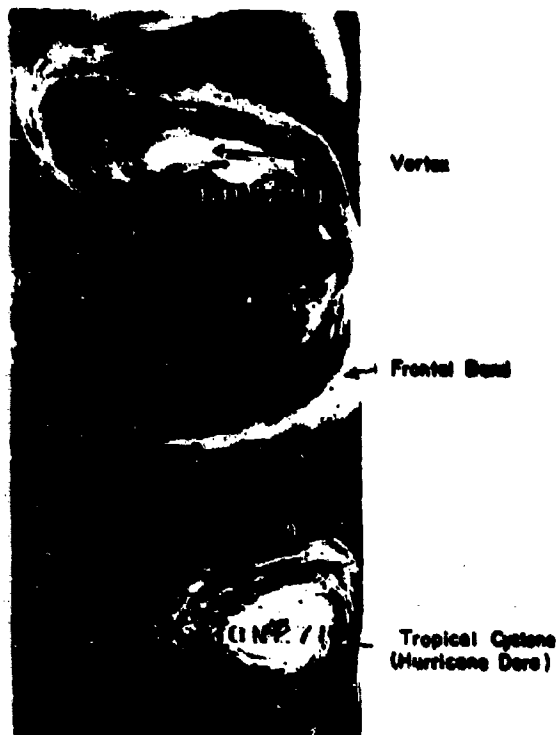


Figure 104c. Nimbus I HRIR Data for Orbit 174, 9 September 1964

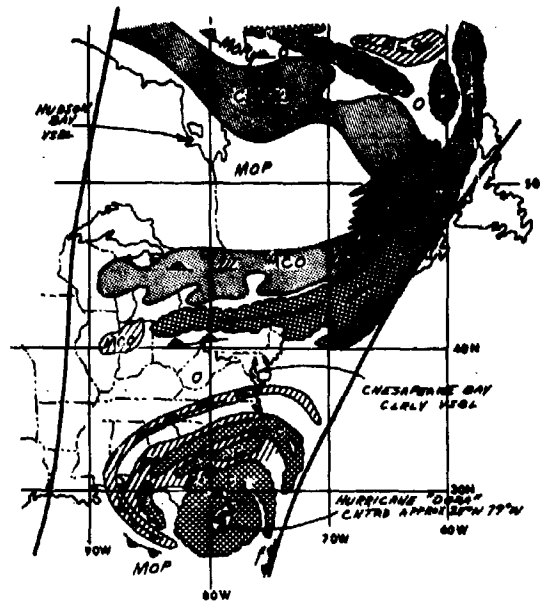


Figure 104d. Nephanalysis Prepared from Orbit 174, Nimbus I HRIR



Figure 104e. TIROS VII Television Picture Mosaic, Orbit 6614/6612
1611 GMT, 8 September 1964

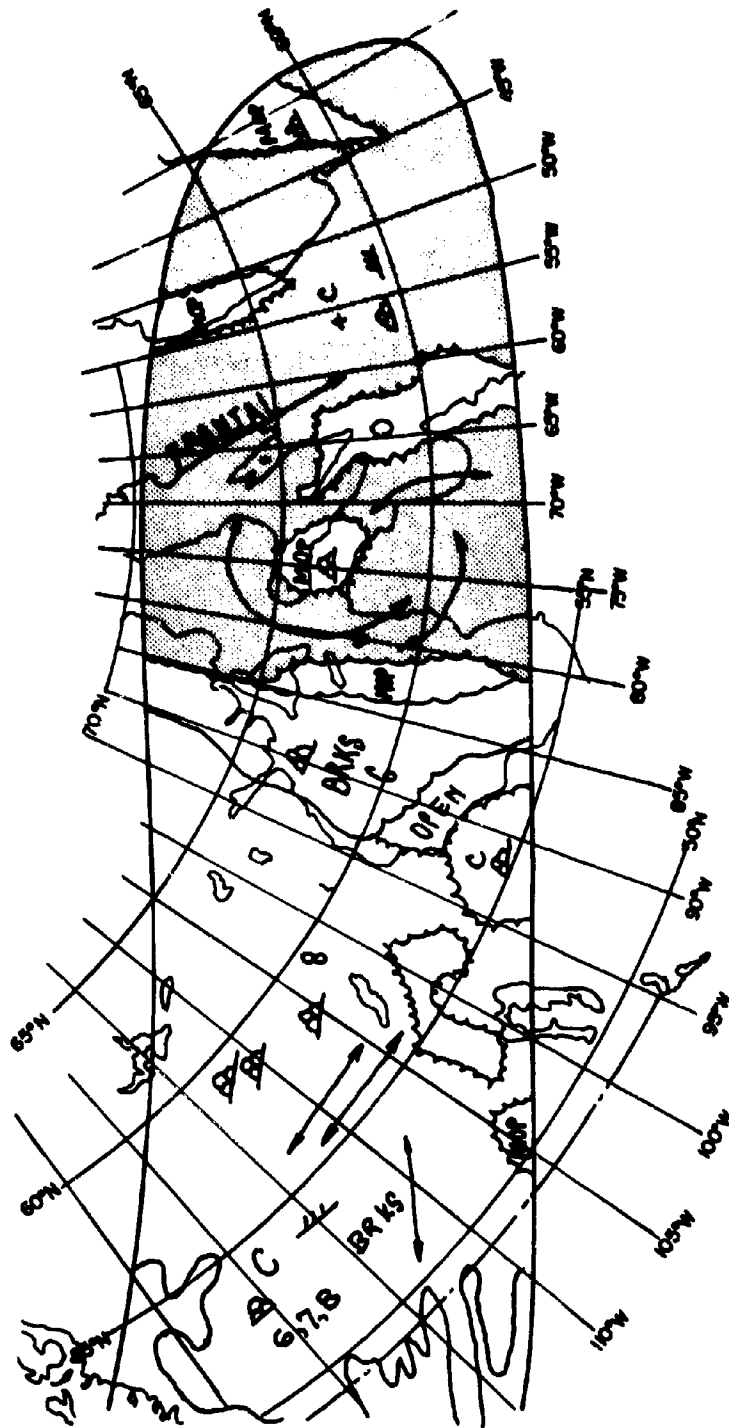
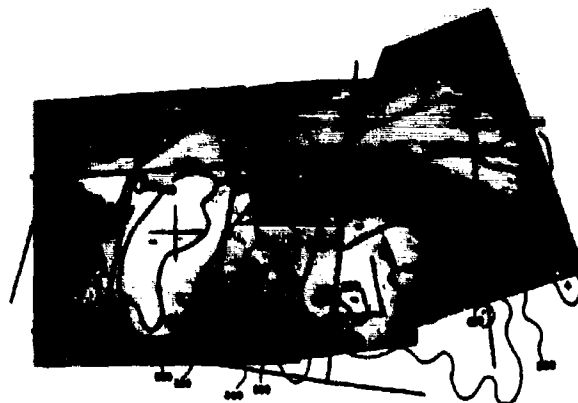


Figure 104f. Nephanalysis Prepared from Mosaic of Figure 104e



Television Picture



"Window" IR Effective Temperature Analysis Superimposed

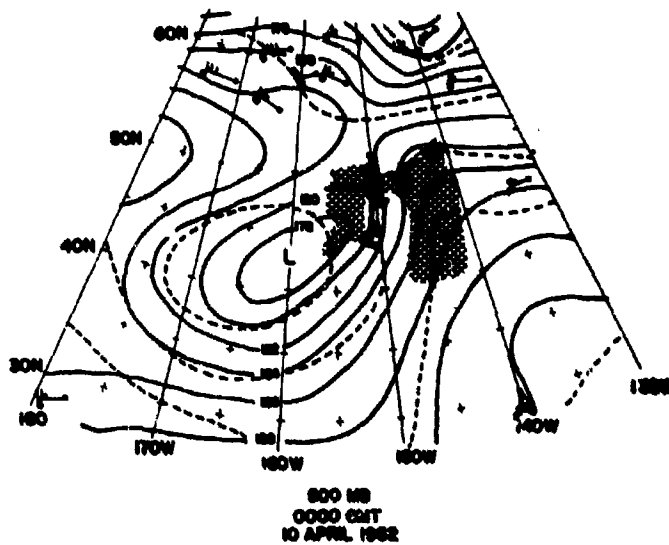
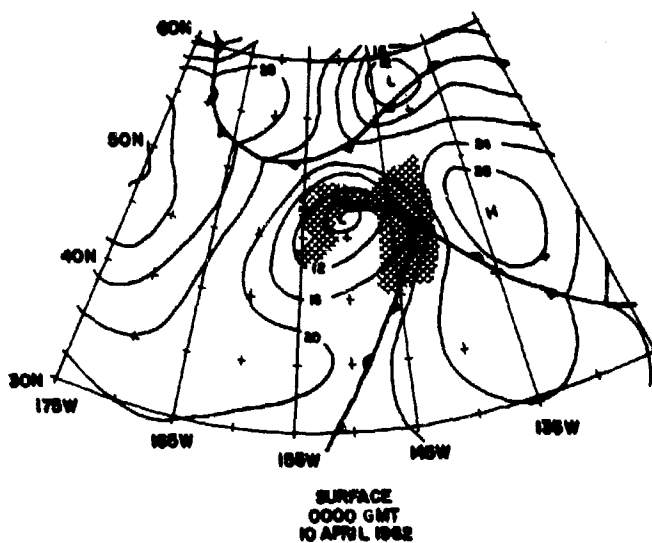
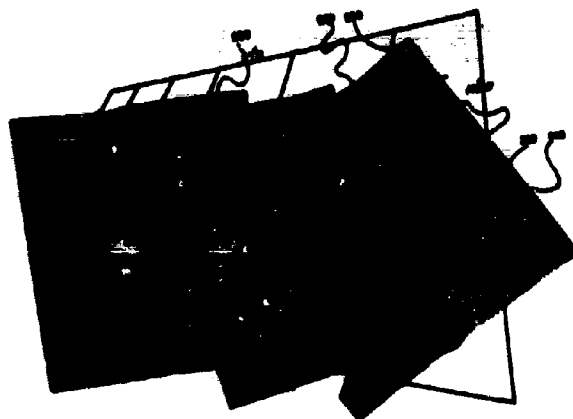


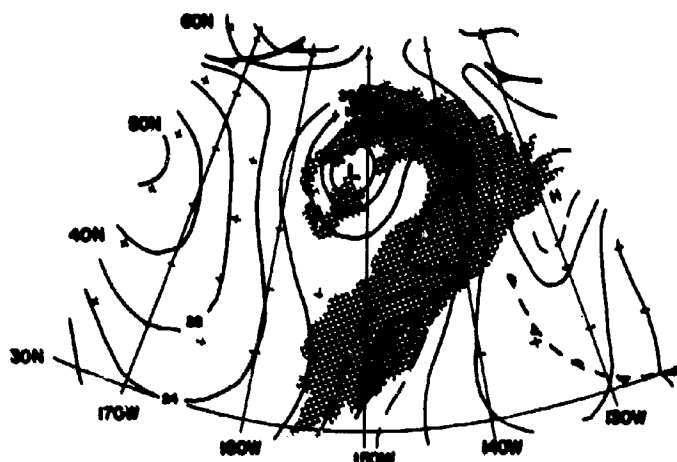
Figure 105. Relation of Observed Channel 2 IR Cloud Pattern, (Orbit 867) to Picture and Conventional Data, 2215 GMT, 9 April 1967



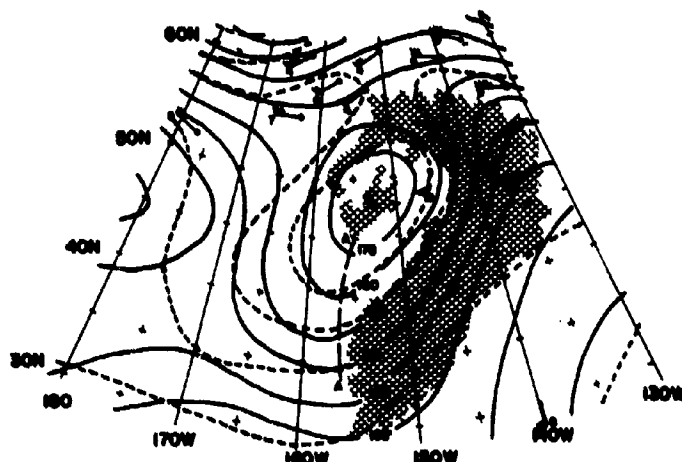
Television Picture



"Window" IR Effective Temperature Analysis Superimposed



SURFACE
0000 GMT
11 APRIL 1962

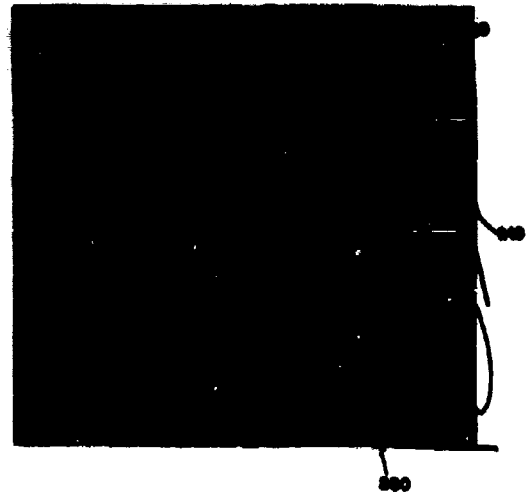


500 MB
0000 GMT
11 APRIL 1962

Figure 106. Relation of Observed Channel 2 IR Pattern (Orbit 881) to Picture and Conventional Data, 2140 GMT, 10 April 1962



Television Picture



"Window" IR Effective Temperature Analysis Superimposed

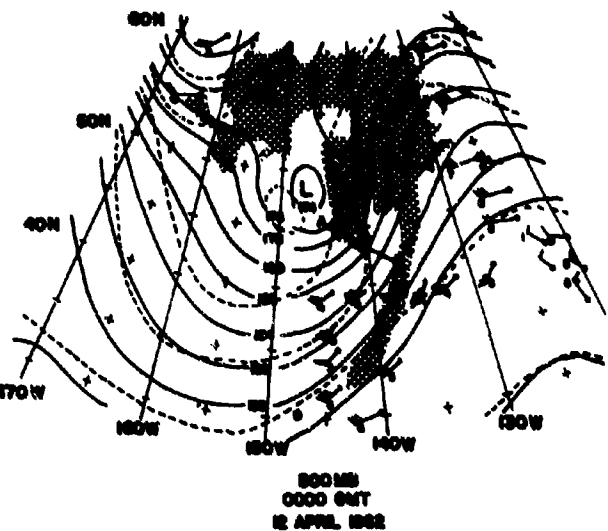
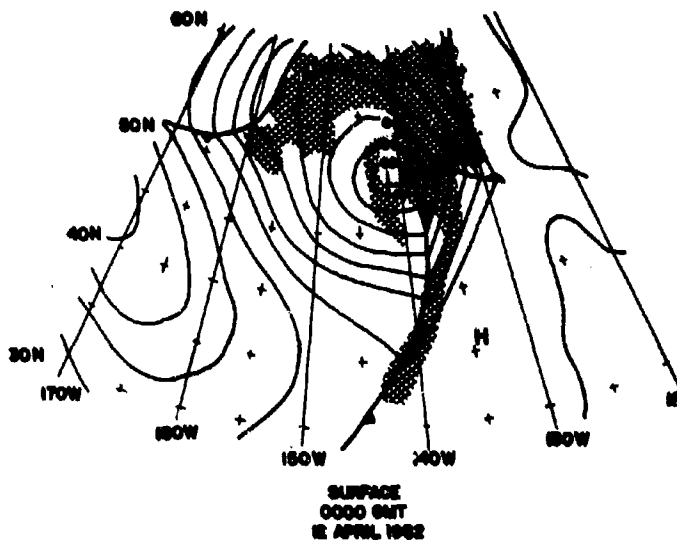
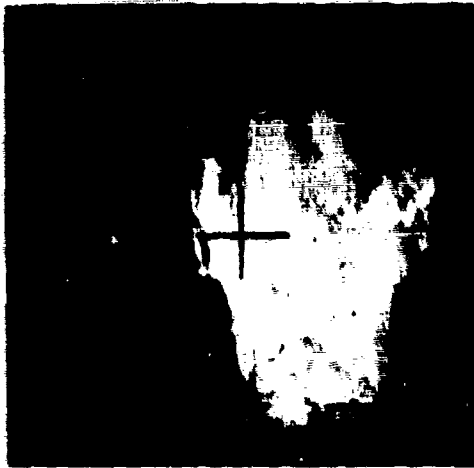
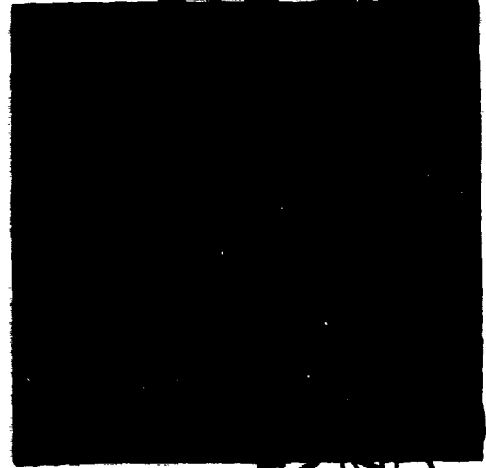


Figure 107. Concurrent Picture and Conventional Data for Orbit 895, 2100 GMT, 11 April 1962



Television Picture



"Window" IR Effective Temperature Analysis Superimposed

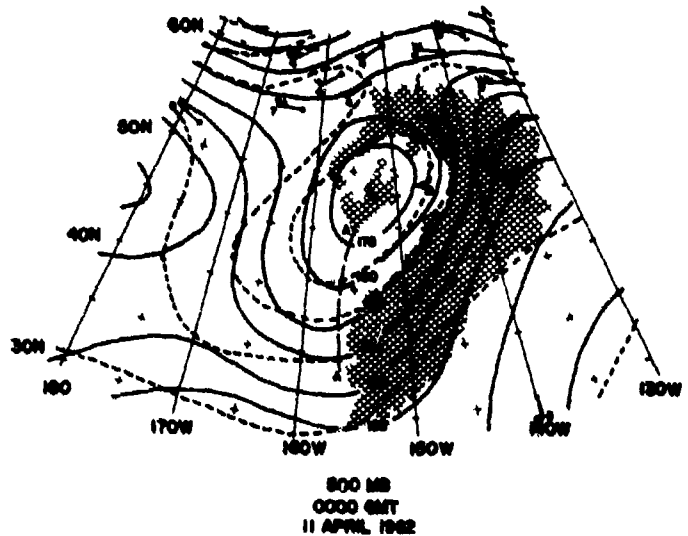
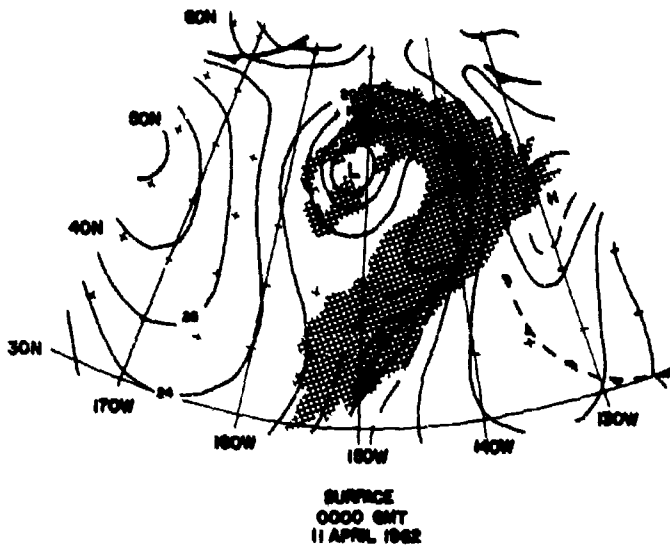


Figure 108. Relation of Observed Channel 2 IR Pattern (Orbit 880) to Picture and Conventional Data, 1955 GMT, 10 April 1962



Television Picture



"Window" IR Effective Temperature Analysis Superimposed

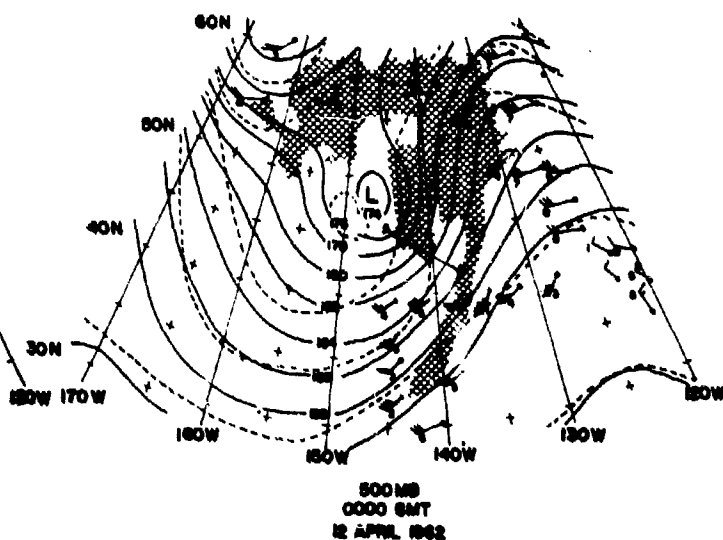
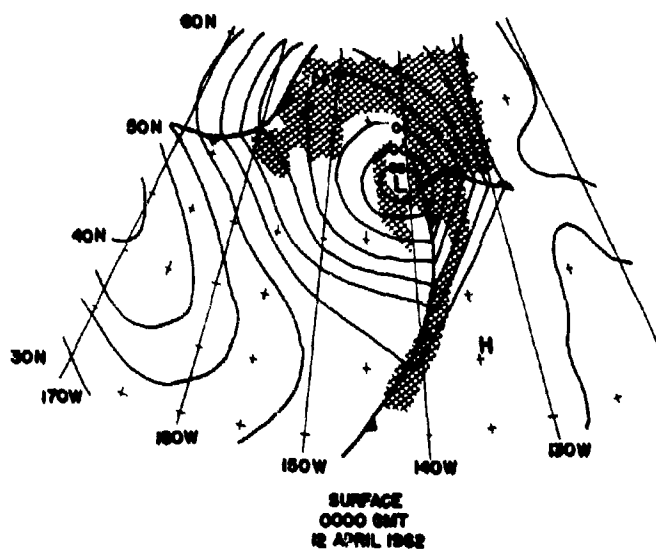


Figure 109. Relation of Observed Channel 2 IR Pattern (Orbit 984) to Picture and Conventional Data, 1915 GMT, 11 April 1962

Each kit would include some or all of the following:

1. Centrally-acquired satellite TV pictures and/or infrared data, gridded, for those cases simulating conditions at major weather centrals. (In the first cases, the geographical grids should be precise; later, practice in cases requiring grid verification and correction should be included.)
2. APT pictures and/or DRIR data,[†] when simulating stations with APT equipment. In the early cases, at least, the data should be gridded. Later, the total operational situation might be more fully simulated by providing orbital data and requiring the students to perform their own geographical location.
3. Conventional weather maps: surface, 500 mb, 200 mb, and/or others as appropriate.
4. Hourly teletype sequences, for U.S. cases.
5. Local observations, especially for cases simulating isolated stations and/or ships at sea.
6. Radiosonde, radar, and/or aircraft reconnaissance data.
7. Fleet Numerical Weather Facility and/or National Meteorological Center numerical prognostic charts.
8. All required base maps, forecast or other forms, etc.

In the early cases, all data provided should be as compatible as possible. Later, discrepancies requiring student resolution or choice between alternatives should be introduced, as well as data with various degrees of degradation likely to be encountered in operational practice.

The first few cases should be meteorologically straight forward, with more complicated cases being progressively introduced. The early cases will presumably require several days for student completion. In the later portions of the curriculum, the cases should be handled at a real time rate.

Each case will require the student to determine present, and/or forecast future, weather conditions of the types of operational interest. Usually a group discussion will follow the student's individual work; and the instructions will require

[†] Selected frames of the global-type TV and/or HRIR data can be used to simulate APT and/or DRIR data, when actual data from appropriate cases are not available.

verification information, which obviously will be withheld from the students until the post-analysis discussions. In some cases, specific parts of the data may be deliberately withheld, and then later discussed by the instructors, as a method illustrating or providing practice in pertinent points.

In later stages of the training, cases sufficiently complex to require coordinated group activity, thereby further simulating an operational situation, would be desirable.

The first cases should be for the continental United States or North America simulating a typical shore base situation, with APT and/or DRIR data, conventional data and analyses, and perhaps centrally prepared prognostic charts provided. Later, cases for various parts of the world (oceanic areas, Eurasia, tropics, etc.) must be included. Situations which might be simulated would include:

1. Data sparse areas: APT and/or nephanalyses and local observations provided little or no conventional data or analyses for area of interest. Cases both with and without APT or nephanalysis data should be simulated.
2. Major weather central:
 - a. Nephanalyses for operational dissemination to be student prepared from satellite data, with and without the aid of conventional data or maps for the area of interest.
 - b. Satellite data to be integrated with conventional data and/or charts and used to prepare, correct, and/or amend analyses and forecasts.

The cases analyzed in Chapter 10 of AWSTR 185, and several of the individual cases described in Reference 34, provide examples of types of situations for which case study training kits could readily be prepared. For example, the Autumn Case in AWSTR 185 (Section 10.4.1) would provide a relatively complex situation over the United States. The Spring Case in AWSTR 185 (Section 10.4.4) could be used to demonstrate how satellite data can be used to aid in improved analyses and forecasts over a mildly data sparse area (the North Atlantic). The Antarctic cases in Reference 34 (sections 6 and 7) provide examples of cases that might be used to provide training in the use of satellite data and truly data sparse areas; and the Eurasian case (Section 5) could provide an example of the integration, over a large land mass, of satellite and conventional data.

16.4 Devices for Simulating Satellite Orbital Geometry

All personnel participating in any area of satellite geophysics should have at least a rudimentary knowledge of the physical meanings of the various parameters used to describe satellite orbits and their constraints on data acquisition. Consequently, it would be desirable if such matters can be shown by means of demonstration devices. In the following two such devices are discussed.

16.4.1 Global Simulator

Figure 110 shows a schematic of a device which would be useful to demonstrate orbital parameters. It consists of (a) a globe which can be rotated by a motor mounted on the base, and (b) an orbital ring fastened to the axis of the globe by means of the retaining ring shown.

The retaining ring is slotted such that the orbital inclination can be adjusted. On the orbital ring is mounted a simulated satellite which is driven by a motor along a track, on the inside diameter of the orbital ring. The simulated satellite is designed to hold a stylus which traces a line on the globe surface as it moves along the orbit ring. The speed of the simulated satellite along the orbital track and the rate of rotation of the globe on its axis should be made controllable.

In addition to these features, it would be highly desirable to design the simulated satellite such that a small divergent light beam can be mounted on it, in place of the writing stylus. The beam should be free to scan over the surface of the globe if desired.

With such a simple device, a large number of orbital parameters can be demonstrated. These would include such matters as

1. Polar limits of coverage imposed by orbital inclination.
2. Change of longitudinal coverage from orbit to orbit.
3. The difference between subpoint tracks and heading lines.
4. Variations of resolution or coverage as a function of sensor nadir angles.
5. Definitions of various orbital terms, and their physical implications.

The number of significant orbital effects which can be demonstrated by a device such as that shown in Figure 110 would depend of course on the degree of sophistication to which the device is designed. For instance, if the distance between the simulated satellite and the surface of the globe can be made variable, the effects of orbit altitude on resolution and coverage can be demonstrated. However, even

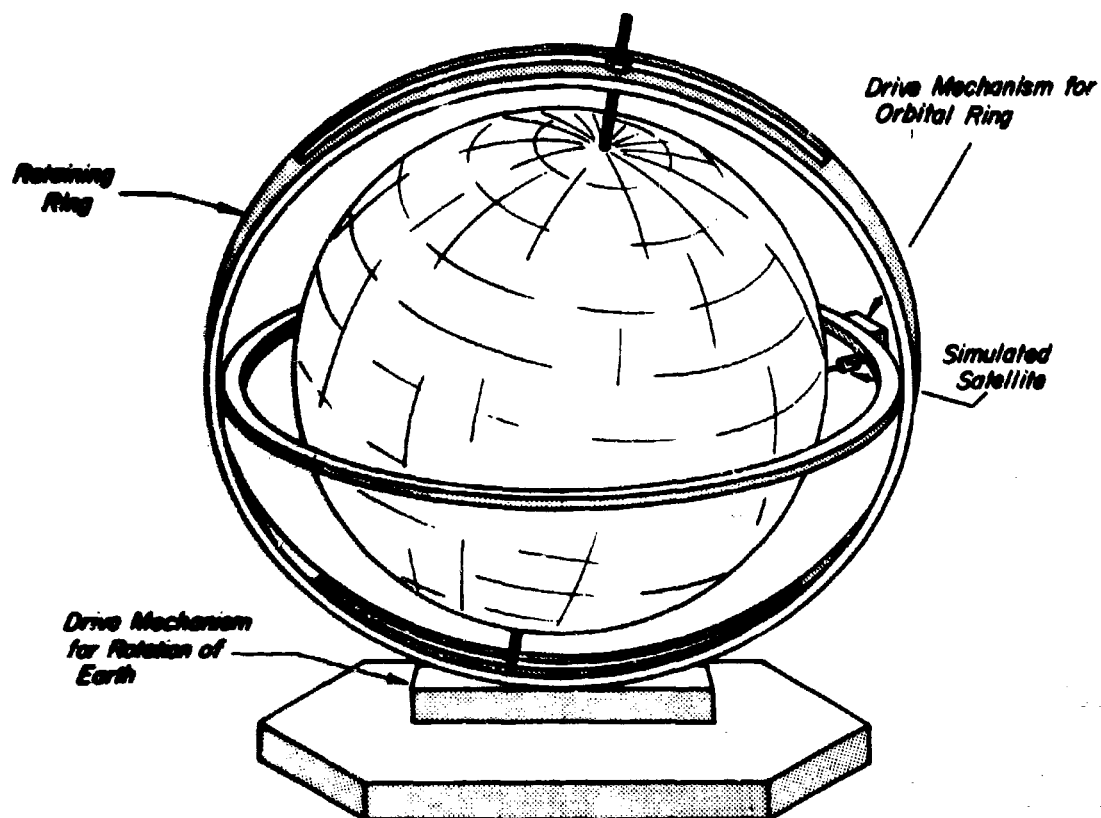


Figure 110. Schematic of a Global Orbital Simulator

in a simple form, a device such as that proposed can be useful to provide visualization of the three-dimensional aspects of orbital geometry which cannot be easily obtained from diagrams alone.

16.4.2 Polar Projection Plotting Board

A relatively simple device that is extremely useful for demonstrating many aspects of orbit geometry is the polar projection plotting board, developed by ARACON, for the orbital calculations required to acquire and locate APT data.

The APT Tracking Board (Fig. 111) is a polar projection diagram of the earth centered at a pole and extending 30 degrees of latitude past the equator into the other hemisphere. The actual board has concentric circles of latitude, and radials of longitude, at one-degree intervals, with those for every five-degree interval accentuated. (Because of the reduced scale of Fig. 111, only the ten-degree latitude and longitude lines are shown.) The equator is represented by a heavier circle since several aspects of the satellite tracks are referenced to the equator or to distances along it.

For convenience, the latitude circles are marked on a separate arm which pivots about the pole. Longitudes are marked around the circumference.

It is to be noted that, after exchanging the east and west labeling of longitudes, the board can be used in either hemisphere.

The associated orbital overlay is a sheet of clear plastic which is fastened to and can rotate about the pole of the Tracking Board. It can be used to plot satellite subpoint track(s), heading lines, and satellite equator crossings. Because of the frequent use of equator crossings (ascending and descending nodes), the equatorial circle is also printed on this overlay. Two or more transparent orbital overlays can be mounted one above the other on the board where the matters to demonstrated make it desirable.

Also available with the tracking boards are sets of tracking diagrams which can be useful in demonstrating some aspects of satellite viewing geometry. The tracking diagrams are drawn to the scale of the Tracking Board, and show the direction from the central point in azimuth and the distance in degrees of great circle arc (see smaller diagram on Fig. 111). The exact directions, shapes, and sizes of the lines on the tracking diagrams change with station latitude. Diagrams are available for five-degree increments of latitude, and the diagram drawn for the latitude closest to that of a given ground station location should be used.

APT SYSTEM

METEOROLOGICAL SATELLITE
PLOTING BOARD
AND
TRACKING DIAGRAM

APT STATION: SHANAHAN, ALA.
LOCATION: 32°N. LAT., 122°W. LONG.
ARACON LABORATORIES
A DIVISION OF ALLIED TELEGRAPH & TELEPHONE CO.
LONDON ENGLAND 1963

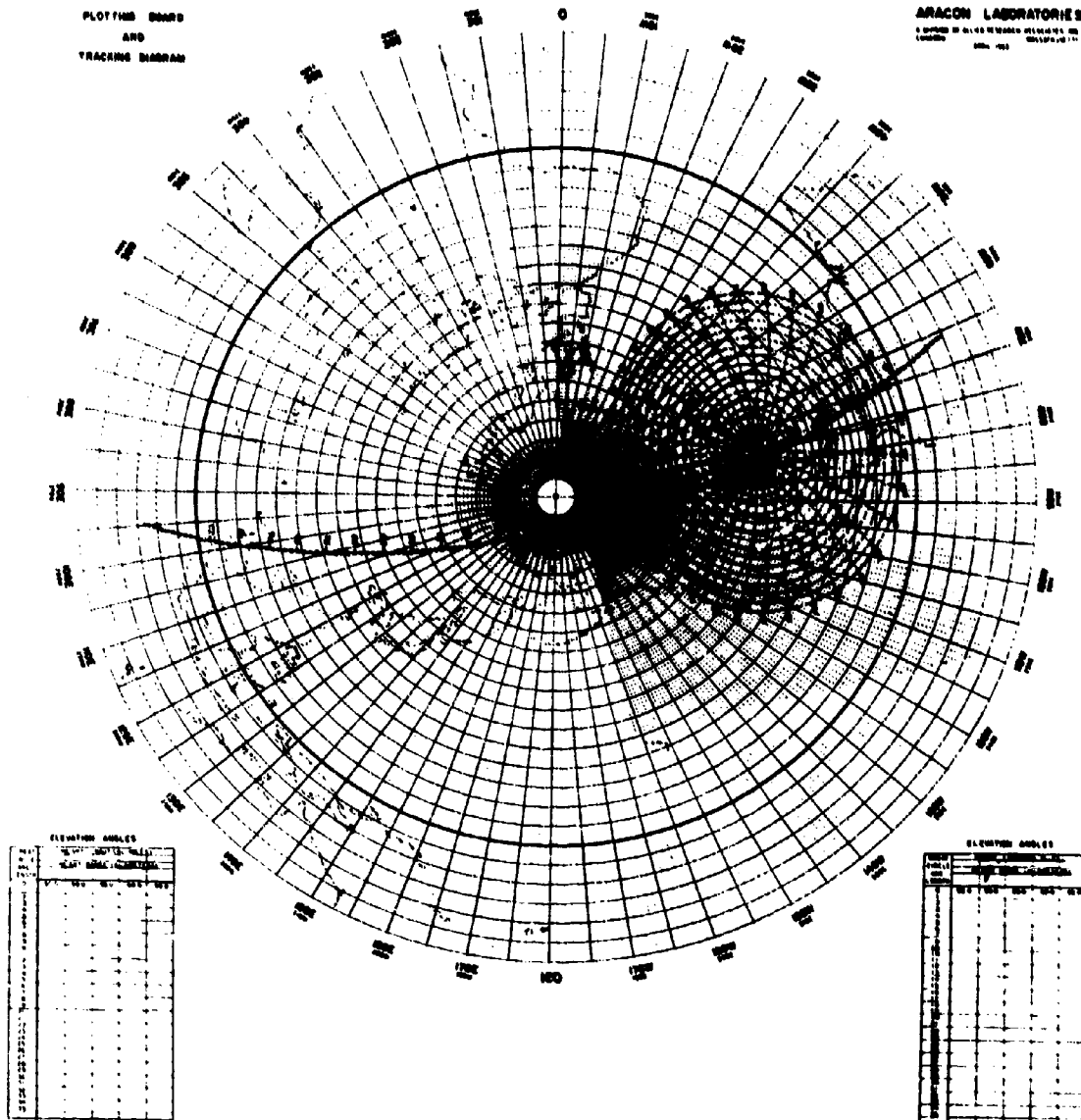


Figure 111. The APT Tracking Board

For use as training demonstrators, subpoint tracks[†] and heading lines (for various representative orbital inclinations and altitudes) would be drawn on separate transparent orbital overlays, and placed or superimposed on the plotting board as appropriate. Matters that could be demonstrated would include:

1. Effects of orbital inclination on coverage.
2. Change of longitudinal coverage from orbit to orbit, using two subpoint tracks (on same or different overlay) with appropriate ascending node differences.
3. Effects of highly elliptical orbits, by marking equal time increments (say two minute intervals) along subpoint track and showing how they are farther apart near perigee (greater velocity) and closer together near apogee.
4. Differences between subpoint tracks and heading lines, using related subpoint track and heading line plots on superimposed transparent overlays.
5. Relationships between argument, inclination, and latitude, using several subpoint tracks for different inclinations on a single overlay, with argument marked along each track.
6. Orbital velocities, by marking equal time intervals along subpoint tracks.
7. Viewing coverage, or ground station readout range, using the tracking diagram and/or circles of appropriate diameters for different satellite altitudes.
8. Differences and relationships between Right Ascension and longitude, using a transparent overlay with a Right Ascension scale, and possibly also the directions to the sun at different times of the year.
9. An overlay which is opaque or semi-opaque over a semi-circle of the board, placed over an overlay with a subpoint track plotted on it, could be used to illustrate illumination considerations and their variations relative to ascending node.

16.5 Techniques for the Demonstration of the Effects of Satellite Viewing Geometry

The large quantities of satellite data that are already in existence, form an excellent basis for demonstrating many aspects of satellite viewing geometry.

Existing satellite data can be placed into the following classes when considered in terms of this objective:

[†] The RAND Corporation has developed a specific polar projection calculation for subpoint tracks (Myland, F.S., 1965: A Calculator for Satellite Ground Tracks, Memorandum RM-3741-1-PR, and the associated calculator).

1. TIROS Television Data: Taken at a wide variety of camera nadir angles ranging from zero to well above the horizon. Most sequences will include a number of successive, overlapping pictures; this permits objects to be illustrated at several object nadir angles and resolutions (the two being correlated).

a. Wide Angle Camera (Elgeet): 2-3 mile resolution[†], 700 n.mile coverage[†], 104° diagonal field of view. This is the only camera so far used in meteorological satellites that showed significant lens distortion. (In TIROS IX, subpoint resolutions varied from about 2-10 miles due to the eccentric orbit. The cameras were at nominal nadir angles of 26.5° - often near 30° in practice - at the instant of picture taking.)

b. Medium Angle Camera (Tegea): 1 1/2 - 2 mile resolution, 450 - 500 n.mile coverage, 76° diagonal field of view.

c. Narrow Angle Camera: 0.2 mile resolution, 80 n.mile coverage, 12.7° diagonal field of view. The amount of this type of data is limited, since this camera was flown only on TIROS I and II.

2. Nimbus AVCS: This system has three cameras, each with a 37° (frame side) field of view. The center camera points vertical, the side cameras at 35° nadir angles. Resolutions vary from 0.2 - 0.3 n. miles (Nimbus I) to nominal values of 0.5 n. miles at 600 n. mile altitude (Nimbus C).

3. Nimbus APT, and TOS (ESSA) AVCS and APT: A single camera with a vertical axis, and a 108° diagonal field of view. Nominal resolutions are of the order of 1 - 2 miles.

Tables 16, 17, and 18 provide additional nominal camera characteristics for the TIROS, APT, and AVCS cameras.

4. Nimbus HRIR: A cross-tracking scanning sensor operating in the 3.7μ infrared window. Horizon-to-horizon scan, 3-5 mile resolution. Sensor acceptance angle is about 0.5°.

5. TIROS Channel 2 Infrared: This sensor had a complex scan pattern since the sensor looked at 45° to the spin axis and scanned through the combination of satellite velocity and rotation. Sensor nadir angles range from zero to the horizon. Resolution was about 30 miles (5° sensor acceptance angle).

[†] Unless otherwise specified, resolutions and coverages are nominal values for nadir angles of zero. Coverage is specified as the side of a frame.

Table 16

Camera Characteristics

Camera	Diagonal or Full Fields of View (Degrees)	Effective (Square Format) Field of View (Degrees)
Elgeet	104	84
Tegsa	76	58
TIROS Narrow Angle	12.67	9.0
Nimbus AVCS* †	—	37
Nimbus APT † ‡	108	88

Table 17

Nimbus Camera Fields of View

Altitude (N. Mi.)	Camera	<u>Coverage</u>	
		Along Track (N. Mi.)	Across Track (N. Mi.)
450	AVCS † Center	300	300
450	AVCS Side	350	570
450	APT † ‡	960	960
500	AVCS Center	320	320
500	AVCS Side	420	660
500	APT ‡	1,080	1,080
600	AVCS Center	400	400
600	AVCS Side	490	840
600	APT ‡	1,320	1,320
750	AVCS Center	500	500
750	AVCS Side	630	1,260
750	APT ‡	1,680	1,680

* The AVCS side cameras are mounted with the principal axis inclined 35° to the satellite axis.

† AVCS = Advanced Vidicon Camera System
APT = Automatic Picture Transmission

‡ Values also apply to TOS, AVCS, and APT.

Table 18

Approximate Best Practically Available Resolution of
Satellite Cameras

Satellite	Camera	Relative Location	Approximate Resolution (n. mi.)
TIROS	Wide Angle	Directly below satellite	2
		Straight down view, near picture edge	4
		Straight down view, near picture corner	7
		1/10 frame width from horizon	10
	Medium Angle	Directly below satellite	1-1/2
		Straight down view, near picture edge	2
		Straight down view, near picture corner	3
		1/10 frame width from horizon	8
Nimbus	Center	Directly below satellite	2/3
		Near picture edge	3/4
	Side	Nearer edge of picture	3/4
		Further edge of picture	3
	APT [‡]	Directly below satellite	2
		Near picture edge	4
		Near picture corner	7

* Values also apply to TOS, AVCS and APT.

For the purpose of showing the effects of satellite viewing geometry, it is suggested that prominent geographical features, for which adequate satellite pictures exist, be chosen. (There is no lack of such features; to list only a few cases in point: Italy, Egypt and Nile River, Great Lakes, Australia, Baja California, Spain, Florida, North and Northwest African coasts, Gulf of Newfoundland, Greenland, etc.) A training display would consist of a suitable standard map of the area, and several satellite views showing the geographical features at different nadir angles and resolutions.

**16.6 Techniques for the Demonstration of the Radiation Processes of
Significance to Satellite Geophysics**

In the interpretation of satellite data, an understanding of the relationships between the radiation processes of the earth and atmosphere, and the data obtained by the satellite sensor. This is especially true in the case of measurements made in the infrared.

Fundamental to IR sensing techniques are the relationships between the temperature and emissivity of a surface and the intensity of the radiation emitted by the surface. These principles can be readily demonstrated by means of the following classroom equipment:

- a. A calibrated radiometer
- b. Sets of targets with, respectively, different temperatures and different surface emissivities. Included in this set of target elements should be the following:

Blackbody cavities with controllable temperatures

Grey bodies

Samples of natural surfaces, such as water, sand, soil, etc.

With such simple devices, it would be possible to demonstrate the basic relationships between the physical properties of the surface in question and the surface emitted radiation.

If a more sophisticated radiometer is used, many more relationships can be demonstrated. For example, if the radiometer is provided with interchangeable filters (with the output calibrated for each of the filters), the following significant relationships can be qualitatively demonstrated:

- a. The spectral dependence of surface emissivity
- b. The effects of solar radiation contamination in the various spectral intervals in the infrared (using either actual sunlight or suitable artificial light sources).

The choice of target elements for these demonstrations should be made to maximize the matters to be illustrated.

In addition to the above relationships, it would be possible to demonstrate the effects of instrument resolution on the measured data. A radiometer having an adjustable field of view can be caused to view directly an adjacent pair of contrasting targets. The radiometer is first adjusted so that only one of the targets fills the

field of view. The output is recorded and compared to the output when the field of view includes both targets. The same demonstration can be performed by a non-adjustable radiometer by varying the distance between the radiometer and the target elements.

Many possibilities exist with this equipment. For example, the possibilities of "target" identification in IR window measurements, by noting variations in the sensor output, can be demonstrated.

Although these basic relationships are of particular significance in IR window sensing, they are also essential to an understanding of measurements made in absorption bands. This is especially true if surface emission is a significant factor in the measured radiation as in the case of thin or broken clouds.

In Section X, the radiation processes involved in absorption band measurements were discussed in detail. It was shown that these processes are highly complex. Unfortunately they are not easily simulated or realistically demonstrated. The effects are useful in satellite sensing due mainly to:

- a. The long path lengths involved
- b. The peculiar distribution of certain properties of the atmosphere.

Neither of these factors can be easily simulated. For example, in order to demonstrate the effect of atmospheric water vapor absorption on radiation at 6.3μ , it would be necessary to pass the radiation through an absorption cell with an equivalent path length, for reasonable moisture concentration, on the order of many hundreds of feet.

Several other possibilities have been considered during this study, such as optical analogues using a liquid medium. However, the problem still remains of demonstrating the combined effects of absorption, emission and the structure of the atmosphere. No solution has yet been found to this basic problem.

It does appear, however, that the basic processes can be adequately demonstrated by means of charts and graphs which show, for example:

- a. The spectral locations of the significant atmospheric absorption bands
- b. The variations of gaseous absorption (and emission) with gas concentration, pressure and temperature
- c. The history of the changes in beams of radiation, of various wavelengths, propagating through the atmosphere under various atmospheric conditions.

Figure 66 in Section X is an example of such a diagram. It should be noted that these illustrations can be animated.

SECTION XVII

APT TRAINING SIMULATOR

17.1 Introduction

It was pointed out previously that much of the details in the global satellite data, available at the National Meteorological Center (NMC) and the Suitland Fleet Weather Central, is not available to units of the fleet or to other Navy shore stations. The APT mode of data acquisition, and the related DRIR (Direct Readout Infrared) mode are the only current systems which can provide detailed satellite data to local Navy Weather units. These units must, of course, be equipped with suitable receiving sets. Such sets are relatively inexpensive; and it is probable that most significant naval stations, and many ships, will be equipped with them in the near future.

The APT permits stations to obtain satellite TV cloud data, in considerable detail, from an area within a radius of nearly 2,000 miles about the station. These data, available each day to a single station from a single satellite, consist of some three to nine (or more) pictures taken on one to three (or more) consecutive orbits. The coverage of each picture is 1,500 miles or more on a side. The Nimbus II DRIR mode provides nighttime cloud coverage through a similar mode of data transmission. The equipments necessary to receive these IR data are modified versions of those also used with the APT system.

Navy use of the APT and the DRIR requires both (1) the proper receiving equipment, and (2) trained personnel to operate the equipment and to process and interpret the received data. Accordingly, there exists a need to establish simulation schemes for the training of personnel in all aspects of APT (and DRIR) data acquisition and interpretation.

17.2 Summary of Operational Procedures Associated with the APT

The APT operational procedures are described in detail in a number of documents. The following outline provides a summary of the basic procedural steps:

1. Steps After Establishment of New Station, or Relocation of Station or Launch of New Satellite
 - a. Determine and plot current or nominal subpoint track
 - b. Determine limits of receivable orbits
2. Daily Preparation (Prior to Satellite Pass)
 - a. Obtain and interpret orbital message
 - b. Plot equator crossings and subpoint track
 - c. Determine usable passes
 - d. Determine antenna tracking data and record on worksheet i.e., determine, at one-minute or 30-second intervals, the antenna elevation and azimuth pointing angles, and the corresponding times, for each of the usable passes of the satellite.
3. Satellite Tracking and Data Acquisition
 - a. Set antenna to azimuth and elevation determined previously for initial satellite acquisition.
 - b. At appropriate times, move antenna rapidly and smoothly to new antenna pointing angles, based on previous calculations.
 - c. Record time of each APT picture. (For DRIR data, record times of points marked along data.)
4. Data Location and Geographical Gridding

17.3 Description of Ancillary Equipment

Based on the above summary of procedural steps, it may be seen that proper simulation training in the acquisition of APT or DRIR data requires the use of more than just an operational APT receiver console simulator, although the use of such a simulator is essential. In order to perform the steps listed above, the operator must make use of various ancillary devices and aids. These additional materials are listed and described below:

1. Tracking board
2. Transparent orbital overlay
3. Tracking diagrams
4. Tracking data worksheets
5. Tables and charts
6. Geographical grids

17.3.1 Tracking Board and its Associated Orbital Overlay and Tracking Diagram

The tracking board and its associated orbital overlays and tracking diagrams were described in Section XVI. In APT operations, they are used to assist the operator in locally determining tracking data (antenna pointing angles) from a generally disseminated set of orbital data (ephemeris). The details of the uses of these devices are described in References 12 and 43.

It should be noted that the tracking board is adaptable for classroom demonstration use. An enlarged version of it (analogous to a classroom demonstration model of a slide rule) can be made, and used to demonstrate the principles of its operation. Such a demonstration model can also be used with the three-dimensional orbital parameter simulator discussed previously to illustrate the relationships between (1) the orbit geometry in space and (2) its representation on the two-dimensional plotting board.

17.3.2 Charts and Tables

Unlike a slide rule, the tracking board has to be used in conjunction with sets of tables. These include, for example, tables of elevation angle as a function of great circle arc length and satellite altitude. Furthermore, the operator has to be able to interpret the daily APT orbital messages before he can plot the required data. The message is sent in a form analogous to many weather teletype messages. An example of such a message is shown in Figure 112. The key or explanation of the code symbols is shown in Table 19. Obviously, enlarged versions of this key, and of the aforementioned tables, would be invaluable for classroom instructional use. The same holds true for the tracking data worksheet.

17.3.3 Geographical Grids

From an APT picture alone, it is impossible to determine the geographical locations of the data unless a number of landmarks happen to be visible. To properly reference the data, geographical grids must be used. An example of such a grid is shown in Figure 113. Such grids are prepared to the scale of the satellite pictures. The correct use of these grids in geographical referencing of the data is discussed in step-by-step detail in References 12 and 43.

TBUS 2 KWBC 171810Z

APT PREDICT

051902

PART I

00639	01900	02716	27318	T0722	L2684
06430	73643	36582			
06471	44611	04155			
06512	15538	14891			

PART II

02112	067715	04112	133699
06112	199681	08122	266662
10122	331642	12122	397619
14122	462593	16122	527561
18132	591519	20132	653461
22132	712372	24132	764215
26132	798727	28133	795545

PART III

02117	067749	04117	133765
06117	199783	08126	266798
10126	331775	12126	397755
14121	462729	16126	527697
18136	591655	20136	653597
22136	712508	24136	764351
26136	798063	28135	795681

PART IV

Figure 112. Sample APT Daily Message

Table 19

Interpretation of Sample APT Daily Message

Message	TBUS 2 KWBC 171810Z
Interpretation	Satellite APT bulletin for south-north portion of orbit on the 17th day of the month (the month is determined from the third line of the message) Message originating at Washington, D. C. at 1810 GMT
Message	APT PREDICT
Interpretation	Predictions of subsatellite points and heights of satellite on the date and for the time specified in the message.
Message	051902
Interpretation	May 19 (year understood) second Nimbus satellite.
Message	PART I
Interpretation	Part I of message follows
Message	00639 01900 02716 27318 T0722 L2684
Interpretation	Reference Orbit is 639 and occurs on the 19th day of the month, equator crossing time 002716 GMT, equator crossing longitude 173.18°E (Octant 2), successive equator crossing time increments are 107 mins 22 secs, successive equator crossing longitude increments are 26.84 degrees.
Message	06430 73643 36582
Interpretation	Reference Orbit plus 4 = 643, equator crossing time 073643 GMT, equator crossing longitude 65.82°E (Octant 3).
Message	06471 44611 04155
Interpretation	Reference Orbit plus 8 = 647, equator crossing time 144611 GMT, equator crossing longitude 41.55°W (Octant 0).
Message	06512 15538 14891
Interpretation	Reference Orbit plus 12 = 651, equator crossing time 215538 GMT, equator crossing longitude 148.91°W (Octant 1).

Table 19 (cont'd)

Message	PART II
Interpretation	Coordinates of subsatellite points of Reference Orbit in northern hemisphere at two-minute increments from equator crossing.
Message	02112 067715 04112 133699
Interpretation	At 2 mins after equator crossing satellite height = 1110 km \pm 5 km, subsatellite point is at 6.7°N, 171.5°E (Octant 2); At 4 mins after equator crossing satellite height = 1110 km \pm 5 km, subsatellite point is at 13.3°N, 169.9°E (Octant 2)
Message	06112 199681 etc to last line of PART II:
Message	26132 798927 28133 795545
Interpretation	At 26 mins after equator crossing satellite height = 1130 km \pm 5 km, subsatellite point is at 79.8°N, 92.7°E; At 28 mins after equator crossing satellite height = 1130 km \pm 5 km, subsatellite point is at 79.5°N, 54.5°E
Message	PART III
Interpretation	Coordinates of subsatellite points of Reference Orbit in southern hemisphere at two-minute increments from equator crossing.
Message	02117 067749 04117 133765
Interpretation	At 2 mins before equator crossing satellite height = 1110 km \pm 5 km, subsatellite point is at 6.7°S and 174.9°E (Octant 7); At 4 mins before equator crossing satellite height = 1110 km \pm 5 km, subsatellite point is at 13.3°S and 176.5°E (Octant 7)
Message	06117 199783 08126 266798
Interpretation	At 6 mins before equator crossing satellite height = 1110 km \pm 5 km, subsatellite point is at 19.9° and 178.3°E (Octant 7); At 8 mins before equator crossing satellite height = 1120 km \pm 5 km, subsatellite point is at 26.6°S and 179.8°W (Octant 6) etc.

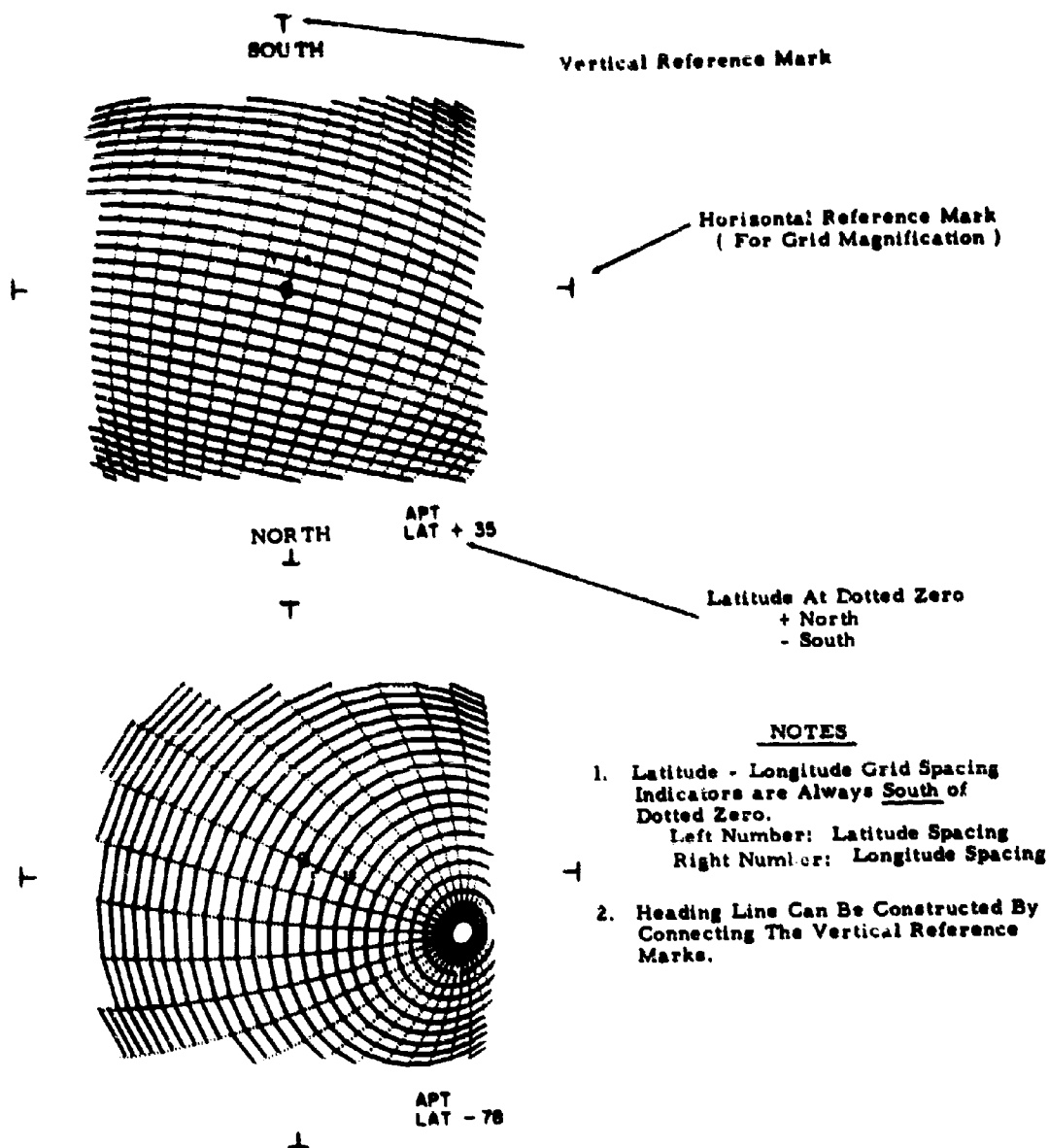


Figure 113. Sample APT Grids.

NAVTRADEVCEEN 66-C-0031-1

Classroom instruction in the proper use of the grids can be provided by having enlarged samples of actual APT pictures, with enlarged and possibly transparent grids which can be superimposed (or projected) on the pictures. The sample data used should reveal recognizable landmarks to demonstrate not only the use of landmarks in geographical referencing, but also to serve as indicators of the "correctness" of the gridding.

17.4 Simulation of APT Procedures

Besides classroom training in the uses of the various ancillary devices, it is necessary to provide the trainee with the opportunity to apply the techniques in a simulated operational environment. The procedures and equipment envisioned for such a simulation training scheme are as follows:

The trainee is placed in a physical environment similar to that found in a weather station on board ship, or at a Navy land station. Besides the normal equipment found in such a station, there is an APT simulator console. The design features of this console are discussed in Section 17.5. In addition, the trainee is provided with copies of the various devices and materials, discussed in the previous sections, needed for APT operations.

The trainee is then provided with appropriate orbital data and the assumed location of the station. (These data should correspond to the taped APT pictures to be generated by the console simulator, as will be discussed below.) Based on this information, he then proceeds through the steps given in Section 17.2 (1).

Having established the limits of useful orbits, he then uses the APT daily message (again corresponding to the data to be generated) and is required to go through the procedures in Section 17.2 (2).

The trainee then operates the console simulator in accordance with the steps outlined in Section 17.2 (3). Any antenna pointing errors are reflected in degradation of the pictures generated by the simulator.

After data reception, he is then required to geographically reference and grid the pictures. (A set of correctly referenced pictures should be available to check the trainee's progress.)

Those who must also be trained in the interpretation and utilization of the data, are also provided with the following additional items: (1) the operational requirements for the data (simulated operational Navy situation); (2) conventional data normally available under such operational conditions.

From these, he is required to prepare the weather analysis and forecast he would make in a similar operational situation.

In this scheme of APT simulation training, the most important item is the APT console simulator which not only serves to train operators in an entirely realistic way, but also generates data in an operational environment. The design features for such a simulator are discussed in the next section.

17.5 Simulator Description

In order to give the trainee a realistic "feel" of the operational situations he will face, the simulator will closely approximate, both in appearance and performance, the actual ground station equipment for which he is to be trained. In an operational situation, a man is usually faced with the following tasks at the time of the pass:

1. Antenna pointing, using azimuth and elevation controls to obtain predetermined settings as a function of time.
2. Monitoring of signal strength from meter reading and audio signal for verification or correction of his antenna pointing.
3. Tuning adjustments, for compensation of Doppler and transmitter or receiver drifts.
4. Maintenance of constant output level from receiver.
5. Determination of the time of occurrence of picture start tones.
6. Phasing of the facsimile recorder at the start of data reception.

The proposed simulator will require all of the above listed functions. The student "sees" the operational ground station sketched in Figure 114. A control panel, which permits the instructor to "setup" the pass, is available on the rear of the console.

Figure 115 shows the elements of the simulator in block diagram form. Figure 116 depicts the controls and meters to which the student addresses himself.

The input material for a simulated pass consists of APT or DRIR data recorded on magnetic tape, a card indicating the initial clock and antenna pointing angles and signal attenuation factor, and a paper tape from which the simulator generates the correct antenna pointing angles as a function of time. (The signal attenuation factor depends on the minimum slant range to be experienced during the pass.)

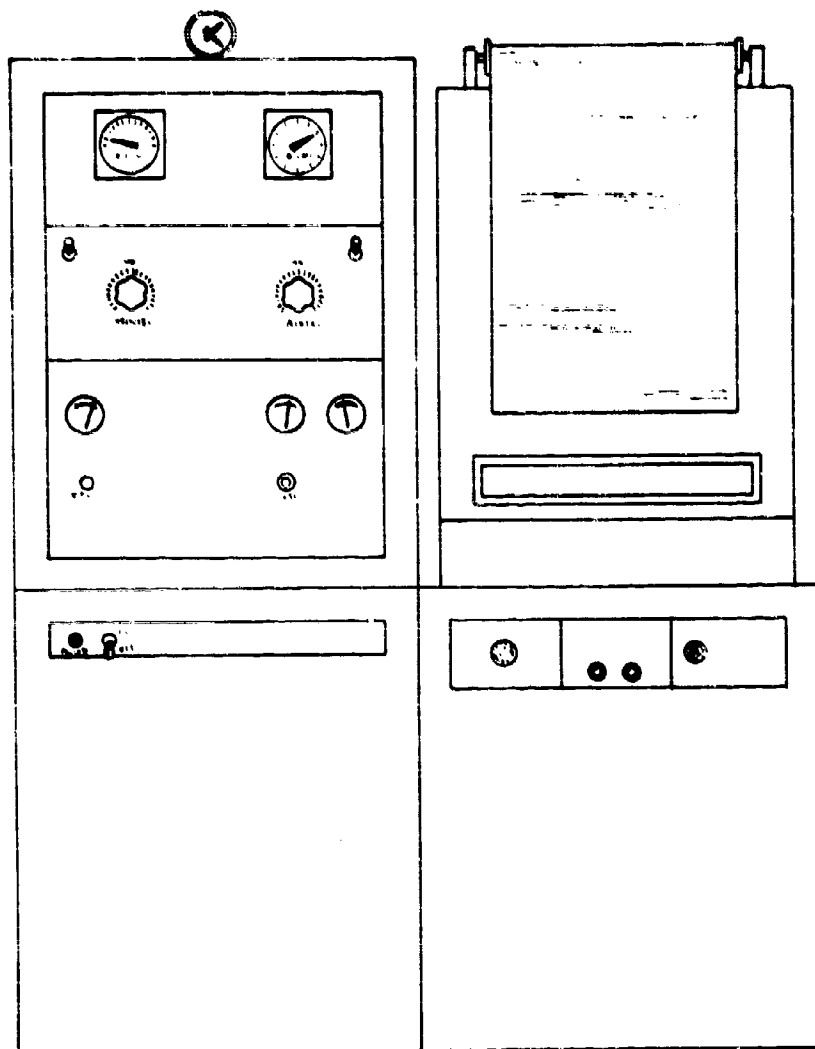


Figure 114. Sketch of APT Training Simulator

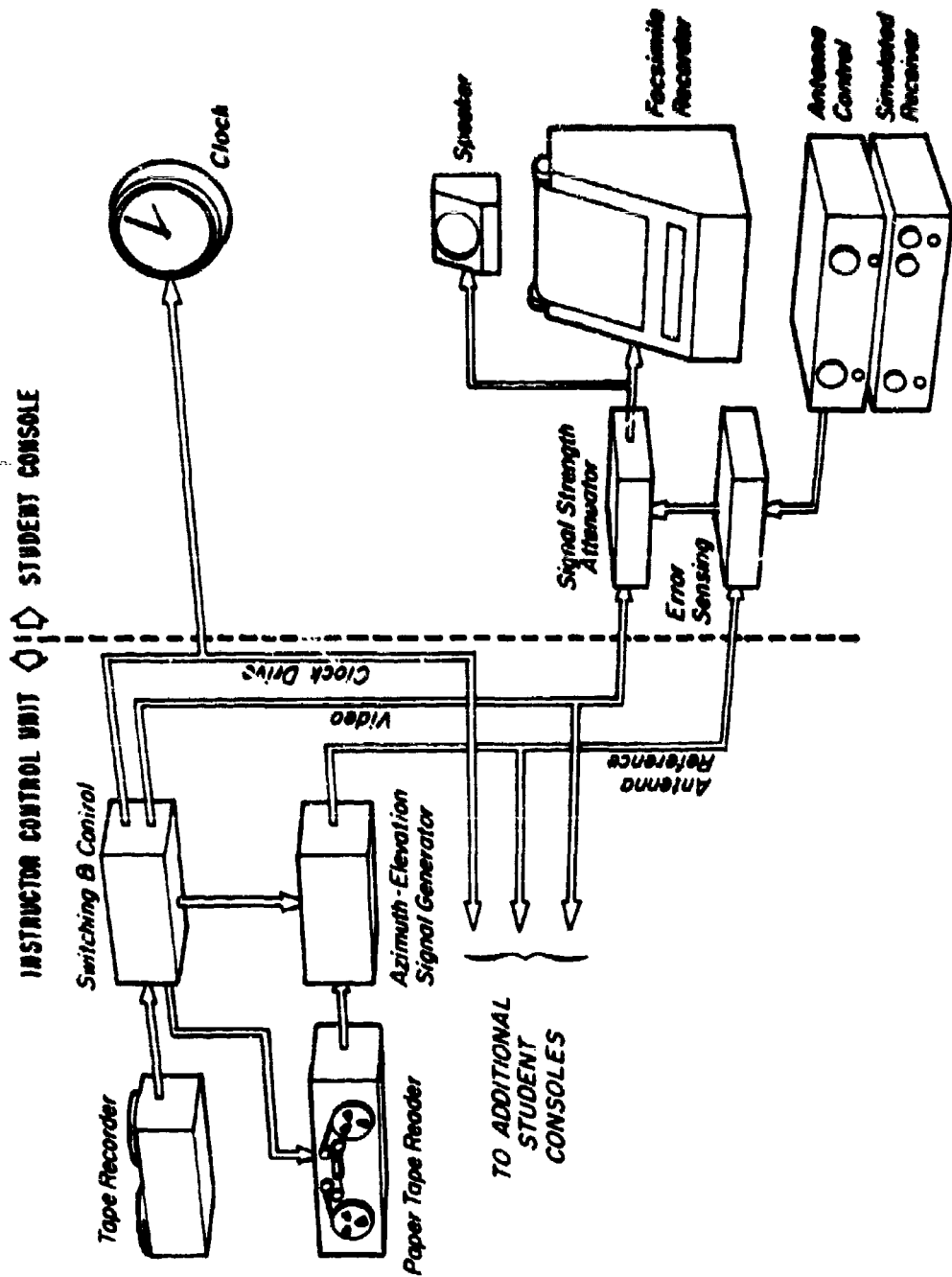


Figure 115. Block Diagram of APT Simulator

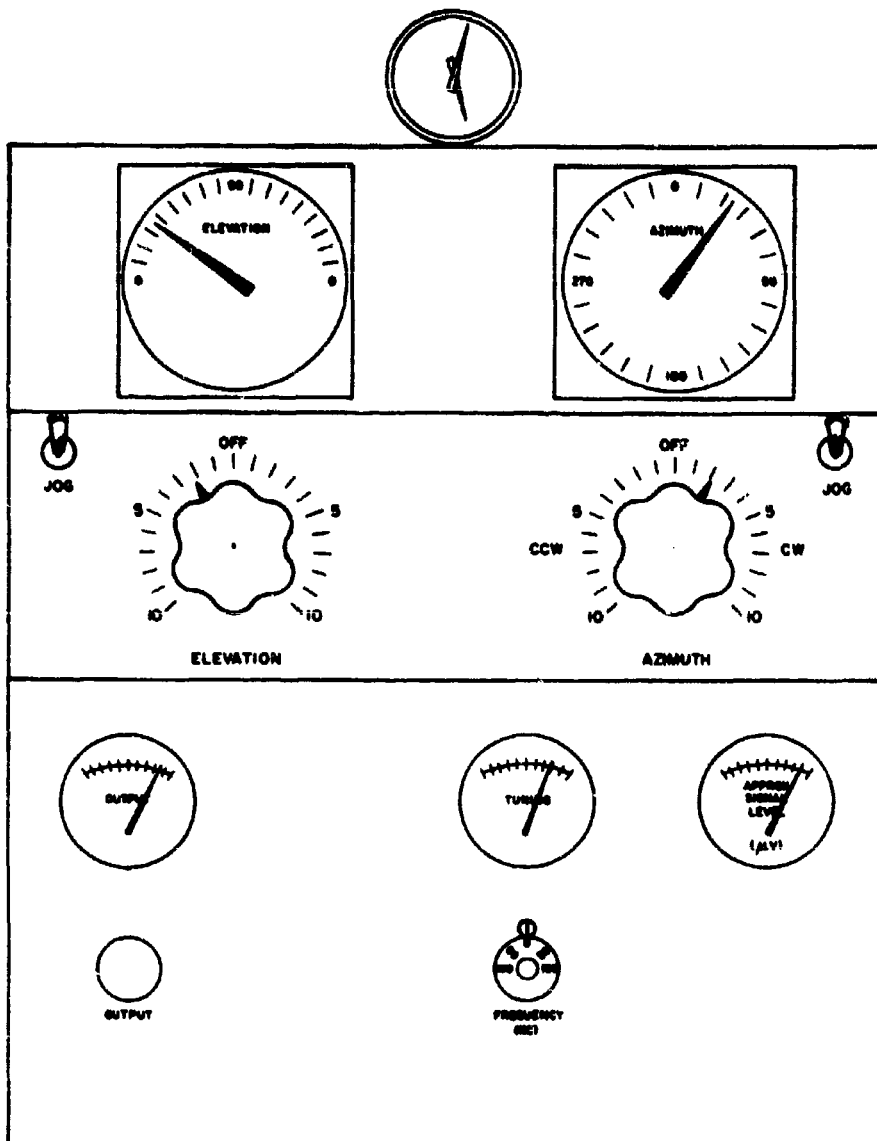


Figure 116. Students Control Panel

After the instructor sets up a pass, he starts the tape recorder. A carrier signal on the magnetic tape advances the facsimile in synchronism with the video data. The carrier also drives the paper tape reader and the clock, thus completely negating the effects of the magnetic tape recorder speed variations and tape stretch.

An azimuth-elevation signal generator produces analog signals from the data on paper tape. These signals are continually compared with those derived from the student's antenna rate settings. An antenna pointing error signal is generated from the difference between the true values and the values produced by the student, and the video signal is attenuated in proportion to the pointing error. The signal attenuation can be audibly and visibly detected by the student (from speaker output and signal level meter). In addition, the imagery degrades with the increase in pointing error.

Provision is made to vary the receiver signal strength and the Doppler in accordance with the change in satellite-to-ground-station slant range. Frequency deviations, due to Doppler shifts and instability in the satellite and receiver oscillators, should be compensated by an operator frequency adjustment. The facsimile recorder input signal level should be maintained at about -10 dbm. An output attenuator on the receiver panel permits the operator to maintain the receiver output meter reading at the 10 dbm level. The simulated frequency and output drifts can be entered into the system through potentiometers adjusted by the instructor.

The facsimile recorder used in the simulator can be identical to the recorder contained in the ground station. Manual phasing, required when the first received signal occurs after the picture start tone, is accomplished by the operator-trainee using the phasing switch.

The controls mentioned above include all those which usually require use in a normal pass. The remaining recorder and receiver controls are not adjusted on a pass-by-pass basis and would not seem to justify simulation.

REFERENCES

1. Fujita, T., 1963: A Technique for Precise Analysis for Satellite Data; Volume I - Photogrammetry, USWB, Meteorological Satellite Laboratory Report No. 14.
2. Goldshlak, L., and R. B. Smith, 1964: Nimbus Backup Gridding: AVCS and HRIR, Technical Report No. 1, Contract No. NAS 5-3253, ARACON Geophysics Company.
3. Glasstone, S., 1965: Sourcebook on the Space Sciences, Van Nostrand, Princeton, N.J., 937 pp.
4. Bandeen, W.R., 1961: Earth Oblateness and Relative Sun Motion Considerations in the Determination of an Ideal Orbit for the Nimbus Meteorological Satellite, NASA, Technical Note D-1045.
5. King-Hele, D., 1960: Satellites and Scientific Research, Routledge and Kegan Paul, London, or Dover, N.Y.
6. Widger, W.K., Jr., 1966: Meteorological Satellites, Holt, Rinehart and Winston, New York
7. Widger, W.K., Jr., and C.P. Wood, 1961: "An Explanation of the Limitations to the Coverage Provided by TIROS," Weatherwise, 14(6), pp. 230-237.
8. Goldshlak, L., and W.K. Widger, Jr., 1966: The Nimbus II Data Code Experiment, Technical Note No. 1, Contract No. NAS 5-10114, ARACON Geophysics Division, Allied Research Associates, Inc.
9. Christ, R.H., 1965: Computation of Sub-Satellite Point from Orbital Elements, NASA, Technical Note D-2771.
10. Siry, J.W., 1964: Goddard Orbit Information Systems, NASA, Goddard Space Flight Center, Document No. X-547-64-108.
11. Markham, T.R., and J.H. Willand, 1964: Operational Procedures Manual for the TIROS CDA Attitude and Gridding Teams, Technical Report No. 6, Contract No. NAS 5-1204, ARACON Geophysics Company.
12. Goldshlak L., 1963: APT User's Guide, Scientific Report No. 1, Contract No. AF 19(628)-2471, Allied Research Associates, Inc.
13. Smithsonian Institution, 1951: Smithsonian Meteorological Tables, Publication 4014, Washington, D.C.
14. Hovis, H., 1966: "Optimum Wavelength Intervals for Surface Temperature Measurements," Applied Optics, 5(5), pp. 815-818.

15. Kern, C.D., 1964: Evaluation of Infrared Emission of Clouds and Ground as Measured by Weather Satellites, Ph.D. Thesis, Department of Atmospheric Sciences, University of Washington (AD 617 417)
16. Lyon, R.J.P., 1962: Evaluation of Infrared Spectrophotometry for Compositional Analysis of Lunar and Planetary Soils, Final Report, Contract NASr-49(04), Stanford Research Institute, Menlo Park, California.
17. Centeno, V.M., 1941: "The Refractive Index of Liquid Water in the Near Infrared Spectrum," J. Opt. Soc. Am., 31, pp. 244-274.
18. Hyatt, H.A., 1965: Airborne Measurements of Microwave Emission from the Earth's Surface and Atmosphere, Douglas Paper No. 3684, Space Sciences Department, Missile and Space Systems Div., Douglas Aircraft Company, Inc., Santa Monica, California.
19. Barath, F.T., 1965: "Microwave Radiometry and Application to Oceanography," Oceanography from Space, The Woods Hole Oceanographic Institution, Woods Hole, Mass. (pp. 235-239).
20. McSwain, B. and J. Bernstein, 1961: Specular Reflectance of Water in the 1.5 to 15 Micron Region as a Function of Wavelength and Incidence Angle, Navwets Report 7162, Naval Ordnance Laboratory, Dept. of the Navy.
21. Gast, P.R., 1965: Solar Electromagnetic Radiation, in Handbook of Geophysics and Space Environments, (Edited by Shea L. Valley), AFCRL, Office of Aerospace Research, U.S. Air Force.
22. Krinov, E.L., 1953: Spectral Reflectance Properties of Natural Formations, National Council of Canada Technical Translation TT-439, Ottawa, Canada.
23. Glossary of Meteorology, 1959: (Edited by R.E. Huschke), American Meteorological Society, Boston, Mass.
24. Conover, J.H., 1965: "Cloud and Terrestrial Albedo Determinations from TIROS Satellite Pictures," J. of Applied Meteorology, 4(3), pp. 378-386.
25. Panndorf, R., 1956: Luminous and Spectral Reflectance As Well As Colors of Natural Objects, GRP No. 44, GRD, AFCRL, Air Research and Development Command. (AD-98766).
26. Shaw, J.H., 1954: Infrared Studies of Atmospheric Constituents, Final Report, Contract No. AF 19(122)-65, Ohio State University, Columbus, Ohio.
27. Kellogg, W.W., K.J.K. Buettner and E.C. May, 1964: Meteorological Satellite Observation of Thermal Emission, (Part 2 of An Examination of the Application to Satellite Meteorology of Various Segments of the Electromagnetic Spectrum), NASA Memorandum RM-4392, National Aeronautics and Space Administration.

28. Elterman, L., 1965: Atmospheric Optics, in Handbook of Geophysics and Space Environments, (Edited by Shea L. Valley), AFCRL, Office of Aerospace Research, U.S. Air Force.
29. Mazurowski, M.J., F.B. Silvestro, and J.D. Rinaldo, 1963: A Study of Photographic Contrast Attenuation by the Atmosphere, Technical Documentary Report ASD-TDR-63-541, Wright-Patterson Air Force Base, Ohio.
30. Duntley, S.Q., 1961: Ground Based Measurements of Earth to Space Beam Transmittance, Path Radiance, and Contrast Reduction, Contract No. AF 33(657)-7739, Visibility Lab., U. of California, Scripps Institution of Oceanography.
31. Zdunkowski, W., D. Henderson, J.V. Hales, 1964: The Influence of Haze on Infrared Radiation Measurements Detected by Space Vehicles, Final Report, Contract No. Cwb-10648, Inter-mountain Weather, Inc.
32. Richards, W.J., 1960: A Proposed Method for Locating Sferic Sources from an Earth Satellite, U.S. Army Signal Research and Development Laboratory, Fort Monmouth, New Jersey.
33. Foshee, L.L., I.L. Goldberg, and C.E. Catoe, 1964: The High Resolution Infrared Radiometer (HRIR) Experiment In: Observations from the Nimbus I Meteorological Satellite, NASA SP-89.
34. Widger, W.K., Jr., J.C. Barnes, E.S. Merritt, and R.B. Smith, 1965: Meteorological Interpretation of Nimbus High Resolution Infrared (HRIR) Data, Final Report, Contract No. NAS 5-9554, ARACON Geophysics Co., (Republished as NASA CR-352).
35. Smith, R.B., 1965: Manual Gridding of DRIR Facsimile Pictures, Technical Note No. 7, Contract No. NAS 5-3253, ARACON Geophysics, Allied Research Associates, Inc.
36. ARACON Geophysics Company, 1966: Proposal for an HRIR Rectification System.
37. Glaser, A.H., 1961: TIROS Meteorology, Final Report, Contract No. AF 19(604)-5581, Allied Research Associates, Inc.
38. Erickson, C.O., and L.F. Hubert, 1961: Identification of Cloudforms from TIROS I Pictures, Meteorological Satellite Laboratory Report No. 7, USWB, Washington, D.C.

39. ARACON Geophysics Company, 1965: Nimbus I User's Catalog: AVCS and APT, Aeronomy and Meteorology Division, NASA, Goddard Space Flight Center.
40. Staff Members, 1965: Nimbus I High Resolution Radiation Data Catalog and User's Manual: Volume I - Photofacsimile Film Strips, Aeronomy and Meteorology Division, Goddard Space Flight Center, NASA.
41. Glaser, A.H., 1959: A System for the Meteorological Operational Use of Satellite Television Observations, First Semi-Annual Technical Report, Contract No. AF 19(604)-5581, Allied Research Associates, Inc. (Reprinted in Contributions to Satellite Meteorology, GRD Research Note No. 36, AFCRC.)
42. Hubert, L.F., 1961: Canadian Grids for TIROS I, Supplement to Meteorological Satellite Report No. 5, UWSB, Washington, D.C.
43. National Weather Satellite Center, 1965: APT User's Guide, Environmental Science Services Administration, Washington, D.C.
44. Sanford, L.C., and D.I. Harvey, 1965: Evaluation of the Ground Recorder System of the Nimbus Project Advanced Vidicon Camera System, Final Report, Contract No. P.O. 33003 with ARACON Geophysics, prepared by Itak Corp.
45. Fujita, T. and W. Bandeen, 1965: "Resolution of the Nimbus High Resolution Infrared Radiometer," J. of Applied Meteorology, 4(4), pp. 492-503.
46. Allison, L.J., J.S. Kennedy, and G.W. Nicholas, 1964: "Examples of Meteorological Capability of the Nimbus I Satellite," In: Observations from the Nimbus I Meteorological Satellite, NASA SP-89.
47. Cooper, G., 1960: "Orbital Sampling Characteristics," Meteorological Satellite Systems Analyses, Second Semi-Annual Technical Summary Report, Contract No. AF 19(604)-5582, Allied Research Associates, Inc. (reprinted in Valocin, F.R. (Editor), 1961: Contributions to Satellite Meteorology, Vol. II, GRD Research Notes No. 36, AFCRL, pp. 351-367).
48. Soules, S.D., 1965: Infrared Photography of the Earth from Mercury Spaceflight MA-9, Meteorological Satellite Laboratory Report No. 25, ESSA.
49. Sledy, F., W.A. Morgan, and D.Q. Wark, 1965: "Determination of Cloud Altitudes from Gemini-Titan 5," Nature, 208, p. 775.
50. Wark, D.Q., and D.M. Mercer, 1965: "Absorption in the Atmosphere by Oxygen "A" Band," Applied Optics, 4(7), pp. 839-846.
51. Widger, W.K., Jr., P.E. Sherr and C.W.C. Rogers, 1964: Practical Interpretation of Meteorological Satellite Data, Final Report, Contract No. AF 19(628)-2471, ARACON Geophysics Company.

52. Fritz, S., 1963: "The Variable Appearance of the Earth from Satellites," Monthly Weather Review, 91, pp. 613-620.
53. Davis, P.A. 1964: Satellite Radiation Measurements and Atmospheric Heat Balance, Contract No. NAS 5-2919, Stanford Research Institute.
54. Prabhakara, C. and S.I. Rasool, 1963: "Evaluation of TIROS Infrared Data," Proceedings of First International Symposium on Rocket and Satellite Meteorology, H. Wexler and J.E. Caskey, Jr., Editors, North-Holland Publishing Company, Amsterdam.
55. Greaves, R.J., R. Wexler, and C.J. Bowley, 1965: The Feasibility of Sea Surface Temperature Determination Using Satellite Infrared Data, Final Report, Contract NASW-1157, ARACON Geophysics Co.
56. Long, R.K., 1963: Absorption of Laser Radiation in the Atmosphere, Contract No. AF 33(657)-10824, the Ohio State University Research Foundation, Columbus, Ohio.
57. Wark, D.Q., G. Yamamoto, and J.H. Lienesch, 1962: "Methods for Estimating Infrared Flux and Surface Temperatures from Meteorological Satellites," J. of the Atmos. Sciences, 19, pp. 369-384.
58. Kunde, V.G., 1964: "Theoretical Relationships Between Equivalent Blackbody Temperatures Measured by the HRIR," In: Observations from the Nimbus I Meteorological Satellite, NASA SP-89.
59. Nordberg, W., and R.E. Samuelson, 1964: "Terrestrial Features Observed by the HRIR," In: Observations from the Nimbus I Meteorological Satellite, NASA SP-89.
60. Rao, P.K. and J.S. Winston, 1963: "An Investigation of Some Synoptic Capabilities of Atmospheric 'Window' Measurements from Satellites," J. of Appl. Met., 2(1), pp. 12-23.
61. Winston, J.S., 1961: "Applications of Radiation Data to Synoptic Analysis and to Studies of the General Circulation," Proceedings of the International Meteorological Satellite Workshop, NASA-USWB, U.S. Government Printing Office, pp. 129-137.
62. Sherr, P.E. and C.W.C. Rogers, 1965: The Identification and Interpretation of Cloud Vortices Using TIROS Infrared Observations, Final Report, Contract No. Cwb-10812, ARACON Geophysics Co.
63. Elliot, R.D. and E.L. Hovind, 1965: "Heat, Water, and Vorticity Balance in Frontal Zones," J. Of Appl. Met., 4(2), pp. 196-211.

64. Merritt, E.S., 1963: Fleet Applications, Meteorological Operational Satellites, (Antarctic Area), Final Report, Contract No. N189(188)-56507A, ARACON Geophysics Co.
65. Colwell, R.N., 1966: "Aerial Photography of the Earth's Surface: Its Procurement and Use," Applied Optics, 5(6), pp. 883-892.
66. Moller, F., and E. Raschke: Evaluation of TIROS III Radiation Data, NASA CR-112.
67. Kennedy, J.S., 1966: An Atlas of Stratospheric Mean Isotherms Derived from TIROS VII Observations, NASA X-622-66-307.
68. Merritt, E.S. and D. Chang, 1966: Synoptic Studies of Satellite Measurements in the 15 μ CO₂ Band, Final Report, Contract No. N189(188)-59192A, ARACON Geophysics Division, Allied Research Associates, Inc.
69. Kaplan, L.D., 1959: "Inference of Atmospheric Structure from Remote Radiation Measurements," J. of Optical Society of America, 49, pp. 1004-1007.
70. King, J.F., 1965: Meteorological Inferences from Radiance Measurements, Final Report, Contract No. Cwb-10883, Geophysical Corporation of America.
71. Elsasser, W.M. (with M.F. Colbertson), 1960: "Atmospheric Radiation Tables," Meteorological Monographs, 4(23), 4311.
72. Goody, R.M., 1964: Atmospheric Radiation, I, Oxford University Press, London, 436 pp.
73. Howard, J.N., D.L. Burch and D. Williams, 1956: Infrared Transmission of Synthetic Atmospheres, Geophysical Research Paper No. 40, AFCRC, 245 pp.
74. Bardeen, W.R., B.J. Conrath, and R.A. Hanel, 1963: "Experimental Confirmation from the TIROS VI Meteorological Satellite of the Theoretically Calculated Radiance of the Earth Within the 15 Micron Band of Carbon Dioxide," J. of the Atmos. Sciences, 20(6), pp. 609-614.
75. Nordberg, W., W.R. Bardeen, G. Warnecke, and V. Kunde, 1964: "Stratospheric Temperature Pattern Based on Radiometric Measurements from the TIROS VII Satellite," Paper presented at the Fifth International Space Science Symposium, COSPAR, Florence, May 1964.
76. Wark, D.Q. and H.E. Fleming, 1966: "Indirect Measurements of Atmospheric Temperature Profile from Satellites," Monthly Weather Review, 94(6), pp. 351-362.

77. Morrison, A., and M.C. Chown, 1965: Photography of the Western Sahara Desert from the Mercury MA-4 Spacecraft, NASA Contractor Report CR-126, and
Bird, J.B., A. Morrison, and M.C. Chown, 1964: World Atlas of Photography from TIROS Satellites I to IV, NASA Contractor Report CR-98.
78. Long, R.K., 1963: Absorption of Laser Radiation in the Atmosphere, Contract No. AF 33(657)-10824, Ohio State University Research Foundation, Columbus Ohio.
79. Van de Hulst, H.C., 1957: Light Scattering by Small Particles, John Wiley and Sons, Inc., New York, 470 pp.
80. Coulson, K.L., J.V. Dave, and Z. Sekena, 1960: Tables Related to Radiation Emerging from a Planetary Atmosphere with Rayleigh Scattering, University of California Press.
81. Junge, C.E., Chagnon, C.W., 1961: "The Vertical Distribution of Submicron Particles in the Stratosphere," J. Meteor., 18, pp. 746-752.
82. The Boeing Company, 1961: Infrared Satellite Backgrounds, Part I, Atmospheric Radiative Processes, Final Report, Contract AF 19(604)-7457, The Boeing Company, Aerospace Division, Seattle, Washington
83. Dalgarno, A., 1962: Spectral Reflectivity of the Earth's Atmosphere III, Technical Report, Contract No. AF 33(657)-9199, Geophysics Corporation of America, Bedford, Massachusetts.
84. Schotland, R.M., A.M. Nathan, E.E. Chermack, and E.E. Uthe, 1962: Optical Sounding, Technical Report No. 2, Contract DA-36-039, New York University, Dept. of Meteorology and Oceanography.
85. Bandeen, W.R., B.J. Conrath, W. Nordberg, and P.H. Thompson, 1962: "A Radiation View of Hurricane ANNA from the TIROS II Meteorological Satellite," Proceedings of the First International Symposium on Rocket and Satellite Meteorology, John Wiley and Sons, Inc., New York.
86. Glaser, A.H., and S.N. Milford, 1960: "A Preliminary Investigation of the Nature of the Infrared View of the Atmosphere from a Satellite," Contributions to Satellite Meteorology, (Edited by W.K. Widger, Jr.), GRD Research Notes No. 36, AFCRC-TN-60-427.
87. Hanel, R.A., and L. Chaney, 1965: The Infrared Interferometer and Spectrometer Experiment (IRIS), Volume II, Meteorological Mission, Goddard Space Flight Center, Report X-650-65-75.

88. Vivian, W.E., 1963: "Principles of Radiometry Present State-of-the-Art," The Application of Passive Microwave Technology to Satellite Meteorology: A Symposium, (Edited by Y.H. Katz), NASr-21(07), The Rand Corporation, California.
89. Conway, W.H., and A. Mardon, 1965: "Microwave Radiometers for Ocean and Weather Measurements," Oceanography from Space, Woods Hole Oceanographic Institution, Woods Hole, Massachusetts.
90. B. Scheps, 1958: Terrains (Terrain Radar Interpretation Study), U.S. Geological Survey, (Reprint, U.S. Navy Antarctic Projects Office).
91. Pierson, W.J., B.B. Scheps and D.S. Simonett, 1965: Some Applications of Radar Return Data to the Study of Terrestrial and Oceanic Phenomena, NASA N 66-17345.
92. Wexler, R., 1960: "Satellite Observations of Infrared Radiation," Contributions to Satellite Meteorology, (Edited by W.K. Widger, Jr.), GRD Research Notes No. 36, AFRCRC-TN-60-427.
93. Hall, A.R., L. Berry, 1966: NASA/ESSA WEFAX Experiment, Technical Report No. 1, Contract NAS 5-10204, Allied Research Associates, Inc., Concord, Massachusetts.

U.S. NAVAL TRAINING DEVICE CENTER

January 1968
UNCLASSIFIED

Tech. Rept. NAVTRADEVEN 66-C-0031-1

STUDY, SIMULATION OF OCEANOGRAPHIC
AND GEOPHYSICAL SPACE-SENSOR DISPLAYS,
D. Chang, W.K. Widger, Jr., Allied Research
Associates, Inc., Concord, Massachusetts
(Contract N-61339-66-C-0031), xvi, 350p., 116 illus,
19 Tables, 93 Refs.

Detailed analyses have been performed of the
factors which affect the acquisition of geophysical
data by earth oriented satellites. Techniques and
devices for the simulation of satellite data and for
the training of personnel participating in satellite
geophysics are discussed.

Descriptors

SATELLITE
METEOROLOGY
OCEANOGRAPHY
GEOPHYSICS
TRAINING
SIMULATION

U.S. NAVAL TRAINING DEVICE CENTER

January 1968
UNCLASSIFIED

Tech. Rept. NAVTRADEVEN 66-C-0031-1

STUDY, SIMULATION OF OCEANOGRAPHIC
AND GEOPHYSICAL SPACE-SENSOR DISPLAYS,
D. Chang, W.K. Widger, Jr., Allied Research
Associates, Inc., Concord, Massachusetts
(Contract N-61339-66-C-0031), xvi, 350p., 116 illus,
19 Tables, 93 Refs.

Detailed analyses have been performed of the
factors which affect the acquisition of geophysical
data by earth oriented satellites. Techniques and
devices for the simulation of satellite data and for
the training of personnel participating in satellite
geophysics are discussed.

Descriptors

SATELLITE
METEOROLOGY
OCEANOGRAPHY
GEOPHYSICS
TRAINING
SIMULATION

U.S. NAVAL TRAINING DEVICE CENTER

January 1968
UNCLASSIFIED

Tech. Rept. NAVTRADEVEN 66-C-0031-1

STUDY, SIMULATION OF OCEANOGRAPHIC
AND GEOPHYSICAL SPACE-SENSOR DISPLAYS,
D. Chang, W.K. Widger, Jr., Allied Research
Associates, Inc., Concord, Massachusetts
(Contract N-61339-66-C-0031), xvi, 350p., 116 illus,
19 Tables, 93 Refs.

Detailed analyses have been performed of the
factors which affect the acquisition of geophysical
data by earth oriented satellites. Techniques and
devices for the simulation of satellite data and for
the training of personnel participating in satellite
geophysics are discussed.

Descriptors

SATELLITE
METEOROLOGY
OCEANOGRAPHY
GEOPHYSICS
TRAINING
SIMULATION

U.S. NAVAL TRAINING DEVICE CENTER

January 1968
UNCLASSIFIED

Tech. Rept. NAVTRADEVEN 66-C-0031-1

STUDY, SIMULATION OF OCEANOGRAPHIC
AND GEOPHYSICAL SPACE-SENSOR DISPLAYS,
D. Chang, W.K. Widger, Jr., Allied Research
Associates, Inc., Concord, Massachusetts
(Contract N-61339-66-C-0031), xvi, 350p., 116 illus,
19 Tables, 93 Refs.

Detailed analyses have been performed of the
factors which affect the acquisition of geophysical
data by earth oriented satellites. Techniques and
devices for the simulation of satellite data and for
the training of personnel participating in satellite
geophysics are discussed.

Descriptors

SATELLITE
METEOROLOGY
OCEANOGRAPHY
GEOPHYSICS
TRAINING
SIMULATION

Unclassified

Security Classification

DOCUMENT CONTROL DATA - R & D

(Security classification of title, body of abstract and indexing annotation must be entered when the overall report is classified)

1. ORIGINATING ACTIVITY (Corporate author) Allied Research Associates, Inc. Virginia Road Concord, Massachusetts 01742		2a. REPORT SECURITY CLASSIFICATION Unclassified	
		2b. GROUP N/A	
3. REPORT TITLE Study, Simulation of Oceanographic and Geophysical Space-Sensor Displays			
4. DESCRIPTIVE NOTES (Type of report and inclusive dates) Final Report			
5. AUTHOR(S) (First name, middle initial, last name) David T. Chang and Dr. William K. Widger, Jr.			
6. REPORT DATE January 1968		7a. TOTAL NO. OF PAGES 366	7b. NO. OF REFS 93
8a. CONTRACT OR GRANT NO. N61339-66-C-0031		8a. ORIGINATOR'S REPORT NUMBER(S) 9G28-F	
b. PROJECT NO. 7918-1			
c.		9b. OTHER REPORT NO(S) (Any other numbers that may be assigned this report) NAVTRADEVCEEN 66-C-0031-1	
d.			
10. DISTRIBUTION STATEMENT Each transmittal of this document outside the Department of Defense must have prior approval of the Naval Training Device Center (Code 424), Orlando, Florida 32813			
11. SUPPLEMENTARY NOTES		12. SPONSORING MILITARY ACTIVITY Naval Training Device Center Orlando, Florida 32813	
13. ABSTRACT <p>Detailed analyses have been performed of the factors which affect the acquisition of geophysical data by earth-oriented satellites. These factors include geophysical, instrumental, and display. Based on these analyses, techniques for the simulation of satellite data and for the training of personnel participating in satellite geophysics are discussed.</p> <p>Devices useful for training have been conceptually designed. In particular, the design and use of an APT (Automatic Picture Transmission) simulator trainer are analyzed in detail.</p>			

DD FORM 1 NOV 65 1473

(PAGE 1)

S/N 0101-807-6801

Unclassified

Security Classification

14. KEY WORDS	LINK A		LINK B		LINK C	
	ROLE	WT	ROLE	WT	ROLE	WT
Displays Geophysics Meteorology Oceanography Satellite Simulation Space Sensors Training						